CHEMIA

STUDIA
UNIVERSITATIS BABEŞ-BOLYAI

CHEMIA

S T U D I A
UNIVERSITATIS BABEŞ-BOLYAI
CHEMIA

4

Tom I

Dedicated to the Memory of Prof. Emil Chifu

CUPRINS – CONTENT – SOMMAIRE – INHALT

IN MEMORIAM

EMIL CHIFU (1925-1997)

This year **2017** *marks the* **20th** **year** *from the death of Professor* **Emil Chifu**. This year also signifies **40 years** *from the first scientific research project proposed by Professor* **Chifu** and accepted for exploring in cosmos by **NASA** (National Aeronautics and Space Administration) of the United States of America.

The prominent Romanian scientist, Professor Emil Chifu was an outstanding physical chemist, recognized by the international scientific community. He was one of the founders of the modern science of colloids, surfaces and membrane phenomena, thermodynamics and hydrodynamics of thin layers formed by surface active substances self-assembled into supramolecular structures at liquid interfaces [1].

Professor Emil Chifu has created a modern research school in thermodynamics and physical chemistry of colloids and surfaces, at the Faculty of Chemistry and Chemical Engineering, "Babes-Bolyai" University of Cluj-Napoca (UBB) [1-7]. Currently, this school is known as the Center of Research in Physical Chemistry and it is accredited in the UBB.

Professor Emil Chifu was the *first Romanian scientist* whose original research proposal "Surface Flow of Liquids in the Absence of Gravity", based on the highest rank scientific results [8], was selected in 1977 by NASA**,** of the USA, and after being rigorously valued by NASA, it was approved on the 28th of March, 1978, to be experimented on Space Laboratory (SpaceLab) in 1981. This research project proposed by Professor Emil Chifu represents the *first Romanian cosmic experiment* approved by the NASA of USA in 1978, and it refers to *two types* of space investigations: ♦surface flow between two liquid surfaces joined by surface channels and ♦surface flow on a liquid drop in the absence of gravity; both were planned by NASA to be realized on the *first flight* of the *Drop Dynamics Module* (DDM) known as *"Chifu's experiment"*. The DDM experiment was scheduled by NASA to be explored on the SpaceLab-3.

On the basis of this research project, a *Framework Agreement (FA)* was settled between the Romanian Commission for Space Activities (CRAS) and the NASA of USA, as reported by Ioan Ursu, the president of the National Council for Science and Technology (CNȘT) in Romania, in the address no. 2460/16th December 1978 to the Ministry of National Education and Instruction.

The preparatory experiments in the laboratory phases were performed within the framework of a contract between UBB, Professor Emil Chifu being the project responsible and simultaneously the chair of the physical chemistry department and the CNŞT for the period of 1977-1980.

The setup model of *Chifu's experiment* was performed in the Jet Propulsion Laboratory (JPL) of the California Institute of Technology, Pasadena, USA in 1981, and it was implemented on the DDM in the NASA mission of the SpaceLab-3.

Professor Chifu and his research team studied the dynamics of a "free" liquid drop immersed in another liquid with equal density, in simulated microgravity laboratory conditions in UBB, Romania. Valuable theoretical and experimental results have been advanced by professor Chifu and his co-workers aiming at exploring the drop dynamics in cosmos, on SpaceLab-3, in which the microgravity conditions were rigorously satisfied.

The investigation of the professor Chifu's proposal in space conditions is a *premiere* in the study of the drop dynamics in imponderability, because the implied physical and chemical phenomena are of a major interest, both for the science and technology of liquids in the cosmic space and for industrial process as well as for examination of cell movements and biological membrane mobility.

The space experiment of professor Chifu has started the Romanian multi-disciplinary frontier research in the physical chemistry of thin films; over 60 published papers of which we recorded some [9-25] have been awarded with the "Gh. Spacu" Prize by the Romanian Academy in 1983. Professor Chifu became Emeritus Professor in 1990 at Babes-Bolyai University of Cluj-Napoca.

He published over 160 research articles and 14 books; 4 books were revised and completed posthumously by his collaborators [26-29].

The results of the scientific investigations in domains such as: thermodynamics of irreversible phenomena, liquid/liquid extraction, studies on nickel carbonyl powders, on sulphurous ores, on the foaming power of detergents have been implemented in the economic sphere on the basis of the research contracts concluded with important mining centres in Deva and Baia Mare, with chemical industries in Victoria, Ploiesti, Fagaras, as well as with the Central for drugs and cosmetics, in Bucharest.

REFERENCES

1. M. Tomoaia-Cotisel and D.A. Cadenhead, *Journal of Colloid and Interface Science*, **1997**, *195,* 271.
2. M. Tomoaia-Cotisel and J. Zsako, *Studia Universitatis Babes-Bolyai, Chemia*, **1998**, *43* (1-2), 3.

3. P.T. Frangopol, *Revista de Chimie (Bucureşti),* **2002**, *53* (6), 495.

4. M. Tomoaia-Cotisel, A. Chifu, *Studia Universitatis Babes-Bolyai, Chemia*, **2007**, *52* (3), 3.

5. P.T. Frangopol, *Emil Chifu* în Personalităţi ale Istoriei Chimiei Româneşti, *Mediocritate şi Excelenţă, O radiografie a ştiinţei şi învăţământului din România,* Chapter III, vol. 3, Casa Cărţii de Ştiinţă, Cluj-Napoca, **2008**, pp. 175-180.

6. P.T. Frangopol, *The first Romanian cosmic experiment approved by NASA- proposed by Emil Chifu,* în *Revista de Politica Ştiinţei şi Scientometrie - Serie nouă*, **2015**, *4* (2), 155.

7. P.T. Frangopol, *Emil Chifu,* în *Mediocritate şi Excelenţă, O radiografie a ştiinţei şi învăţământului din România,* Chapter VIII, vol. **6**, Casa Cărţii de Ştiinţă, Cluj-Napoca, **2016**, pp. 272-275.

8. E. Chifu, "Surface flow of liquids in the absence of gravity", ***Proposal*** selected by NASA's Office of Aeronautics and Space Technology, **1977**.

9. E. Chifu, I. Stan, Z. Finta and E. Gavrilă, Marangoni type surface flow on an undeformable free drop, *Journal of Colloid and Interface Science*, **1983**, *93* (1), 140.

10. E. Chifu, I. Stan, Z. Finta and E. Gavrilă, The Marangoni effect and translation of free non-deformable drops, *Revista de Chimie (Bucureşti),* **1980**, *31* (8), 765.

11. E. Chifu, I. Albu, C. I. Gheorghiu, E. Gavrilă, M. Sălăjan and M. Tomoaia-Cotişel, Marangoni flow-induced by temperature gradients-against gravity forces, *Revue Roumaine de Chimie,* **1986**, *31* (1), 105.

12. E. Chifu and I. Albu, Interfacial tension variation in the course of liquid-liquid extraction. II. Molecular associations on extracting some monocarboxylic aliphatic acids, *Annali di Chimica (Rome).***1975**, *65* (9-10), 519.

13. E. Chifu, M. Tomoaia, and A. Ioanette, Behaviour of canthaxanthin at the benzene/water and air/water interfaces, *Gazzetta Chimica Italiana,* **1975**, *105* (11-12), 1225.

14. M. Tomoaia-Cotisel, E. Chifu, V. Tămaş and V. Mărculeţiu, Behaviour of some apocarotenoid derivatives at the air/water interface, *Revue Roumaine de Chimie,* **1980**, *25* (2), 175.

15. E. Chifu, J. Zsakó, and M. Tomoaia-Cotişel, Xanthophyll films. I. Single-component monolayers at the air/water interface, *Journal of Colloid and Interface Science*, **1983**, *95* (2), 346.

16. M. Tomoaia-Cotişel, J. Zsakó, E. Chifu and P. J. Quinn, Influence of electrolytes on the monolayers properties of saturated galactolipids at the air/water interface, *Chemistry and Physics* of *Lipids,* **1983**, *34* (1), 55.

17. J. Zsakó, M. Tomoaia-Cotisel and E. Chifu, Insoluble mixed monolayers. I. Phase equilibria at the collapse of binary monolayers at gas/liquid interfaces, *J. Colloid Interface Sci.*, **1984**, *102* (1), 186.

18. E. Chifu, J. Zsakó, M. Tomoaia-Cotişel, M. Sălăjan and I. Albu, Xanthophyll films. **IV**. Interaction of zeaxanthin and astaxanthin with electrolytes at the air/water interface, *Journal of Colloid and Interface Science*, **1986**, *112* (1), 241.

19. M. Tomoaia-Cotisel, J. Zsakó, E. Chifu and P.J. Quinn, Intermolecular interactions in lipid-carotenoid monolayers, *Biochemical Journal*, **1987**, *248*, 877.

20. M. Tomoaia-Cotisel, J. Zsakó, A. Mocanu, E. Chifu, P.J. Quinn, Monolayer properties of membranes lipids of the extreme *Halophile Halobacterium Cutirubrum* at the air *I* water interface, *Biochimica et Biophysica Acta,***1988**, *942*, 295.
21. M. Tomoaia-Cotisel, J. Zsakó, E. Chifu and D.A. Cadenhead, Relaxation phenomena in apocarotenoid monolayers, *Langmuir*, **1990**, *6* (1), 191.
22. J. Zsakó, M. Tomoaia-Cotisel, E. Chifu, A. Mocanu and P.T. Frangopol, Influence of stearic acid monolayers upon the procaine adsorption from underlying alkaline aqueous solutions, *Biochimica et Biophysica Acta,* **1990**, *1024*, 227.
23. M. Tomoaia-Cotisel, E. Chifu, J. Zsakó, A. Mocanu, P.J. Quinn and M. Kates, Monolayer properties of archaeol and caldarchaeol polar lipids of a methanogenic archaebacterium, *Methanospirillum hungatei*, at the air/water interface, *Chemistry and Physics* of *Lipids,* **1992**, *63,* 131.
24. J. Zsakó, M. Tomoaia-Cotisel, E. Chifu, A. Mocanu and P.T. Frangopol, Procaine interactions with phospholipid monolayers at the air/water interface, *Gazzetta Chimica Italiana,* **1994**, *124*, 5.
25. M. Tomoaia-Cotisel, L.C. Stewart, M. Kates, J. Zsakó, E. Chifu, A. Mocanu, P.T. Frangopol, L.J. Noe and P.J. Quinn, Acid dissociation constants of diphytanyl glycerol phosphorylglycerol-methylphosphate, and diphytanyl glycerol phosphoryl glycerophosphate and its deoxy analog, *Chemistry and Physics* of *Lipids,* **1999**, *100,* 41.
26. E. Chifu, *"Chemistry of Colloids and Interfaces"*, Editors: M. Tomoaia-Cotisel, I. Albu, A. Mocanu, M. Salajan, E. Gavrila and Cs. Racz, University Press*,* Cluj-Napoca, **2000**.
27. E. Chifu, M. Tomoaia-Cotisel, I. Albu, A. Mocanu, M.-I. Salajan, Cs. Racz and V.D. Pop, *"Experimental Methods in Chemistry and Biophysics of Colloids and Interfaces"*, University Press*,* Cluj-Napoca, **2004**.
28. M. Tomoaia-Cotisel, I. Albu and E. Chifu, "Chemical Thermodynamics", The 2nd Edition, University Press, Cluj-Napoca, **2009***.*
29. M. Tomoaia-Cotisel, I. Albu and E. Chifu, "Chemical Thermodynamics", The First Edition, University Press*,* Cluj-Napoca, **2009***.*

Alexandra Chifu, Aurora Mocanu,
Maria Tomoaia-Cotisel

CATECHIN OXIDATION PRODUCTS: MECHANISTIC ASPECTS AND KINETICS

ANCA - RUXANDRA LEONTIEŞ[a]*, ADINA RĂDUCAN[b], IOANA CATALINA GÎFU[a], DAN FLORIN ANGHEL[a]

ABSTRACT. The oxidation of catechin in the presence of atmospheric oxygen in a methanol/buffer model solution was studied by investigating generated products using LC/MS and spectrophotometry. It was proved that catechin was slowly converted to dimeric species with similar structures and properties. The catechin autoxidation was investigated spectrophotometrically at different pH ranging between 5 and 10. Using the initial linear dependence of the kinetic curves [Dimers] = f(t) the initial reaction rates were estimated for the autoxidation of catechin in methanol/buffered solutions. It was found that the dimer formation is favored at pH 8.

Keywords: catechin, autoxidation, dehydrocatechin

INTRODUCTION

Polyphenols are widely distributed in plants and in plant-derived products, mostly in wines and teas, where they contribute to food organoleptic properties and oxidative stability [1]. Polyphenols have several health benefits, acting as antioxidant, anticarcinogen, antimicrobial, anti-inflammatory and UV protection agents [2].

One of the most common natural polyphenols from the class of flavanols is catechin (Scheme 1). As polyphenol, catechin is susceptible to enzymatic and non-enzymatic oxidation. The oxidation products are the oxidation dimers. The dimers are linked either by C6 → C8 or C 6→ C6 interflavan linkages

---

[a] *Ilie Murgulescu Institute of Physical Chemistry, Spl. Independentei 202, Bucharest, 060021, Romania*
[b] *University of Bucharest, Faculty of Chemistry, Bulevardul Regina Elisabeta 4-12, Bucharest, 030018, Romania*
* *Corresponding author: ancaleonties@gmail.com*

and are classified as B-type dehydrodicatechins, resulting from the repeated condensation reactions between the A-ring of the lower unit and the B-ring of the upper unit through a mechanism of so-called 'head to tail' polymerization [3] or they contain additional C–O–C ether-type interflavan linkages and are classified as A-type dehydrodicatechins [4].

During the past decades many studies focused on the protective effects on flavanols against lipid peroxidation and low-density lipoproteins, oxidation as well as on their antiproliferative and anticarcinogenic actions [5,6]. On the other hand, polyphenols are susceptible to autoxidation. In this process are generated large amounts of free radicals and active oxygen species, such as hydrogen peroxide, which are able to induce DNA damage and diseases [7, 8]. Therefore, much discussion and contradiction exist regarding the structure and activity of oxidation products resulting from the autoxidation process.

In the present paper, we describe the autoxidation of catechin in aqueous/methanol model solution under pH ranging between 5 and 10. On the basis of the LC-MS and HPLC we identified a series of B-type and A-type dimeric autoxidation products and proposed their structures and dissociation mechanisms. Furthermore, using a simple spectrophotometrical method we analyzed the kinetics of catechin autoxidation.
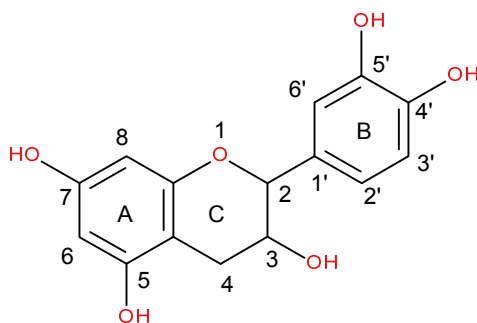
Scheme 1. Catechin structure

RESULTS AND DISCUSSION

The autoxidation of catechin was carried out in aqueous/ methanol solution under mildly basic conditions (pH 8.0). By using a LC-MS system the autoxidation products were identified (**Figure 1**).
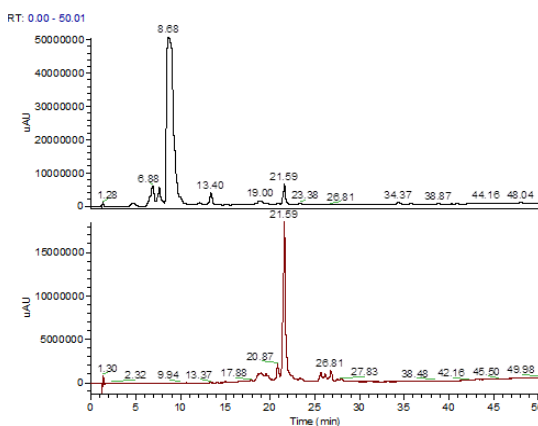
Figure 1. LC-MS cromatogram for the catechin autooxidation products

The peaks of the compounds eluted at retention times of 6.88 and 7.60 minutes were assigned to a dimer product resulted from autoxidation. These compounds have the same UV-Vis absorption spectrum with double maxima at 240 and 280 nm and similar ion fragments (**Figure 2**. A and B).
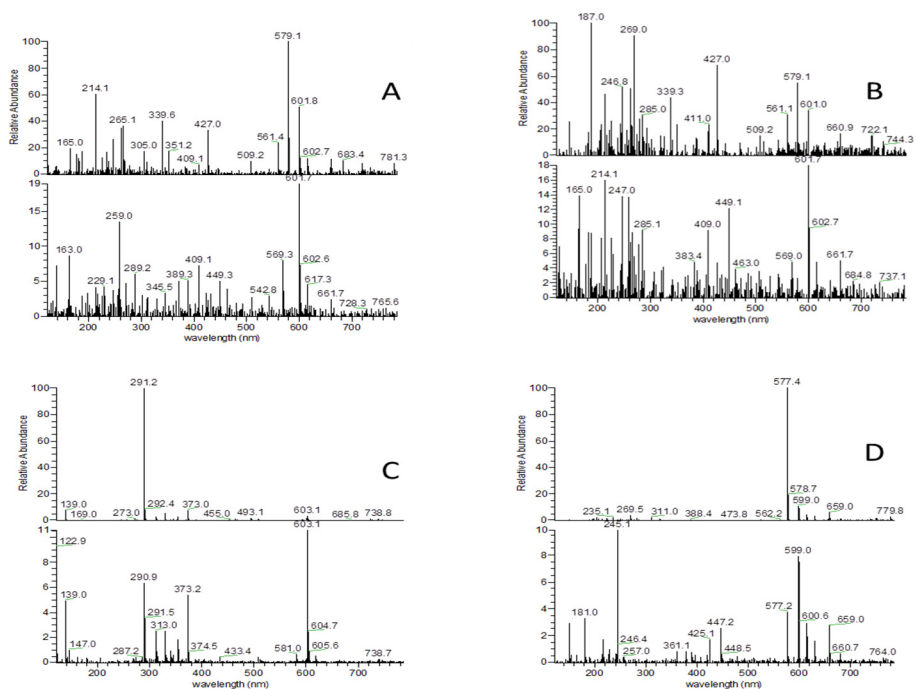
Figure 2. Mass spectra of identified catechin autoxidation products (retention time 6.88 minute - A, retention time 7.60 minutes - B, retention time 8.68 - C, retention time 21.59 D)

13

At retention time 8.68 minutes the peak of the eluted compound was assigned to the remaining non-reactive catechin. **Figure 2**.B shows the majority ion with mass *m/z* 291.2 typical for catechin. The compound eluted at retention time 13.40 minutes corresponds to catechin which lost a hydrogen atom, this fact being confirmed by the presence in the mass spectrum of the fragment ion with *m/z* 290 (**Figure 2**.C). The compound with the peak at the retention time of 21.59 minutes (**Figure 2**.D) was established as another type of dimer product due to the presence in the mass spectrum of the fragment *m/z* 577.4. It has also been observed that the products with peaks at retention times 18.64, 19.57 and 26.81 minutes have the same UV-Vis spectrum. Three maxima at 240, 256 and 376 nm in absorption spectrum were identified and similar ionic fragments to the compound found at retention time of 21.59 minutes. These compounds were supposed to be fragments of dimers resulting from MS fragmentation. During the autoxidation process, the B-type dehydrocatechin results from repeated condensation reactions between the A-ring of the lower unit and the B-ring of the upper unit in a 'head to tail' polymerization. At 6.88 and 7.60 minutes the elution peak was attributed to this type of dimer. The mechanistic formation of *m/z* 579 = M+1and *m/z* 601= M+23(M_{Na+}) sustains this idea. The supposed fragmentation path of B-type dehydrocatechin is presented in **Scheme 2**.

Scheme 2. Fragmentation of B-type dehydrocatechin dimer

Another type of dimer formed during autoxidation is the A-type dehydrodicatechin. These compounds have C–O–C ether-type interflavan linkage. For retention time of 21.59 minutes the m/z 577 = M + 1 and m/z 599 = M + 23 (M_{Na+}) were assumed. Fragmentation mechanisms for obtaining the daughter fragments m/z 425, m/z 151, m/z 245 from m/z 577, m/z 360 were proposed. **Scheme 3**. shows the proposed fragmentation path for a A-type dehydrodicatechin. It was also explained the formation of m/z 561 as M-H_2O+H^+ and m/z 463 as m/z 449 + CH_3OH- H_2O. Fragments with a mass greater than m/z 599 may be adducts of the dimer with solvents and other molecules. Other fragments were obtained as follows: m/z 447= 424 + 23 (M_{Na+}), m/z 217 = m/z 245 - M_{CO}.

In order to analyze the kinetics of catechin autoxidation by atmospheric oxygen, the accumulation of oxidation products at different pH values was recorded in time. During the autoxidation of catechin the effect of pH cannot be ruled out, as the basic pH should increase the proportion of phenolate anions leading to a larger quantity of reaction dimers than the protonated phenol. **Figure 3** A shows absorption spectra for dimers at different pHs. The characteristic absorbance of catechin reaction products indicated a bathochromic shift with the pH increase. The maxima present at 280 and 430 are characteristic for the autoxidation products obtained at neutral and basic pH and at 280 and 390nm for pH 5.5 reaction products.

The characteristic bands of the dimers were used for further kinetic analysis by monitoring and recording consecutive spectra for 90 minutes.

The UV-Vis spectra of catechin solution mixed with acidic buffer presents a minimal variation where dehydrocatechin dimers have characteristic wavelengths of 280 and 390 nm. For neutral and basic pHs the reaction takes place with a decrease in absorbance at 280 and an increase at 430 nm.

The dimers concentrations were calculated from their absorbance. The kinetic curves of dimer concentration ([Dimer]) as function of time are shown in **Figure 3** B. Using the initial linear dependence of the kinetic curves [Dimers] = f(t)], the initial reaction rates for the autoxidation of catechin, in methanolic solutions with buffers of various pH were estimated. The results are presented in **Table 1**. In mild alkaline media (pH=8) the conversion of catechin in dimers is maximum.
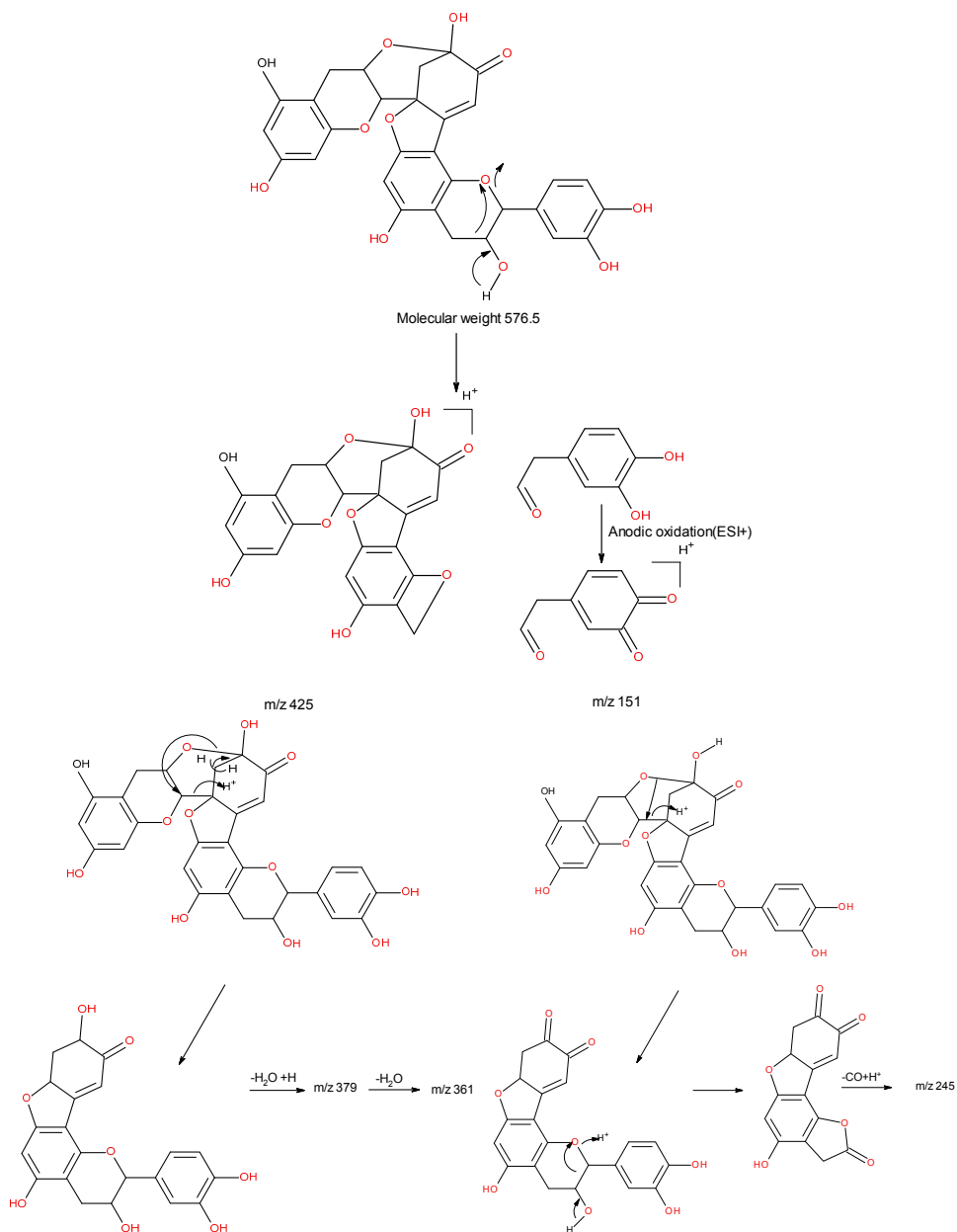
Scheme 3. Fragmentation of A type dehydrocatechin dimer
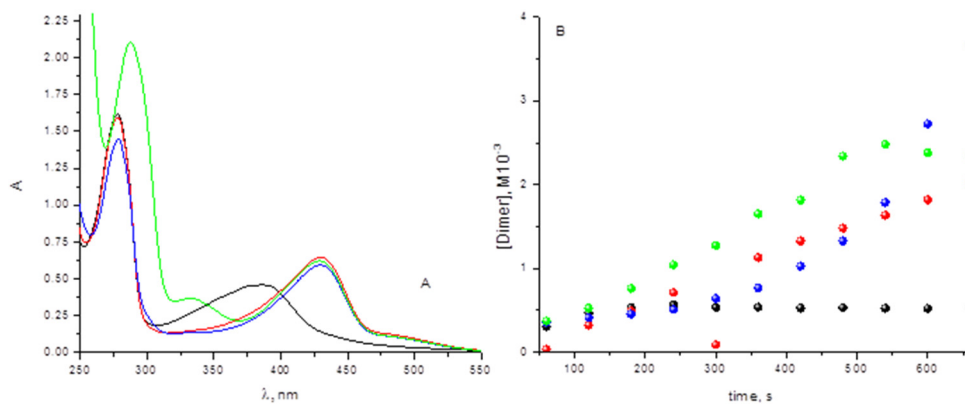
Figure 3. (A) Dimers spectra at different pHs and (B) Kinetic curve for dimer formation in catechin autoxidation process at different pHs: 5.5 (black), 7 (red), 8 (blue),10 (green)

Table 1. The variation of the initial reaction rate with the pH for the autooxidation reaction of catechin solutio

pH	$v_R^0 \cdot 10^8/(Ms^{-1})$
5.5	(0.241±0.072)
7.2	(3.05±0.07)
8.0	(5.31±0.12)
9.9	(0.299±0.042)

CONCLUSIONS

The autoxidation of catechin was investigated in buffered methanolic solutions. The analysis of the reaction mixture indicates the presence of catechin dimers (dehydrocatechin A and B) with similar structures and properties. From the analysis of the UV-VIS absorption spectra, the dimers characteristic bands were identified and further used for the kinetic analysis. It was found that in catechin autoxidation the dimer formation is favored at pH 8. The results are in agreement with other literature data confirming an oxidation mechanism implying dimers as products, with intermediate formation of semiquinons.

EXPERIMENTAL SECTION

Materials

Methanol and glacial acetic acid were HPLC grade. Deionized water (<18 M resistance) was obtained from a Milli-Q Element water purification system (Millipore, Bedford, MA). Catechin and all the other chemicals were purchased from Sigma Aldrich.

Preparation of autoxidation products of catechin

In order to analyse the products resulting from the catechin autoxidation process, catechin was solubilized in methanol and a 0.1 mM solution was obtained. The catechin solution was diluted with phosphate buffer (0.1 M, pH 8) to a final concentration of 0.03 mM in catechin. The final mixture (100 mL) was incubated in dark at room temperature, in the presence of atmospheric oxygen. After 24 hours, the mixture was washed with ethyl acetate. The upper layer was collected and dried using a rotary evaporator with a water bath at 40° C for 40 minutes, during which complete evaporation of the ethyl acetate was carried out. The 0.02 mg of yellow powder obtained in the flask was solubilized in 2.5 mL of methanol.

Liquid chromatography–mass spectrometry

A Finnigan MAT Spectra System P4000 pump was used coupled with a UV6000LP diode array detector and a Finnigan AQA mass spectrometer. Analyses were carried out on a Superspher 100-RP18, 125 • 2 mm, 4 µm, column (Macherey-Nagel, Germany), protected by a guard column packed with the same material, and maintained at 40° C. Analyses were carried out employing electrospray ionization (ESI) at the positive ion mode, with acquisition set at 12 and 80 eV, capillary voltage 3.5 kV, source voltage 4.9 kV, detector voltage 650 V and probe temperature 400 C. Eluent (A) and eluent (B) were 2.5% aqueous acetic acid solution and methanol, respectively. The flow rate was 0.300 mL • min^{-1}, and the elution program used was as follows: 0–15 min, 80% A. 20%B; 15–25 min, 100% B. The injection volume was 2µL.

UV-Vis spectrophotometry

A stock solution of catechin in methanol 10^{-3} M was prepared. The dilution was made with buffer at pH 5.5, 7, 8 and 9.9 to a final concentration of 1.5 • 10^{-4} M. Catechin autoxidation process was recorded using a JASCO V-350 spectrophotometer. Kinetic studies in the presence of isolated strawberry peroxidases [9] have shown that the product formed at 5.5 pH has

a molar absorption coefficient ε = 4600 $M^{-1}cm^{-1}$. This value was used to determine the concentration of dimers at this pH and then extrapolated to the rest of pH, under conditions where Lambert-Beer law was tested for the range of concentrations considered. From the absorbance characteristic of the dimer wavelengths, the concentration was calculated. For catechin autoxidation process, the characteristic absorbance of the dimers at 430 nm was measured in time to obtain extended kinetic curves and estimate the initial reaction rates.

REFERENCES

1. J.M. Landete, *Critical Review in Food Science and Nutrition*, **2012**, *52*, 936.
2. M. Friedman, *Journal of Agricultural and Food Chemistry*, **2014**, *62*, 6025.
3. T. Tanaka, Y. Matsuo, I Kouno, *Internationa Journal of Molecular Science*, **2010**, *11*, 14.
4. S. Guyot, V.B. Chewier, J.M. Souquet, M.Moutounet, *Journal of Agricultural and Food Chemistry*, **1995**, *43*, 2458.
5. E.L. da Silva, D.S.P. Abdalla, J. Terao, *IUBMB Life*, **2000**, *49*, 289.
6. M.K. Chahar, N.Sharma, M.P. Dobhal, Y.C. Joshi, *Pharmacognosy Reviews*, **2011**, *5*, 1.
7. S.C. Forester, J.D. Lambert, *Molecular Nutrition & Food Research*, **2011**, *55*, 844.
8. L. Pourcel, J.M. Routaboul, V.Cheynie, L.Lepiniec, I. Debeaujon, *Trends in Plant Science*, **2006**, *12*, 29.
9. Reaction, M. Lopez-Serrano, A. Ros Barcelo, *Journal of Agricultural and Food Chemistry*, **2002**, *50*, 1218.

THE EFFECT OF POSITIONAL ISOMERISM OF PROPANEDIOL ON THE FORMATION OF COBALT OXIDES

THOMAS DIPPONG[a], FIRUTA GOGA[b], ALEXANDRA AVRAM[b]

ABSTRACT. This paper focuses on a comparative analysis between the carboxylate precursors obtained through the redox reaction between cobalt nitrate and 1,2-propanediol, and cobalt nitrate with 1,3-propanediol, respectively. The formation of the lactate and malonate precursors was followed with thermal analysis, FTIR spectrometry and acido-basic analysis (conductometric/ potentiometric titrimetry). The decomposition of the carboxylate precursors and the formation rate of cobalt oxides were observed by X-ray diffractometry and FTIR spectrometry, following advanced thermal treatments at 500°C, 800°C and 1000°C, with a pretreatment at 300°C. The differences between the two positional diol isomers are comparatively discussed.

Keywords: lactate, malonate, Co_3O_4, electrometric titrimetry, thermal treatment

INTRODUCTION

Transitional metal oxides include a large spectrum of inorganic materials with distinctive compositions and morphologies, leading to a wide variety of characteristics [1,2].

Cobalt oxides have drawn increasing attention due to their unique size, shape dependent properties [3] and diverse spectrum of applications such as, ethylene oxidation [1], energy storage and conversion, glucose detection, water spitting [4], catalytic oxidation [5], lithium ion batteries [6], as a contrasting agent for magnetic resonance, in biomedical sensors [3] and targeted drug delivery [3,4,7].

[a] *Technical University of Cluj-Napoca, Faculty of Sciences North University Center at Baia Mare, Department of Chemistry and Biology, 76 Victoriei Street, 430122 Baia Mare, Romania*
[b] *Babeş-Bolyai University, Faculty of Chemistry and Chemical Engineering, 11 Arany Janos Street., RO-400028, Cluj-Napoca, Romania,*
Corresponding author: fgoga@chem.ubbcluj.ro

When falling in the nanosized range, cobalt oxides have been proven to exhibit even more attractive applications [8-9]. Up until now, cobalt oxide in the form of nanoparticles has been obtained through a number of methods, namely, thermal decomposition [4,10], sol-gel [2], hydrothermal [11], solvothermal [11], co-precipitation [12], photochemical synthesis, reversed micelles [13], microwave heating [9] etc. All these systems, comprising cobalt oxides of various compositions and stoechiometry, rely on the thermodinamic stability of Co^{2+}/Co^{3+} oxidation states.

In solution-phase synthesis, the main cobalt oxide crystal phase is Co_3O_4, followed by the less common CoO [1], both states being the most stable [8]. The greater thermodinamic stability of Co_2O_3 followed by the instant reducibility of CoO to Co, makes the synthesis of CoO in pure phase difficult. Relevant literature [14-15] studies the synthesis of single cobalt oxides and compound oxide nanoparticles through the redox reaction of metal salts with various diols, in different molar ratios.

This paper presents the synthesis of cobalt oxide precursors by the redox reaction between cobalt nitrate and 1,2-propandiol respectively 1,3-propandiol and the characterization of the precursors by Thermal analysis, FTIR and study of acido-basic properties, using conductometric and pH-metric titrations. Titration techniques have the advantage of ease of implementation, cost-effectiveness and accuracy. Electrometric titrations also have the advantage of automation, increasing the analysis throughput and securing the consistent quality of the results.

RESULTS AND DISCUSSION

Previous studies have shown the redox reactions between cobalt nitrate and diols (ethylene glycol, 1,2 propanediol, 1,3 propanediol) leads to the formation of coordination compounds of Co(II) with the carboxylate anions, diols' oxidation product, where only the primary C – OH groups participate. The secondary C –OH groups are not involved in the redox reactions. Thus, the oxidation of 1,2 propanediol leads, in particular working conditions, to the formation of lactate anions, according to the following equations (Scheme 1)

$$3\ H_3C-\underset{OH}{\overset{H}{C}}-\underset{OH}{\overset{H_2}{C}} + 3\ H_2O \longrightarrow 3\ H_3C-\underset{OH}{\overset{H}{C}}-\underset{O^-}{C=O} + 12e^- + 15\ H^+$$

$$4NO_3^- + 12\ e^- + 16\ H^+ \longrightarrow 4\ NO + 8H_2O$$

$$3\ H_3C-\underset{OH}{\overset{H}{C}}-\underset{OH}{\overset{H_2}{C}} + 4\ NO_3^- + H^+ \longrightarrow 3\ H_3C-\underset{OH}{\overset{H}{C}}-\underset{O^-}{C=O} + 4\ NO + 5H_2O$$
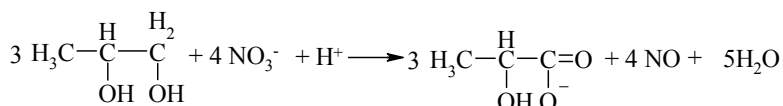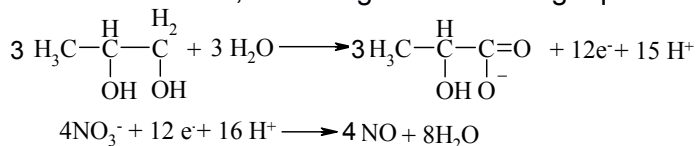
Scheme 1. The redox reaction leading to the formation of the lactate precursor

Similarly, the redox reaction between nitrate and 1,3-propanediol leads to the formation of malonate anions (Scheme 2).

$$3\ HO{-}\underset{H_2}{C}{-}\underset{H_2}{C}{-}\underset{H_2}{C}{-}OH\ +\ 6H_2O\ \longrightarrow\ 3\ \overset{O^-}{\underset{O}{C}}{-}\underset{H_2}{C}{-}\overset{O}{\underset{O^-}{C}}\ +\ 24e^-+\ 30\ H^+$$

$$8NO_3^-\ +\ 24\ e^-\ +\ 32\ H^+\ \longrightarrow\ 8\ NO\ +\ 16\ H_2O$$

$$3\ HO{-}\underset{H_2}{C}{-}\underset{H_2}{C}{-}\underset{H_2}{C}{-}OH\ +\ 8\ NO_3^-\ +\ 2H^+\ \longrightarrow 3\ \overset{O^-}{\underset{O}{C}}{-}\underset{H_2}{C}{-}\overset{O}{\underset{O^-}{C}}\ +\ 8\ NO\ +\ 10\ H_2O$$
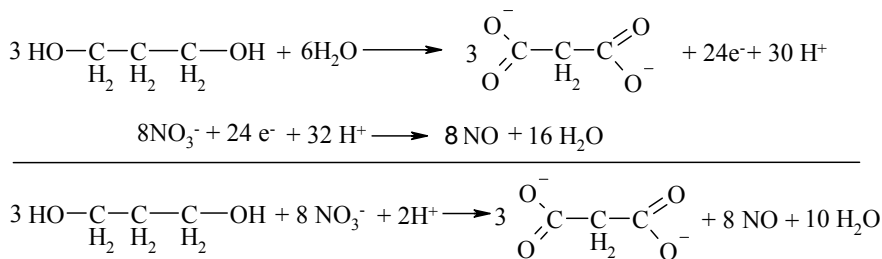
Scheme 2. The redox reaction leading to the formation of the malonate precursor

The reaction is promoted by the formation of the coordination compounds between the resulted carboxylate ions and the Co(II) cations (the diol does not only interact with HNO_3).

The redox reaction between $Co(NO_3)_2$ şi 1,2-PG, and $Co(NO_3)_2$ and 1,3-PG, respectively, was studied by thermal analysis. This entails the thin layer deposition of cobalt nitrate-diol solutions onto Pt pans, followed by an air heating up to 500ºC. Figure 1 presents the thermal curves for the 1,2 propanediol, and 1,3 propanediol containing mixtures.

The presented DTA thermal curves show two exothermic processes. The first exothermic process, around 170°C, is attributed to the development of the $Co(NO_3)_2$-1,2PG redox reaction. The reaction unfolds integraly with the formation of a single oxidation product, respectively, of Co (II) combinations (visualy confirmed by the evolving of the brown gas-nitrogen oxides). The second effect, around 280ºC, corresponds to the oxidative decomposition of cobalt lactate into cobalt oxide.
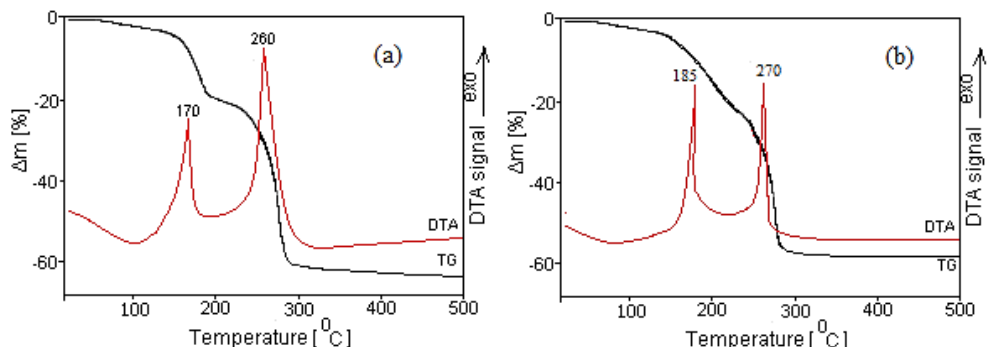
Figure 1. Thermal curves for the Co $(NO_3)_2$-1,2PG (a) and Co $(NO_3)_2$-1,3PG (b) solutions

In the case of 1,3 propanediol, the exothermic effects are slightly carried towards higher temperatures, the formation of cobalt malonate occuring at 185°C, and its decomposition at 270°C. Given the usage of 1,3 propandiol, the mass loss presented on the TG curve amounts to 21% for the first process, and 17% for the second one, a half reduced loss being observed in the case of utilizing a primary diol as opposed to a primary-secondary one.

In the case of 1,2 propanediol, the mass loss seen on the TG curve is 20% for the first process, and 41% for the second one.

Following the thermal analysis, the optimal carboxylate precursors synthesis temperature was established at 140°C. The products obtained at this temperature were characterized by FTIR analysis (fig 2). FTIR spectra of the lactate precursor obtained from 1,2 propanediol and malonate, and 1,3 propanediol, respectively, present all the characteristic bands of the carboxylate anions coordinated at metalic ions: $v_{as}(COO^-)$ la 1646 cm^{-1}, $v_s(OCO)$ la 1360 cm^{-1}, and $v_s(CO) + \delta (OCO)$ la ~ 1310 cm^{-1}, confirming the formation of this type of compound [18]. In the case of the lactate procursor's spectra, an intense band can be observed from 1070 cm^{-1}, characteristic to the secondary C-OH group (1,2-propandiol) that does not take part in the redox reaction, thus confirming the formation of the lactate precursor. The absence of bands characteristic to O-H groups suggests the formation of the carboxylate dianion (malonate) [17]. The bands at 2974 cm^{-1}, 2940 cm^{-1} and 2870 cm^{-1} are characteristic to the stretching vibrations of the C-H bonds from-CH$_3$ [16-17].
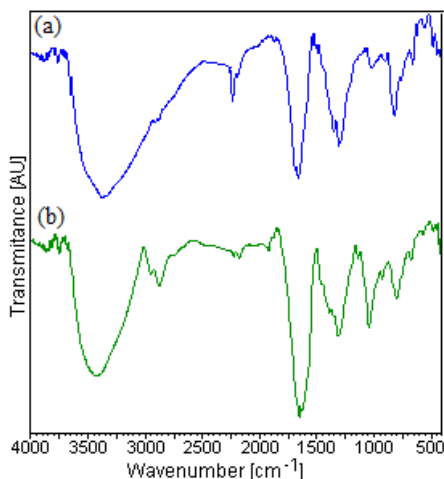
Figure 2. FTIR spectrum of the lactate (a), malonate (b) precursors synthesized at 140°C

Figure 3 presents the comparative thermal curves (TG, DTA) for the decomposition of lactate and malonate precursors, up to 1000°C. The 20% mass loss up to ~210°C can be attributed to the elimination of water from the complex combination. The one from the 220-300°C temperature range (42% for 1,2 propanediol and 21% for 1,3 propanediol), accompanied by an acute exothermic effect (at 280°C for 1,2-propanediol and 240°C for 1,3 propanediol, corresponds to the oxidative decomposition of formed complex combinations (lactate, malonate). This decomposition takes place with an *in-situ* generation of a reductive atmosphere, causing the reduction of Co(II) to metallic Co, followed by its reoxidation to a weakly crystallized oxide with an increased reactivity [21]. Between 950-1000°C, a final mass loss (4%) can be observed, corresponding to the transformations in the oxidic system, the reduction of Co_3O_4 to CoO, an endothermic effect on the DTA curve (950-960°C).
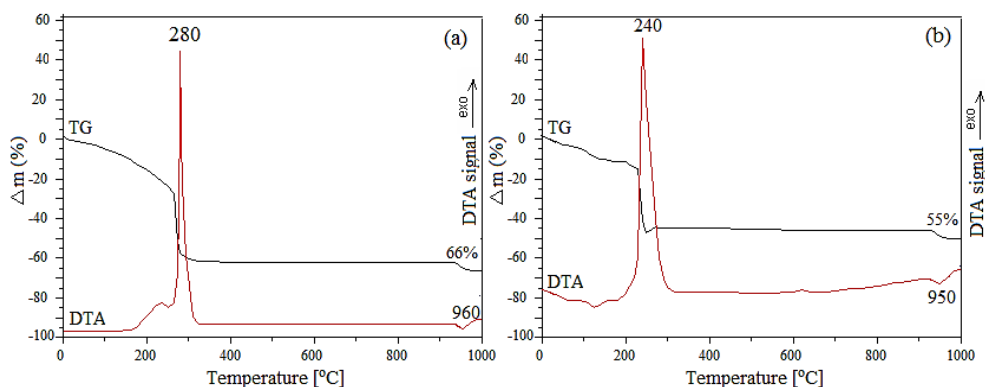
Figure 3. Thermal behaviour of the lactate (a) and malonate (b) precursors synthesized at 140°C

In order to establish if the precursor is a Co(II) lactate or a Co(II) hydroxylactate, and malonate or hydroxymalonate we have studied the acido-basic properties, by using conductometric and pH-metric titrations.

The processes that can take place in the precursor treated with a HCl solution, and NaOH respectively, are presented in schemes 3 and 4.

Consum H^+ | Consum OH^-

$$C_3H_5O_3^- + H_a^+ \longrightarrow C_3H_6O_3$$

$$COOH^+ + H_a^+ \longrightarrow Co^{2+} + H_2O$$

$$Co^{2+} + 2OH^- \longrightarrow Co(OH)_2$$

$$COOH^+ + OH^- \longrightarrow Co(OH)_2$$
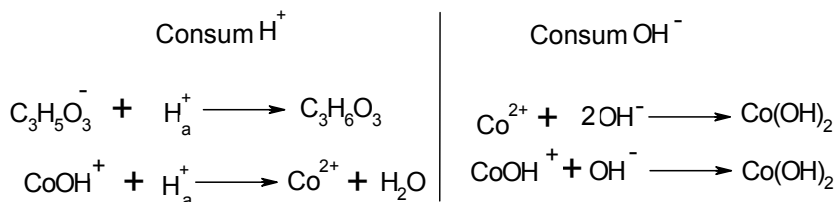
Scheme 3. The processes that can take place in the precursor (lactate) treated with HCl (left) and with NaOH (right)

$$C_3H_2O_4^{2-} + 2H^+ \longrightarrow C_3H_4O_4$$

$$C_3H_3O_4^- + H_a^+ \longrightarrow C_3H_4O_4$$

$$COOH^+ + H_a^+ \longrightarrow Co^{2+} + H_2O$$

$$Co^{2+} + 2OH^- \longrightarrow Co(OH)_2$$

$$COOH^+ + OH^- \longrightarrow Co(OH)_2$$
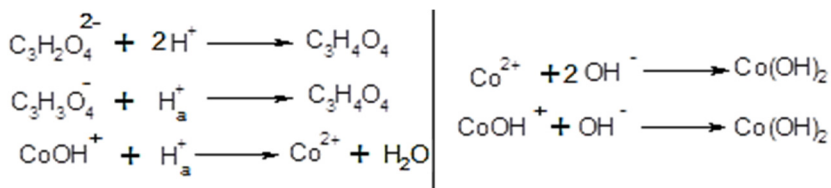
Scheme 4. The processes that can take place in the precursor (malonate) treated with HCl (left) and with NaOH (right)

The consumed acid amount is calculated from the difference between the initial and the unreacted HCl volume (corresponding to the first point of equivalence). The utilized amount of NaOH is evaluated through the difference between the NaOH volume corresponding to the second point of equivalence and the volume of initial HCl. When the consumed HCl quantity (for the protonation of the lactate ion) is equal to the quantity of consumed NaOH (for the precipitation of Co(II) to Co(OH)$_2$) ($H^+/OH^-=1$), it can be considered that cobalt (II) lactate (Co(C$_3$H$_5$O$_3$)$_2$) is the precursor. Cobalt (II) hydroxylactate precursor (Co(OH)C$_3$H$_5$O$_3$) is formed when the volume of consumed HCl (for the precipitation of lactate and hydroxide ions) is double (H^+/OH^- =2) when compared to the consumed NaOH (for the precipitation of Co(OH) to Co(OH)$_2$). The precursor of cobalt malonate (CoC$_3$H$_2$O$_4$), has a similar formation, when the quantity of consumed HCl is equal with the quantity of consumed NaOH (for the precipitation of Co(II) as Co(OH)$_2$). To confirm the formation of the hydroxycarboxylate anion (lactate), and dicarboxylate (malonate), neutral, basic or hydroxyde, studies on the acido-basic properties were carried out (conductometric and pH-metric titrations) Figure 4 presents the conductometric titration (Figure 4a), and pH-metric titration (Figure 4b) curves of the acid solutions of the sample with 1,2 propanediol and HCl solution (volume used to disolve the precursor and process the experimental results).
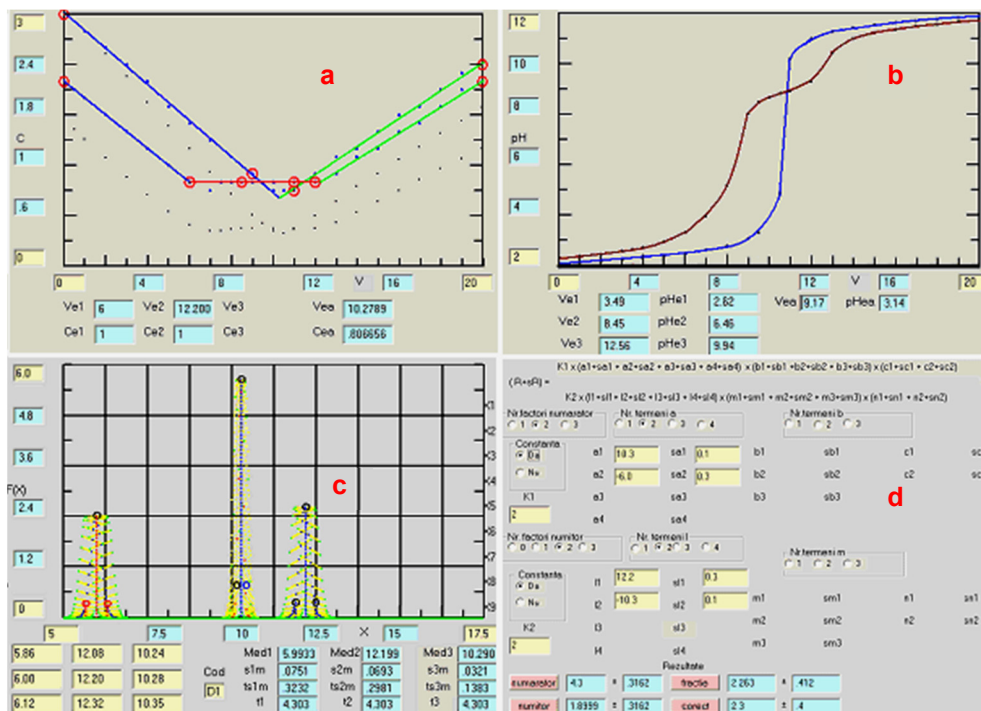
Figure 4. Conductometric titration curve (a), pH-metric titration curve (b), calculation of the medium equivalence volume (c), calculation of the reaction ratio (d) for the 1,2 propanediol sample

Figure 4c shows the statistical calculus method for the equivalence volumes, while figure 4d, presents the statistic calculus method for the consumed acid/ consumed base ratios from the equivalence volumes. In the case of using 1,2 propanediol, a mixture of neutral and basic salts is obtained, whereas in the case of 1,3 propanediol isomer, only hydroxymalonate is obtained. Similarly, the acido-basic curves in the case of 1,3-propanediol are presented (Figure 5a and 5b), followed by the statistical calculation of the acid/ base ratio (Figure 5c and 5d).
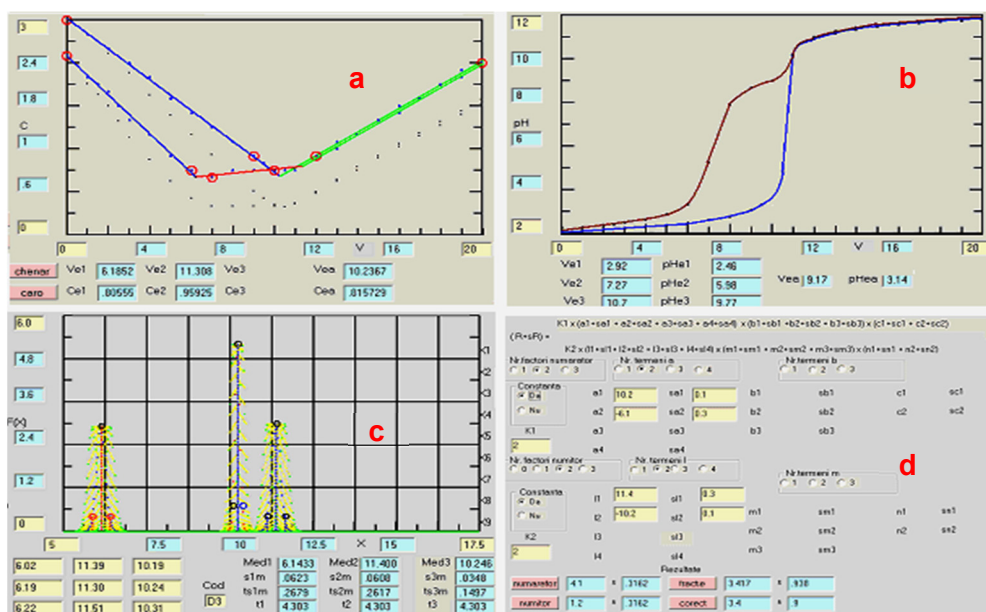
Figure 5. Conductometric titration curve (a), pH-metric titration curve (b), calculation of the medium equivalence volume (c), calculation of the reaction ratio (d) for the 1,3 propanediol sample

The results obtained following the conductometric and pH-metric titrations are presented in table 1.

Table 1. H^+/OH^- molar ratios and the compounds formed
following the acido-basic titrations

Experimental molar ratio H^+/OH^-			Corresponding compound
Sample obtained from	Conductometric	pH-metric	$Co(C_3H_5O_3)_2$
1.2 propanediol	$2.3 \pm 0,4$	1.5 ± 0.3	$(COOH)C_3H_5O_3$
1.3 propanediol	4.0 ± 0.2	$4,2 \pm 0.3$	$n(COOH)_2 \cdot CoC_3H_2O_4$

The acido-basic properties of the synthesized compounds confirm the results of thermmal analysis and FTIR, advocating that the redox reaction forms carboxylate or hydroxycarboxylate compounds, that coordinate Co(II) ions in the form of a compound with either a basic or a neutral character.

The precursor was thermally decomposed at 300°C for 6 hours and then annealed for 3 hours at 500°C, at 800°C and at 1000°C. Following the thermal analysis, it was observed that the thermal decomposition of the carboxylate precursors occured up until 300ºC with the formation of cobalt

oxides through the in situ generation of a reductive atmosphere (C,CO) depending on the nature of the presumed complex combination. The reductive atmosphere can be influenced by the nature of the diol and the manner in which the decomposition (thermal treatment) takes place. The annealing products were studied by XRD analysis (fig. 6). Following the 500°C decomposition of cobalt lactate, a mixture of cobalt oxides (CoO and Co_3O_4) is formed. At 800°C Co_3O_4 is obtained as a single phase, while at 1000°C, CoO forms as a single phase (JCPDS 75-0393 chart [18]). In the case of cobalt malonate decomposition, Co_3O_4 is obtained as a single, crystalline phase (JCPDS 42-1467 chart [18]), both at 500 and 800°C, while at 1000°C, CoO becomes the unique crystalline phase. The reduction of Co_3O_4 to CoO takes place following the reaction:

$$Co_3O_4 \rightarrow 3\ CoO + \tfrac{1}{2}\ O_2$$
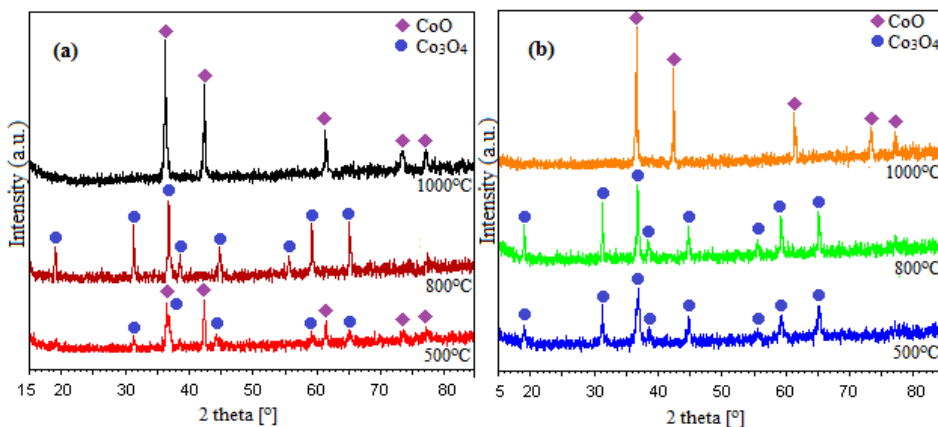
Figure 6. XRD difractogram of samples obtained from 1-2-propanediol (a), 1,3-propanediol (b) at 500°C, 800°C and 1000°C

The average crystallite size (D) of CoO and Co_3O_4 was calculated from the XRD data using Debye-Scherrer formula ($D=C\cdot\lambda/\beta_{1/2}\cdot\cos\theta$) [19] and is presented in table 2.

Table 2. Average diameters of nanoparticles calculated with Scherrer equation

Temperature / °C	Average diameter / nm			
	din 1.2 propandiol		din 1.3 propandiol	
	CoO	Co_3O_4	CoO	Co_3O_4
500	20	23	-	26
800	-	28		30
1000	32	-	35	-

According to the data in table 2, the dimension of the nanoparticles increases with the increase in temperature and with that of the crystallization degree. In addition, purer oxides with larger nanoparticles are obtained from 1,3 propanediol when compared to those synthesized from 1,2 propanediol.

CONCLUSIONS

The redox reaction $Co(NO_3)_2$–1,2-propandiol and $Co(NO_3)_2$–1,3-propandiol, as evidenced by thermal analysis, takes place in the range of 160-190°C. The cobalt lactate and cobalt malonate formation of the redox reaction was confirmed by means of FT-IR spectrometry, thermal analysis and acido-basic analysis (conductometric and pH-metric). All techniques have evidenced the formation of coordination compounds of Co(II) with the lactate anions, resulted through 1,2-propandiol oxidation. According to the study of acido-basic properties of the product obtained from 1,2-propandiol, a mixture of Co(II) lactate and Co(II) hydroxylactate was obtained, while from 1,3-propandiol only cobalt malonate was synthesized. By thermal treatment of this product at 500°C, through the decomposition of cobalt lactate, a mixture of CoO and Co_3O_4 is obtained, while at at 800°C only the Co_3O_4 crystalline phase results, phase that at 950°C reduces to the well crystallized CoO. In the case of cobalt malonate decomposition, Co_3O_4 results as a single phase, while at 1000°C the unique phase is CoO, the crystallization degree increasing with the increase in temperature. The size of nanoparticles increases with temperature, where Co_3O_4 obtained from 1,2 propanediol at 800°C has 28 nm, and from 1,3 propanediol, 30 nm. In a similar manner, the dimensions of CoO obtained through the decomposition of cobalt lactate, following the 1000°C thermal treatment, increases from 32 to 35 nm from the decomposition of malonate. In conclusion, it can be stated that the position of the second OH group can influence the conditions related to the formation of the carboxylic precursor, as well as the nature of oxides formed by advanced treatments.

EXPERIMENTAL SECTION

The reagents used in synthesis were: $Co(NO_3)_2 \cdot 6H_2O$ and 1,2 propanediol respectively 1,3-propandiol of purity p.a. (Merk). The synthesis method consists in dissolving cobalt nitrate in the corresponding 1,2PG respectively 1,3-propanediol in stoichiometric ratio, amount followed by controlled heating at 140°C. At these temperatures, the redox reaction

begins accompanied by nitrogen oxide emission (brown-reddish gas). The isolated reaction products were maintained at 140°C until the emission of brown gas stops (reaction end). The powder obtained at 140°C was washed with acetone for removing of the reactant excess. The obtained products were characterized by thermal analysis, FT-IR spectrometry and conductometric/ pH-metric acido-basic titrations

For the conductometric and potentiometric titrations 0.2 mmoli Co(II) were used, adding volumes of 10,0 cm^3 HCl 0.1M and subjected to titrations with NaOH 0.1M. The acido-basic properties of the precursors were studied through conductometric and pH-metric titrations using a Crison MM41 multimeter. The formation process of cobalt oxides was followed with thermogravimetry (TG), derivative thermogravimetry (DTG) and differential thermal analysis (DTA) using a SDT Q600 type instrument, in air up to 1000^oC at 10 ^oC min^{-1} and alumina standards. The FTIR spectra were recorded on 1% KBr pellets using a Spectrum BX II spectrometer. The XRD patterns were recorded using a high resolution Bruker D8 Advance diffractometer with Cu ($\lambda_{CuK\alpha1}$=1,54056 Å) radiation.

REFERENCES

1. L. Qiao, M.T. Swihart, *Advances in Colloids and Interface Science*, **2017**, *244*, 199.
2. H.M. Khaled, *Polymer Composites*, **2016**, *37*, 1881.
3. E. Papis, F. Rossi, M. Raspanti, I. Dalle-Donne, G. Colombo, A. Milzani, G. Bernardini, R. Cornati, *Toxicology Letters*, **2009**, *189,* 253.
4. H. Heli, J., Pishahang, *Electrochimica Acta*, **2014**, *123*, 518.
5. M. Allen, D. Willits, M. Young, T. Douglas, *Inorganic Chemistry*, **2003**, 42, 6300.
6. S. Kundu, M. Jayachandran, *Journal of Nanoparticle Research*, **2013**, *15*, 1.
7. Q.A. Pankhurst, J. Connolly, S.K. Jones, J. Dobson, *Journal of Physiscs D: Applied Physics*, **2003**, *36*, 167.
8. R. Manigandan, K. Giribabu, R. Suresh, L. Vija Yalakshmi, V. Narayanan, *Chemical Science Transactions*, **2013**, *2*, 47.
9. A. Ashok, A. Kumar, R.R. Bhosale, M.A.H. Saleh, U.K. Ghosh, M. Al-Marri, F.A. Almomani, M.M. Khader, *Ceramic International*, **2016**, *42*, 12771.
10. S. Chattopadhyay, S.P. Chakraborty, D. Laha, R. Baral, P. Pramanik, S. Roy, *Cancer Nanotechnology*, **2012**, *3*, 13.
11. K. Slinko, G. Szabo, M. Zrinyi, *Journal of Nanoscience and Nanotechnology*, **2011**, *11*, 1.
12. K.F. Wadekar, K.R. Nemade, S.A. Waghuley, *Research Journal of Chemical Sciences*, **2017**, *7*, 53.

13. M. Yarestani, A.D. Khalaji, A. Rohani, D. Das, *Journal of Sciences, Islamic Republic of Iran*, **2014**, *25*, 339.
14. Q. Liu, X. Guo, J. Chen, J. Li, W. Song, W. Shen, *Nanotechnology*, **2008**, *19*, 365608.
15. C. Luna, M. del Puerto Morales, C.J. Serna, M. Vazquez, *Nanotechnology*, **2003**, *14*, 268.
16. R. Prasad, Sulaxna and A. Kumar, *Journal of Thermal Analysis and Calorimetry*, **2005**, *81*, 441.
17. Vencat Narayan R., Kanniah V., Dhathathreyan A., *Journal of Chemical Sciences*, **2006**, *118*, 179.
18. Joint Committee on Powder Diffraction Standards. International Center for Diffraction Data, **1999**.
19. Klug HP, Alexander LE. *X-Ray Diffraction Procedures*. 2nd ed. John Wiley & Sons Inc, **1974**.

PHYSICO-CHEMICAL STUDY CONCERNING ATMOSPHERIC PARTICULATE MATTER HAZARD

**IOAN PETEAN[a], AURORA MOCANU[a],
GERTRUD-ALEXANDRA PĂLTINEAN[a], RALUCA ŢĂRCAN[a],
DANA FLORINA MUNTEAN[b], LIANA MUREŞAN[b], GEORGE ARGHIR[c]*,
MARIA TOMOAIA COTIŞEL[a,d]**

ABSTRACT. The particulate matter (PM) from the atmosphere is able to penetrate in the respiratory system presenting several health risks such as acute respiratory items, allergic issues, and chronic risks such as silicosis and asthma. PM from atmosphere is classified by diameter as PM10 – particles with aerodynamic diameter up to 10 μm, PM2.5 – particles with aerodynamic diameter up to 2.5 μm, and PM1 - particles with aerodynamic diameter up to 1 μm. The first major PM source is the street dust (SD) which induces mineral fraction into the atmosphere such as: quartz, kaolinite, calcite, muscovite, and goethite. The second PM source is the pollen from several species like *Tilia Cordata*, *Sambucus Nigra*, *Jasminus Communis, Rosaceae* Family, *Lilium Candidum*, and *Brassica Rapa*, during later spring and early summer. Elements from both sources were found in PM samples collected from atmosphere: sedimentary particles, PM10 and PM2.5. In vivo experiments show that PM10 affects upper respiratory pathways such as nasal cavity and pharynges meanwhile PM2.5 was found in the expectoration matter from tracheal area. These studies reveal that 5 minutes of exposure at a concentration of 125 μg/m^3 conducts to formation of severe deposits on respiratory mucosa.

Keywords: PM 10, PM 2.5, hazard

[a] *Babeş-Bolyai University, Faculty of Chemistry and Chemical Engineering, Arany Janos Str., No. 11, RO-400084 Cluj-Napoca, Romania.*
[b] *Environmental Protection Agency Cluj, Calea Dorobanţilor Str., No. 99, RO-400609, Cluj – Napoca, Romania.*
[c] *Technical University of Cluj - Napoca, Faculty of Materials and Environment Engineering, Muncii Ave., No. 103 -105, RO-400641 Cluj – Napoca, Romania.*
[d] *Academy of Romanian Scientists, 54 Splaiul Independentei, 050094, Bucharest, Romania*
*Correspondent author: georgearghir@hotmail.com

I. PETEAN, A. MOCANU, G. PĂLTINEAN, R. ŢĂRCAN, D. MUNTEAN, L. MUREŞAN, G. ARGHIR, M. COTIŞEL

INTRODUCTION

Particulate matters (PM) dispersed in the atmosphere represent a great concern for the human health due to their ability to be inhaled [1 - 4]. Such particles are trapped by the respiratory system mucosa to prevent their penetration in the lungs. Thus, the hazard is a matter of particle size related to the penetration depth in the respiratory system. PM10 is usually trapped into the nose cavity and nasal passages; meanwhile PM2.5 is able to be inhaled down to trachea and primary bronchi [5, 6]. The effect of inhaled particles leads to specific affections such as: acute pathologies including allergies, inflammations and respiratory insufficiency [7, 8]. Longer exposure to inhaled PM leads to the chronic affections such as: silicosis, lung cancer and autoimmune responses due to the disturbed neuronal activity of receptors sensing the presence of the particles [9 -12].

Recent developed studies related to the atmospheric PM evidence the silicate particles occurrence due to the environmental condition in the urban area [13 - 15]. Such particles could be very harmful if inhaled. The aim of this paper is to establish PM10 and PM2.5 ability to be inhaled and to identify which kind of particles are able to penetrate in the respiratory system. Therefore, we consider some in vivo tests for the identification of those particles.

RESULTS AND DISCUSSION

The data in literature state that street dust (SD) is the most important source of atmospheric PM [13]. Therefore, we select a complex area situated in Dâmboviţei Street, Cluj – Napoca, Romania, for present study. It features a street with average car traffic, around 15 cars per minute, bordered with complex environment containing decayed soils and green areas (e.g. Dâmboviţei Park and Expo Transilvania Park) containing various plant species. The representative SD sample for this environment was physico – chemical investigated.

The minerals were identified by XRD analysis, Figure 1. Resulted XRD pattern has very well-developed peaks proving the cristalinity of SD sample.
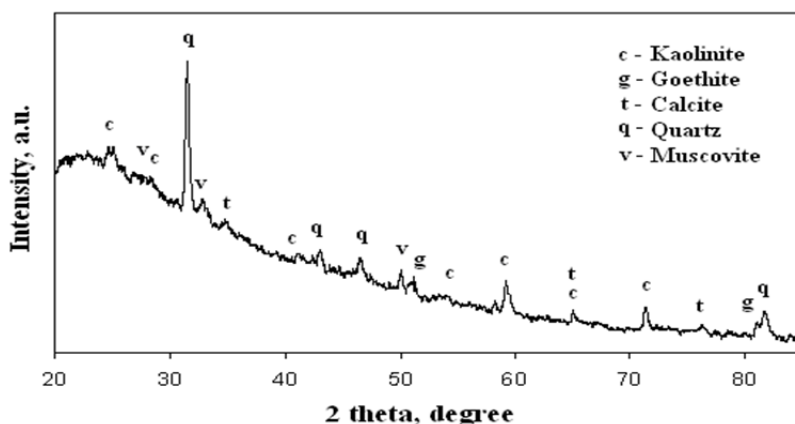
Figure 1. The X-ray spectrum for SD sample collected from Dâmboviţei Street.

The dominant mineral is quartz followed by clay mixture (e.g. kaolinite and muscovite), calcite and goethite are the last minerals. XRD data were correlated with mineralogical microscopy performed in cross polarized light, Figures 2.
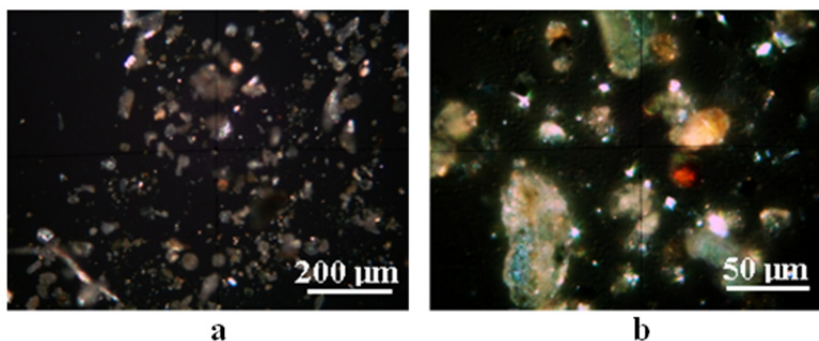
Figure 2. SD sample collected from Dâmboviţei Street observed in cross polarized light: a) low magnification and b) high magnification.

A wide mixture of particles is observed at low magnification, Figure 2a, their size ranges from small microscopic level to grosser particles having over 100 μm diameter. At high magnification, Figure 2b, particles are seen better, each mineral species having its own specific color. The XRD and mineralogical microscopy data resulted for the SD sample are summarized in Table 1.

Table 1. Components properties of SD sample

Component	Quartz	Kaolinite	Muscovite	Calcite	Goethite
Formula	SiO_2	$Al_2Si_2O_5(OH)_4$	$KAl_2(AlSi_3O_{10})(F,OH)_2$	$CaCO_3$	$\alpha FeO(OH)$
Particle size range, μm	2 - 100	1 – 20	1 - 25	10 - 40	5 - 50
Color in cross polarized light	Green - gray	White-Blue	Pink	Yellow-brown	Reddish - brown

The SD sample has mineral components derived from local decayed soils, representing a fingerprint of the investigated area. All SD particles could be suspended in the atmosphere due to various environmental factors such as natural air currents (affected by regional climate) and anthropogenic factors such as car traffic and industrial activities [16, 17]. Their ascension into the atmosphere depends on the particles physical properties, mainly their diameter. All SD minerals have small micro particles which are able to be lifted in the air.

Minerals are not only one source of particulate matters, pollen from various vegetal species is often found in the atmosphere during April and May. Such organic particles could be hazardous for human health due to the allergenic issues. Therefore, the pollen was extracted from fresh flowers collected during April and May 2017 from the adjacent area of Dâmboviţei Street. These samples were investigated in transmitted light, Figure 3.
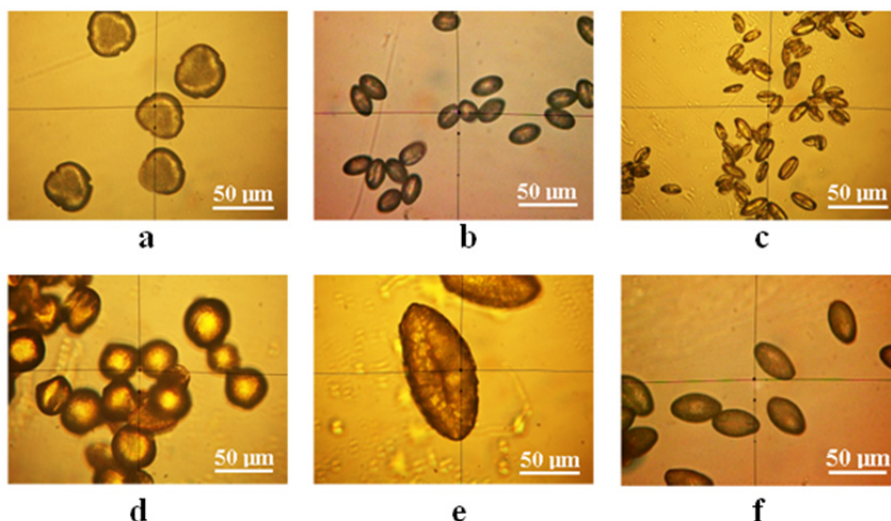
Figure 3. Pollen samples collected from Dâmboviţei Street area observed in transmitted light light: a) *Tilia Cordata*, b) *Sambucus Nigra*, c) *Jasminus Communis*, d) *Rosaceae* Family, e) *Lilium Candidum*, and f) *Brassica Rapa*.

The quantitative measurements performed on images in Figure 3 are centralized and systematized in Table 2. The obtained values related to pollen shape are in good agreement with pallinological databases.

Table 2. Pollen particles characteristics

Plant	*Tilia*	*Sambucus*	*Jasminus*	*Rosa*	*Lilium*	*Brassica*
Shape	sub-triangular	elongated	elongated	round	elongated	elongated
Length, μm		25	20		125	35
Diameter, Mm	35	10	5	25 - 30	50	15

Pollen particles from *Sambucus Nigra* and *Jasminus Communis* presents characteristic dimensions for PM10 being the most susceptible to be inhaled from all investigated range. The most inoffensive is the *Lilium Candidum* pollen due to its larger size and sticky surface.

Floating particles (FP) from atmosphere represents the most heterogenic particulate matter sample containing all kind of solids suspended in air due to various conditions, that's why some authors refer to total sedimentary particles [18, 19]. The maximum accepted level of FP emission is 17 g/m^2/h according to Romanian and UE laws. The representative FP sample collected with the Automatic Station of Air Quality Monitoring was subjected to the XRD analysis, Figure 4a.
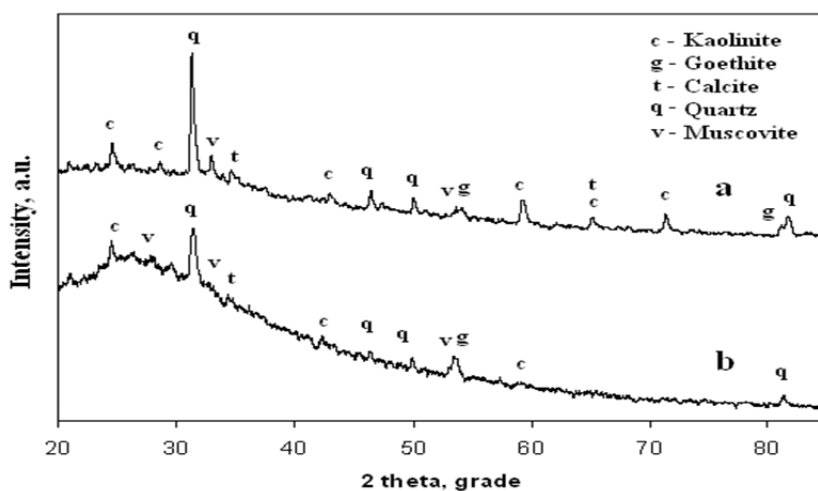
Figure 4. The X-ray spectra for FP (a) and PM10 (b) collected from Dâmboviţei Street with Automatic Station for Air Quality Monitoring.

It features well developed peaks proving the high level of cristallinity of FP sample, Figure 4a. A great similitude with SD sample is observed, Figure 4b. Minerals found in FP sample are the same as in SD: quartz, kaolinite and muscovite, calcite and goethite. Optical microscopy performed on FP reveals two areas of interest, Figure 5.
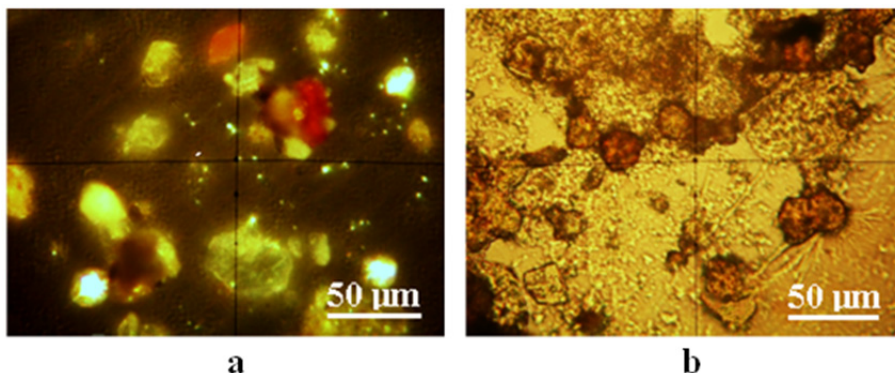
Figure 5. FP sample collected from Dâmboviţei Street: a) reach mineral area observed in cross polarized light and b) organic reach area observed in transmitted light.

The first is the reach mineral area, Figure 5a, where appear fine particles with tabular aspect like kaolinite and muscovite [20, 21] mixed up with a various mixture of quartz calcite and goethite. A dimensional hierarchy is observed: clay particles are present mostly in PM2.5 area meanwhile quartz and calcite are rather found in PM10 category, Table 3.

Table 3. Components properties of FP sample

Component	Quartz	Kaolinite	Muscovite	Calcite	Goethite
Formula	SiO_2	$Al_2Si_2O_5(OH)_4$	$KAl_2(AlSi_3O_{10})(F,OH)_2$	$CaCO_3$	$\alpha FeO(OH)$
Particle size range, μm	2 - 50	1 - 20	1 – 25	10 - 40	5 - 60
Color in cross polarized light	Green - gray	White- blue	Pink	Yellow- brown	Reddish - brown
Particle shape	round	tabular	tabular	round	elongated

The second is organic reach area, Figure 5b. A lot of organic matter is situated in micro-scaled conglomerates, but there are a few distinct pollen grains evidenced. Their shape and size is altered by the FP collecting method which uses sedimentation in bi–distilled water, most likely they are Tillia Cordata or Sambucus Nigra grains. This proves the importance of pollen as PM source during spring and early summer. It results that FP sample is SD lifted in the atmosphere combined with pollen from the in-blossom flowers in April and May 2017.

PM10 fraction contains also similar minerals like in SD and FP, fact evidenced by the pattern in Figure 4b. The diffraction peaks are no longer so well developed due to the smaller size of the diffractant particles. Quartz is the dominant mineral, proving that PM is mostly silica, followed by the clay mixture. The mineral arrangement in PM10 is observed by SEM imaging in Figure 6a: where several quartz particles having the range of 2.5 – 10 µm diameter surrounded by smaller particles which are supposed to be clay. Certain evidences were obtained by EDX analysis, Table 4. The major elements in the PM10 composition are Si and O, fact in good agreement with XRD information. Presence of significant amount of Al, K, and Mg certify the presence of clay particles into the PM 10 sample. Lower amount of C found in PM10 could be related by the traces of calcite found in XRD pattern and possibly to belong to some organic features.

PM2.5 shape is revealed in the SEM image, Figure 6b. There is a complex conglomerate based on lamellar – tabular particles having sizes below 2.5 µm. There are also found some rounded particles having typical aspect for grinded quartz. Particles shape and distribution in PM2.5 proves their origin in SD.
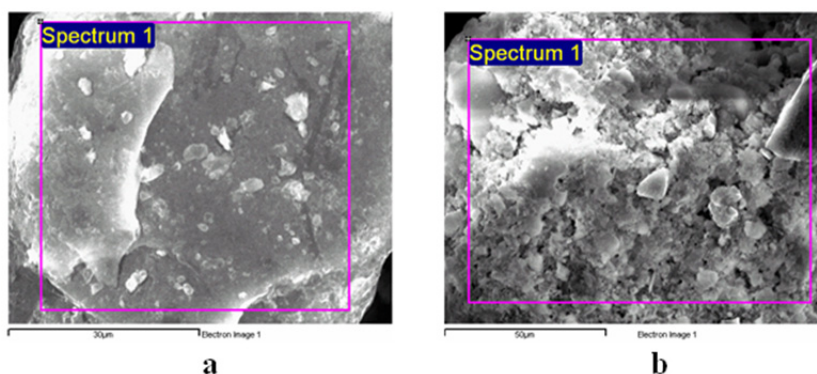
Figure 6. SEM images for particulate matters: a) PM10 and b) PM2.5.

PM2.5 was subjected also to the EDX analysis, results being displayed in Table 4. A significant amount of Al and K was observed proving the predominance of clay particles instead quartz ones. The amount of C is increased than in PM10 sample, fact sustained by traces of calcite (around of 1.38 wt. % Ca) and organic amorphous carbon.

Table 4. Elemental composition for PM10 and PM2.5 resulted from EDX

Element	PM10		PM2.5	
	weight %	atomic %	weight %	atomic %
C	2.86	4.62	13.04	19.99
O	56.27	68.27	55.77	64.18
Mg	1.54	1.23	0.61	0.46
Al	14.52	10.45	12.08	7.04
Si	17.31	11.96	5.09	3.34
S	-	-	0.25	0.14
K	5.65	2.80	10.39	4.06
Ti	0.52	0.21	-	-
Ca	-	-	1.39	0.33
Fe	1.33	0.46	1.38	0.46
Total	100.00	100.00	100.00	100.00

EDX analysis confirms the reach mineral composition of PM formed in Dâmboviţei street area containing minerals with hazardous features which if are inhaled could lead to acute respiratory affections and to silicosis at longer term of exposure. The positive aspect revealed by EDX is the lack of heavy metals and or radioactive isotopes in PM10 and PM2.5 samples. This situation decreases the hazard because lack of carcinogenic elements.

Another aspect connected to the respiratory health is the emission level of each PM pollutant category. The data measured from the atmosphere with the Automatic Air Quality Monitoring Station are displayed in Table 5.

Table 5. PM emission level in Dâmboviţei Street for April and May 2017

Emission type		April 2017	May 2017
PM2.5, $\mu g/m^3$	minim	5.43	12.32
	maxim	24.65	23.75
	average	11.45	18.05
PM10, $\mu g/m^3$	minim	2.35	7.61
	maxim	42.01	42.24
	average	18.18	21.44
FP, $g/m^2/month$	average	9.03	6.67

FP emission level is situated in the safe range, far below maximum limit of 17 g/m^2/month. The average values recorded for April and May 2017 for PM2.5 and PM10 are far below the maximum accepted value. This is due to the relatively humid weather related with a good environmental management applied in the street.

The most humid days with the lowest car traffic lead to the lower values recorded, while the driest days with high car traffic lead to the higher values recorded. Only two limits overtake at PM10 were recorded: 42.01 μg/m^3 on 27 April 2017 and 42.24 μg/m^3 on 12 May 2017. These overtakes do not generate hazard because of their low excess of PM 10 situated around 2 μg/m^3, and happened only once per month.

Nanoparticles from aqueous dispersion were transferred onto solid substrate (e.g. glass slide) by vertical adsorption [22 – 26]. The deposited film was investigated by AFM resulting the image in Figure 7. The film topography is observed in Figure 7a, the deposited layer is uniform and nanoparticles are well individualized. Cross section in Figure 7b allows calculating the average diameter of nanoparticles which is situated around 30 nm.
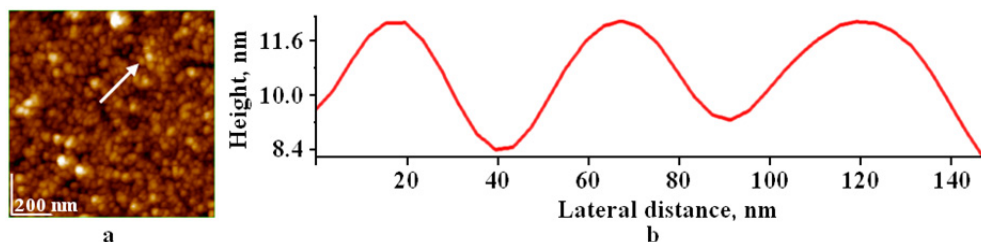
Figure 7. AFM images for nanoparticles derived from PM2.5.

Nanoparticles presence in the PM2.5 sample is a risk factor due to their ability to penetrate tissues such as pulmonary alveoli. Fortunately, nanoparticles have low ability to travel alone into the atmosphere because of their high coalescence tendency. Such coalescence is proved by the formation of nanoparticles clusters observed in AFM images, Figure 7. They are also very sticky and are expected to be trapped into mucus immediately after they are inhaled.

In vivo exposure to the normal atmosphere (e.g. PM level below 40 μg/m^3) does not affect the nasal mucosa, or the mucus from trachea. It is clearly observed in cross polarized light Figures 8a and 8d: only organic compounds of the mucus are observed with no trace of mineral particles.

At an exposure of 5 minutes to a polluted air with PM10 level around of 125 µg/m^3 leads to mineral deposits of PM10 in nose mucus consisting mainly in quartz and fewer clay particles, Figure 8b. The expectoration product contains some PM2.5 particles consisting in kaolinite and muscovite as seen in Figure 8e. The exposure to a polluted air with PM10 level around of 200 µg/m^3 for 5 minutes leads to massive deposits of PM10 into the nose mucus containing mainly quartz particles followed by calcite and goethite, Figure 8c.
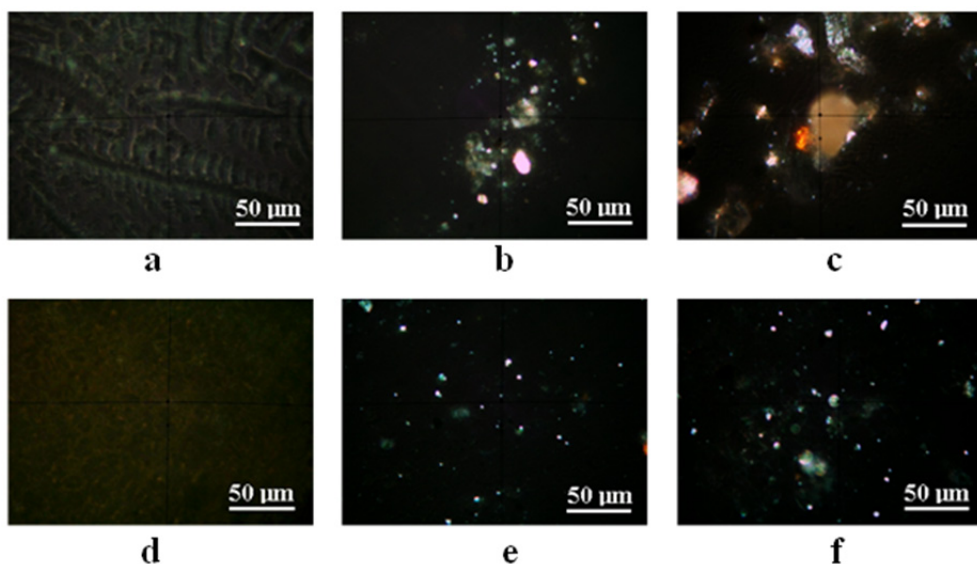
Figure 8. Cross polarized light images for in vivo experiment:
Nose mucus: a) normal atmosphere, b) polluted atmosphere up to 125 µg/m^3 PM10, and c) polluted atmosphere up to 200 µg/m^3;
Expectoration product: d) normal atmosphere, e) polluted atmosphere up to 125 µg/m^3 PM10, and f) polluted atmosphere up to 200 µg/m^3.

Significant mineral deposits are found in the expectoration product where PM2.5 consisting in clay particles is found predominantly, Figure 8f. There are found also some PM10 particles with quartz aspect, which means a severe penetration of PM into the respiratory system.

CONCLUSIONS

The analysis performed in present article proves that SD is the major source of PM in the atmosphere in environmental conditions from Dâmboviţei Street, Cluj – Napoca. The minerals from SD are found in FP sample: quartz as dominant mineral followed by clay mixture with kaolinite and muscovite, calcite and goethite. Pollen was found in FP sample, proving that pollen could be considered as PM which could affect respiratory system especially in allergic affections. PM10 contains mainly quartz particles meanwhile PM2.5 contains kaolinite and muscovite predominantly. Such composition depends on the investigated specific area; some other sites could report other compositions. AFM imaging reveals some nanoparticles in PM2.5.

The minerals in PM10 and PM2.5 could be very hazardous for the respiratory system, if the standard limit is exceeded and the exposure time is long enough in vivo experiments. A short exposure at an intense dose of PM leads to an acute respiratory affection, and chronic affections could appear if exposure is extended for long time.

The air monitoring data shows that the PM emissions in the Dâmboviţei Street area are below standard limit and no hazard risk appears if the environmental condition is maintained.

EXPERIMENTAL SECTION

The experimental area is situated in Dâmboviţei Street, Cluj – Napoca. The SD samples were collected weekly during April and March 2017. Each week was taken 10 grams of SD and mixed together to obtain an average representative sample of SD. Dâmboviţei Street has a lot of vegetal species which flowers during April and May. Therefore, the resulted pollen could emerge in the atmosphere like PM. Pollen from *Tilia Cordata*, *Sambucus Nigra*, *Jasminus Communis*, *Rosaceae* Family, *Lilium Candidum*, and *Brassica Rapa* was collected and investigated.

PM samples: FP, PM10, and PM2.5 were collected using Automatic Air monit oring Station from Environmental Protection Agency of Cluj-Napoca, and their level of emission in the atmosphere was monitored during April and May 2017 and the results were centralized.

In vivo experiment consists in a human subject (volunteer agreement) exposed for 5 minutes to normal atmosphere, average polluted atmosphere (aprox. 125 µg/m^3 of PM10), and high polluted atmosphere (up to 200 µg/m^3 of PM10). The polluted atmosphere was produced by street dust agitation with an air blower in the Dâmboviţei Street area. Nose mucus and expectoration product was collected after each exposure. The exposures were effectuated in different days to avoid the cumulative effect on the subject.

The X–ray diffraction analysis was performed on a DRON 3 diffractometer equipped with data acquisition module and MATMEC VI.0 soft. A monochrome $Co_{k\alpha}$ radiation was used for all X ray spectra. The mineral identification was effectuated using MATCH 1.0 X – ray standard data base from Crystal Impact co.

Optical microscopy was performed on a Laboval 2 microscope produced by Karl Zeiss Jena equipped with digital capture Kodak 10 Mpx camera. Quantitative analysis on the optical microphotographs was done using the Image J professional soft as freeware resource from National Institutes of Health USA.

SEM microscopy associated with EDX analysis was performed on a Jeol JSM 5600 LV microscope in secondary electrons imaging mode coupled with Everhart Thornley detector for EDX analysis

Samples for AFM investigation were prepared according to the data in literature [27 - 34]. The AFM investigation was performed on a Jeol JSPM 4210 microscope in tapping mode using NSC 15 cantilever. Topography, phase, and amplitude images were acquired simultaneously and were processed into the standard manner using Win SPM 2.0 processing soft.

REFERENCES

1. L.A. Jimoda, *Facta Universitatis, Series: Working and Living Environmental Protection*, **2012**, *9* (1), 27.
2. J.S. Le Blond, S. Woskie, C.J. Horwell, B.J. Williamson, *Atmospheric Environment*, **2017**, *149*, 34.
3. W.C. Lo, R.H. Shie, C.C. Chan, H.H. Lin, *Journal of the Formosan Medical Association*, **2017**, *116*, 32.
4. M.R. Perrone, S. Becagli, J.A. Garcia Orza, R. Vecchi, A. Dinoi, R. Udisti, M. Cabello, *Atmospheric Environment*, **2013**, *71*, 176.
5. K.H. Kim, E. Kabir, S. Kabir, *Environment International*, **2015**, *74*, 136.
6. J. Londhal, J. Pagels, E. Swietlicki, J. Zhou, M. Ketzel, A. Massling, M. Boghard, *Aerosol Science*, **2006**, *37*, 1152.
7. Q. Xu, S. Wang, Y. Guo, C. Wang, F. Huang, X. Li, Q. Gao, L. Wu, L. Tao, J. Guo, W. Wang, X. Guo, *Environmental Pollution*, **2017**, *220*, 317.
8. M. Watanabe, H. Noma, J. Kurai, H. Sano, D. Hantan, M. Ueki, H. Kitano, E. Shimizu, *Allergology International*, **2017**, *66*, 52.
9. A.C. Güngen, Y. Aydemir, H. Çoban, H. Düzenli, C. Tasdemir, *Respiratory Medicine Case Reports*, **2016**, *18*, 93.
10. A.G. Cohen, F. Romero Ruperto, F.J. G. Sendra, M.J. Sánchez García-Altares, M.L. Parra Gordoc, *Medicina General y de Familia*, **2016**, *5* (4), 169.
11. M. Tsugita, N. Morimoto, M. Tashiro, K. Kinoshita, M. Nakayama, *Cell Reports*, **2017**, *18*, 1298.

12. P. Solaimani, A. Saffari, C. Sioutas, S.C. Bondy, *Neuro Toxicology*, **2017**, *58*, 50.
13. G.A. Păltinean, I. Petean, G. Arghir, D.F. Muntean, L.-D. Boboş, M. Tomoaia-Cotişel, *Particulate Science and Technology*, **2016**, *34* (5), 580.
14. G.A. Păltinean, I. Petean, G. Arghir, D.F. Muntean, M. Tomoaia-Cotişel, *Revista de chimie*, **2016**, *67* (6), 1118.
15. D.F. Muntean, D. Ristoiu, G. Arghir, R.F. Campean, I. Petean, *Carpathian Journal of Earth and Environmental Sciences*, **2012**, *7* (3), 175.
16. S.S. Ram, R.V. Kumar, P. Chaudhuri, S. Chanda, S.C. Santra, M. Sudarshan, A. Chakraborty, *Ecological Indicators*, **2014**, *36*, 334.
17. L. Makra, I. Ionel, Z. Csépe, I. Matyasovszky, N. Lontis, F. Popescu, Z. Sümeghy, *Science of the Total Environment*, **2013**, *458-460*, 36.
18. J. Novak, K. Hilscherová, L. Landlová, P. Čupr, L. Kohút, J.P. Giesy, J. Klánová, *Environment International*, **2014**, *63*, 64.
19. F. Mirante, P. Salvador, C. Pio, C. Alves, B. Artinano, A. Caseiro, M.A. Revuelta, *Atmospheric Research*, **2014**, *138*, 278.
20. W. De Poel, S. Pintea, J. Drnec, F. Carla, R. Felici, P. Mulder, J. Elemans, W. Van Enckevort, A.E. Rowan, E. Vlieg, *Surface Science*, **2014**, *619*, 19.
21. M. S. Żbik, N.A. Raftery, R.S.C. Smart, R.L. Frost, *Applied Clay Science*, **2010**, *50*, 299.
22. O. Horovitz, Gh. Tomoaia, A. Mocanu, T. Yupsanis, M. Tomoaia-Cotisel, *Gold Bulletin*, **2007**, *40* (4), 295.
23. M. Tomoaia-Cotisel, A. Tomoaia-Cotisel, T. Yupsanis, Gh. Tomoaia, I. Balea, A. Mocanu, Cs. Racz, *Revue Roumaine de Chimie,* **2006,** *51* (12),1181.
24. M.A. Naghiu, M. Gorea, E. Mutch, F. Kristaly, M. Tomoaia-Cotisel, *Journal of Material Science and Technology,* **2013**, *29* (7), 628.
25. G. Tomoaia, O. Soritau, M. Tomoaia-Cotisel, L.-B. Pop, A. Pop, A. Mocanu, O. Horovitz, L.-D. Bobos, *Powder Technology*, **2013**, *238*, 99.
26. Gh. Tomoaia, O. Horovitz, A. Mocanu, A. Nita, A. Avram, C.P. Racz, O. Soritau, M. Cenariu, M. Tomoaia-Cotisel, *Colloids and Surfaces B: Biointerfaces*, **2015,** *135*, 726.
27. P.T. Frangopol. D.A. Cadenhead, Gh. Tomoaia, A. Mocanu, M. Tomoaia-Cotisel, *Revue Roumaine de Chimie,* **2015***, 60* (2-3), 265.
28. R.D. Pasca, G. Tomoaia, A. Mocanu, I. Petean, G.A. Paltinean, O. Soritau, M. Tomoaia-Cotisel, *Studia Univ. Babes-Bolyai, Chemia*, **2015**, *60* (3), 257.
29. G. Tomoaia, A. Mocanu, L.D. Bobos, L.B. Pop, O. Horovitz, M. Tomoaia-Cotisel, *Studia Univ. Babes-Bolyai, Chemia*, **2015**, *60* (3), 265.
30. G. Tomoaia, M. Tomoaia-Cotisel, L.B. Pop, A. Pop, O. Horovitz, A. Mocanu, N. Jumate, L.-D. Bobos, *Revue Roumaine de Chimie*, **2011**, *56*, 1039.
31. M. Tomoaia-Cotisel, A. Mocanu, *Revista de Chimie (Bucharest),* **2008**, *59* (11), 1230.
32. G. Furtos, M.A. Naghiu, H. Declercq, M. Gorea, C. Prejmerean, O. Pana, M. Tomoaia-Cotisel, *Journal of Biomedical Materials Research Part B. Applied Biomaterials,* **2015**, *104* (7), 1290.

33. F. Goga, E. Forizs, A. Avram, A. Rotaru, A. Lucian, I. Petean, A. Mocanu, M. Tomoaia-Cotisel, *Revista de Chimie (Bucuresti),* **2017**, *68* (6), 1193.
34. I. Cojocaru, A. Tomoaia-Cotisel, A. Mocanu, T. Yupsanis, M. Tomoaia-Cotisel, *Revista de Chimie (Bucuresti),* **2017**, *68* (7), 1470.

POLIMERIC MEMBRANES PREPARED WITH SURFACTANTS USED FOR ULTRAFILTRATION OF AQUEOUS SOLUTIONS OF FOOD DYE

GEORGE ALEXANDRU POPA[a], GHEORGHE NECHIFOR[a,*],
DANIELA FLORENTINA ENACHE (POPA)[a],
SZIDONIA-KATALIN TANCZOS[b], ADRIAN CIOCANEA[c]

ABSTRACT. The experiments carried out in this paper tested the effectiveness of the polysulfone-dimethyldioctodecylammonium bromide (PSU-DMOA) and polysulfone-Tween 80 in dead-end facilities. The efficiency of these membranes has been proved by determining the permeate flow and the retention coefficient. Analyzing the experimental data, it was found that for the polysulfone-dimethyldioctodecylammonium bromide composite membrane the retention rate is higher than for the polysulfone-Tween 80 composite membrane, the t values being obtained for the highest pressure used in the system.

Keywords: composite membranes, ultrafiltration, surfactants, food dye

INTRODUCTION

Polymeric membranes can be used in many simple and complex systems [1-3]. Obtaining membranes can be influenced by the addition of small amounts of surfactants [4,5]. The membrane process can be controlled by using surfactants [6,7].

---

[a] *University Politehnica of Bucharest, Department of Analytical Chemistry and Environmental Engineering, 1-3 Gh. Polizu Str.,011061, Bucharest, Romania*
[b] *Sapientia University, Liberty St., 500104, Miercurea Ciuc, Romania*
[c] *Politehnica University of Bucharest, Power Engineering Faculty-Hydraulics, Hydraulic Machinery and Environmental Engineering Department, 313 Splaiul Independentei, 060042, Bucharest, Romania*
* *Corresponding author: gheorghe.nechifor@upb.ro*

Surfactants are chemicals which, in solutions, concentrate on the surface and solubilize materials that have little affinity with each other [8]. Accumulating on the separation surfaces, the surfactants are able to alter strongly, even in very low concentrations, the superficial properties of the liquids in which they dissolve [9-11].

The composite polymeric membranes are currently one of the most viable solutions for increasing process membrane performance in terms of permeability as well as selectivity [12-15]. Currently, the improvement of the membrane techniques culminated in their transition to the industrial area of applicability [16,17].

This paper presents the experimental results obtained from the use of polysulfone-dimethyldioctodecylammonium bromide (PMU-DMOA) and polysulfone-Tween 80 composite.

RESULTS AND DISCUSSION

Experiments were carried out to test the effectiveness of polysulfone-dimethyldioctodecylammonium bromide (PMU-DMOA) and polysulfone-Tween 80 membranes. The efficiency of these membranes has been proved by the calculation of permeate flow and retention coefficient [18-22].

The results obtained for the polysulfone-dimethyldioctodecyl ammonium bromide (PMU-DMOA) membranes:

Figure 1. Time variation of the permeate mass at 0.1 MPa pressure for polysulfone - dimethyldioctodecylammonium bromide

Figure 2. Flow variation at 0.1 MPa for polysulfone -
dimethyldioctodecylammonium bromide

Working conditions: Initial solution: $C_{18}H_{13}NO_{5/8/11}S_{1/2/3}Na_{1/2/3}$, 10% (equivalent to 100 g / m^3) - E104; Process duration: 30 minutes; Spectrophotometric measurements at the wavelength of 575nm; Initial temperature: 21,1°C; Final temperature: 23,8°C; Pressure: 0.1MPa; Operation of the installation: dead-end.

Compared to classical polysulfone membranes, the membrane incorporating surfactant has a better flow for the same operating pressure, ranging from 0,7471 to 1,2463 m^3/m^{2}day.
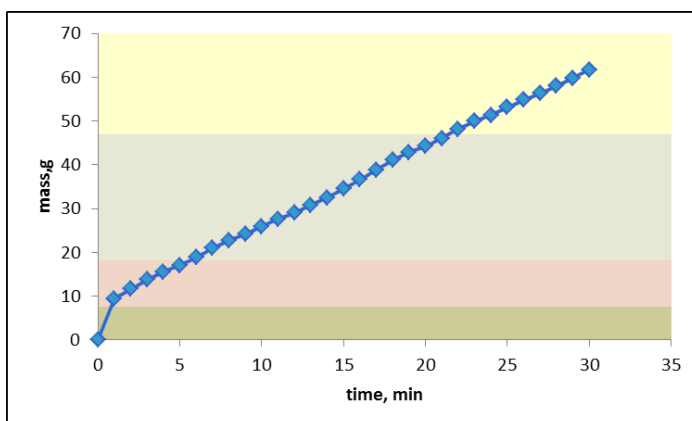
Figure 3. Time variation of the permeate mass at 0.2 MPa pressure for polysulfone -dimethyldioctodecylammonium bromide
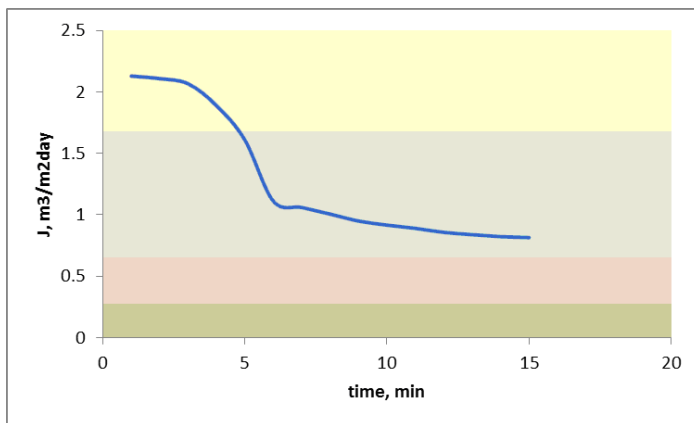
Figure 4. Flow variation at 0.2 MPa for polysulfone - dimethyldioctodecylammonium bromide

Working conditions: Initial solution: $C_{18}H_{13}NO_{5/8/11}S_{1/2/3}Na_{1/2/3}$, 10% (equivalent to 100 g / m^3) - E104; Process duration: 30 minutes; Spectrophotometric measurements at the wavelength of 575nm; Initial temperature: 21,3°C; Final temperature: 23,1°C; Pressure: 0.2MPa; Operation of the installation: dead-end.

For the same solution analyzed, at a pressure of 0.2MPa, the flow value ranged between 0,8145 and 2,129 $m^3/m^2 day$, considerably higher than those obtained under the same conditions at 0.1MPa.
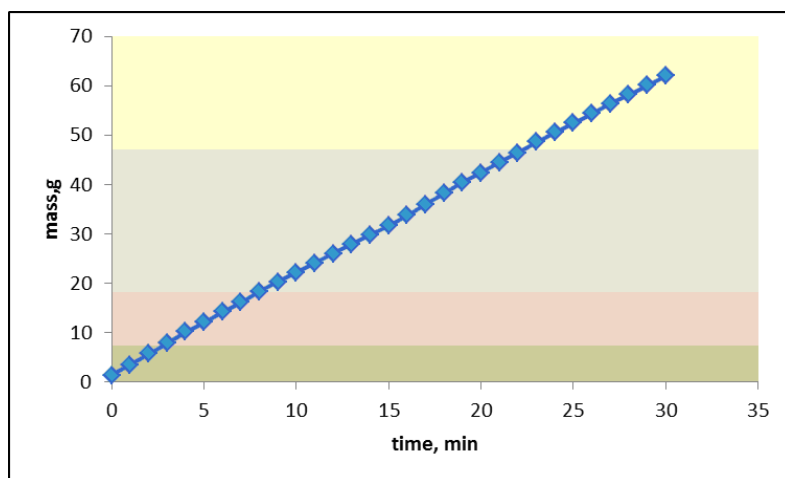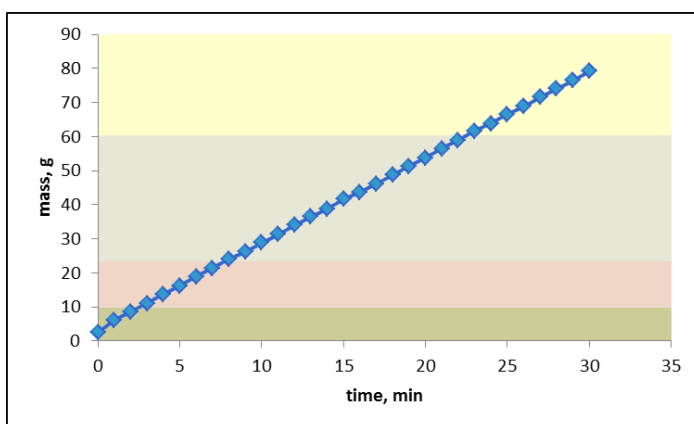

Figure 5. Time variation of the permeate mass at 0.3 MPa pressure for polysulfone - dimethyldioctodecylammonium bromide
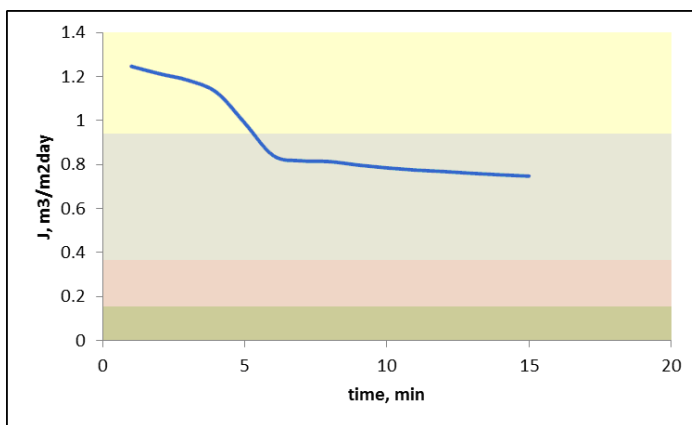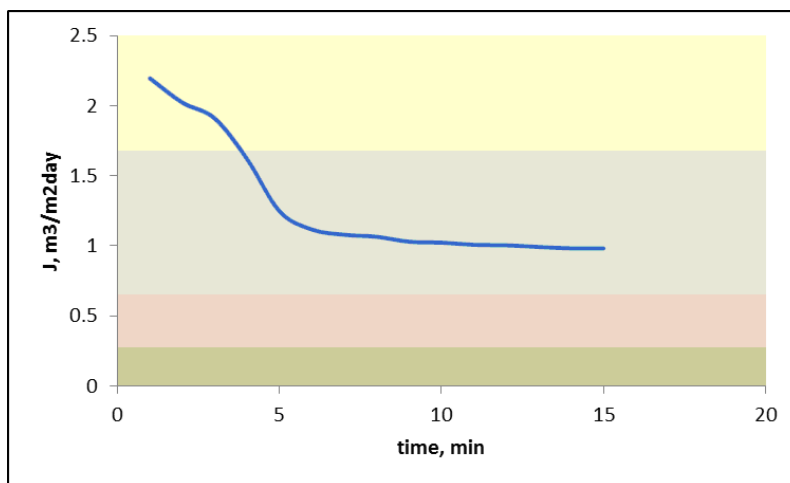
Figure 6. Flow variation at 0.3 MPa for polysulfone - dimethyldioctodecylammonium bromide

Working conditions: Initial solution: $C_{18}H_{13}NO_{5/8/11}S_{1/2/3}Na_{1/2/3}$, 10% (equivalent to 100 g / m^3) - E104; Process duration: 30 minutes; Spectrophotometric measurements at the wavelength of 575nm; Initial temperature: 20,2°C; Final temperature: 24,5°C; Pressure: 0.3MPa; Operation of the installation: dead-end;

The flow value ranges from 0,9818 to 2,1577 m^3/m^{2}day, also maintaining a downward trend. The flow values for the highest pressure are also high. It can be seen that the polysulfone-dimethyldioctodecyl ammonium bromide composite membrane presents a better flux compared to the polysulfone membrane and polysulfone-polyaniline membrane.

Also, the degree of retention for this type of membrane was higher, given that the presence of the surfactant in the membrane structure caused the formation of micelles and the retention of a considerable amount of dye. The retention determined for the composite polysulfone-dimethyldiocto decylammonium bromide membrane is shown graphically below.

The retention coefficient for solution containing dye E 104 ranged from 34,3 to 43,8% for composite membranes made of polysulfone-dimethyldioctodecylammonium bromide using dead-end filtration. To determine the retention coefficient, we measured the concentration of permeate and retentate solutions using spectrophotometric measurements of absorbance at the wavelength of 575 nm.
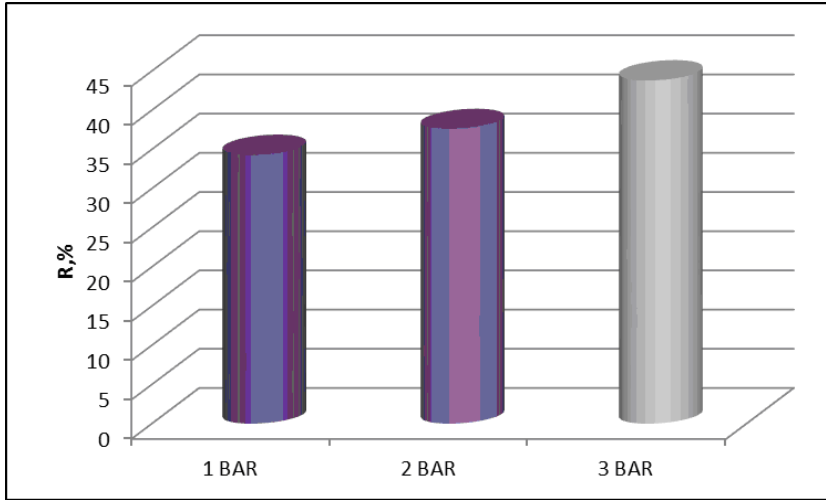
Figure 7. The retention ratio of the dye (R) for the polysulfone-
dimethyldioctodecylammonium bromide

The results obtained for polysulfone - Tween 80 composite membrane:
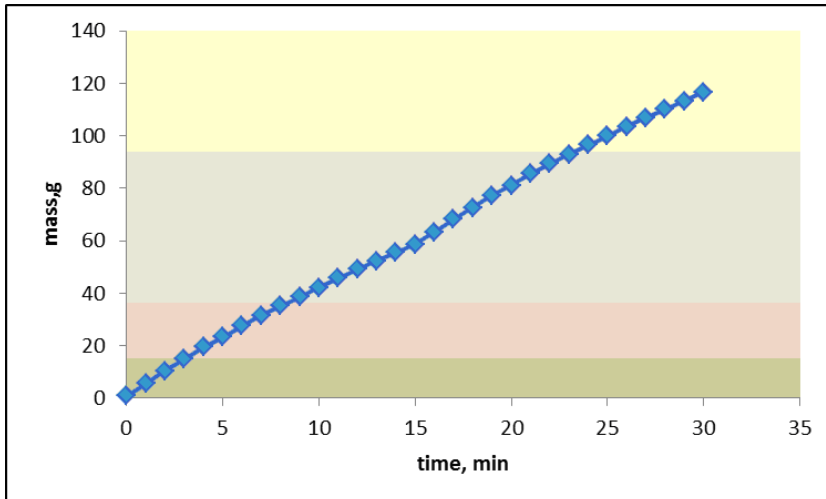
Figure 8. Time variation of the permeate mass at 0.1 MPa pressure for
polysulfone – Tween 80
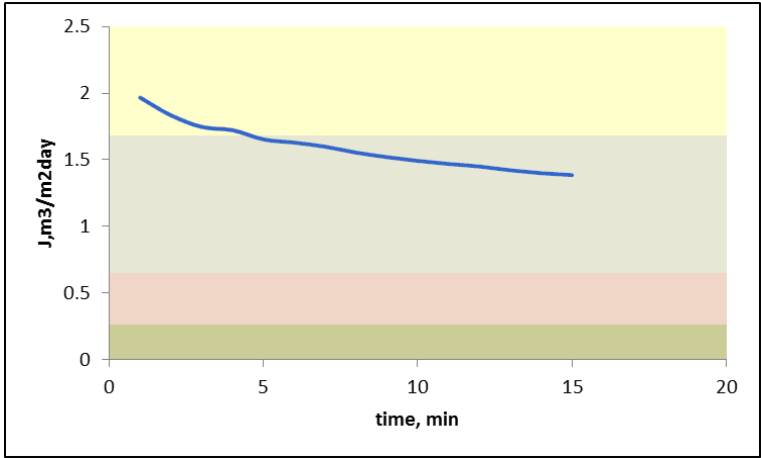
Figure 9. Flow variation at 0.1 MPa for polysulfone – Tween 80

Working conditions: Initial solution: $C_{18}H_{13}NO_{5/8/11}S_{1/2/3}Na_{1/2/3}$, 10% (equivalent to 100 g / m³) - E104; Process duration: 30 minutes; Spectrophotometric measurements at the wavelength of 575nm; Initial temperature: 19,8°C; Final temperature: 21,4°C; Pressure: 0.1MPa; Operation of the installation: dead-end.

For this membrane, flows were obtained which varied at an operating pressure of 0.1MPa, from 1,3862 to 1,9671 m³/m²day.
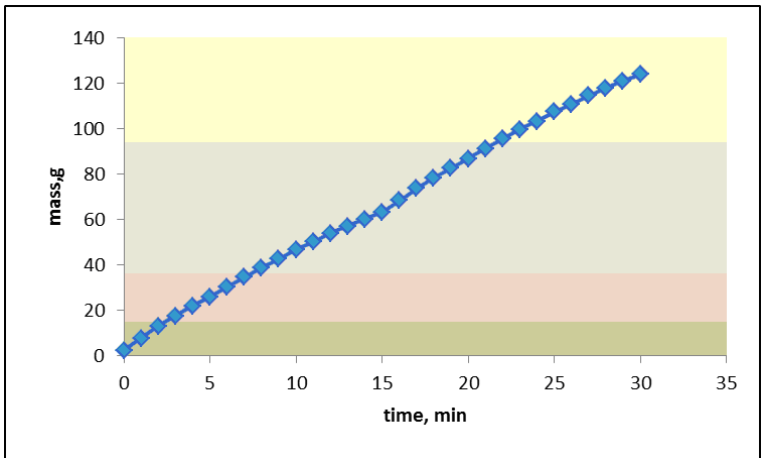
Figure 10. Time variation of the permeate mass at 0.2 MPa pressure for polysulfone – Tween 80
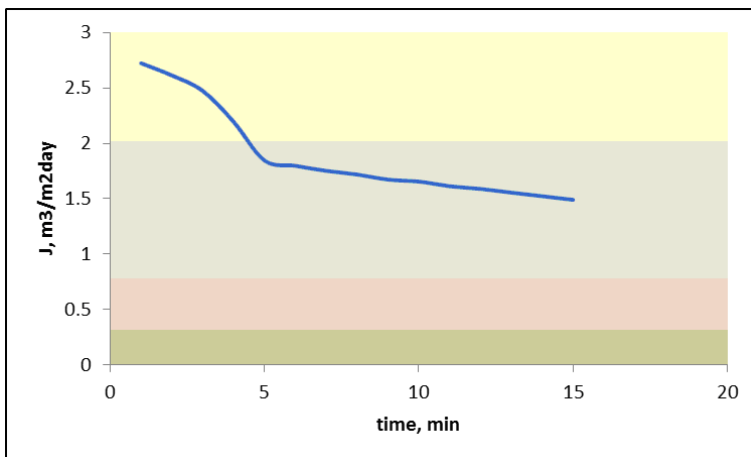
Figure 11. Flow variation at 0.2 MPa for polysulfone – Tween 80

Working conditions: Initial solution: $C_{18}H_{13}NO_{5/8/11}S_{1/2/3}Na_{1/2/3}$, 10% (equivalent to 100 g / m^3) - E104; Process duration: 30 minutes; Spectrophotometric measurements at the wavelength of 575nm; Initial temperature: 20°C; Final temperature: 22,2°C; Pressure: 0.2MPa; Operation of the installation: dead-end.

For the 0.2MPa, the flow value is between 1,491 and 2,7226 m^3/m^{2}day, considerably higher than those obtained under the same conditions at 0.1MPa.
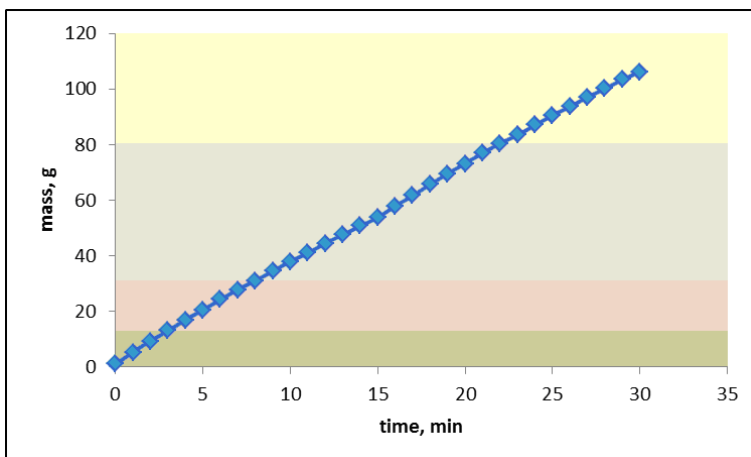
Figure 12. Time variation of the permeate mass at 0.3 MPa pressure
for polysulfone – Tween 80
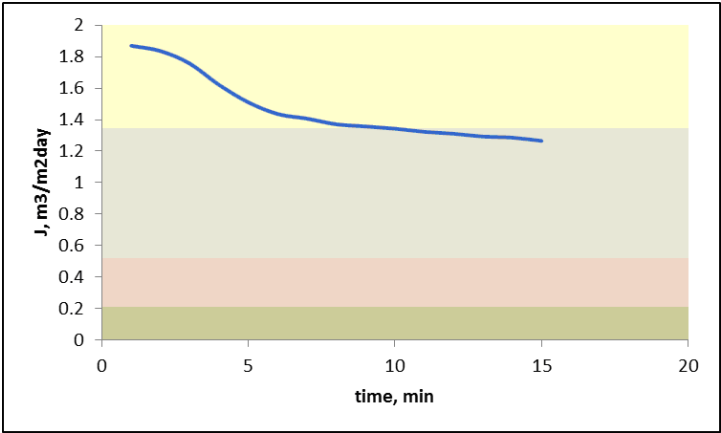
Figure 14. Flow variation at 0.3 MPa for polysulfone – Tween 80

Working conditions: Initial solution: $C_{18}H_{13}NO_{5/8/11}S_{1/2/3}Na_{1/2/3}$, 10% (equivalent to 100 g / m³) - E104; Process duration: 30 minutes; Spectrophotometric measurements at the wavelength of 575nm; Initial temperature: 20,3°C; Final temperature: 24,2°C; Pressure: 0.3MPa; Operation of the installation: dead-end;

The flow rate at 0.3MPa is between 1,2657 and 1,8695 m³/m²day. For this type of membrane, the best fluxes were obtained for the pressure of 0.2MPa, and for the other pressure values the data obtained is similar. The retention degree for this type of membrane can be compared to that obtained for the other membrane types, the results being represented graphically.
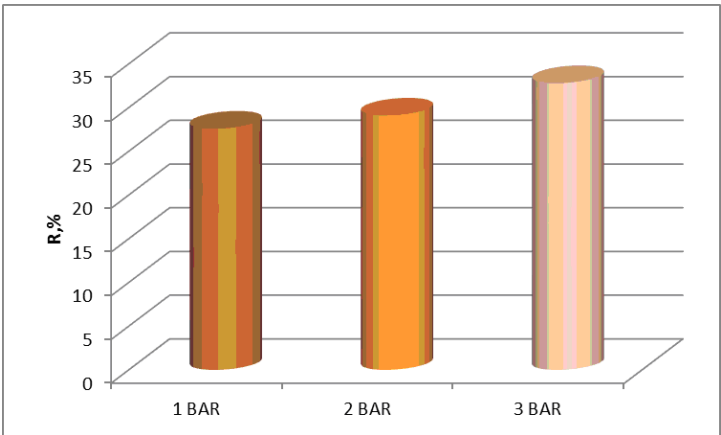
Figure 15. The retention ratio of the dye (R) for the polysulfone - Tween 80

The retention coefficient for solution containing dye E 104 ranged from 27,6 to 32,8% for Tween 80 polysulfone - based composite membranes using dead - end filtration. The results are similar to those obtained for polysulfone - polyaniline and polysulfone membranes.

To determine the retention coefficient, we measured the concentration of permeate and retentate solutions using spectrophotometric measurements of absorbance at the wavelength of 575 nm.

CONCLUSIONS

Membranes undergoing this experimental study showed good mechanical and chemical resistance. Flows presented comparative values with literature data.

The best fluxes were obtained for the polysulfone – dimethyl dioctadecylammonium bromide membrane at 0.2 MPa and at the highest pressure used in the instalation, 0.3 MPa for the polysulfone - Tween 80 membrane.

Regarding the retention, it was observed that the best results were recorded for the dimethyldioctodecylammonium polysulfone - bromide membrane compared to the polysulfone - Tween 80 membrane.

EXPERIMENTAL SECTION

This study used non-commercial membranes [13-16]. The ultafiltration membranes developed were polysulfone-dimethyldioctodecylammonium bromide (PMU-DMOA) and polysulfone-Tween 80.

The properties of the ultrafiltration membranes regarding transport and separation were determined on solutions containing E104 quinoline yellow synthetic dye. The molecular formula of E 104 is: $C_{18}H_{13}NO_{5/8/11}S_{1/2/3}Na_{1/2/3}$ and the molecular weight amounts to 477.38g/mol. It is used as a synthetic colouring agent in food and drink products, as well as in cosmetics.

The ultrafiltration process in the presence of surfactants was investigated in a pilot laboratory set – up [14]. The membrane being tested had a diameter of 36mm. The pressures used in the ultrafiltration process were 0.1, 0.2 and 0.3 MPa. Permeate volume fluxes and retention coefficients were determined on steady flow conditions. Permeate volume flow was calculated as shown below: $J = \dfrac{V}{t \cdot A}(m^3 / m^2 day)$, where V is the permeate volume (m^3), t stands for the time (day), and A represents the effective membrane surface area (m^2).

Dye retention coefficient (R) was determined as: $R = \dfrac{C_k - C_p}{C_k} \cdot 100(\%)$

where Ck and Cp denote the dye concentration (g/m^3) in retentate and permeate, respectively [16].
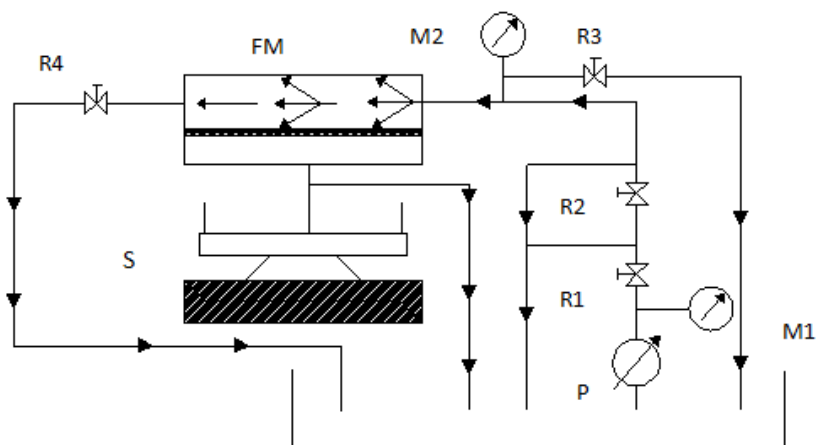
Scheme 1. Pilot set-up: P –centrifugal pump, FM – filtration module, S –digital scale, R – valve, M – manometer

To obtain a wider range of flow a centrifugal pump was used (Q= 40 l/min), driven by a variable speed (n = 287rpm). A digital laboratory balance, Mettler Toledo model, was used for weighing. The substrate surfaces used for the membranes will be molecular sieves, made of stainless steel. For this, AISI304MESH94 mesh sieve 110µ (0,11mm) mesh opening 150µ (0,15mm) was used. This is mainly used in the pharmaceutical industry. To track the flow parameters through the membrane, equipment has been developed to highlight these aspects.

ACKNOWLEDGMENTS

REFERENCES

1. G. Nechifor, N. Luca, G. Popescu, M. Nechifor, *Revue Roumaine de Chimie*, **1989**, *34*, 2047.
2. G. Batrinescu, M.A. Constantin, A. Cuciureanu, G. Nechifor, *Polymer Engineering and Science*, **2014**, *54*, 1640.
3. K. Scott, „Handbook of industrial membranes", First edition, Elsevier Science Publishers Ltd, **1995**.
4. G., Nechifor, B. Albu, D. Rata, G. Popescu, Revista de Chimie, **1996**, *47*, 260.
5. K. Lintner, S. Bragulla, *Internationale Zeitschrift fur Lebensmittel*, **1987**, *38*, 120.
6. K. Majewska-Nowak, *Environment Protection Engineering*, **2009**, *4*, 111.
7. G. Nechifor, S.I. Voicu, A.C. Nechifor, S. Garea, *Desalination*, **2009**, *241*, 342.
8. E. Chifu, "Chimie coloidala" Editura Didactică şi Pedagogică, Bucuresti, **1969**.
9. N. Rubingh, P. M. Holland (ed.), "Cationic Surfactants – Physical Chemistry", Marcel Dekker, New York, **1991**.
10. M.J. Schick (ed.), "Nonionic Surfactants", Marcel Dekker, New York, **1966**.
11. K.L. Mittal, D.O. Shoh, "Surfactants in solution", Vol. 11, Springer Science & Business Media, New York, **1991**.
12. B. Van der Bruggen, B. Daems, D. Wilms, C. Vandecasteele, *Separation and Purification Technology*, **2001**, *22-23*, 519.
13. Ştefan Ioan Voicu, Florin Aldea, Marin Răduţ, Gheorghe Nechifor, Nanostructured polysulfone composite membranes, *U.P.B. Sci. Bull., Series B,* **2008**, *70*, 3.
14. G.A. Popa, D.F. Popa (Enache), D.D. Slave (Clej), I.S. Din, C.M. Mirea, A., Ciocanea, *Revista de Chimie*, **2017**, *68*, 6.
15. A. Cuciureanu, G. Batrinescu, N.N. Badea, D.A. Radu, G. Nechifor, *Materiale Plastice*, **2010**, *47*, 416.
16. A.A.K.K. Rikabi, A. Cuciureanu, M. Chelu, A.R. Miron, C. Orbeci, A.G. Popa, M.E. Craciun, *Revista de Chimie*, **2015**, *66***,**1093.
17. C.K. Kima, S.S. Kimb, J.C. Limc, J.J. Kimd, *Journal of Membrane Science*, **1998**, *147*, 13.
18. K. Majewska-Nowak, I. Kowalska, M. Kabsch-Korbutowicz, *Desalination*, **2006**, *198*, 157.
19. K. Majewska-Nowak, I. Kowalska, M. Kabsch-Korbutowicz, *Desalination,* **2006**, *200*, 283.
20. C.K. Kima, S.S. Kimb, J.C. Limc, J.J. Kimd, *Journal of Membrane Science,* **1998**, *147*,13.
21. A.C. Archer, A.M. Mendes, R.A.R. Boaventura, *Environmental Science and Technology*, **1999**, *33*, 2758.
22. K. Majewska-Nowak, *Environment Protection Engineering*, **2005**, *31*, 229.
23. J. Huang, L. Peng, G. Zeng, X. Li, Y. Zhao, L. Liu, F. Li, Q. Chai, *Separation and Purification Technology,* **2014**, *125*, 83.

PERIODATE-OXIDIZED ALGINATE AS POLYCONDENSATION REAGENT FOR HEMOGLOBIN

FLORINA SCURTU[a], ANAMARIA POPA[a], RADU SILAGHI-DUMITRESCU[a*]

ABSTRACT. We have previously demonstrated that derivatization of hemoglobin with periodate-modified sugar derivatives incurs increases in the pro-oxidant reactivity and, also, that serum bovine serum albumin can resolve this problem entirely. Here, we described a new polymer based on hemoglobin and another oxygen-containing compound, alginate. The rate of autooxidation increases after derivatization, but serum albumin alleviates this problem. The peroxide reactivity and oxygen affinity were also tested but no significant differences were observed between derivatized and native hemoglobin.

Keywords: blood substitute, hemoglobin, alginate, oxidative stress

INTRODUCTION

It was demonstrated that acellular hemoglobin, even when carefully purified, does not represent by itself a solution for hemoglobin-based oxygen carriers (HBOC) because of negative side-effects:[1-3] the first key problem with free hemoglobin is it slow molecular volume, leading to extravasation and indirectly other to problems(high oxygen affinity, vasoactive properties, renal toxicity).[4,5] The challenge in creating a reasonable blood substitute is to increase their molecular weight by chemical and/or genetic modification.[6-8] On the other hand, modification of the protein structure can affect other properties, including autooxidation rates, oxygen affinity, cooperativity, affinity for nitrosative and/or oxidative stress agents, and other functions of hemoglobin such as NO and CO_2 transport.[9]

---

[a] *Babes-Bolyai University, Faculty of Chemistry and Chemical Engineering, 11 Arany Janos str. RO-400028, Cluj-Napoca, Romania*
Corresponding author; email: rsilaghi@chem.ubbcluj.ro

Intermolecularly-crosslinked hemoglobins produced using polyaldehydes have been used extensively to modify the negative properties of native Hb. The most common reagents in this respect are glutaraldehyde, formaldehyde, acetaldehyde;[10,11] however, a variety of dialdehydes can also be obtained via oxidation by sodium periodate of diverse water-soluble sugar derivatives (dextran, ATP, starch), or even compounds like polyethylene glycol.[12,13] Here, for the first time, we report that sodium alginate can also be used for crosslinking hemoglobin. Parameters like molecular size, autooxidation rate and oxygen affinity appears to be affected after the polymerization process. The process may in principle be applicable to crosslinking of other materials as well.

RESULTS ANS DISCUSSION

Oxidation of alginate with sodium periodate was performed in order to ring-open the 1,2-diols to yield dialdehydes (Figure 1) which can then be employed for polycondensation of proteins, namely hemoglobin and albumin. Figure 2 shows an SDS-PAGE gel and gel-filtration chromatograms illustrating that oxidized alginate indeed induces an increase in molecular weight. Introduction of BSA in the reaction mixture leads to lower molecular weights for copolymers comparative to the polymers as illustrated in Table 1.
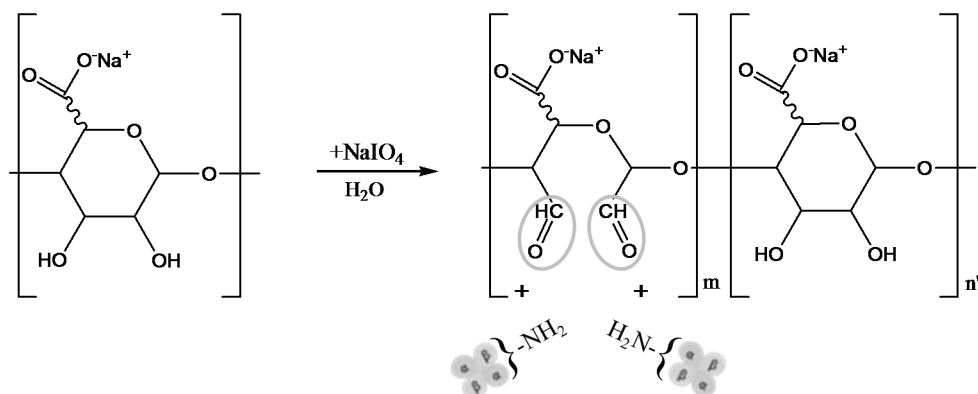
Figure 1. Oxidation of sodium alginate by periodate
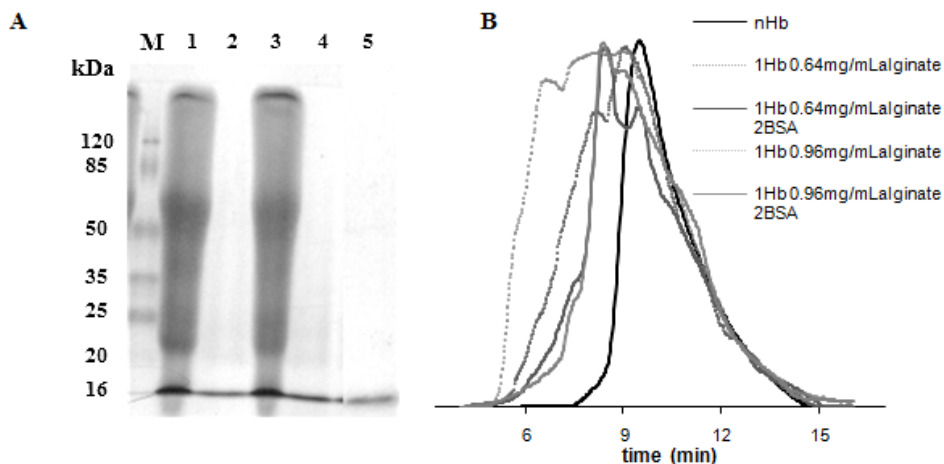
Figure2.A) SDS-PAGE illustrating the influence of alginate concentration upon polymerization degree. **1**- 1 mM Hb + 0.96 mg/mL alginate + 2 mM BSA, **2**- 1mM Hb + 0.96 mg/mL alginate, **3**- 1 mM Hb + 0.64 mg/mL alginate + 2 mM BSA, **4**- 1 mM Hb + 0.64 mg/mL alginate, **5**- native Hb. **B)**Size-exclusion chromatograms for Hb derivatized with different concentration of alginate. Conditions: 20mM Tris pH 7.4, 150 mM NaCl, room temperature

Table 1 also shows the autooxidation rate values. While oxidized alginate induces drastic autooxidation, bovine serum albumin can alleviate this problem. Thus, the amount of metHb formed is ~two times lower if in the reaction mixture is added BSA.

Table 1. Molecular weight and autooxidation rates (express in percentage of metHb formed) values.

	Molecular weight [kDa]	Autooxidation rate(%)
native Hb	64	14.29
1Hb + 0.64 mg/mL alginate	210 – 77	30.81
1Hb + 0.64 mg/mL alginate + 2BSA	230 – 64	18.22
1Hb + 0.96 mg/mL alginate	>500(850) – 80	44.82
1Hb + 0.96 mg/mL alginate + 2BSA	170 – 64	22.03

61

Figure 3 illustrates the time course at 425 nm during the reaction of hydrogen peroxide with poly- and copolymerized Hb. This wavelength is characteristic of ferryl form (FeIV – so called Compound II). [7,14,15] There is no significant difference between the derivatized Hb and the native: both the yield of ferryl form and its stability is similar with to that of native Hb.
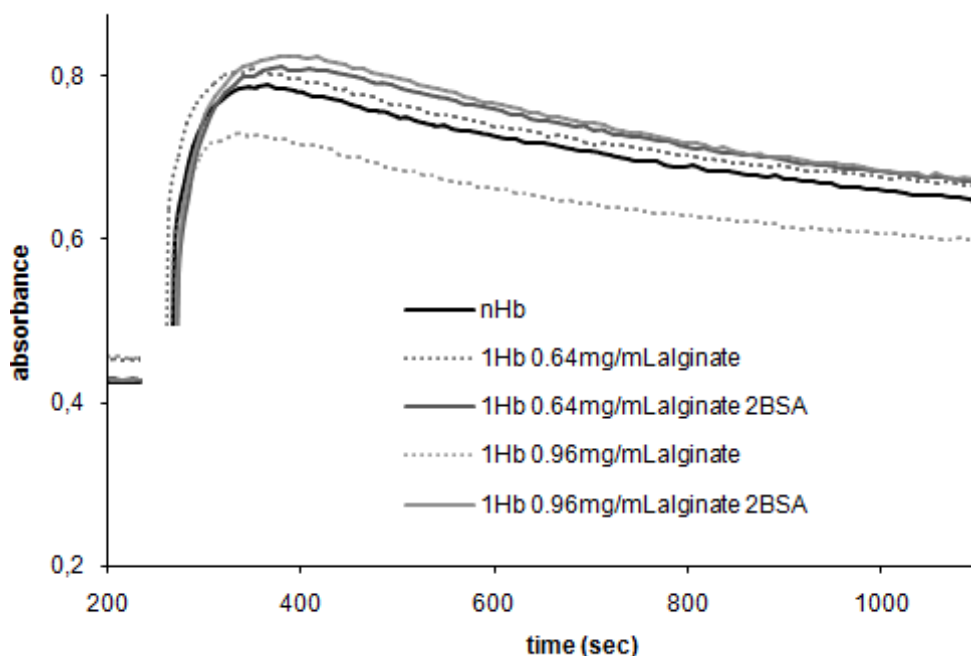
Figure 3. Time course for the reaction of ferric native Hb, poly- and copolymerized Hb with hydrogen peroxide. Conditions: 10 µM protein, 80 µM peroxide, PBS, room temperature

Figure 4 illustrates oxygen binding curves for copolymerized and native hemoglobin. It may be seen that the cooperativity effect disappears in derivatized Hb while affinity towards oxygen increases compared with native hemoglobin, in line with observations previously noted for most other polycondensates based on hemoglobin or other related proteins.[10,16-22]
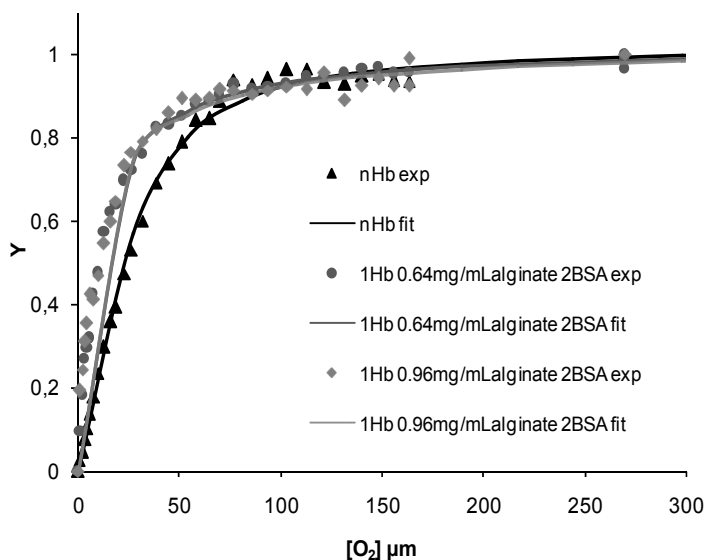
Figure 4. Oxygen saturation curves of native Hb and polymerized Hb. Conditions: PBS, room temperature

Table 2. K_d values and Hill coefficients (n) for poly- and copolymers.

	K_d	n
native Hb	22.99	1.55
1Hb + 0.64 mg/mL alginate +2BSA	10.46	1.04
1Hb + 0.96 mg/mL alginate + 2BSA	9.11	0.92

CONCLUSIONS

The derivatization procedure described here show that polymerization of hemoglobin with oxidized alginate lead to an increase in autooxidation rate, but addition of bovine serum albumin alleviates this problem. Also, molecular size and oxygen affinity was higher in polyHb than in nativeHb. By analogy with other periodate-derived hemoglobin polymers,[13] one should expect this lack of reactivity to be paralleled by improved performance on cellular cultures if using such polycondensates as (semi)-artificial carriers for molecular oxygen. On the other hand, the protocol described here can be viewed as generally applicable for protein derivatization/conjugation.

EXPERIMENTAL SECTION

Bovine hemoglobin was purified from bovine blood following a general protocol of Antonini and Brunori.[23] The blood, freshly drawn on citrate, was centrifugated 15 minutes at 5000 rpm to separate the red blood cells, which were then washed three times with 5 mM phosphate pH 7.4 + 150 mM NaCl. Hemoglobin was manipulated in phosphate buffer saline (PBS) unless otherwise mentioned and concentration in text are given per heme rather than per tetramer. The met form of the hemoglobin were prepared by ferricyanide treatment as previously described.[24-26] Bovine serum albumin (BSA, fraction V, from Sigma-Aldrich, Germany) was used as provided without further purification.

For alginate oxidation 0.01 g/mL solution were prepared in 18.1 MΩ deionized water. The solution was oxidized with sodium periodate ($NaIO_4$, Merck) (0.1 g/mL) for 1 hour at room temperature in order to ring-open the 1,2-diols to yield dialdehydes (Figure 1). For polymerization of Hb with alginate, 1 mM Hb was reacted with 0.64 mg/mL or 0.96 mg/mL alginate oxidized. The reaction was performed under stirring at 4ºC. The reaction was stopped by addition of $NaBH_4$, which reduces imine bonds to stable amines and also quenches excess carbonyl groups. The product was dialyzed in 50 mM Tris buffer with 150 mMNaCl, 7.4 to remove excess $NaBH_4$ and side-products. The resulting protein solutions were subsequently analyzed by 15% SDS-PAGE and by analytical size exclusion chromatography on a Superdex 200 5/150 GL column (GE Healthcare, Sweden), 0.25 mL/min flow rate with a mobile phase of 20 mM Tris pH 7.4 buffer with 150 mM NaCl. The absorbance was monitored at 280 nm. Molecular weights were determined based on a calibration curve employing a molecular weight standard kit (Sigma-Aldrich) containing carbonic anhydrase (29 kDa), bovine serum albumin (BSA, 66 kDa), alcohol dehydrogenase (150 kDa), amylase (200 kDa), apoferritin (443 kDa), thyroglobulin (669 kDa) and blue dextran (void volume marker).

Autooxidation experiments were performed by incubation of oxy-Hb (native or polymerized) at 37ºC in an incubator and measuring UV-vis spectra of the Hb before and after incubation times of up to 4 hours. The change in absorbance at 630 nm was used to determine the rate of autooxidation. UV-vis spectra were recorded on Agilent 8453 (Agilent, Inc.) and Cary 50 (Varian, Inc) instruments Cary 50 (Varian, Inc) instruments.

Dioxygen affinity and autooxidation measurements were in PBS 7.4 at room temperature.

REFERENCES

1. H. Bunn, J.H. Jandl, *Journal of Experimental Medicine*, **1969**, *129*, 925
2. X. Liu, M. J.S. Miller, M.S. Joshi, H. Sadowska-Krowicka, D.A. Clark, J.R. Lancaster, *Journal of Biological Chemistry*, **1998**, *273*, 18709
3. J.R. Hess, R.F. Reiss, *Translational Medicine Reviews*, **1996**, *10*, 276
4. A.I. Alayash, *Nature Reviews in Drug Discovery*, **2004**, *3*, 152
5. D.H. Doherty, M.P. Doyle, S.R. Curry, R.J. Vali, T.J. Fattor, J.S. Olson, D.D. Lemon, *Nature Biotechnology*, **1998**, *16*, 672
6. R.M. Winslow, *Artificial Organs*, **2004**, *28*, 800
7. B.J. Reeder, M. Grey, R.L. Silaghi-Dumitrescu, D.A. Svistunenko, L. Bulow, C.E. Cooper, M.T. Wilson, *Journal of Biological Chemistry*, **2008**, *283*, 30780
8. I. Portoro, L. Kocsis, P. Herman, D. Caccia, M. Perrella, L. Ronda, S. Bruno, S. Bettati, C. Micalella, A. Mozzarelli, A. Varga, M. Vas, K.C. Lowe, A. Eke, *Biochimica Biophysica Acta*, **2008**, *1784*, 1402
9. J.G. Riess, *Chemical Reviews*, **2001**, *101*, 2797
10. F. Deac, A. Todea, R. Silaghi-Dumitrescu *Glutaraldehyde derivatization of hemoglobin: a potential blood substitute*; Silaghi-Dumitrescu, R. and Garban, G., Ed.; Cluj University Press: Cluj-Napoca, Romania, 2009, pp 165
11. S.G.R.C., H.H.D., *Journal of Biological Chemistry*, **1986**, *261*, 6811
12. J.H. Eike, A.F. Palmer, *Biotechnology Progress*, **2004**, *20*, 953
13. F. Deac, B. Iacob, E. Fischer-Fodor, G. Damian, R. Silaghi-Dumitrescu, *Journal of Biochemistry*, **2011**, *149*, 75
14. B.J. Reeder, D.A. Svistunenko, C.E. Cooper, M.T. Wilson, *Antioxidants& Redox Signaling*, **2004**, *6*, 954
15. R. Silaghi-Dumitrescu, B.J. Reeder, P. Nicholls, C.E. Cooper, M.T. Wilson, *Biochemical Journal*, **2007**, *403*, 391
16. A.C. Mot, A. Roman, I. Lupan, D.M. Kurtz, R. Silaghi-Dumitrescu, *Protein Journal*, **2010**, *29*, 387
17. M. Arkosi, F. Scurtu, A. Vulpoi, R. Silaghi-Dumitrescu, D.M. Kurtz, Jr., *Artificial Cells and Blood Substitutes*, **2016**, *45*, 218
18. D. Hathazi, A.C. Mot, A. Vaida, F. Scurtu, I. Lupan, E. Fischer-Fodor, G. Damian, D.M. Kurtz, Jr., R. Silaghi-Dumitrescu, *Biomacromolecules*, **2014**, *15*, 1920
19. F. Scurtu, O. Zolog, B. Iacob, R. Silaghi-Dumitrescu, *Artificial Cells, Nanomedicine and Biotechnology*, **2014**, *42*, 13
20. V.F. Scurtu, A.C. Mot, R. Silaghi-Dumitrescu, *Pharmaceuticals*, **2013**, *6*, 867
21. F. Deac, B. Iacob, E. Fischer-Fodor, G. Damian, R. Silaghi-Dumitrescu, *Journal of Biochemistry*, **2011**, *149*, 75
22. O. Zolog, A. Mot, F. Deac, A. Roman, E. Fischer-Fodor, R. Silaghi-Dumitrescu, *Protein Journal*, **2011**, *30*, 27
23. E. Antonini, M. Brunori, *Hemoglobin and Myoglobin in their Reaction with Ligands*; North-Holland: Amsterdam, 1971

24. B.J. Reeder, D.A. Svistunenko, M.A. Sharpe, M.T. Wilson, *Biochemistry*, **2002**, *41*, 367
25. J. Dunne, D.A. Svistunenko, A.I. Alayash, M.T. Wilson, C.E. Cooper, *Advances in Experimental Medicine and Biology*, **1999**, *471*, 9
26. J. Dunne, A. Caron, P. Menu, A.I. Alayash, P.W. Buehler, M.T. Wilson, R. Silaghi-Dumitrescu, B. Faivre, C.E. Cooper, *Biochemical Journal*, **2006**, *399*, 513

SILICON RELEASE FROM HYDROXYAPATITES
IN WATER AND SIMULATED BODY FLUID

**OANA CADAR[a], PETRE T. FRANGOPOL[b], GHEORGHE TOMOAIA[c,d],
DANIEL OLTEAN[c], GERTRUD A. PALTINEAN[b], AURORA MOCANU[b],
OSSI HOROVITZ[b], MARIA TOMOAIA-COTISEL[b,d] ***

ABSTRACT. Nanostructured hydroxyapatite (HAP) and silicon substituted hydroxyapatites (HAP-Si), with 0.47 and 2.34 wt% Si, were prepared by wet precipitation method. Their structure was investigated by X rays diffraction (XRD), FTIR spectroscopy, energy dispersive X ray (EDX) spectroscopy and their images were obtained by TEM, SEM and AFM. Their behavior in water and SBF was investigated by inductively coupled plasma optical emission spectrometry (ICP-OES) for an immersion time from 1 to 90 days. While Ca and P release from HAP is very low, the presence of Si enhances greatly their release in water, along with a continuous and long lasting Si release. In simulated body fluid, SBF, Ca, P and Mg are removed from the solution, by the formation of a new HAP enriched in Mg, while silicon is released as in water. Thus, Si doped HAP might have advantageous applications as bone and tooth materials.

Keywords: hydroxyapatite, silicon doped HAP, elements release, simulated body fluid

---

[a] *INCDO INOE 2000, Research Institute for Analytical Instrumentation, 67 Donath str., RO-400293, Cluj-Napoca, Romania*

[b] *Babeş-Bolyai University, Faculty of Chemistry and Chemical Engineering, 11 Arany Janos str., RO-400028, Cluj-Napoca, Romania*

[c] *Iuliu Hatieganu University of Medicine and Pharmacy, Orthopedics and Traumatology Department, 47 Traian Mosoiu Str., RO-400132 Cluj-Napoca, Romania*

[d] *Academy of Romanian Scientists, 54 Splaiul Independentei, RO-050094 Bucharest, Romania*

* *Corresponding author: mcotisel@chem.ubbcluj.ro*

O. CADAR, P.T. FRANGOPOL, G. TOMOAIA, D. OLTEAN, G.A. PALTINEAN,
AURORA MOCANU, O. HOROVITZ, M. TOMOAIA-COTISEL

INTRODUCTION

Silicon is shown to be an essential element in biological bone growth and development [1]. Therefore, silicon substituted hydroxyapatites (HAP-Si) are a promising biomaterial for bone grafting [2, 3], and different methods were proposed in order to synthesize and characterize them from chemical, physical and biological point of view [3-7]. The role of HAP-Si based biomaterials in bone formation, mineralization and remodeling, by stimulation of human osteoblasts bioactivity and promotion of bone regeneration is approached by numerous investigations, both *in vitro* and *in vivo* [3, 7-13].

Silicon may enter in the hydroxyapatite, $Ca_{10}(PO_4)_6(OH)_2$ (HAP) lattice as silicate ions, SiO_4^{4-}, substituting phosphate ions, PO_4^{3-}, but for the conservation of electroneutrality, some of the OH^- ions should be eliminated, leading to the formula $Ca_{10}(PO_4)_{6-x}(SiO_4)_x (OH)_{2-x.}$ Obviously, x should remain less than 2; for x = 2 the maximum theoretically possible Si content in HAP-Si would be 5.8 wt%. But because of lattice distortions, the real limit should be lower, e.g. 5 wt% (x = 1.7) [14, 15], 4.35 wt% (x = 1.5) [16], 4 wt% (x = 1.4) [17, 18], 3.1 wt% (x = 1.1) [19]. But silicon can also be present as SiO_2, crystallized as quartz or as amorphous silica. There are authors suggesting the optimal bioctivity of HAP-Si to be attained for 0.8 wt% Si (x = 0.28) [13, 20, 21], but also for 0.47% and 2.34% Si an enhanced adhesion and proliferation of osteoblasts was observed [3].

In order to achieve its biological effect, HAP-Si has to release the necessary elements in the biological medium. For osteoblast activity and new bone tissue formation and development a continuous supply of elements is essential [22]. This is why in the present article we investigate the behavior of HAP-Si samples as compared with HAP in presence of water and simulated body fluid for a long time (90 days).

RESULTS AND DISCUSSION

Two silicon containing hydroxyapatites (HAP-Si) were prepared and compared with pure hydroxyapatite (HAP). Their composition is given in Table 1. The theoretical formulas where calculated assuming the entire amount of Si to be included in SiO_4^{4-}, which partially substitutes PO_4^{3-} ions.

Table 1. Composition of HAP and HAP-Si

Name	Composition (wt%)			Theoretical formula
	Ca	P	Si	
HAP	39.89	18.50	0	$Ca_{10}(PO_4)_6(OH)_2$
HAP-Si0.47	40.03	18.04	0.47	$Ca_{10}PO_4)_{5.83}(SiO_4)_{0.17}(OH)_{1.83}$
HAP-Si2.34	40.56	16.22	2.34	$Ca_{10}PO_4)_{5.18}(SiO_4)_{0.82}(OH)_{1.18}$

In order to identify the crystalline phosphate species present, the XRD spectra of the three samples were compared with Powder Diffraction Files (PDF) for pure hydroxyapatite (HAP) and pure β-calcium phosphate (TCP). As an example, the spectrum of the sample containing 0.47% Si is compared with the PDF no. 09-0432 for stoichiometric HAP in Fig. 1a. HAP was the only phase identified in the pure hydroxyapatite sample and in HAP-Si0.47, while in HAP-Si2.34 a content of 83.6% HAP and 16.4% β-TCP was estimated. Thus, the increasing Si content favours the conversion of HAP to β-TCP, as observed also in literature [4, 23-25]. No quartz phase was identified in the XRD patterns, but this fact does not exclude the presence of amorphous silica (SiO_2).

From the breadth of the peaks as compared to the XRD pattern of crystalline HAP taken as etalon, it is evident that all samples present a nanocrystalline structure. The average size of crystallites was calculated from the Debye-Scherrer relation. The estimated size of the crystallites in the samples is about 47 nm for HAP, 23 nm for HAP-Si0.47 and 25 nm for HAP-Si2.34. The crystallinity degree of the samples, also estimated from the XRD patterns, was about 40-50% for all the samples.

a   b
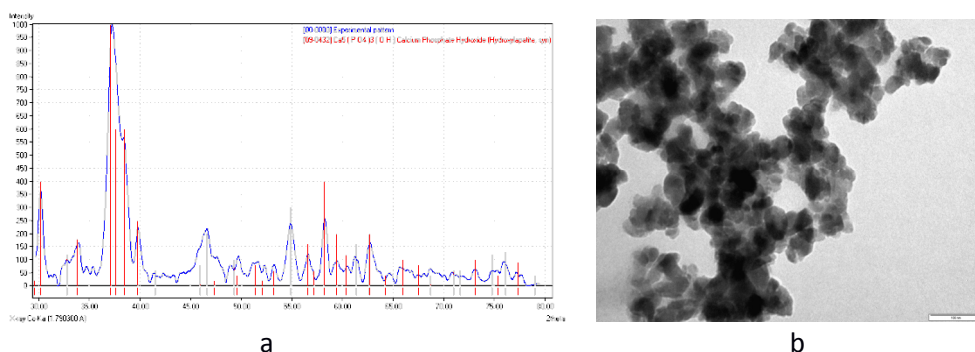
Figure 1. XRD patterns (a) for HAP-Si(.47 and the PDF no. 09-0432 file for stoichiometric HAP. (b) TEM image of a HAP-Si2.34 sample; bar length is 100 nm.

As an example, a TEM image for HAP-Si 2.34 is given in Fig. 1b. From TEM images the sizes of several hundreds of particles were measured, and the mean particle diameter was found to be about 26.5 ± 5.2 nm, with sizes between 16 and 42 nm. The mean value is in substantial agreement with the particle diameter estimated from X-ray diffraction.

a

b

c

d
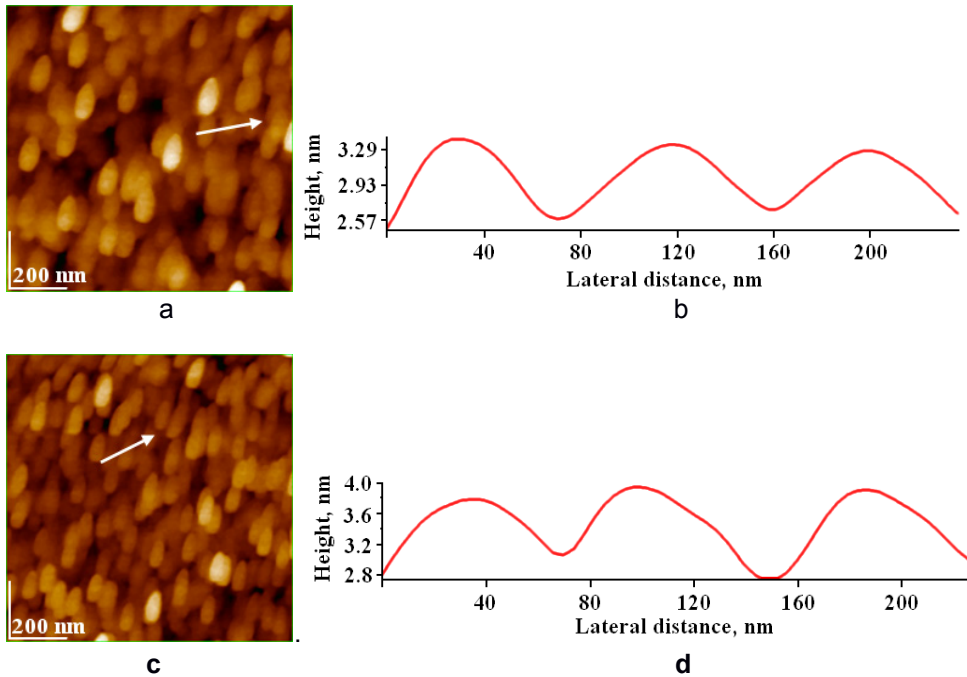
Figure 2. AFM images 2D-topography (ac) and cross section profile (b, d) along the arrows in pannel (a) and (c) respectively, for HAP-Si 0.47 (a, b) and HAP--Si2.34; scanned areas: 1 µm x 1 µm; surface roughness, RMS, on area 1.00 nm (a) and 0.90 nm (c); RMS profile 0.34 nm (b), 0.24 nm (d).

AFM images (Figure 2) also confirmed for HAP-Si powders the average size of particles in the nanoscale range, as following 42 ± 3 nm for HAP-Si 0.47, and 45 ± 4 nm for HAP-Si2.34. Thus, AFM images indicated that the nano suspensions of HAP-Si powders are formed of particles of almost identical size in good agreement with TEM values.
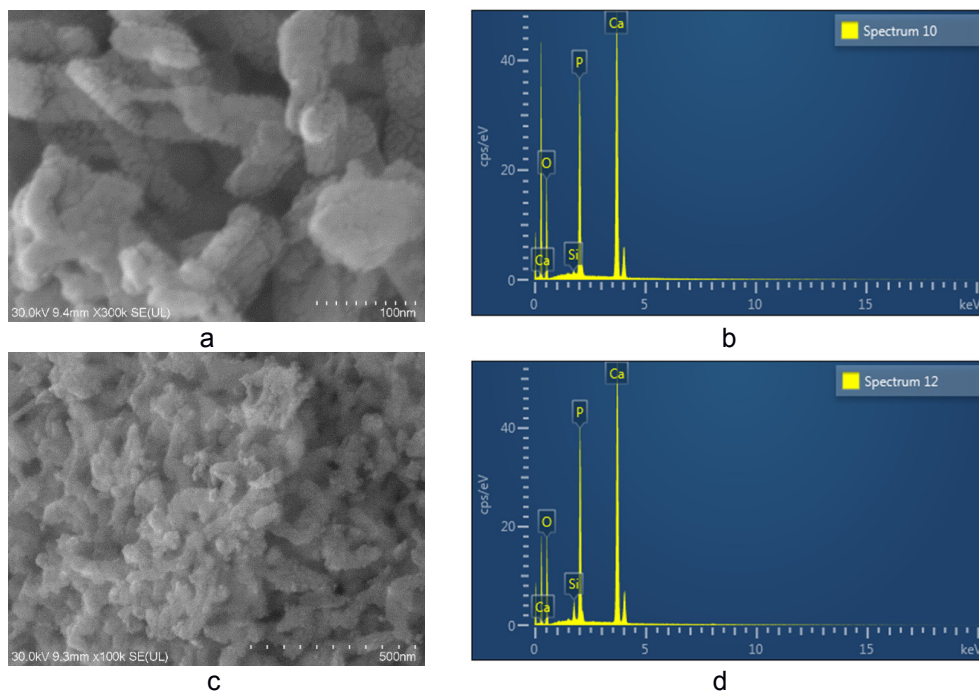
Figure 3. SEM image (a) and EDX spectrum (b) of HAP-Si0.47; SEM image (c) and EDX spectrum (d) of HAP-Si2.34. Bar length: 100 nm (a), and 500 nm (c) Examples of SEM images are given in Fig.3 for the HAP-Si0.47 and HAP-Si2.34, along with EDX spectra, which confirm the presence of Si, together with Ca and P in both samples.

The FTIR spectrum of the HAP-Si0.47 sample is presented in Fig. 4a. The IR spectra of the HAP-Si samples are very similar to each other. Like the HAP sample, they present the characteristic peaks of the PO_4 group: stretching vibrations: v_3 at 1032-1033 and 1089-1091 cm^{-1}; v_1 at 962 cm^{-1}; bending vibrations: v_4 at 565 and 602-603 cm^{-1}; v_2 at 473 cm^{-1} and of the structural OH (stretching at 3571-3572 cm^{-1} and libration at 633 cm^{-1}. The last reduced to a shoulder in HAP-Si2.34 (Fig. 4b) as a consequence of the diminution of the OH groups in HAP by the substitution of phosphate by silicate ions. Peaks for absorbed water are visible at 3420 - 3440 and 1637 cm^{-1}. Peaks for the SiO_4 group have their frequencies very near to those of PO_4, and are therefore not observable. Nor can be detected vibrations characteristic for Si-O-Si bridges from silica [27, 28], and this could be an argument against the presence of free SiO_2 in the HAP-Si samples.

71
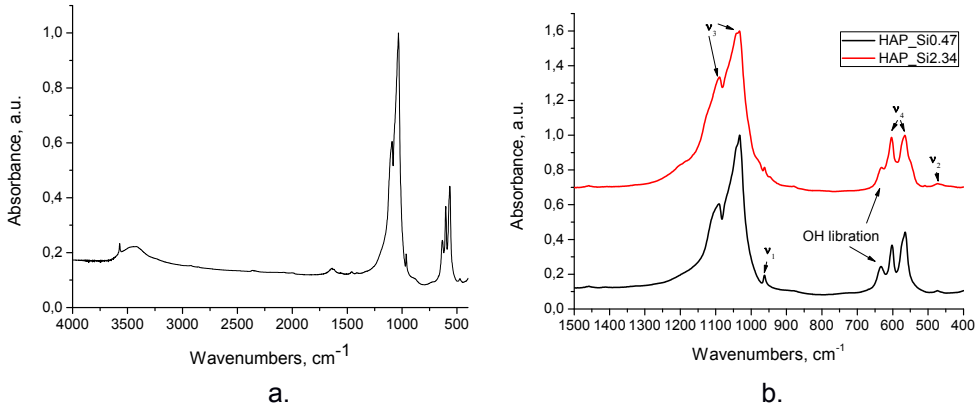
Figure 4. FTIR spectrum for HAP-Si0.47 (a) and comparison between FTIR spectra for HAP-_Si samples (detail) (b).

The Ca, P, and Si contents in the solution resulted after contact of the samples with ultrapure water, for 1, 3, 7, 14. 21, 30, 60, and 90 days are presented graphically in Fig. 5 a, b and c respectively.

Pure HAP has a very low solubility in water; its solubility product

$$K_{sp} = [Ca^{2+}]^{10}[PO_4^{3-}]^6[OH^-]^2$$

is very difficult to assess, and values in literature vary between 10^{-114} and 10^{-120} [29]; an international standard [30] recommends the value $(4.12\pm0.16)\cdot10^{-118}$. Therefore, the Ca and P content in the aqueous solution in contact with the HAP sample is very low and nearly constant in time (Fig 5a, b). The Ca/P ratio in the solution is different from that in the solid because of the incongruent (nonstoichiometrical) solubility of HAP in water [29, 31, 32]. There is not a simple dissolution process, but a series of complex chemical reactions, with the formation of different calcium phosphate phases as surface coats [33, 34]. In the solution, P appears mainly as HPO_4^{2-} ions, the predominant form at nearly neutral pH.

a.

b.

c.
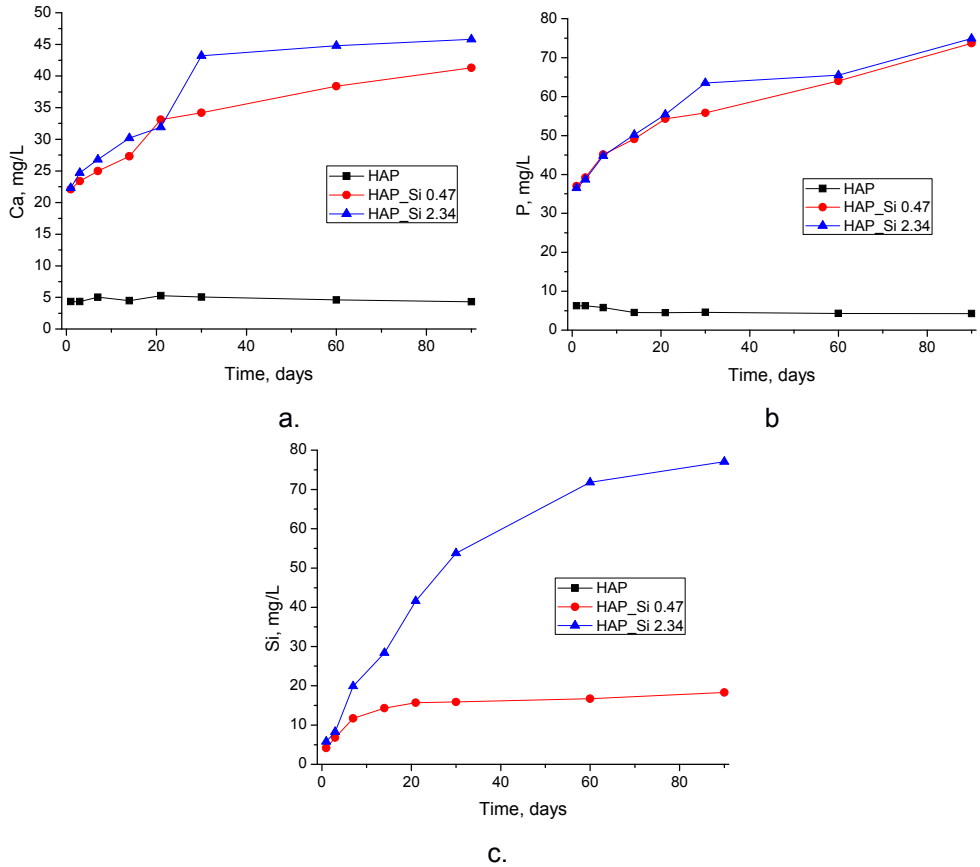
Figure 5. Ca (a), P (b) and Si (c) release from HAP and HAP-Si samples in water

The presence of Si dramatically enhances both the Ca and P release, therefore it increases the solubility of the calcium phosphate, and the amount released increases continuously in time. Such an augmentation of the HAP solubility due to the presence of Si was observed both *in vivo* [12], and *in vitro* [9, 22, 25, 26]. This ion release over a long period of time is important for the biomedical applications of substituted apatites, since this continuous supply of elements is essential for osteoblast activity and new bone tissue formation and development [22]. Based on HR-TEM results, it was suggested that an increased number of defects in the HAP-Si lattice causes the increase of calcium, phosphate and silicate ions release in the solution [12] The Si release also is increasing in time, especially for the HAP-Si2.34 sample. The values

of Si/Ca and Si/P ratios in the solution are much higher than in the solid, thus there is much more Si in the solution than expected from a congruent dissolution of HAP-Si. Probably not only the silicate ions in the crystals are released, but also Si from amorphous silica in the sample.

The elements contents (Ca, P, Mg) in pure SBF are compared with those in SBF in presence of the samples for immersion times from 1 to 90 days in Fig. 6 a-c, while the variation in time of the Si content in the solution in contact with HAP-Si samples is shown in Fig. 6 d.

a.

b.

c.

d.
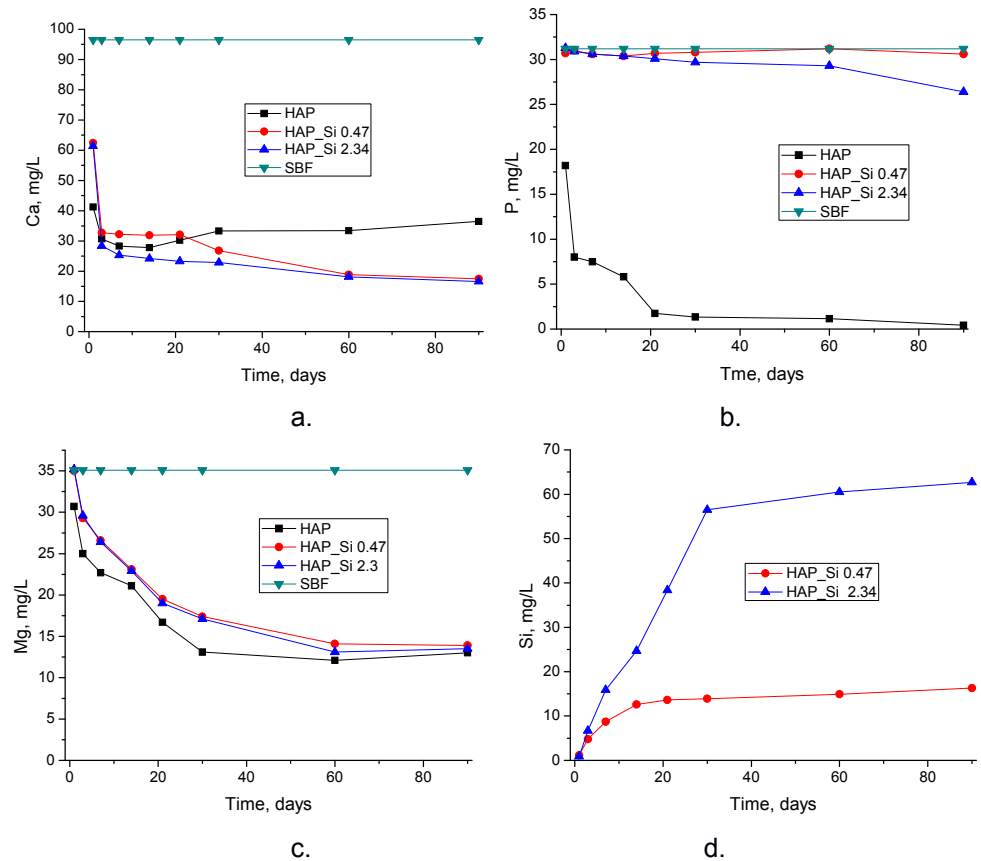
Figure.6. Ca (a), P (b), Mg (c) and Si (d) content in SBF in absence and in presence of the HAP and HAP-Si samples.

In SBF the Ca^{2+} concentration in presence of HAP is decreasing in time from its initial value in SBF (96.5±0.5 mg/L) as seen in Fig. 6a. The diminution is rapid in the first 30 days, then it is much slower, and even a slight increase is observed. It can be explained by uptake of Ca^{2+} along with PO_4^{3-} ions from SBF for the building of new sold HAP and/or the sorption of Ca^{2+} in the HAP lattice, which are partially counterbalanced by the release of Ca^{2+} ions from the HAP lattice and/or the ion exchange with Mg^{2+} ions from the SBF solution, leading to new HAP enriched in Mg.

The decrease of the P content in the SBF, from the initial value (31.2±1.3 mg/L) is more pronounced, and continues down to its near consumption from the solution (Fig. 6b). In the HAP-Si samples, this P uptake is compensated by the increased release of P due to the enhanced dissolution of the HAP-Si.

There is also a decrease in the Mg^{2+} content (Fig. 6c) of the SBF, from its initial value (35.1±3.6 mg/L), probably due to the ion exchange with Ca^{2+} from HAP and formation of Mg substituted HAP.

The Si release in SBF shows the same trends as in water, but the released amount is somewhat diminished. It was signalled in literature that the simultaneous presence of Mg and Si diminishes the elements release [22]. This could suggest the formation of complexes containing these two ions, more strongly bound to the HA crystal structure or to its amorphous part [22]. The excess of Ca^{2+} ions in SBF could also downgrade the dissolution equilibrium of HAP-Si. The Si content in the solution was larger for higher Si content in the HAP-Si.

In histological studies, an increase in the rate of bone apposition to HAPs implants by the substitution of silicate ions into HAP has been observed [12]. This higher bioactivity of HAP-Si was assigned to the effect of the accelerated dissolution caused by the silicate ions.

CONCLUSIONS

HAP and silicon substituted HAPs (0.47 and 2.34 wt% Si) were prepared by wet precipitation method. XRD investigations showed the presence of the HAP lattice as single phase present in HAP and HAP-Si0.47, and as majoritary phase in HAP-Si2.34. They possess nanostructure and a medium crystallinity degree. The HAP structure was confirmed by FTIR spectroscopy and the particles were visualized by TEM, AFM and SEM imaging. The elements release in water was much higher in HAP-Si than in pure HAP and continued till the end of the experiments. This long lasting elements release is an important premise for biomedical use of HAP-Si based biomaterials.

The behavior of the samples in SBF could be explained in terms of Ca, P and Mg uptake in the new HAP lattice and/or ion exchange, with a precipitation of HAP enriched in magnesium. The Si release showed a similar responsive behavior of HAP-Si, both in water and in SBF. Also, the increased Si concentration in HAP-Si significantly influenced the Si release in both media. Therefore, silicate ions have an important role in the structure of HAP-Si and might simultaneously bring physiological effects as a result of Si release.

EXPERIMENTAL SECTION

The nanostructured phosphates were prepared by the precipitation method previously developed by us for the synthesis of HAP and substituted HAPs [3, 35-38]. Briefly, HAP was obtained by rapidly mixing, at room temperature, equal volumes of 0.15 M calcium nitrate solution [$Ca(NO_3)_2 \cdot 4H_2O$ from Merck] and 0.09 M diammonium phosphate solution [$(NH_4)_2HPO_4$ from Sigma-Aldrich] at pH 11.5 (settled by adding a 25% ammonia solution). The maturation of the obtained suspension was achieved by maintaining it for 24 h at 22 °C, and for another 24h at 70ºC, in a reactor, under intermittent stirring. The so obtained precipitate was filtered and washed repeatedly with ultrapure water until nitrate free. It was dried by lyophilization, then calcined at 300ºC for one hour and disintegrated in a ball mill.

For the preparation of HAP-Si samples [3], in each solution nonylphenol was added (this surfactant helping to control nucleation and growth of nuclei). Sodium silicate ($Na_2O:SiO_2 = 1:3.2$) was introduced in the phosphate solution in amounts calculated for the respective Si content in the final product. The pH of both solutions was adjusted to 11, using ammonia solution. The solutions were fast mixed.at 60°, and the maturation was achieved at 80 °C for 48 h. After filtration, washing and lyophilisation the samples were calcined at 650 ºC for 6-8 h.

The *X-rays diffraction* (XRD) patterns were investigated with a DRON-3 diffractometer, in Bragg-Brentano geometry, using a X-ray tube with cobalt target (K_α line, wavelength 1.79030 Å).

FTIR spectra were measured on KBr pellets, containing the samples powders with a spectrometer JASCO 6100 in the 4000-400 cm^{-1} range of wave numbers, with a 2 cm^{-1} resolution.

Transmission electron microscope: TEM JEOL –JEM 1010 was used to determine the shape and the size of the phosphates nanoparticles. The samples were dispersed in deionized water, and the resulted colloidal dispersion was adsorbed on the TEM grids.

For the examination with the *scanning electron microscope* SEM JEOL 5600 LV (backscattered-electron imaging technique, BSE), the samples were deposited as an uniform layer an adhesive graphitized tape. For local elemental analysis of different samples the energy-dispersive X-ray (EDX) spectroscopy was used coupled with SEM imaging.

Atomic force microscopy (AFM) images were obtained using the AFM JEOL 4210 equipment, operated in tapping mode [39-48], using standard cantilevers with silicon nitride tips (resonant frequency in the range of 200-300 kHz, and spring constant 17.5 N/m). The particles were adsorbed from their aqueous dispersion for 20 s on optically polished glass support.

Elements release tests: The Ca, P, Si and Mg amounts were measured in the solutions after immersion of 0.15 g of each sample in 15 mL ultrapure water, respectively Kokubo simulated body fluid (SBF) and incubation 37°C in separated closed flasks for each sample/day. SBF solutions were prepared according to *Kokubo's SBF* solution [49], containing the following ions (mmol/dm^3): Na^+ (142.0); K^+ (5.0); Mg^{2+} (1.5); Ca^{2+} (2.5); Cl^- (147.8); HCO_3^- (4.2); HPO_4^{2-} (1.0); SO_4^{2-} (0.5), and buffered at the physiologic pH 7.40 at 37 °C, with tris(hydroxymethyl)amino methane and hydrochloric acid.

After 1, 3, 7, 14, 21, 30, 60, and 90 days, the supernatant (after centrifugation) was filtered through 0.45 µm paper filter Ca, Mg, P and Si contents were determined using an inductively coupled plasma optical emission spectrometer (ICP-OES) OPTIMA 3500 DV (Perkin-Elmer, USA) . For calibration, multi-element standard solutions were prepared by the dilution of stock multi-element 1000 mg/L solutions Merck IV (0, 0.1, 0.5, 1, 2, 4, 6, 8 and 10 mg/L).

All the experiments were performed in triplicate and the results were calculated as average values. The elements content in SBF solution without samples was also measured in the same days, and the average value was calculated.

ACKNOWLEDGMENTS

REFERENCES

1. E.M. Carlisle, *Calcified Tissue International*, **1981**, *33*, 27.
2. W. Waked, J. Grauer, *Orthopaedics*, **2008**, *31*, 591.
3. Gh. Tomoaia, A. Mocanu, I. Vida-Simiti, N. Jumate, L.-D. Bobos, O. Soritau, M. Tomoaia-Cotisel, *Materials Science and Engineering C*, **2014**, *37*, 37.
4. I.R. Gibson, S.M. Best, W. Bonfield, *Journal of Biomedical Materials Research,* **1999**, *44*, 422.
5. T. Leventouri, C.E. Bunaciu, V. Perdikatsis, *Biomaterials*, **2003**, *24*, 4205.
6. C.M. Botelho, M.A. Lopes, I.R. Gibson, S.M. Best, J.D. Santos, *Journal of Material Science: Materals in Medicine*, **2002**, *13*, 1123.
7. Z.Y. Qiu, I.S. Noh, S.M. Zhang, *Frontiers of Materials Science*, **2013**, *7*, 40.
8. A.F. Khan, M. Saleem, A. Afzal, A. Ali, A. Khan, A.R. Khan, *Materials Science and Engineering C*, **2014**, 35*,* 245.
9. F. Balas, J. Pérez-Pariente, M. Vallet-Regí, *Journal of Biomedical Materials Research*, **2003**, *66*, 364.
10. A.E. Porter, N. Patel, J.N. Skepper, S.M. Best, W. Bonfield, *Biomaterials*, **2003,** *24*, 4609.
11. A.E. Porter, N. Patel, J.N. Skepper, S.M. Best, W. Bonfield, *Biomaterials*, **2004**, *25*, 3303.
12. A.E. Porter, C.M. Botelho, M.A. Lopes, J.D. Santos, S.M. Best, W. Bonfield, *Journal of Biomedical Materials Research*, **2004**, *69A*, 670.
13. K.A. Hing, P.A. Revell, N. Smith, T. Buckland, *Biomaterials*, **2006**, *27*, 5014.
14. E.S. Thian, J. Huang, M.E. Vickers, S.M. Best, Z.H. Barber, W. Bonfield, *Journal of Materials Science*, **2006**; *41*, 709.
15. M. Vallet-Regí, D. Arcos, *Journal of Materials Chemistry*, **2005**, *15*, 1523.
16. D. Marchat, M. Zymelka, C. Coelho, L. Gremillard, L. Joly-Pottuz, F. Babonneau, C. Esnouf, J. Chevalier, D. Bernache-Assollant, *Acta Materialia*, **2013**, *9*, 6992
17. G. Gasquères, C. Bonhomme, J. Maquet, F. Babonneau, S. Hayakawa, T. Kanaya, A. Osaka, *Magnetic Resonance in Chemistry*, **2008**, *46,* 342.
18. X.L. Tang, X.F. Xiao, R.F. Liu, *Materials Letters*, **2005**, *59*, 3841.
19. S. Gomes, J.M. Nedelec, E. Jallot, D. Sheptyakov, G. Renaudin, *Crystal Growth and Design*, **2011**, *11*, 4017.
20. .S.M. Best, S. Zou, R.A. Brooks, J. Huang, N. Rushton, W. Bonfield, *Key Engineering Materials*, **2008**, *361-363*, 985.
21. C.M. Bothelo, R.A. Brooks, S.M. Best, M.A. Lopes, J.D. Santos, N. Rushton, W. Bonfield, *Journal of Biomedical Materials Research*, **2006**, *79A*, 723.
22. S. Sprio, A. Tampieri, E. Landi, M. Sandri, S. Martorana, G. Celotti, G. Logroscino, *Materials Science and Engineering C*, **2008**, *28*, 179.
23. J.L. Xu, K.A. Khor, *Journal of Inorganic Biochemistry*, **2007**, *101*, 187.

24. A.J. Ruys, *Journal of the Australan Ceramic Society,* **1993**, *29*, 71.
25. S.L. Seet, *Science Asia*, **2009,** *35*, 255.
26. D.M. Ibrahim, A.A. Mostafa, S. Ibrahim Korowash, *Chemistry Central Journal*, **2011**, *5:74*, 11 pp
27. M.A. Karakassides, D. Gournis, D. Petridis, *Clay Minerals*, **1999**, *34*, 429.
28. E.R. Lippincott, A. Van Valkenburg, C.E. Weir, E.N. Bunting, *Journal of Research of the National Bureau of Standards*, **1958**, *61*, 61.
29. H.W. Kaufman, I. Kleinberg, *Calcified Tissue International*, **1979**, *27*, 143.
30. *** International Standard ISO 13779-6 *Implants for Surgery – Hydroxyapatite*, *Part 6: Powders*, **2015**.
31. A.N. Smith, A.M. Posner, J.P. Quirk, *Journal of Colloid and Interface Science*, **1974**, *48*, 442.
32. S.V. Dorozhkin, *Journal of Colloid and Interface Science*, **1997**, *191*, 489.
33. R.P. Shellis, F.K. Wahab, B.R. Heywood, *Caries Research,* **1993,** *27*, 365.
34. R.P. Shellis, B.R. Heywood, F.K. Wahab, *Caries Research*, **1997**, *31*, 71.
35. Gh. Tomoaia, M. Tomoaia-Cotisel, L.B. Pop, A. Pop, O. Horovitz, A. Mocanu, N. Jumate, L.-D. Bobos, *Revue Roumaine de Chimie,* **2011,** *56*, 1039.
36. Gh. Tomoaia, O. Soritau, M. Tomoaia-Cotisel, L.-B. Pop, A. Pop, A. Mocanu, O. Horovitz, L.D. Bobos, *Powder Technology*, **2013**, *238*, 99.
37. C. Garbo, M. Sindilaru, A. Carlea, G. Tomoaia, V. Almasan, I. Petean, A. Mocanu, O. Horovitz, M. Tomoaia-Cotisel, *Particulate Science and Technology,* **2017**, *35*, 29.
38. A. Mocanu, R. Balint, C. Garbo, L. Timis, I. Petean, O. Horovitz, M. Tomoaia-Cotisel, *Studia Universitatis Babes-Bolyai, Chemia*, **2017**, *62*(*2*), *Tom I*, 95.
39. M.A. Naghiu, M. Gorea, E. Mutch, F. Kristaly, M. Tomoaia-Cotisel, *Journal of Material Science and Technology,* **2013**, *29*(7), 628.
40. O. Horovitz, Gh. Tomoaia, A. Mocanu, T. Yupsanis, M. Tomoaia-Cotisel, *Gold Bulletin*, **2007**, *40* (4), 295.
41. M. Tomoaia-Cotisel**,** A. Tomoaia-Cotisel, T. Yupsanis, G. Tomoaia, I. Balea, A. Mocanu, Cs. Racz, *Revue Roumaine de Chimie,* **2006,** *51* (12),1181.
42. A. Danistean, M. Gorea, A. Avram, S. Rapuntean, Gh. Tomoaia, A. Mocanu, C. Garbo, O. Horovitz, M. Tomoaia-Cotisel, *Studia Universitatis Babes-Bolyai, Chemia*, **2016,** *61* (3), 275.
43. Gh. Tomoaia, O. Horovitz, A. Mocanu, A. Nita, A. Avram, C.P. Racz, O. Soritau, M. Cenariu, M. Tomoaia-Cotisel, *Colloids and Surfaces B: Biointerfaces*, **2015,** *135*, 726.
44. P.T. Frangopol. D.A. Cadenhead, Gh. Tomoaia, A. Mocanu, M. Tomoaia-Cotisel, *Revue Roumaine de Chimie,* **2015***, 60*(2-3), 265.
45. G. Furtos, M.A. Naghiu, H. Declercq, M. Gorea, C. Prejmerean, O. Pana, M. Tomoaia-Cotisel, *Journal of Biomedical Materials Research Part B. Applied Biomaterials,* **2016**, *104*, 1290.
46. M. Tomoaia-Cotisel, A. Mocanu, *Revista de Chimie (Bucharest),* **2008**, *59*, 1230.

47. R.D. Pasca, G. Tomoaia, A. Mocanu, I. Petean, G.A. Paltinean, O. Soritau, M. Tomoaia-Cotisel, *Studia Universitatis Babes-Bolyai, Chemia*, **2015**, *60*(3), 257.
48. G. Tomoaia, A. Mocanu, L.D. Bobos, L.B. Pop, O. Horovitz, M. Tomoaia-Cotisel, *Studia Universitatis. Babes-Bolyai, Chemia*, **2015**, *60* (3), 265.
49. T. Kokubo, H. Kushitani, S. Sakka, T. Kitsugi, T. Yamamuro, *Journal of Biomedical Materials Research*, **1990,** *24*, 721.

PORTLAND CEMENT ENRICHED WITH HYDROXYAPATITE FOR ENDODONTIC APPLICATIONS

ALEXANDRA AVRAM[a], MARIA GOREA[a,*], REKA BALINT[a], LUCIA TIMIS[a,b], STEFAN JITARU[a,b], AURORA MOCANU[a], MARIA TOMOAIA-COTISEL[a,c]

ABSTRACT Endodontic cement based on calcium silicate has been the focus of many studies. However, the quality of resulted endodontic cement needs improvement. This paper focuses on endodontic cement obtained from Portland cement enriched with two types of hydroxyapatite, simple and doped with 5% Zn. Hydroxyapatites were synthesized using a wet precipitation method and investigated by X-ray diffraction, FTIR, TEM and AFM. From a structural point of view, both hydroxyapatites were obtained in a single crystalline phase, containing particles in the nanometric range, as judged by XRD, TEM and AFM. FTIR analysis presents O-H and P-O bands specific to those in pure hydroxyapatite, confirming a hydroxyapatite lattice in both materials. Several experimental compositions of commercial Portland cement mixed with hydroxyapatite were prepared. The influence of stoichiometric and Zn doped hydroxyapatite on the resulted endodontic cement was observed in the setting time. The setting time for both cements decreased exponentially at both temperatures (22 ^{0}C and 37 ^{0}C). The normal consistency water remains constant for all experimented slurries.

Keywords: Endodontic cement, hydroxyapatite, Zn doped hydroxyapatite, Portland cement

[a] *Babeş-Bolyai University, Faculty of Chemistry and Chemical Engineering, 11 Arany J. Str., 400028, Cluj-Napoca, Romania*
[b] *Iuliu Haţieganu University of Medicine and Pharmacy, Faculty of Dentistry, 8 Babeş V. Str., 400012, Cluj-Napoca, Romania*
[c] *Academy of Romanian Scientists, 54 Splaiul Independentei, 050094, Bucharest, Romania*
Corresponding author: mgorea@chem.ubbcluj.ro

INTRODUCTION

Cement and ceramic-based biomaterials have been the subject of a wide number of studies regarding root repair cements, due to their properties: nontoxicity, biocompatibility, non-shrinkage, and chemical stability in biological conditions [1,2]. Their ability to chemically bond to the tooth, forming an hermetic seal, promote osseoconductivity, as well as having a good radiopacity have led to these material being widespread in the area of endodontics [3,4]. Endodontic bioceramics have the advantage of not being moisture or blood sensitive, therefore not being technique sensitive. When unset, they present antibacterial properties and when set, bioactive capabilities [2].

While the field of material science has produced no ideal material, synthetic hydroxyapatite (HAP, $Ca_{10}(PO_4)_6(OH)_2$) has become one of the most interesting bioceramics, being similar to inorganic components from the human body [4-8]. Its ability to generate hard tissue, thus increasing the bioactivity of dental cements is of particular significance. The bioactivity of hydroxyapatite is closely related to both the type and size of the amorphous and crystalline phases present in its structure as well as in its ion release capability [9]. Due to the promising endodontic applications of hydroxyapatite, several studies have analyzed its addition to dental fillers [10].

Water-based cements have been introduced to dentistry through the use of MTA or mineral trioxide aggregate [11,12]. Broadly defined as a fine inorganic powder that has the ability to set and harden independently [13], cement is another material clinically used in dentistry. Used as filling materials, endodontic cements come in direct contact with the alveolar bone having many applications, namely: root canal fillings and sealers, apical replacement of dentine, pulp capping and root perforation repair [9,14]. Bone defects can be easily filled by the cement paste without leaving any gap between the two interfaces.

Due to its self-setting property at physiological temperatures, ample availability and lower cost, Portland cement has a long history in the reconstruction of bone defects. These materials could be an alternative to MTA, and are currently the main focus of studies in the dental fields [4,13,15,16]. This hydraulic material is mainly composed of dicalcium ($2CaO \cdot SiO_2$), and tricalcium silicate ($3CaO \cdot SiO_2$), tricalcium aluminate ($3CaO \cdot Al_2O_3$) and tetracalcium aluminoferrite ($4CaO \cdot Al_2O_3 \cdot Fe_2O_3$) [17].

Portland cement has been proven to be biocompatible through previous studies that showed cements are not genotoxins [17-20]. The main component in cement, namely tricalcium silicate (C3S), has been shown to induce cell proliferation and HAP deposition on its surface [21]. Endodontic materials using a mixture of tricalcium silicate and calcium phosphates have been reported to present a modified hydration process [22].

Endodontic cements present many disadvantages, the main one being a delayed setting time, limiting its uses [23-25]. The advertised setting time of commercial endodontic cements ranges from 2 to 3 minutes (EndoChe Zr) to 4 hours (Trioxident) [15] and even 72 hours [25,26]. Given this discrepancy that can be confusing to clinicians, the influence of different additives, such as synthetic hydroxyapatite, on cement characteristics, especially setting time, is very important to know.

There are few studies on endodontic sealers with Ca and P ions release abilities and antibacterial properties [14].

Thus, our main purpose was to study the characteristics and influence of two types of synthetic hydroxyapatite, namely stoichiometric and Zn doped, on the setting time of endodontic cement.

RESULTS AND DISCUSIONS

Nanomaterials

The hydroxyapatite compositions, with and without Zn as dopant for Ca ions, are presented in Table 1.

Table 1. Composition of hydroxyapatites, stoichiometric and doped with Zn

Nanomaterial	Zn [wt%]	Ca substituted with Zn [mol%]	Theoretical formula
Stoichiometric hydroxyapatite	0	0	$Ca_{10}(PO_4)_6(OH)_2$
Zn doped hydroxyapatite	5.0	7.83	$Ca_{9,217}Zn_{0,783}(PO_4)_6(OH)_2$

In the experiments, the stoichiometric, uncalcined hydroxyapatite and Zn doped hydroxyapatite were mixed together with Portland cement. The compositions of endodontic cement samples are presented in Table 2.

Table 2. The studied compositions of endodontic cements

Sample/material [%]	Stoichiometric HAP	Zn doped HAP	Portland Cement
S0	-	-	100
S1	1	-	99
S2	2	-	98
S3	3	-	97
S4	5	-	95
S5	-	1	99
S6	-	2	98
S7	-	3	97

The S0 sample is composed only of Portland cement and is the standard sample. The S1, S2, S3 and S4 cements contain the various amounts of stoichiometric hydroxyapatite, while the S5, S6 and S7 cements comprise different quantities of Zn doped hydroxyapatite.

X-ray diffraction of hydroxyapatite

The X-ray diffraction (XRD) patterns of synthetized hydroxyapatite presented in Figure 1 (up) for uncalcined hydroxyapatite and in Figure 1 (down) for Zn doped hydroxyapatite, calcined at 300 ºC, reveal the presence of crystalline hydroxyapatite in both samples.
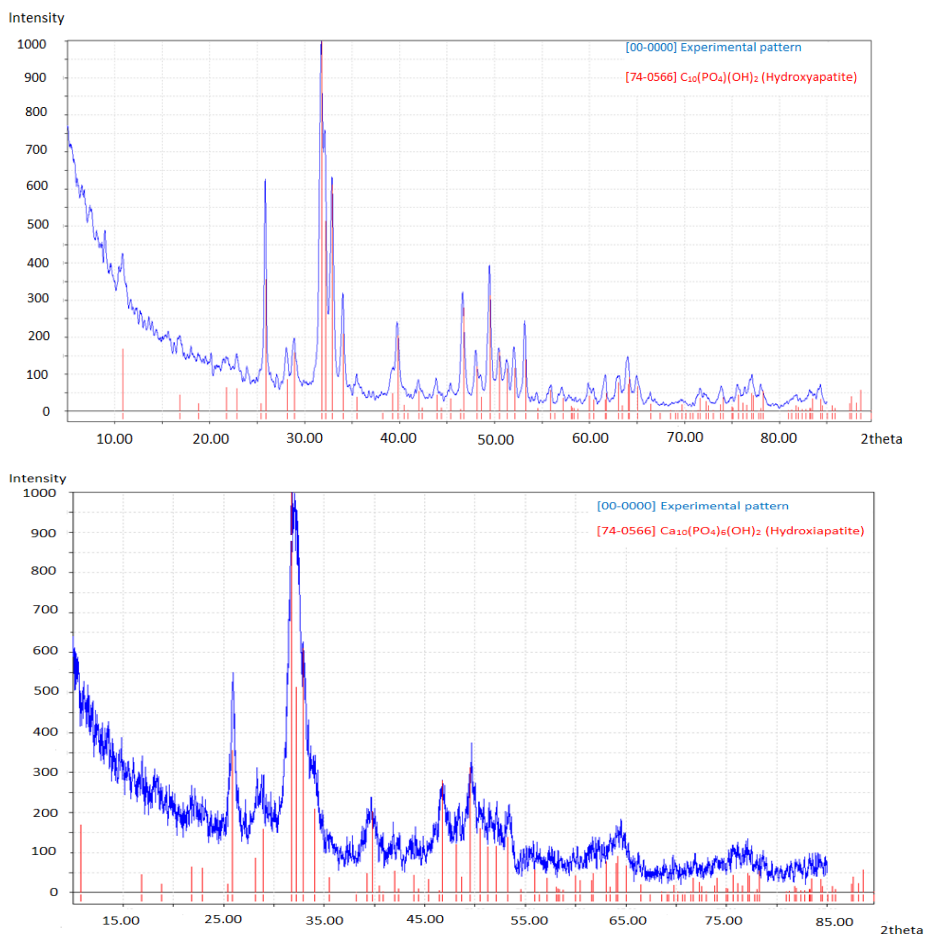
Figure 1. XRD pattern for pure, uncalcined hydroxyapatite (up) and Zn doped hydroxyapatite (down) compared with PDF 74-0566 for stoichiometric hydroxyapatite, $Ca_{10}(PO_4)_6(OH)_2$.

A decrease in crystallite size and crystallinity index for Zn doped hydroxyapatite can be observed. These effects are supposedly determined by the presence of Zn ions and the sample calcination at 300 ºC (Table 3).

Table 3. Crystallite sizes and crystallinity index of hydroxyapatites

Nanomaterial	Average crystallite size [nm]	Crystallinity index [%]
Stoichiometric hydroxyapatite	35.6	50.4
Zn doped hydroxyapatite	24.7	38.6

FTIR analysis for studied HAP

The FTIR spectra for both hydroxyapatite samples are presented in Figure 2. The specific vibration bands of P-O bonds from PO_4 groups can be evidenced. The peak from 962-963 cm^{-1} appears in the apatite spectra because of the low symmetry of elemental tetrahedral cells of doped hydroxyapatite compared to free PO_4 ions from phosphates.
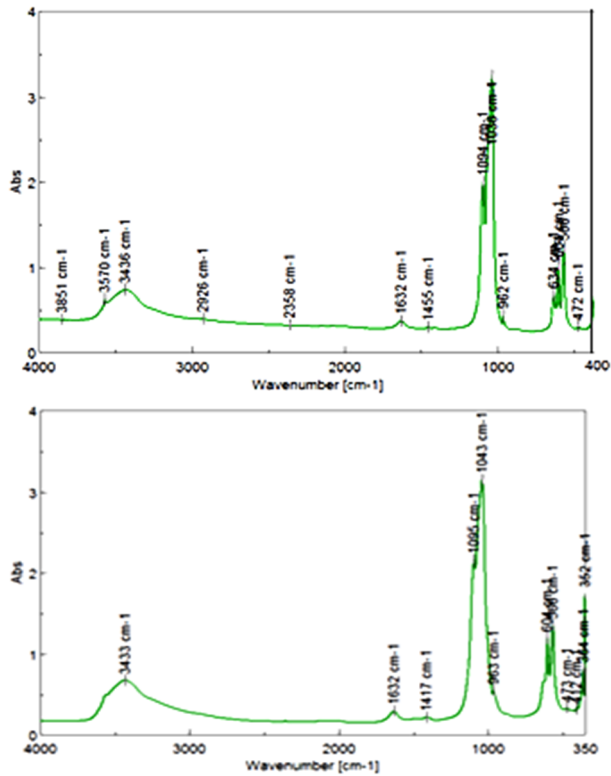
Figure 2. FTIR analysis for stoichiometric, uncalcined hydroxyapatite (up) and Zn doped hydroxyapatite calcined at 300 ^{0}C for 1h (down)

The most intense absorption band of apatite is formed from two peaks, at 1035-1044 cm^{-1} and 1093-1096 cm^{-1}. The P-O asymmetric distortion is cleaved in two peaks, at 566 and 603-604 cm^{-1}. The wide band at 3600-3300 cm^{-1} (with a maximum at 3420-3440 cm^{-1}) is attributed to the O-H vibrations in the adsorbed water molecules. The narrow band at 3579-3571 cm^{-1}, overlaid on the wide band attributed to water, is due to OH structural groups of hydroxyapatite. This observation is in accordance to the increase of water quantities in the hydroxyapatite network at a higher Zn content.

TEM images for HAP biomaterials

Transmission electron microscopy was used for investigating the morphology and size of particles in the hydroxyapatite powder (Figure 3). The image illustrates that polycrystalline hydroxyapatite with rather uniform sized particles is formed by this process. The crystallite size of hydroxyapatite measured from TEM is in the nanometric range, with a length of 40-50 nm and a diameter of 20-30 nm, in accordance to XRD patterns.
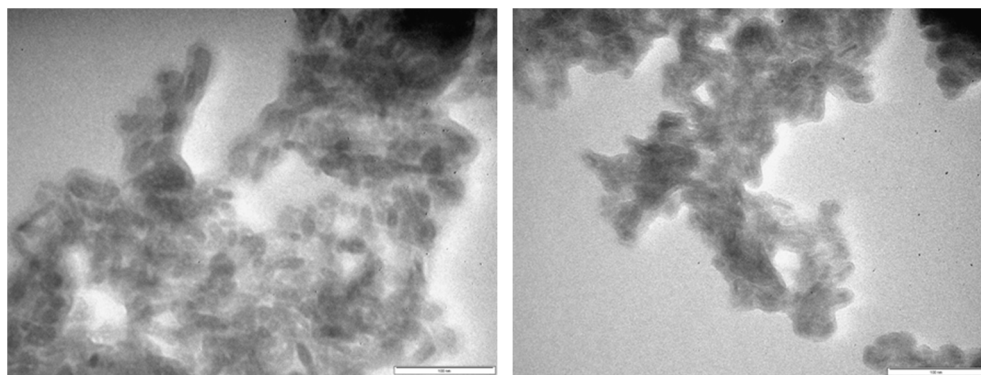
Figure 3. TEM images for stoichiometric, uncalcined hydroxyapatite (left) and Zn doped hydroxyapatite calcined at 300 ^{0}C for 1h (right); 100 nm scale.

Atomic force microscopy (AFM)

AFM images and cross section profiles are given in Figure 4, for uncalcined hydroxyapatite and in Figure 5 for Zn doped hydroxyapatite, calcined at 300 ^{o}C for 1h.
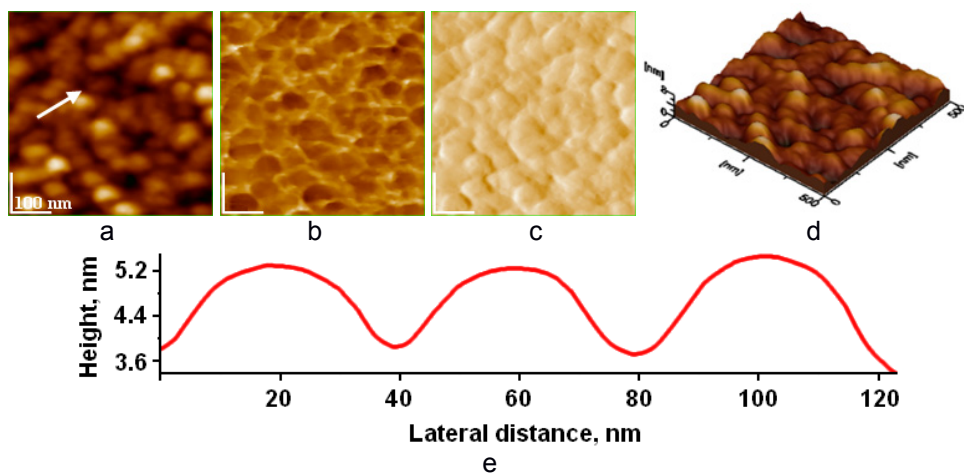
Figure 4. AFM images of HAP particles adsorbed on glass for 10 sec from aqueous dispersion: 2D topography (a), phase (b), amplitude (c), 3D- topography (d) and cross section profile (e) along the arrow in image (a); scanned area of 0.5 μm x 0.5 μm; average nanoparticle size of 32 nm.
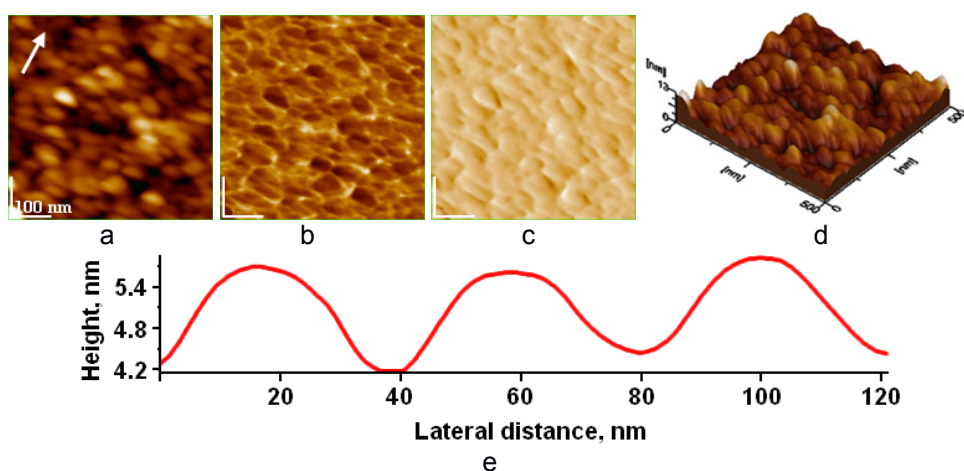
Figure 5. AFM images of HAP-5%Zn particles adsorbed on glass for 10 sec from aqueous dispersion: 2D topography (a), phase (b), amplitude (c), 3D- topography (d) and cross section profile (e) along the arrow in image (a); scanned area of 0.5 μm x 0.5 μm; average nanoparticle size of 27 nm.

There are mostly oblong particles, with a length of about 50 nm and diameters of 30 nm for stoichiometric hydroxyapatite and 40/20 nm for Zn doped hydroxyapatite. The size of particles is found to be in the range of 27-32 nm. These values are comparable with those determined by X-ray diffraction and SEM analysis.

Consistency water for investigated endodontic cements

Determining the normal consistency water of cement (the water quantity needed for cement slurry consistency) is an important first step towards proceeding with setting time experiments. After several trials, the normal consistency water of 87 ml for Carpat Cement Portland cement slurry was found. The predetermined consistency water for Portland cement slurry remained constant for all hydroxyapatite/cement ratios of the endodontic cements. It can be said that hydroxyapatite does not have any influence on this parameter. So, the porosity of the endodontic cement is maintained constant and, consequently, the mechanical strength.

Setting time for studied endodontic cements

The experimental data of setting time obtained from studied endodontic cements containing a consistency water of 87 ml, at temperatures of 22 °C and at 37°C, are presented in Table 4.

Table 4. Setting time of Portland cement and studied endodontic cements

Sample	Consistency water [ml]	Setting time [min]	
		at 22°C	at 37°C
S0		85	70
S1		70	60
S2	87	70	60
S3		55	45
S4		45	35
S5		70	65
S6		65	60
S7		55	45

The setting times for all experimental samples, including the standard, S0, decreases with the increasing in temperature from 22°C to 37°C, the normal body temperature. No difference can be seen through the addition of 1 and 2 wt% uncalcined hydroxyapatite (samples S1 and S2). Sample S3, containing 3 wt% hydroxyapatite, shows a more pronounced decreasing of the setting

time at both working temperatures. By increasing the hydroxyapatite content to 5 wt%, as seen in sample S4, a halving of the endodontic cement setting time can be observed. A progressive decrease of setting time in all samples containing Zn doped hydroxyapatite, namely S5, S6 and S7, can also be evidenced. Sample S7, containing 3 wt% Zn doped hydroxyapatite, shows similar behavior to that of sample S3, containing 3 wt% stoichiometric hydroxyapatite. The two types of hydroxyapatite present comparable results in the decrease of endodontic cement setting time.

CONCLUSIONS

Endodontic cements containing Portland cement and stoichiometric hydroxyapatite as well as Portland cement and Zn doped hydroxyapatite in different ratios were realized. Commercial Portland cement, having as main mineralogical components calcium silicates, was used as binder. Nanometric uncalcinated stoichiometric hydroxyapatite and Zn doped hydroxyapatite were successfully synthesized.

Quantities of 1, 2, 3 and 5 wt% of both types of hydroxyapatite were mixed with Portland cement and processed in accordance to cement standards. The workability of the cement mixtures was not influenced by adding small amounts of hydroxyapatite. The normal consistency water remains constant for all experimental slurries. The setting time for both sets of samples, with added stoichiometric, uncalcined hydroxyapatite (S1-S4) and Zn doped hydroxyapatite (S5-S7) has decreased exponentially at both working temperatures.

In conclusion, the properties, especially the setting time of studied endodontic cements obtained by adding nanometric stoichiometric and Zn doped hydroxyapatites in Portland cement mixtures can be improved. The research will continue with the testing of biological compatibility and antimicrobial activity of endodontic cements enriched with Zn doped hydroxyapatite.

EXPERIMENTAL SECTION

Materials and methods

The nanometric hydroxyapatite was prepared by the direct reaction of calcium nitrate and diammonium hydrogen phosphate at basic pH. A solution of calcium nitrate (0.25 M) was prepared by disolving $Ca(NO_3)_2 \cdot 4H_2O$ (pure p.a., Poch S.A., Merck) in ultrapure water. Then, a 25 wt% ammonia solution was added to reach a pH of 8.5. The final solution was mixed at room temperature

with an equal volume of 0.15 M $(NH_4)_2HPO_4$ (pure p.a., Sigma-Aldrich), with pH 11 (fixed with ammonia solution). A peristaltic pump and an impact reactor type Y were used for a rapid and good homogenization. The obtained dispersion was maintained for maturation at room temperature (22 ^oC) for 24 h. After subsequent filtration and washing with ultrapure water (until no nitrate ions were detected), the wet precipitate was dried by lyophilization (freeze drying).

For Zn doped hydroxyapatite, a 0.25 M $(Ca^{2+} + Zn^{2+)}$ solution, was prepared by dissolving the calculated amounts of $Ca(NO_3)_2\cdot4H_2O$ and $Zn(NO_3)_2\cdot6H_2O$ (from Sigma-Aldrich) in ultrapure water. The second solution was a 0.15 M PO_4^{3-} solution with L-asparagine monohydrate (purity ≥99.0%, from Merck, Germany) as surfactant. The identical processing steps were followed. The dried solid was calcined at 300 ^oC for one hour.

X-ray diffraction analysis was carried out using a Brucker D8 Advance diffractometer in Bragg Brentano geometry, equipped with an X-ray tube with copper K_a line and a wavelength of 1.541874 Å.

The size and morphology of hydroxyapatite crystallites were investigated by transmission electron microscopy (TEM) on a JEOL-type JEM 1010 equipment.

Atomic force microscopy analysis was carried out on a JEOL 4210 AFM apparatus, operated in tapping mode [27-35], using standard cantilevers with silicon nitride tips (resonant frequency in the range of 200–300 kHz).

Commercial Portland cement (Carpat Cement brand) as the matrix for endodontic cement mixtures was used.

Normal consistency water for investigated endodontic cements was determined following standard laboratory procedures. A quantity of 300 g cement were mixed with water ranging from 85 to 90 ml (standard for the type of Portland cement used) until a slurry was formed in the mixing bowl. The slurry was quickly poured in the mold of the Vicat apparatus and smoothed out. A 10 mm plunger was lowered to the surface of the sample and then let to fall freely. The depth was then read on the Vicat ruler. For a normal consistency, this depth should be in the 5-7 mm range.

The endodontic cement samples were prepared in a standard laboratory cement mixer. The cement and hydroxyapatite, in ratios according to Table 3, were added and homogenized for approximately 30 seconds. After this time, the water was added, the mixing continued for 1 minute on slow speed and 2 minutes on high speed, respectively. The final mixture was poured into a hard rubber truncated cone mold.

To measure the setting time of cement slurry with normal consistency water, a standard VICAT Apparatus was employed.

ACKNOWLEDGMENTS

REFERENCES

1. L.H. Silva Almeida, R.R. Moraes, R.D. Morgental, F.G. Pappen, *Journal of Endodontics*, **2017**, *43*, 527.
2. G. Debelian, M. Trope, *Giornale Italiano di Endodonzia*, **2016**, *30*, 70.
3. P. Bali, A.K. Shivekshith, C.R. Allamaprabhu, H.P. Vivek, *International Journal of Contemporary Dental and Medical Reviews*, **2014**, doi: 10.15713/ins.ijcdmr.17
4. F. Panahi, S.M. Rabiee, R. Shidpour, *Materials Science and Enginneering C*, **2017**, *80*, 631.
5. I.R. Oliveira, T.L. Andrade, K.C.M.L. Araujo, A.P. Luz, V.C. Pandolfelli, *Ceramics International*, **2016**, *42*, 2542.
6. F. Goga, E. Forisz, A. Avram, A. Rotaru, A. Lucian, I. Petean, A. Mocanu, M. Tomoaia-Cotisel, *Revista de Chimie,* **2017**, *68*, 1193.
7. J.A. Lett, M. Sundareswari, K. Ravichandran, *Materials Today: Proceedings*, **2016**, *3*, 1672.
8. S.M. Rabiee, F. Moztarzadeh, M. Solati-Hashjin, *Journal of Molecular Structure*, **2010**, *969*, 172.
9. M. Hosseinzade, R.K. Soflou, A. Valian, H. Nojehdehian, *Biomedical Research*, **2016**, *27*, 442.
10. Y.A. Moreno-Vargas. J.P. Luna-Arias, J.O. Flores-Flores, E. Orozco, L. Bucio, *Ceramics International*, **2017**, *43*, 13290.
11. J. Camilleri, F.E. Montesin, R.V. Curtis, T.R. Pitt Ford, *Dental Materials*, **2006**, *22*, 569.
12. V. Bortolotti, P. Fantazzini, R. Mongiorgi, S. Sauro, S. Zanna, *Cement and Concrete Research*, **2012**, *4*2, 577.
13. K. Ishikawa, *Bioactive Ceramics: Cements*, Comprehensive Materials II, Elsevier, **2017**, 369.
14. S. Jitaru, I. Hodisan, L. Timis, A. Lucian, M. Bud, *Clujul Medical,* **2016**, *89*, 470.
15. W.N. Ha, D.P. Bentz, B. Kabler, L.J. Walsh, *Journal of Endodontics*, **2015**, *41*, 1146.
16. A.M. Negm, E.E. Hassanien, A.M. Abu-Seida, M.M. Nagy, *Experimental and Toxicologic Pathology*, **2017**, *69*, 115.
17. M.G. Gandolfi, P. Taddei, A. Tinti, E. De Stefano Dorigo, C. Prati, *Materials Science and Engineering C*, **2011**, *31*, 1412.
18. N.J. Coleman, J.W. Nicholson, K. Awosanya, *Cement and Concrete Research*, **2007**, *37*, 1518.

19. D. Araki Ribeiro, M.A. Hungaro Duarte, M. Akemi Matsumoto, M.E. Alencar Marques, D.M. Favero Salvadori, *Journal of Endodontics*, **2005**, *31*, 605.
20. A. Chaipanich, P. Torkittikul, *Applied Surface Science*, **2011**, *257*, 8385.
21. J. Camilleri, *Dental Materials*, **2011**, *27*, 836.
22. P. Scembri-Wismayer, J. Camilleri, *Journal of Endodontics*, **2017**, *43*, 751.
23. N. Wongkornchaowalit, V. Lertchirakarn, *Journal of Endodontics*, **2011**, *37*, 387.
24. P. Torkittikul, A. Chaipanich*, Materials Science and Engineering C*, **2012***, 32*, 282.
25. K.B. Wiltbank, S.A. Schwartz, W.G. Schindler, *Journal of Endodontics*, **2007**, *33*, 1235.
26. L. Wang, X. Xie, C. Li, H. Liu, K. Zhang, Y. Zhou, X. Chang, H.H.K. Xu., *Journal of Dentistry*, **2017**, *60*, 25.
27. G. Tomoaia, O. Soritau, M. Tomoaia-Cotisel, L.-B. Pop, A. Pop, A. Mocanu, O. Horovitz, L.-D. Bobos, *Powder Technology*, **2013**, *238*, 99.
28. G. Tomoaia, M. Tomoaia-Cotisel, L.B. Pop, A. Pop, O. Horovitz, A. Mocanu, N. Jumate, L.-D. Bobos, ***Revue Roumaine de Chimie*, 2011, *56*, 1039.**
29. A. Mocanu, R. Balint, C. Garbo, L. Timis, I. Petean, O. Horovitz, M. Tomoaia-Cotisel, *Studia Universitatis Babes-Bolyai, Chemia*, **2017**, *62*(*2*), *Tom I*, 95.
30. R.D. Pasca, G. Tomoaia, A. Mocanu, I. Petean, G.A. Paltinean, O. Soritau, M. Tomoaia-Cotisel, *Studia Universitatis Babes-Bolyai, Chemia*, **2015**, *60*(3), 257.
31. M.A. Naghiu, M. Gorea, E. Mutch, F. Kristaly, M. Tomoaia-Cotisel, *Journal of Material Science and Technology,* **2013**, *29*(7), 628.
32. G. Tomoaia, O. Horovitz, A. Mocanu, A. Nita, A. Avram, C.P. Racz, O. Soritau, M. Cenariu, M. Tomoaia-Cotisel, *Colloids and Surfaces B: Biointerfaces*, **2015,** *135*, 726.
33. O. Horovitz, G. Tomoaia, A. Mocanu, T. Yupsanis, M. Tomoaia-Cotisel, *Gold Bulletin*, **2007**, *40* (4), 295.
34. M. Tomoaia-Cotisel**,** A. Tomoaia-Cotisel, T. Yupsanis, G. Tomoaia, I. Balea, A. Mocanu, Cs. Racz, *Revue Roumaine de Chimie,* **2006,** *51* (12),11832.
35. P.T. Frangopol. D.A. Cadenhead, G. Tomoaia, A. Mocanu, M. Tomoaia-Cotisel, *Revue Roumaine de Chimie,* **2015***, 60*(2-3), 265.

HYDROXYAPATITE FOR REMOVAL OF HEAVY METALS FROM WASTEWATER

ALEXANDRA AVRAM[a], TIBERIU FRENTIU[a], OSSI HOROVITZ[a,*], AURORA MOCANU[a], FIRUTA GOGA[a], MARIA TOMOAIA-COTISEL[a,b]

ABSTRACT. HAP powder of a low crystallinity and rather large specific surface area was synthesized by an environmentally friendly, cost effective precipitation method, and characterized by XRD, FTIR, and BET isotherms. TEM and AFM are used to envisage the surface of HAP nano particles, showing a high porosity of this ceramic powder. It was used for the removal of metals (Al, Cd, Co, Cr, Cu, Fe, Mn, Ni, Pb, and Zn) from mine wastewater. Metal contents in the initial and treated samples were quantified by inductively coupled plasma atomic emission spectrometry and high-resolution continuum source atomic absorption spectrometry. By the use of HAP, an efficient removal of all metals was ensured. The increase of Ca^{2+} ions content in the treated water suggests an ion exchange mechanism.

Keywords: hydroxyapatite, heavy metal removal, mine wastewater, sorption kinetics

INTRODUCTION

The presence of heavy metals in wastewater [1-6], resulting from mining operations, various manufacturing industries, leather tanning, paper production, fertilizers, photographic materials, explosives, is a major environmental concern. These elements can enter the human body both in a direct manner and following the food chain [7, 8]. Easily accumulated by organisms and non-biodegradable [1] heavy metals can lead to a large number of potentially deadly health issues [8-10] Some metals can be toxic even in small concentrations [11]. The admissible levels of heavy metals are regulated in most countries [12, 13], during the wastewater treatment.

[a] *Babeş-Bolyai University, Faculty of Chemistry and Chemical Engineering, 11 Arany Janos str., RO-400028, Cluj-Napoca, Romania*
[b] *Academy of Romanian Scientists, Splaiul Independenţei 54, 050094 Bucharest, Romania*
*Corresponding author: ossihor@yahoo.com

With water playing a crucial role in a sustainable development, the removal of heavy metals from contaminated waters has been the subject of many studies. Some examples are: strontium [14], iron [2, 15-18], lead [1-4, 6, 15, 18-28], cadmium [2, 3, 7, 18, 25, 29-33], zinc [2, 5, 15, 16,18, 22, 23, 29, 32], nickel [2, 8, 10, 17, 18, 31], chromium [18, 32, 35], arsenic [9], copper [17-20, 22, 24, 25, 32, 33], manganese [15, 16, 23], mercury [36], cobalt [18, 37]).

Some of the methods employed in the removal of these elements involve physical (e.g., membrane filtration, coagulation, adsorption on both stable and floating beds, reverse osmosis), chemical (such as, neutralization with various materials, including lime, ion exchange, adsorption, chemical oxidation or reduction) and biological processes [2-4, 9, 14, 15, 23, 34, 35]. The latter category presents certain models that are not easily implemented in industrial conditions as they require high manufacturing costs and are too complex [2].

The published data revealed that adsorption onto solids has been a preferred method, due to being simple, highly-selective, relatively low cost and showing very few to no problems [11, 14]. Among organic and inorganic materials used are: both natural [7, 10, 32, 35] and synthetic hydroxyapatite (HAP) [1, 2, 19, 21, 24], and various composites containing it [3, 4, 6, 25, 37], zeolites [23] polymers, organic resins [8], silicate sand, bentonite [6, 23], carbon nanotubes [4], coals [8, 9], bone charcoals [17], and natural waste materials (spent coffee grounds, fruit waste, nut and eggshells, rice husks, bamboo, saw dust, tea waste, grape stalks, algae, wood) [1, 9, 26, 32, 34, 37].

Hydroxyapatite (HAP, $Ca_{10}(PO_4)_6(OH)_2$), a naturally available form of calcium phosphate and a component of hard tissues [15, 26, 27]), has been reported to act as an efficient ion removal material for various heavy metals from aqueous solutions due to its excellent reactivity and low water solubility [8, 14, 35]. The high structure stability of HAP, along with its flexibility permit a large variety of substitutions (especially Ca with divalent heavy metal ions, such as Pb, Cu, Sb, Zn, Cd, Co, Ni, U, Hg, As [6, 8, 18, 27, 28, 33, 34, 38-40], of great importance in the field of environmental science [34].

HAP can be synthesized through various methods, including sol-gel [24], wet precipitation [6, 31, 41-44], combustion and ultrasonic [32]. Its slightly-alkaline pH and high biocompatibility will not likely cause any form of secondary environmental damage [19]. The efficiency of HAP in removing heavy metal ions heavily depends on ion nature, charge, diameter and concentration, as well as the properties of the treated water (pH, temperature) [8, 25]. In addition, the removal of HAP from the purified aqueous solution is not without problems [38], as is the isolation of some important heavy metals from it [3, 36].

Some studies have tried to enhance the properties of hydroxyapatite (improved porosity, specific surface area, mechanical properties, etc. [6, 27]) through the addition of non-toxic polymers, abundantly found in nature – dextran [27], chitosan [4, 38], carboxymethyl cellulose [26, 36], alginate, gelatin [21]. However, these additions do tend to increase the manufacturing cost, thus making it difficult to translate from a laboratory level to an industrial one. Other studies have tried to combine the reactivity of hydroxyapatite as an adsorbent with a magnetic separation process for an increased adsorption of heavy metal ions, synthesizing magnetic HAP particles [22] or magnetic core-shell nanocomposites [5]. Ca deficient HAP has also been reported to exhibit different ion substitution ability to stoichiometric HAP [18], due to its large number of Ca-deficient sites. While the main focus of some research groups is to enhance the properties of HAP by using its composites with various polymers, such as chitosan, others choose to focus on cost effectiveness, by synthesizing hydroxyapatite, using environmental friendly methods.

The aim of this study was to develop a rapid and low cost method to remove metal ions from mine wastewaters, using a low crystalline HAP prepared by a precipitation method [41]. This study meant to correlate the ion adsorption behaviour of a low crystallinity HAP, and its efficiency in removal of a large range of various metals (Al, Cd, Co, Cr, Cu, Fe, Mn, Ni, Pb, and Zn) from a multi-component Roșia Montana mine wastewater.

RESULTS AND DISCUSSION

Hydroxyapatite characterization

X-ray diffraction pattern (Fig. 1) shows, by comparison with PDF 74-0566 (characteristic for stoichiometric HAP) that synthesized HAP sample contains only pure hydroxyapatite. Average crystallite size was evaluated, using Scherrer formula, to be 23.3 nm, and the degree of crystallinity was obtained, using Reflex computer program, as 32.3%. This nanoHAP with rather low crystallinity is expected to present good adsorptive properties.

The *FTIR spectrum* (Fig. 2) presents the absorption bands of hydroxyapatite, corresponding to vibrations of PO_4 and OH groups characteristic for HAP, and of OH groups from adsorbed water

An example of *TEM* image (Fig.3) for the HAP sample in aqueous dispersion reveals acicular assemblies of particles, with a diameter of 15-20 nm. These dimensions are confirmed by the *atomic force microscopy* (*AFM)* images (an example is given in Fig. 4).

Brunauer-Emmett-Teller (BET) analysis on HAP powder gave a specific surface area of 106.5 m^2/g and a specific volume of the pores of 0.358 cm^3/g.

The large specific surface area recommends HAP as a good adsorbent. From the surface area, a rough estimation of the particles size is possible, using the formula

$$d = \frac{6}{S\rho} \tag{1}$$

where d is the average diameter of particles, S is the specific surface area and ρ is the density of the material; using the theoretical density of HAP: 3.14 g/cm^3 [45], a value of 17.9 nm is found for the average diameter of a HAP particle.
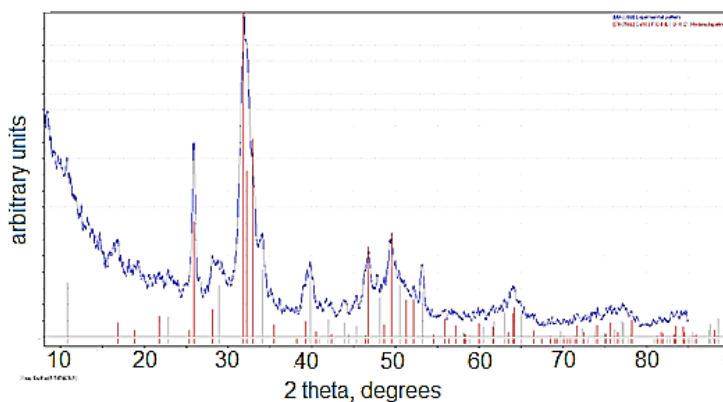
Figure 1. XRD pattern for HAP sample, compared with PDF 74-0566 for stoichiometric hydroxyapatite
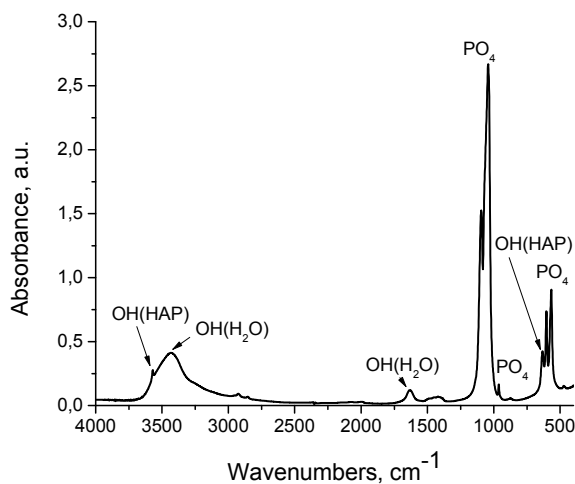
Figure 2. FTIR spectrum of HAP
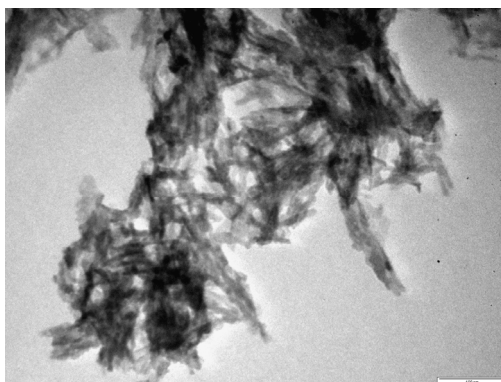
Figure 3. TEM image of HAP; the bar is 100 nm

a   b   c
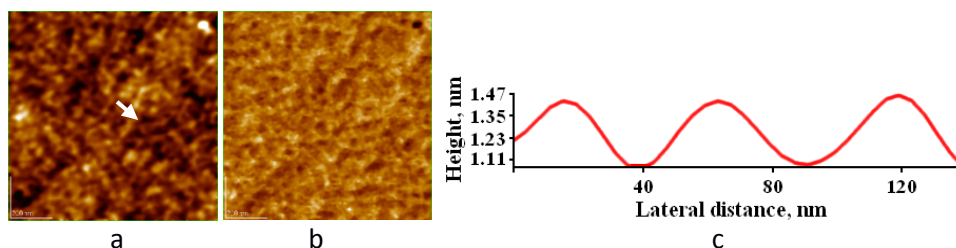
Figure 4. AFM images for HAP, adsorbed on glass support: 2D topography (a), phase image (b), cross section profile (c) along the arrow in panel (a); scanned area of 1µm x 1µm

Metal ions removal from mine wastewater samples

The removal degree, R (%), was calculated as

$$R\ (\%) = \ 100\frac{c_0 - c_e}{c_0} \tag{2}$$

where c_0 is the element' content (mg/L) in the initial mine wastewater sample, while c_e is its final content at equilibrium, after adsorption for 120 min on HAP. The initial and final content, and the calculated removal degree for each metal are given in Table 1, along with the standard errors from determinations on 3 parallel samples. In the same table the limit values for the metal content admissible in wastewater discharged in natural waters [12] are indicated.

All metal ions are removed to final values below the values admitted in standards for wastewaters. The removal degree is near to 100% for metals existent in higher amounts in the wastewater, and lower (60-80%) for those present initially only in very low concentration (even under the admitted limit value – Table 1). Probably, their sorption on the surface of HAP nanoparticles

97

is limited by the simultaneous sorption of ions existent in high excess in the wastewater. The confidence intervals are wide due to the existence of some metals (Cu, Cr, Pb, Ni) near the quantification limit of analytical methods. However, an efficient removal of these metals below the values of admitted levels in wastewater in the presence of those in high concentrations can also be observed.

Table 1. Metal removal from mine wastewaters using nano HAP powder (results are given as mean ± confidence interval for n = 3 and 95% confidence level)

Metal	Initial content c_0, mg/L	Final content c_e, mg/L	Removal degree, %[a]	Limit value for wastewater, mg/L [12]
Al	313 ± 37	1.9 ± 0.6	99 ± 12	5
Cd	0.21 ± 0.07	0.068 ± 0.043	68 ± 58	0.2
Co	1.1 ± 0.6	0.15 ± 0.07	86 ± 63	1
Cr	0.046 ± 0.024	0.009 ± 0.006	80 ± 66	1
Cu	1.0 ± 0.7	0.014 ± 0.011	99 ± 71	0.1
Fe	92 ± 9	0.9 ± 0.6	99 ± 10	5
Mn	190 ± 5	0.81 ± 0.48	100 ± 3	1
Ni	0.47 ± 0.22	0.16 ± 0.09	66 ± 77	0.5
Pb	0.16 ± 0.07	0.066 ± 0.045	59 ± 88	0.2
Zn	14.4 ± 0.9	0.18 ± 0.08	99 ± 6	0.5

[a] the removal degree and its confidence interval were calculated by a concentration difference and pooled standard deviation

Adsorption kinetics of Mn^{2+} ions on HAP

The concentration of Mn^{2+} ions in mine wastewater was measured at different time points. The Mn uptake, x, from the contaminated solution on the HAP, was calculated in mg Mn/g HAP for each moment by the formula:

$$x = \frac{(c_0 - c_t)V}{m} \tag{3}$$

where c_o is the initial Mn^{2+} content, c_t is the content at time t (mg/L), V is the volume of solution (0.1 L), and m is the mass of HAP (10 g).

In order to assess the kinetics of Mn removal from the solution, three kinetic models were used [3], assuming a pseudo-first-order kinetic [46], a pseudo-second order kinetic [47], and an intraparticle diffusion model [48].

The first order kinetic (Lagergren kinetic) would be described by the equation:

$$\frac{dx}{dt} = k_1(x_e - x) \tag{4}$$

where x_e is the sorbed amount at equilibrium, assumed to be the value at 960 min, and k_1 is the first order adsorption rate constant. The representation of the linearized form of the integrated equation:

$$\ln(x_e - x) = \ln x_e - k_1 t \tag{4a}$$

98

as ln $(x_e-x) = f(t)$ should give a straight line if the equation would apply. The poor linearity observed in Fig. 5a ($r^2 = 0.62$) shows this model to be inadequate here.

The 2nd order kinetic equation:

$$\frac{dx}{dt} = k_2(x_e - x)^2 \tag{5}$$

with k_2 as second order sorption rate constant, linearized after integration as:

$$\frac{t}{x} = \frac{1}{k_2 x_e^2} + \frac{t}{x_e} \tag{5a}$$

gives in the representation: $t/x = f(t)$ a perfect straight line (Fig. 5b), with $r^2 = 0.9999$; thus this model best describes the kinetics of Mn sorption on HAP.

The third model assumes the diffusion to be the rate-limiting step in the sorption, using an equation for intraparticles diffusion rate:

$$x = k_d t^{1/2} + const. \tag{6}$$

where k_d is the diffusion rate constant and const. an integration constant. The representation of $x = f(t^{1/2})$ in Fig. 5c shows no linear correlation ($r^2 = 0.32$), so this model is not applicable in our case. Nevertheless, for the first 15 minutes of sample contact with HAP, a quite good correlation is found ($r^2 = 0.985$, Fig. 5d) with $k_d = 0.480 \pm 0.034$ and const. $= 0.02 \pm 0.07$.

From the parameters of the linear plot of equation (5a) for the pseudo second order kinetics: intercept, a = 0.57502, and slope, b = 0.52808, we can calculate the x_e value: $x_e = 1/b = 1.894$ mg/g, very close to the assumed value 1.891, and the pseudo second order rate constant $k_2 = 1/(ax_e^2) = 0.485$ $g \cdot mg^{-1} \cdot min^{-1} = 29.1$ $g \cdot mg^{-1} \cdot h^{-1}$. A second order reaction kinetic was observed also for the sorption on hydroxyapatite of other metal ions, such as Cd^{2+} [3], Cu^{2+} [19], Ni^{2+} [10], Zn^{2+} [34], Cr(VI) [35], or Pb^{2+} [3, 19, 21]. For the adsorption of Co^{2+} on a HAP/zeolite composite [34], Pb^{2+} on a HAP/bentonite composite [6], Cr(VI), Zn^{2+}, and Cd^{2+} on HAP/chitosan composite [38], of Mn^{2+}, Fe^{2+}, Ni^{2+}, and Cu^{2+} on charcoal [17], the same pseudo-second order kinetic was found.

We could assume that for the initial stage (about 15 min), diffusion is important; subsequently, the second order chemical process is rate determining.

Hydroxyapatite immobilizes heavy metal ions from aqueous solutions in various ways. Some of these mechanisms include: surface complexation, ion exchange, dissolution followed by the precipitation of metal phosphates, and the substitution of Ca^{2+} present in the HAP structure by other divalent heavy metals during co-precipitation [16, 18, 28, 34]. Literature presents very little information on the specific contribution of these processes, leading researchers to believe that they are all employed at the same time [16, 34] (in aqueous solutions containing multiple competing heavy metal ions [33]).
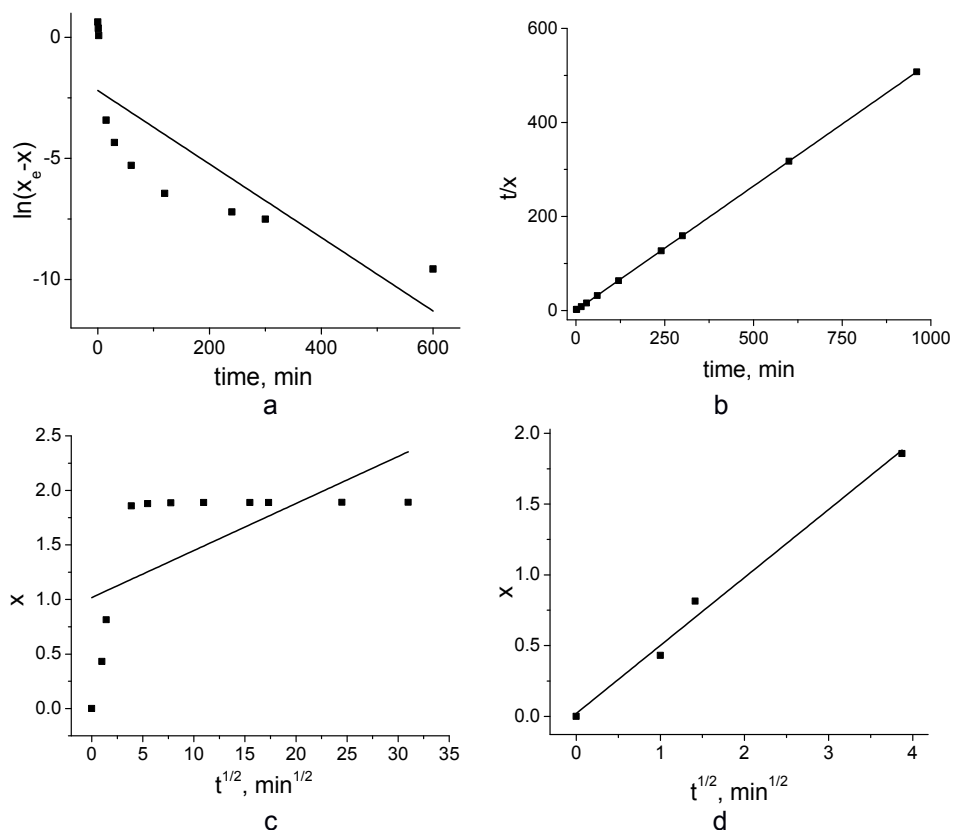
Figure 5. Plots of linearized kinetic equations for pseudo first order (a), pseudo second order (b) and intramolecular diffusion (c, d) kinetics of Mn sorption on HAP

The sorption process of metal ions involves complex adsorption on the adsorption sites on the HAP surface [19]. For the mechanism of ions retention, ion exchange was considered, for instance for Pb^{2+} [1, 15], where the incorporation of Pb in the HAP lattice was evidenced, or for Cd^{2+} [33]. For Zn^{2+}, Fe^{2+} and Mn^{2+} the formation of metal phosphates was considered [15], by dissolution of HAP and precipitation of phosphate ions with the heavy metal ions.

During the metals removal process, an increase of the Ca^{2+} content in the solution was observed, from initially 115.5 mg/L to 287.3 mg/L (after 120 min), which corresponds to the release of 4.29 mmol/L. The total amount of heavy metal ions removed from the solution (Table 1) in the same time is 5.35 mmol/L. So, most of the heavy metal ions were exchanged with Ca^{2+} ions during sorption, while other were simply adsorbed on the surface of HAP.

CONCLUSIONS

Our study has evidenced that low crystallinity HAP can be successfully used in heavy metal removal from mine wastewater. For all the 10 metals analyzed (Al, Cd, Co, Cr, Cu, Fe, Mn, Ni, Pb, and Zn), their content was rapidly reduced by contact with HAP under the legal admissible limits for wastewater discharge in natural environment. The importance of ion exchange in sorption processes was revealed and the pseudo-2nd order kinetics of manganese ions sorption on HAP was assessed.

EXPERIMENTAL SECTION

The nano-hydroxyapatite was prepared by the direct reaction of calcium nitrate and diammonium hydrogen phosphate at basic pH. The calcium nitrate solution (0.25 M), prepared from $Ca(NO_3)_2 \cdot 4H_2O$ (pure p.a., Merck) in ultrapure water, with addition of 25% ammonia solution to pH 8.5 was mixed at room temperature with an equal volume of 0.15 M $(NH_4)_2HPO_4$ (pure p.a., Sigma-Aldrich), with pH 11 (fixed with ammonia solution). The mixing was achieved rapidly, using a peristaltic pump (Masterflex L/S Digital Drive, 600 RPM, 115/230 VAC, EW-07523-80) and an impact reactor type Y To assist the formation of the HAP lattice, the so obtained dispersion was maintained for a maturation stage at room temperature (22°C) for 24 h. After subsequent filtration and washing with ultrapure water (until no nitrate ions were detected), the wet precipitate was dried by lyophilization (freeze drying process). The dried material was dispersed by grinding in an agate mortar.

X-Ray Diffraction (XRD) investigations: a DRON-3 diffractometer was used, in Bragg-Brentano geometry, equipped with a X-ray tube with Co K_α radiation (wavelength 1.79026 Å), 25 kV/20 mA. *FTIR spectra* were determined on the HP powder in KBr pellets, using a FTIR spectrometer JASCO 6100 in the 4000-400 cm^{-1} range of wave numbers, with a 4 cm^{-1} resolution.

TEM images were obtained with a transmission electron microscope (TEM, JEOL – JEM 1010); the aqueous dispersion of the HAP sample was adsorbed on the specimen grids. The same HAP dispersion was used for the preparation of samples for atomic force microscopy, AFM JEOL 4210 used in tapping mode, [49-53], after HAP adsorption for 10 s on glass. The images were processed by the standard AFM-JEOL procedures.

For BET analysis an automated Sorptomatic 1990 instrument was used, with nitrogen adsorption at 77 K. The calculation of surface area was made in the P/P_o range between 0.03 and 0.3, and the total pore volume was determined at $P/P_o = 0.95$. Before the analysis the samples were outgassed for 6 h at 70 °C.

The ion adsorption capacity of synthetic hydroxyapatite was studied using raw, non-treated wastewater collected from Roşia Montană, Alba County, Romania. Adsorption experiments were carried out in controlled conditions using a predetermined wastewater/HAP ratio, namely 100 ml wastewater to 10 g HAP. All experiments were performed by submitting the HAP/wastewater mixture to magnetic stirring for `100 minutes, followed by a 20 minutes sedimentation period. For manganese, samples were collected in a time span ranging from one minute to 960 minutes, for kinetics determination purposes. All samples were filtered using Millipore syringe filters (0.22 μm).

Treated water samples were analyzed by Inductively Coupled Plasma Atomic Emission Spectrometry using a Spectro Ciros CCD spectrometer (Spectro Ciros, Germany) and High-Resolution Continuum Source Atomic Absorption Spectrometry using a ContrAA 300 flame spectrometer (Analytik Jena, Germany). The results are calculated as the mean values of 3 independent measurements.

ACKNOWLEDGMENTS

REFERENCES

1. V.N. Narwade, M.P. Mahabole, K.A., Bogle, R.S. Khaimar, *International Journal of Engineering Science and Innovative Technology*, **2014**, *3*, 324.
2. N. Moayyeri, K. Saeb, E. Biazar, *International Journal of Material Science and Engineering*, **2013**, *3*, 13.
3. S. Park, A. Gomez-Flores, Y.S. Chung, H. Kim, *Journal of Chemistry*, **2015**, Article ID 396290, 12 pp.
4. Y. Lei, J.-J. Guan, W. Chen, Q.-F. Ke, C.-Q. Zhang, Y.-P. Guo, *RCS Advances*, **2015**, *5*, 25462.
5. F. Foroughi, S.A. Hassanzadeh-Tabrizi, J. Amighian, A. Saffar-Teluri, *Ceramics International*, **2015**, *41*, 6844.
6. T.M. Hieu Do, P.T.T. Tran, A.K. Ton, M.V. Le, *Journal of Environmental Science and Technology B*, **2016**, *5*, 371.
7. O.K. Ince, M. Ince, N.M. Karaaslan, V. Yonten, *Analytical. Letters*, **2016**, *49*, 2513.
8. S. Sharma, S. Garg, *Research Cell: An International Journal of Engineering Sciences*, **2014**, *3*, 201.
9. M. Mirhosseini, E. Biazar, K. Saeb, *Current World Environment*, **2014**, *9*, 331.

10. S. Zamani, E. Salahi, I. Mobasherpour, *Canadian Chemical Transactions*, **2013**, *1*, 173.
11. L.V. Constantin, S. Iconaru, C.S. Ciobanu, *Romanian Reports in Physics*, **2012**, *64*, 788.
12. *** HOTĂRÂRE nr. 352 din 21 aprilie 2005 privind modificarea si completarea Hotărârii Guvernului nr. 188/2002 pentru aprobarea unor norme privind condiţiile de descărcare in mediul acvatic a apelor uzate, *Monitorul Oficial* Nr 398, 11 mai **2005**, Art. I, 35.
13. *Guidelines for drinking-water quality: fourth edition incorporating the first addendum*, Geneva, World Health Organization, **2017**, Licence: CC BY-NC-SA 3.0 IGO.
14. Y. Nishiyama, T. Hanafusa, J. Yamashita, Y. Yamamoto, T. Ono, *Journal of Analytical and Nuclear Chemistry*, **2016**, *64*, 1279.
15. J. Oliva, J. De Pablo, J.-L. Cortina, J. Cama, C. Ayora, *Journal of Hazardous Materials*, **2010**, *184*, 364.
16. S. Varvara, M. Popa, R. Bostan, A. Lancranjan, M. Moldovan, C. Rosu, *Studia UBB Ambientum*, **2015**, *60*, 145.
17. J.C. Moreno, R. Gomez, L. Giraldo, *Materials*, **2010**, *3*, 452.
18. T. Miriguchi, S. Nakagawa, F. Kaji, *Phosphorus Research Bulletin*, **2008**, *22*, 54.
19. Y. Song, J. Gao, Y. Zhang, S. Song, *Nanomaterials and Nanotechnology*, **2016**, *6*, 1.
20. J.R. Parga, J.L. Valenzuela, V. Vazquez, M. Rodriguez, H. Moreno, *Materials Sciences and Applications*, **2013**, *4*, 231.
21. K. Sangeetha, G. Vasugi, E.J. Girija, *Journal of Chemtech Research,* **2015***, 8,* 117*.*
22. C. Stotzel, F.A, Muller, F. Reinert, F. Niederdraenk, J.E. Barralet, U. Gbureck, *Colloids and Surfaces B: Biointerfaces*, **2009**, *74*, 91.
23. S. M. Abdallah, *Journal of Novel Applied Sciences*, **2014**, *3*, 5
24. A. Deptula, J. Chwastowska, W. Lada, T. Olczak, D. Wawszczak, E. Sterlinska, B. Sartowska, M. Brykala, K.C. Goretta, *Advances in Science and Technology*, **2006**, *45*, 2198.
25. M. Vila, S. Sanchez-Salcedo, M. Cicuendez, I. Izquierdo-Barba, M. Vallet-Regi, *Journal of Hazardous Materials*, **2011**, *192*, 71.
26. D.C. Manatunga, R.M. De Silva, K.M.N. De Silva, R. Ratnaweera, *RSC Advances*, **2016**, *6*, 105618.
27. A. Costescu, E. Andronescu, B.S. Vasile, R. Trusca, P. Le Coustumer, E.S. Barna, S.L. Iconaru, M. Motelica-Heino, C.S. Ciobanu, *U.P.B. Scientific Bulletin, Series B*, **2014**, *76*, 71.
28. Q.Y. Ma, S.J. Traina, T.J. Logan, *Environmental Science and Technology*, **1993**, *27*, 1803.
29. Y. Feng, J.-L. Gong, G.-M. Zeng, Q.-Y. Niu, H.-Y. Zhang, C.-G. Niu, J.-H. Deng, M. Yan, *Chemical Engineering Journal*, **2010**, *162*, 487.
30. K.A. Matis, A.I. Zoubulis, S. Mandjiny, D. Zamboulis, *Separation Science and Technology*, **1997**, *32*, 2127.
31. M. Nehru, S. Sumathi, *International Journal of Applied Engineering Research*, **2013**, *8*, 2179.

32. K. Chojnacka, I. Michalak, *Global Nest Journal*, **2009**, *11*, 205.
33. A. Corami, S. Mignardi, V. Ferrini, *Journal of Colloid and Interface Science*, **2008**, *317*, 402.
34. R. Bazargan-Lari, M.E. Bahrololoom, A. Nemati, *International Journal of Chemical, Molecular, Nuclear, Materials and Metallurgical Engineering*, **2012**, *6*, 105.
35. T. Faezeh, M. Omid, H. Ebrahimzadeh, *Indian Journal of Science and Technology*, **2015**, *8*, 1.
36. Z. Abbasi, M. Aghababaei, *Universal Journal of Engineering Science*, **2014**, *2*, 124.
37. N. Gupta, A.K. Kushwaha, M.C. Chattopadhyaya, *Advanced Materials Letters*, **2011**, *2*, 309
38. E. Kusrini, N. Sofyan, D.M. Nurjaya, S. Santoso, D. Tristantini, *Advanced Materials Research*, **2013**, *789*, 176.
39. F. Fernane, S. Boudia, H. Saouli, *Matec Web of Conferences*, **2013**, *5*, 1.
40. H. Sawa, A. Takenaka, M. Hasegawa, K. Aoki, *Phosphorus Research Bulletin*, **1998**, *8*, 55.
41. A. Mocanu, R Balint, C. Garbo, L. Timis, I. Petean, O. Horovitz, M. Tomoaia-Cotisel, *Studia UBB Chemia*, **2017**, *62*, 95.
42. C. Garbo, M. Sindilaru, A. Carlea,.G. Tomoaia, V. Almasan, I. Petean, A. Mocanu, O. Horovitz, M. Tomoaia-Cotisel, *Particulate Science and Technology,* **2017**, *35*, 29.
43. Gh. Tomoaia, A. Mocanu, I. Vida-Simiti, N. Jumate, L.D. Bobos, O. Soritau, M. Tomoaia-Cotisel, *Materials Science and Engineering C*, **2014**, *37*, 37.
44. G. Tomoaia, O. Soritau, M. Tomoaia-Cotisel, L.-B. Pop, A. Pop, A. Mocanu, O. Horovitz, L.-D. Bobos, *Powder Technology*, **2013**, *238*, 99.
45. D Loca, M. Sokolova, J. Locs, A. Smirnova, Z. Irbe, *Materials Science and Engineering C*, **2015**, *49,* 106.
46. S. Lagergren, *Kungliga Svenska Vetenskapsakademiens Handlingar*, **1898,** *24*, 1.
47. Y.S. Ho, G. McKay, *Process Biochemistry*, **1999**, *34*, 451.
48. W.J. Weber, J. C.Morris, *Journal of the Sanitary Engineering Division—American Society of Civil Engineers*, **1963**, *89*, 31.
49. Gh. Tomoaia, O. Horovitz, A. Mocanu, A. Nita, A. Avram, C.P. Racz, O. Soritau, M. Cenariu, M. Tomoaia-Cotisel, *Colloids and Surfaces B: Biointerfaces*, **2015**, *135*, 726
50. R.D. Pasca, G. Tomoaia, A. Mocanu, I. Petean, G.A. Paltinean, O. Soritau, M. Tomoaia-Cotisel, *Studia Univ. Babes-Bolyai, Chemia*, **2015**, *60*(3), 257.
51. G. Tomoaia, A. Mocanu, L.D. Bobos, L.B. Pop, O. Horovitz, M. Tomoaia-Cotisel, *Studia Univ. Babes-Bolyai, Chemia*, **2015**, *60* (3), 265.
52. O. Horovitz, Gh. Tomoaia, A. Mocanu, T. Yupsanis, M. Tomoaia-Cotisel, *Gold Bulletin*, **2007**, *40* (4), 295.
53. M. Tomoaia-Cotisel, A. Tomoaia-Cotisel, T. Yupsanis, Gh. Tomoaia, I. Balea, A. Mocanu, Cs. Racz, *Revue Roumaine de Chimie,* **2006**, *51* (12),1181.

THE INFLUENCE OF AZA-SUBSTITUTION ON THE AROMATICITY OF SUMANENE

MIHAI MEDELEANU[a], RALUCA POP[b]*, MIHAIELA ANDONI[b], MIRCEA V. DIUDEA[c]*

ABSTRACT. The influence of aza-substitution on sumanene and C_{52} fullerene was investigated. Various substitution patterns, derived for the structures of pyrrole, indolizine and pyridine have been proposed and aromaticity indices like HOMA, NICS, delocalization indices PDI and FLU were considered, at B3LYP/6-311+G(d) level of theory. The results outlined an enhanced aromatic character for the sumanene derivatives where similar aza-substitution patterns as encountered in pyrrole and indolizine have been considered.

Keywords: sumanene, fullerene, aromaticity, aza-substitution

INTRODUCTION

During the last decades, specific properties of fullerenes – mainly due to their extended π electron system – attracted a continuous interest of scientists, as well as for their possible precursors. The presence of one (or more) isovalent atoms like nitrogen may modify the extended π electron system. Literature survey outlines a number of studies regarding the effects of heteroatoms doping the carbon-based nanomaterials. This way, researches regarding the curvature evolution and cross-linkage in carbon nitride have demonstrated that incorporation of N atom determines an increased reactivity of the C atoms in the vicinity of heteroatom, the most stable isomer being the one containing one N atom per pentagon [1]. Investigations of the structure

[a] *University POLITEHNICA Timisoara, Faculty of Industrial Chemistry and Environmental Engineering, 300006 Timisoara, Romania*
[b] *University of Medicine and Pharmacy "Victor Babeş" Timisoara, Faculty of Pharmacy, Eftimie Murgu Square 2, 300041 Timişoara, Romania*
[c] *Department of Chemistry, Faculty of Chemistry and Chemical Engineering, Babes-Bolyai University, 400028 Cluj, Romania*
Corresponding authors: pop.raluca@umft.ro; diudea@gmail.com

and stability of heteroannulated [8-10] circulenes with N, P and As atoms have proved the influence of steric factors and heteroatom electronegativity on the π electron delocalization [2]. Also, a study, regarding the effects of N doping on the electronic properties of a small carbon chain with distinct sp^2 termination, showed that incorporation of a nitrogen atom influences the conformation, charge distribution and the spin states of structures consisting in corannulene/ coronene-like pieces connected by atomic chains [3]. Another theoretical investigation of nitrogen disubstituted corannulenes suggested an increased stability for the isomer containing two N atoms within the benzene ring, in para position [4].

Concerning the properties of doped fullerenes, their electronic behavior was reported in [5]; then properties of $C_{59}X$-type fullerenes (where X = B, N, Al, Si, P, Ga, Ge and As) [6], applications of N-doped carbon nanotubes [7], electron delocalization and dimerization in solid $C_{59}N$ doped C_{60} fullerene [8], structure and electronic properties of heterofullerene $C_{30}B_{15}N_{15}$ [9], stability of boron nitride fullerenes [10], also small fullerenes doped with boron and nitrogen [11] have been reported. Possible isomers of heterofullerenes of the type X_nC_{20-n} (X = B, N, P and n = 2, 4, 5, 6, 10) were also studied [12]. The stability of compounds is directly related to the number and type of heteroatoms, as well as to the substitution pattern, the N- and P- doped fullerenes being thermodynamically favoured in comparison to their boron analogues [16]. In another study [13], various isomers of N-doped fullerenes of the type $C_{42}N_{18}$ and $C_{40}N_{20}$ have been investigated, including structures with separated N atoms and nitrogen belts. The results outlined a reasonable stability for the compounds with a belt of N atoms, with possible applications in molecular electronics [13].

Researches regarding the influence of hetero-substitution of carbon-based nanomaterials have also been extended to graphenes and nanotubes; properties like magnetism and mobility [14], sensing applications [15], electronic and optical properties [16] have been studied.

Our previous studies dealt with the investigation of aromaticity of fullerenes and their precursors [17-18], as well as of their N- and P-substituted analogues [19-22]. A comparison between the calculated properties of both fullerenes and circulene-type precursors was made.

DATA SET

The present paper is focused on the influence of aza-substitution on both sumanene and C_{52} derivatives, containing a sumanene patch. Three substitution patterns, derived from the structures of pyrrole, indolizine and pyridine, are proposed.

Pyrrole (I)   Indolizine (II-III)   Pyridine (IV)

Figure 1. Substitution patterns: I – pyrrole type; II and III – indolizine type;
IV – pyridine type

The structures of investigated sumanene and its aza-derivatives are depicted in Figure 2; the same pattern has been employed for the design of aza-fullerenes $C_{49}N_3$:

Sumanene [6.(5,6)$_3$]

I   II   III   IV
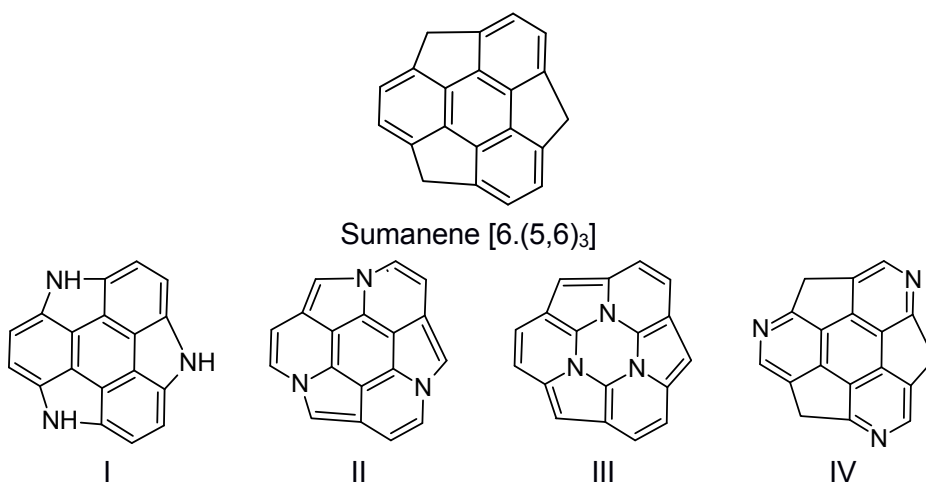
Figure 2. Aza-substitution patterns used throughout the study

Observe the two different indolizine-type patterns: II – with the N atom placed "outer" of the pentagon-hexagon pair, and III - with the N atom in "inner" position. While the all-Carbon structure II is bowl-shaped, the presence of N atoms leads to a planar geometry. Geometry optimization and vibrational analysis showed that structures I, III and IV are true minima, but the compound II is a transition state (with an imaginary frequency).

RESULTS AND DISCUSSION

Various local aromaticity descriptors, like the geometric index HOMA, magnetic index NICS, reactivity descriptors (condensed Fukui functions), and cohesion energy have been computed.

1. Geometric index

The optimized structures of the investigated aza-sumanene derivatives are shown in Figure 3. Values of the convex angle for the sumanene and its four aza-derivatives are listed in Table 1.
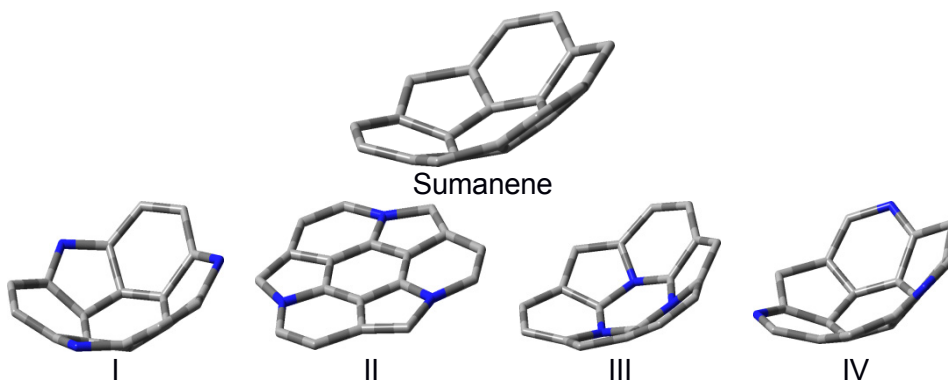
Figure 3. Optimized geometries (B3LYP/6-311+G(d)) of sumanene and its aza-derivatives

Table 1. Values of the convex angle in the bowl-shaped sumanene derivatives

Structure	Convex angle
All C	152.8
I	146.7
II	0.0
III	151.3
IV	145.1

Table 2. HOMA index computed for the core and 5- and 6-membered rings

HOMA	Sumanene	I-aza	II-aza	III-aza	IV-aza
core	0.703	0.853	0.728	0.953	0.738
6- ring	0.862	0.898	0.068	0.364	0.784
5- ring	0.472	0.800	0.354	0.588	0.624

The following observations can be made:

- I-type aza-substitution leads to an improvement of the HOMA index value (compared to the bare sumanene); the most significant difference appears for the 5-membered ring, when the substitution of sp^3 C atom with N leads to a bond shortening from 1.562 Å to 1.420 Å;

- II-type aza substitution is characterized by lower values of the HOMA index for the outer rings, due to the planar conformation;

- III-type substitution: the alternation carbon-nitrogen in the core ring results in the highest value of the HOMA index;

- IV-type substitution shows the smallest differences compared to the reference sumanene molecule.

- The main stabilization seems to appear at the ring bearing N atom and it is higher at the core hexagonal ring (in I-aza and III-aza substitution).

2. Magnetic index

Data on nucleus independent carbon shift NICS are listed in Table 3.

Table 3. NICS(0) values computed for the core and petals of sumanene and aza-sumanenes (B3LYP/6-311+G(d))

Position	Sumanene	I-aza	II-aza	III-aza	IV-aza
core	-3.01	1.05	-8.10	15.39	-3.64
6-ring	-9.03	-11.96	-3.34	0.81	-8.15
	-9.11	-11.96	-3.55	0.90	-8.10
	-9.18	-12.29	-3.34	0.84	-8.08
5- rings	2.47	-8.60	-15.99	-10.74	1.88
	2.41	-8.87	-15.87	-11.00	1.84
	2.47	-8.78	-15.89	-10.87	1.84

The results are in good agreement with the predictions of the geometric index HOMA; this way, similar values have been obtained for the bare sumanene and for the IV-aza substitution (that proves the small influence of replacing by nitrogen one C atom from outer 6-membered rings). The presence of N atom in the 5-membered rings (similar to pyrrole) leads to their "aromatization" (see the negative NICS values). The negative values of NICS index obtained for all the rings of II-type aza-sumanene can be attributed to the stronger electron delocalization, favoured by the planar structure. Again, there are small differences between sumanene and IV-type aza-substitution.

3. Delocalization indices

Smallest values of the FLU index (highest aromaticity) have been obtained for the petal 6-ring of sumanene and IV-type aza-sumanene, proving again the similarity of these two molecules. The presence of N atom within the 5-membered ring of I-, II- and III-aza-sumanenes promotes an increase in their aromaticity.

A lower local aromaticity has been obtained for the 6-membered rings of III-aza-sumanene, result that is in good agreement with NICS(0) values. Concerning the calculated PDI values for the 6-membered rings, closer results to the standard PDI for benzene, 0.105, have been obtained for the 6-outer cycles of sumanene and IV-aza-sumanene. Lowest PDI values are attributed to the 6-core of I- and III-aza-sumanenes and correlate well with FLU and NICS(0) results.

Graphical representation of the Electron Localization Function is shown in Appendix (Figure A1); it outlines the similarity between the structures of sumanene and the aza-derivative IV, as well as the differences among the planar structure of aza-sumanene II and the other bowl-shaped compounds.

Table 4. FLU and PDI results for sumanene and its aza-derivatives

Compound	Cycles	FLU	PDI
Sumanene	core	0.034	0.030
	6-ring	0.008	0.082
	5-ring	0.054	-
I-aza-sumanene	core	0.032	0.029
	6-ring	0.012	0.068
	5-ring	0.039	-
II-aza-sumanene	core	0.021	0.046
	6-ring	0.034	0.041
	5-ring	0.033	-
III-aza-sumanene	core	0.059	0.015
	6-ring	0.039	0.041
	5-ring	0.030	-
IV-aza-sumanene	core	0.034	0.030
	6-ring	0.009	0.082
	5-ring	0.057	-

4. Reactivity indices

In order to investigate the effect of N incorporation on the reactivity of carbon atoms, the condensed Fukui functions (for an electrophilic attack) have been computed (numbering of atoms in the aza-patches is shown in Figure 4).

Sumanene [6.(5,6)₃]
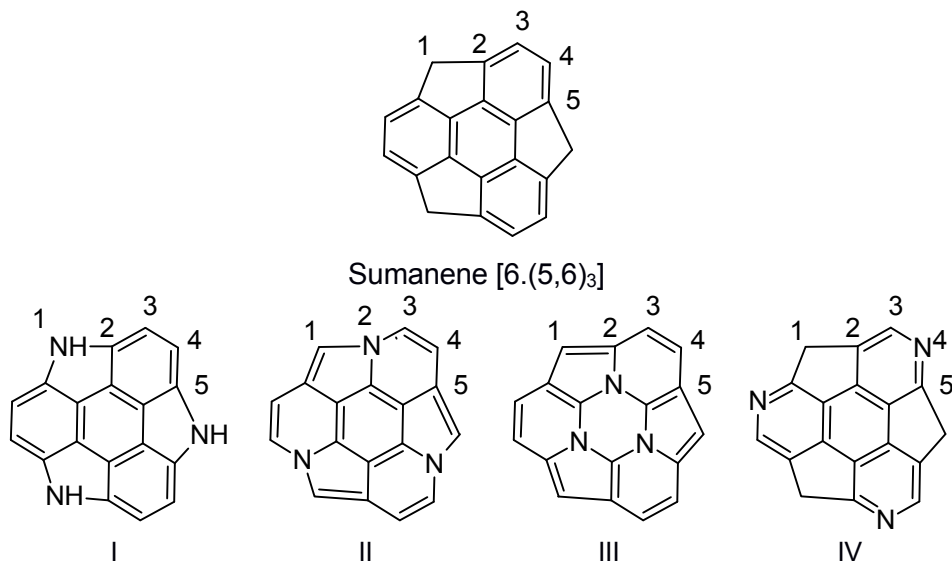
Figure 4. Atom numbering of sumanene and aza-sumanene moieties

The results, listed in Table 5, show an increased reactivity only for the C atoms from structure III, less significant results being obtained for the compounds where the N atom is placed in "outer" rings.

Table 5. Condensed Fukui functions computed for an electrophilic attack

f_- (HOMO)	Sumanene	I-aza	II-aza	III-aza	IV-aza
1	0.370	-	0.078	0.272	0.066
2	0.174	0.078	0.003	0.227	0.094
3	0.182	0.106	0.010	0.055	0.060
4	0.054	0.127	0.002	0.215	-
5	0.149	0.184	-	0.431	0.053

5. Global parameters of the investigated fullerenes: HOMO-LUMO gap, singlet-triplet gap and cohesive energy.

Keeping in mind the above-mentioned aza-patches, the structures including these patches in the molecule of C_{52} fullerene (isomer with four joint sumanene patches, D2 symmetry), namely aza-fullerenes $C_{49}N_3$ have been designed.

C_{52}

| I | II | III | IV |
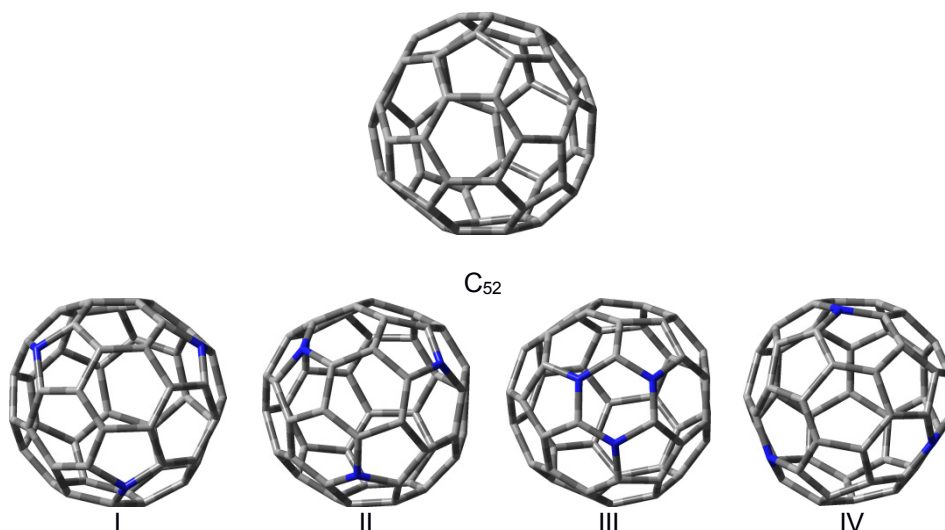
Figure 5. Optimized geometry (B3LYP/6-311G) of C_{52} and $C_{49}N_3$ fullerenes

Computation of global parameter HOMO-LUMO gap for both sumanene and C_{52} derivatives has shown that, the III-aza substitution leads to the less stable compounds (Table 6). The trend within the sumanene series follows the results of magnetic and geometric indices, which outlined the similarities between the all-carbon compound and the IV-aza substitution.

Table 6. HOMO-LUMO gap of sumanene and C_{52}, and of their aza-derivatives

HL gap (eV)	Sumanene	C_{52}
All carbon	4.63	1.09
I	3.94	0.89
II	3.62	0.89
III	3.47	0.62
IV	4.63	0.91

Regarding the C_{52} derivatives, smaller difference appear among C_{52} and $C_{49}N_3$ characterized by I-, II- and IV-aza-substitution.

Computation of the singlet-triplet ST gap, another important parameter for characterizing nanomaterials, shown a significant decrease for the N-substituted fullerenes and especially for the III $C_{49}N_3$ (Table 7).

Table 7. ST gap of C_{52} and $C_{49}N_3$ compounds (B3LYP/6-311+G(d))

Compound	ST gap (eV)
C_{52}	0.257
$C_{49}N_3$ (I)	0.049
$C_{49}N_3$ (II)	0.060
$C_{49}N_3$ (III)	0.008
$C_{49}N_3$ (IV)	0.061

Another parameter that is widely used for characterizing the stability of nanomaterials, like fullerenes, is the cohesive energy, calculated according to the equation:

$$E_{coh\ (at)} = -(E_{total} - n_C E_C - n_N E_N)/(n_C + n_N)$$

The results listed in Table 8 suggest no differences among the four types of aza-substitution herein proposed; however, with respect to the homo-sumanene, the aza-substitution seems to decrease the cohesive energy.

Table 8. Cohesive energy computed for C_{52} and $C_{49}N_3$ fullerenes

Compound	E_{coh} (a.u.)
C_{52}	0.307
$C_{49}N_3$ (I)	0.282
$C_{49}N_3$ (II)	0.282
$C_{49}N_3$ (III)	0.280
$C_{49}N_3$ (IV)	0.280

6. Properties of aza-fullerenes $C_{49}N_3$: polarizability, hyperpolarizability, magnetizability and dipole moment

Properties like polarizability and hyperpolarizability, magnetizability and the dipole moment, playing an important role in the behaviour of nanomaterials, are significantly influenced by the four types of aza-substitution (Table 9).

Table 9. Polarizability, hyperpolarizability magnetizability and dipole moment of the aza-fullerenes (BLYP/TZ2P)

Compound	Polarizability (a.u.)	Hyperpolarizability (a.u.)	Magnetizability (a.u.)	Dipole moment
$C_{49}N_3$ (I)	459.19	563.39	-191.26	0.579
$C_{49}N_3$ (II)	465.18	546.07	-211.26	1.307
$C_{49}N_3$ (III)	472.25	674.61	-250.99	2.112
$C_{49}N_3$ (IV)	469.64	521.93	-209.82	1.465

Also, two types of atomic charges, namely CM5 and the Voronoi Density Deformation (VDD) charges, have been computed. The atomic charges CM5 [33] (Charge Model 5) show an increased accuracy in predicting the dipole moment and are based on the Hirshfeld analysis combined with a parametrization method. The VDD method [34, 35] relies on the dividing of space into non-overlapping atomic areas and the consequent calculation of the deformation density of these cells. Figure A2 (see Appendix) depicts only the charge values of the nitrogen atoms.

CONCLUSIONS

The influence of aza-substitution in sumanene and C_{52} fullerene on their stability/aromaticity was investigated; a bowl-shaped polycyclic aromatic hydrocarbon, four aza-substitution types derived from the structures of pyrrole, indolizine and pyridine have been considered. Structures of aza-fullerenes $C_{49}N_3$, where the aza-substitution follows the same pattern as in case of sumanene, have been optimized and a series of global parameters were computed for their characterization. Calculation of the local aromaticity indices like NICS and HOMA, as well as delocalization indices PDI and FLU outlined the enhanced aromatic character of sumanene derivatives where the 5-membered ring was replaced by a pyrrole moiety (I-aza-substitution type). Also, an increase of the aromaticity has been obtained for the II-aza-sumanene, where the outer 5- and 6-membered rings have a common nitrogen atom at the outer junction (similar to the indolizine ring). No significant variations of aromaticity (compared to the values obtained for the all-carbon sumanene) have been obtained for the structure IV (where the aza-substitution occurs as in the pyridine moiety).

The proposed structures of fullerenes $C_{49}N_3$ were characterized by smaller HL gap and singlet-triplet gap for the III-$C_{49}N_3$ structure, while the computations of cohesive energy lead to similar values for all the four investigated fullerenes. As an overall conclusion, the III-aza patch seems to induce the most reactivity among all the studied aza-containing structures.

COMPUTATIONAL DETAILS

All the computations regarding the sumanene and its derivatives have been carried out at B3LYP/6-311+G(d) level of theory. Geometry optimization and vibrational analysis of the fullerene C_{52} and the corresponding aza-derivatives have been performed by using the basis set 6-311G. The obtained

structures were refined by performing a single point computation at B3LYP/6-311+G(d) level of theory. The calculations of the magnetic index, reactivity descriptors, and delocalization indices were performed by means of the same combination B3LYP/6-311+G(d). The delocalization indices were computed with Multiwfn_3.3.4 software [23], while Gaussian 09W [24] has been employed for the computations of sumanene and its aza-derivatives, as well as for the geometry optimizations of the C_{52} and $C_{49}N_3$. ADF2014 software [25-27] has been employed for the calculation of polarizability [28,29], hyperpolarizability [30,31], magnetizability [32] and dipole moment. Also, the atomic charges CM5 [33] and VDD [34,35] have been computed by means of ADF2014. For the computations performed with the ADF2014 software, the combination of BLYP with basis set TZ2P [36] has been used.

REFERENCES

1. G.K. Gueorguiev, J. Neidhardt, S. Stafstrom, L. Hultman, *Chemical Physics Letters*., **2005**, *410*, 228.
2. T. N. Gribanova, N.S. Zefirov, V. I. Minkin, *Pure and Applied Chemistry*., **2010**, *82(4)*, 1011.
3. R.B. dos Santos, R. Rivelino, F. de Brito Mota, G.K. Gueorguiev, *Physical Review B*, **2011**, *84*, 075417.
4. P.A. Denis, Journal of *Molecular Structure*: THEOCHEM, **2008**, *865*, 8.
5. L. Forro, L. Mihaly, *Reports on Progress in Physics*, **2001**, *64*, 649.
6. H. Bai, W. Ji, X. Liu, L. Wang, N. Yuan, Y. Ji, *Journal of Chemistry*, **2013**, 571709.
7. P. Ayala, R. Arenal, M. Rummeli, A. Rubio, T. Pichler, *Carbon*, **2010**, *48*, 575.
8. A. Rockenbauer, G. Csany, F. Fulop, S. Garaj, L. Korecz, R. Lukacs, F. Simon, L. Forro, S. Pekker, A. Janossy, *Physical Review Letters*, **2005**, *94*, 066603.
9. S. Erkoc, Journal of *Molecular Structure: THEOCHEM*, **2004**, *684*, 117.
10. R.J.C. Batista, M.S.C. Mazzoni, H. Chacham, *Chemical Physics Letters*, **2006**, *421*, 246.
11. L. Viani, M. C. dos Santos, *Solid State Communications*. **2006**, *138*, 498.
12. M.Z. Kassaee, F. Buazar, M. Koohi, *Journal of Molecular Structure*: THEOCHEM, **2010**, *940*, 19.
13. A.-R. Nekoei, S. Haghgoo, *Computational and Theoretical Chemistry*, **2015**, *1067*, 148.
14. Y. Ma, A.S. Foster, A.V. Krasheninnikov, R.M. Nieminen, *Physical Review B*, **2005**, *72*, 205416.
15. K.P. Prathish, M.M. Barsan, D. Geng, X. Sun, C.M.A. Brett, *Electrochimica Acta*, **2013**, *114*, 533.
16. P. Nath, S. Chowdhury, D. Sanyal, D. Jana, *Carbon*, **2014**, *73*, 275.
17. R. Pop, M. Medeleanu, M.V. Diudea, B. Szefler, J. Cioslowski, *Central European Journal of Chemistry*, **2014**, *12(1)*, 90.
18. R. Pop, M. Medeleanu, M.V. Diudea, B. Szefler, J. Cioslowski, *Central European Journal of Chemistry*, **2013**, *11(4)*, 527.

19. R. Pop, M. Andoni, Iulia Pausescu, Mihai Medeleanu, *Revista de Chimie,* **2013**, *64(9)*, 942.
20. R. Pop, J. Van Staden, M. Diudea, *Z. Naturforschung A*, **2015**, *70(3)*, 171.
21. R. Pop, M. Diudea, M. Medeleanu, M. Andoni, *Studia Universitatis Babes-Bolyai Chemia*, **2015**, *60(1)*, 195.
22. R. Pop, M. Andoni, J. Van Staden, I. Păuşescu, M. Medeleanu, *Digest Journal of Nanomaterials and Biostructures*, **2013**, *8(4)*, 1739.
23. T. Lu, F.J. Chen, *Journal of Computational Chemistry*, **2012**, *33*, 580.
24. Gaussian 09, Revision B.01, M.J. Frisch, G.W. Trucks, H.B. Schlegel, G.E. Scuseria, M.A. Robb, J.R. Cheeseman, G. Scalmani, V. Barone, B. Mennucci, G.A. Petersson, H. Nakatsuji, M. Caricato, X. Li, H.P. Hratchian, A.F. Izmaylov, J. Bloino, G. Zheng, J.L. Sonnenberg, M. Hada, M. Ehara, K. Toyota, R. Fukuda, J. Hasegawa, M. Ishida, T. Nakajima, Y. Honda, O. Kitao, H. Nakai, T. Vreven, J.A. Montgomery, Jr., J.E. Peralta, F. Ogliaro, M. Bearpark, J.J. Heyd, E. Brothers, K.N. Kudin, V.N. Staroverov, T. Keith, R. Kobayashi, J. Normand, K. Raghavachari, A. Rendell, J.C. Burant, S.S. Iyengar, J. Tomasi, M. Cossi, N. Rega, J.M. Millam, M. Klene, J.E. Knox, J.B. Cross, V. Bakken, C. Adamo, J. Jaramillo, R. Gomperts, R.E. Stratmann, O. Yazyev, A.J. Austin, R. Cammi, C. Pomelli, J.W. Ochterski, R.L. Martin, K. Morokuma, V.G. Zakrzewski, G.A. Voth, P. Salvador, J.J. Dannenberg, S. Dapprich, A.D. Daniels, O. Farkas, J.B. Foresman, J.V. Ortiz, J. Cioslowski, and D.J. Fox, Gaussian, Inc., Wallingford CT, 2010.
25. G. Te Velde, F.M. Bickelhaupt, E.J. Baerends, C. Fonseca Guerra, S.J.A. van Gisbergen, J.G. Snijders and T. Ziegler, *Journal of Computational Chemistry*, **2001**, *22*, 931.
26. C. Fonseca Guerra, J.G. Snijders, G. Te Velde, E.J. Baerends, *Theoretical Chemistry Accounts*, **1998**, *99*, 391.
27. ADF2014, SCM, Theoretical Chemistry, Vrije Universiteit, Amsterdam, The Netherlands*, http://www.scm.com.*
28. S.J.A. van Gisbergen, J.G. Snijders, E.J. Baerends, *Journal of Chemical Physics*, **1995**, *103*, 9347.
29. S.J.A. van Gisbergen, J.G. Snijders, E.J. Baerends, *Computer Physics Communications*. **1999**, *118*, 119.
30. S.J.A. van Gisbergen, J.G. Snijders, E.J. Baerends, *Journal of Chemical Physics*, **1998**, *109*, 10644.
31. S.J.A. van Gisbergen, J.G. Snijders, E.J. Baerends, *Physical Review Letters*, **1997**, *78*, 3097.
32. M. Krykunov, J. Autschbach, *Journal of Chemical Physics*, **2007**, *126*, 24101.
33. A.V. Marenich, S.V. Jerome, C.J. Cramer, D.G. Truhlar, *Journal of Chemical Theory and Computation*, **2012**, *8*, 527.
34. G. Te Velde, Numerical integration and other methodological aspects of band structure calculations, in Chemistry. 1990, Vrije Universiteit: Amsterdam.
35. C. Fonseca Guerra, J.-W. Handgraaf, E. J. Baerends, F. M. Bickelhaupt, *Journal of Computational Chemistry,* **2004**, *25*, 189.
36. E. van Lenthe, E.J. Baerends, *Journal of Computational Chemistry*, **2003**, 24, 1142.

APPENDIX

sumanene

I-aza-sumanene

II-aza-sumanene

III-aza-sumanene

IV-aza-sumanene
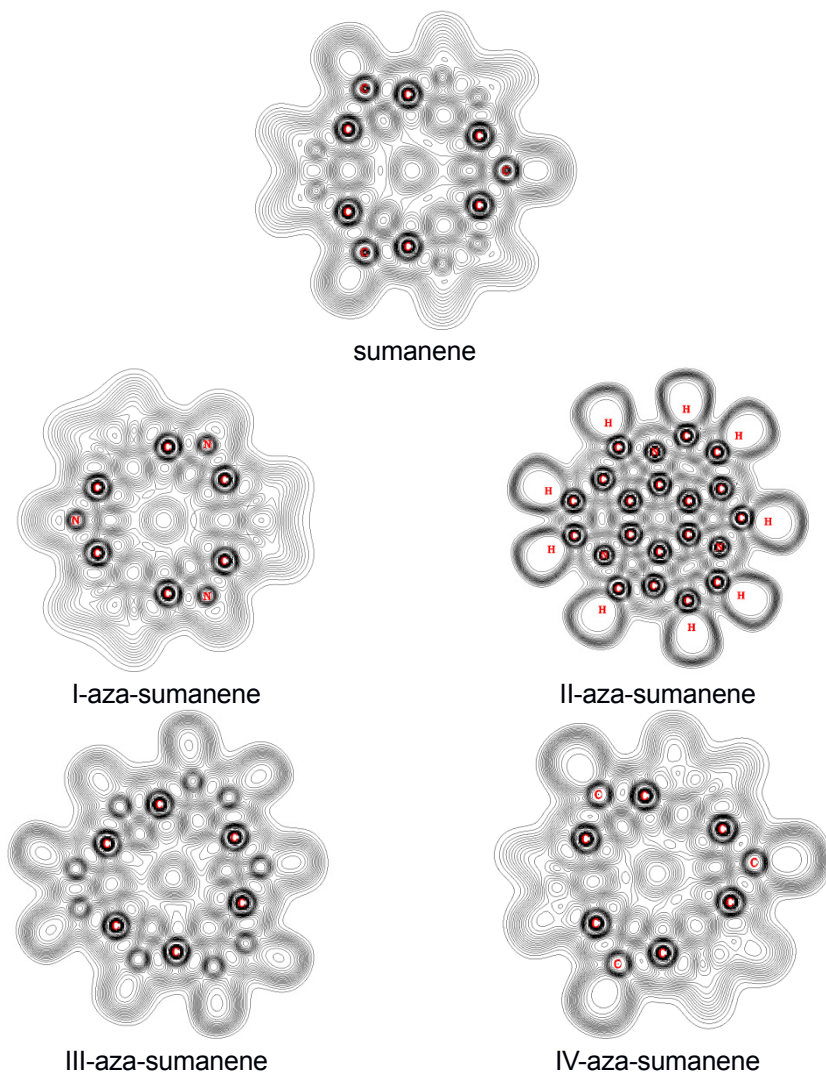
Figure A1. ELF (Electron Localization Function) computed for sumanene
and the four aza-derivatives
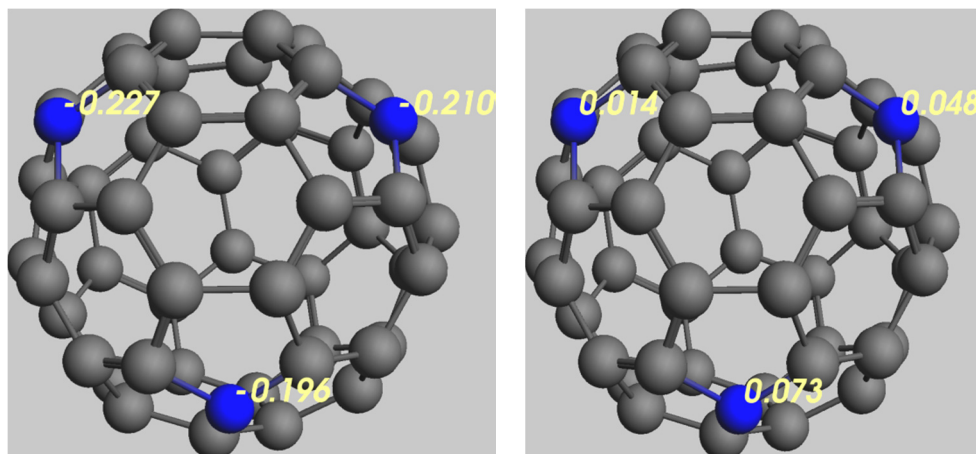
Atomic charges CM5 (left) and VDD (right) computed for $C_{49}N_3$ (I)
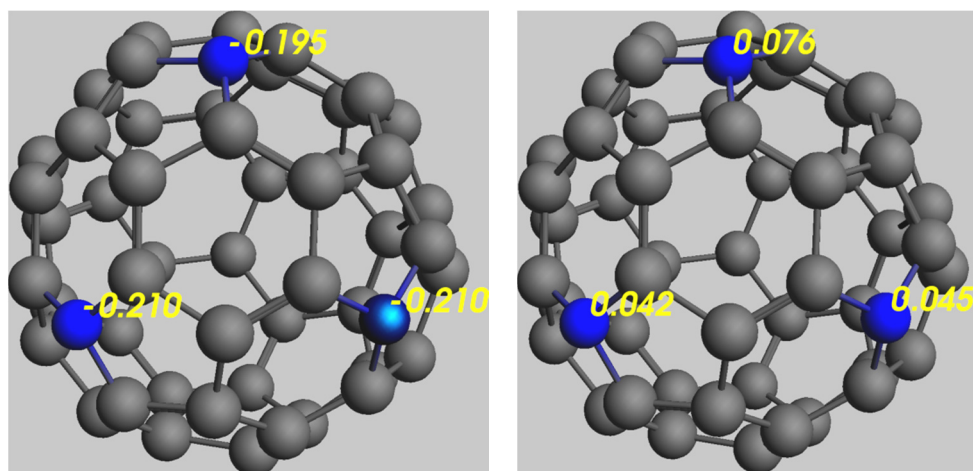
Atomic charges CM5 (left) and VDD (right) computed for $C_{49}N_3$ (II)

Figure A2. CM5 atomic charges of the aza-fullerenes
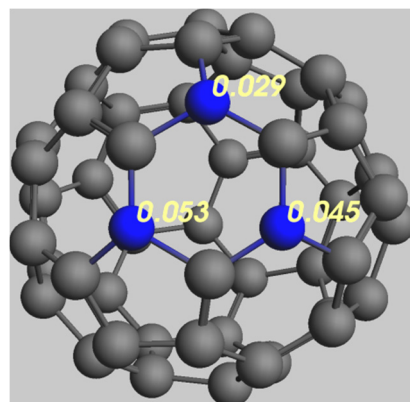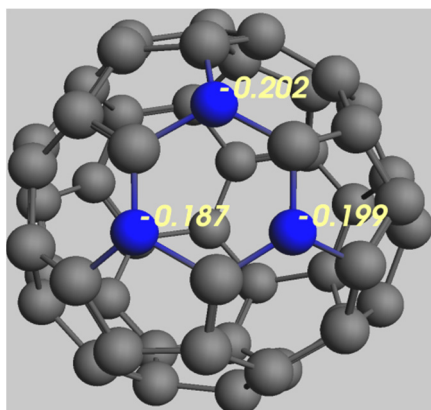
Atomic charges CM5 (left) and VDD (right) computed for $C_{49}N_3$ (III)
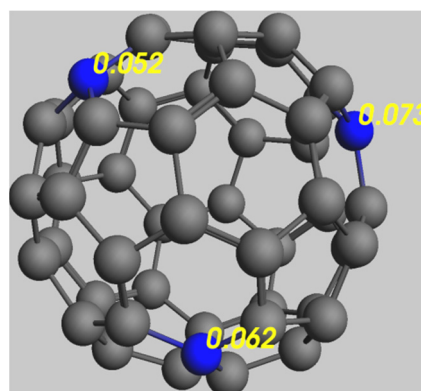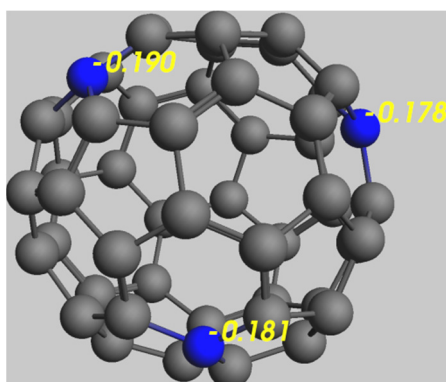
Atomic charges CM5 (left) and VDD (right) computed for $C_{49}N_3$ (IV)

Figure A2 (continued). CM5 atomic charges of the aza-fullerenes

ELECTROCHEMICAL OXIDATION OF
10*H*-PHENOTHIAZINE-1-CARBOXYLIC ACID

**ANA-MARIA SĂCARĂ[a], CASTELIA CRISTEA[a], TAMAS LOVASZ[a],
DAN PORUMB[a], EVA MOLNAR[a] and LIANA MARIA MURESAN[a*]**

ABSTRACT. The electrochemical behavior of 10*H*-phenothiazine-1-carboxylic acid was investigated by square wave anodic stripping voltammetry (SWASV) at a glassy carbon electrode, which evidenced the first monoelectronic oxidation step at low potentials (around 0.25 V), slightly modulated by the nature of the solvent. The effect of three different solvents (acetonitrile, dimethyl sulfoxide and chloroform) on the strength of intramolecular hydrogen bonding associations was evidenced by DFT calculations. The computed electron density at the heterocyclic nitrogen atom appeared well correlated to the recorded oxidation potential. The possibility to use of 10*H*-phenothiazine-1-carboxylic acid as potential mediator for electrochemical detection of Malachite Green was explored, but the phenothiazine derivative appeared not suitable for the detection of the dye.

Keywords: 10H-phenothiazine-1-carboxylic acid, SWASV, intramolecular hydrogen bonds

INTRODUCTION

A significant characteristic of phenothiazine derivatives appeared to be their ability to readily generate various oxidation products under chemical, photochemical, enzymatic, or electrochemical conditions. The redox properties of several phenothiazine derivatives with important medicinal applications were largely exploited in analytical procedures tailored for the advanced detection of phenothiazine based neuroleptic drugs [1,2]. The electrochemical oxidation of phenothiazine and its derivatives proceeds on conventional

[a] *Babeş-Bolyai University, Faculty of Chemistry and Chemical Engineering, 11 Arany Janos str., RO-400028, Cluj-Napoca, Romania*
* *Corresponding author: limur@chem.ubbcluj.ro*

electrodes (Pt, glassy carbon electrode and Au) either in organic or in aqueous acidic medium. The oxidation of the phenothiazine core takes place by the intermediate stage of radical cation with a stability influenced by the nature and position of the substituents on the heterocyclic core, the acidity and the presence of various salts in the reaction medium. Further oxidation steps imply the formation of the phenothiazinium cation which usually generates a colorless phenothiazine sulfoxide, colored hydroxy-substituted or polymeric derivatives [3]. Based on the reversibility of its first monoelectronic redox process, phenothiazine was described to be an efficient mediator in various electrochemical oxidation processes. For instance, it displayed excellent electrochemical catalytic activities for oxidase enzymes (glucose, lactate and cholesterol oxidase) even when immobilised on the surface of the electrode [4,5] and enzyme glucose dehydrogenase [6]. Several phenothiazine derivatives, were studied as electron transfer mediators in different electrochemical systems [7,8]. On the other hand, a series of 1-carboxyphenothiazine derivatives was synthesized and characterized [9], but there are no reported evidences for their utility as mediators for electrochemical systems.

Considering our previous interest in the electrochemical detection of Malachite Green (MG) [10], the aim of this work was to explore the electrochemical reactivity of 10*H*-phenothiazine-1-carboxylic acid and its potential as mediator for the electrochemical detection of the dye. Based on the electrostatic attraction between a carboxy functionality attached to the phenothiazine core and the positively charged MG cationic dye, it was expected that the diffusion/adsorption of the dye to a carboxyphenothiazine modified electrode surface would be facilitated.

RESULTS AND DISCUSSION

10*H*-Phenothiazine-1-carboxylic acid **1** was synthesized by optimizing a previously reported synthetic protocol [9] based on the thiation of N-phenyl-antranilic acid (scheme 1).
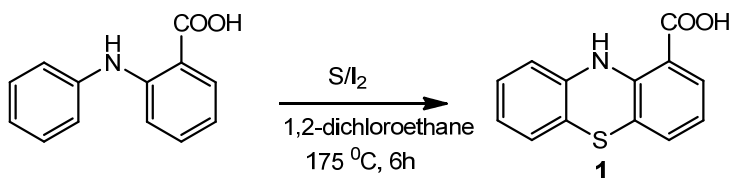
Scheme 1

The structure of **1** was confirmed by spectroscopic methods. ^{1}H-NMR spectrum of **1** displayed a deshielded signal characteristic to the acidic proton situated at 10.15 ppm, accompanied by the signals of aromatic protons situated in the region 6.7-7.6 ppm.

The position of the carboxyl group in the neighborhood of the heterocyclic NH group favors the formation of intramolecular hydrogen bonds. Density functional theory (DFT) calculations were applied to emphasize the possible intramolecular hydrogen bond formation. Thus, the structure of **1** was initially optimized using Spartan 06 with DFT B3LYP 6-31 G* method in gas phase. Free rotation of the carboxyl substituent generated two conformers of **1** with computed minimal energy which are presented in Figure 1. Conformer **1a** is characterized by hydrogen bond interaction between heterocyclic NH and carboxyl substituent, while conformer **1b** does not contain a hydrogen bond.

1a   **1b**
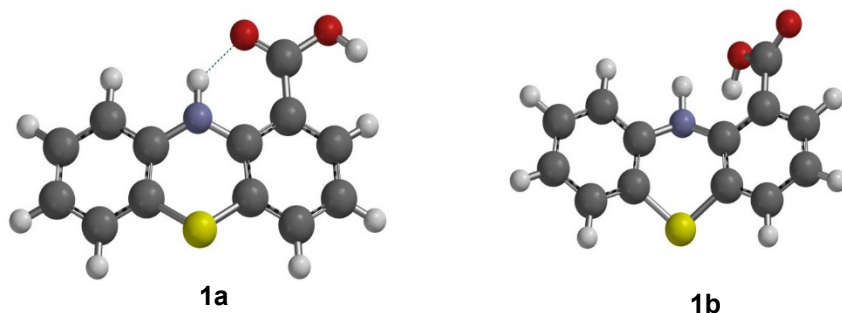
Figure 1. Conformers of 10*H*-phenothiazine-1-carboxylic acid **1**
with optimized geometry

Due to the fact that solvents may influence the hydrogen bonding [11], conformer **1a** has been optimized by B3LYP/6-31++G(d,p) Gaussian method using three data sets for the following solvents: acetonitrile, chloroform and DMSO. The results are illustrated in Table 1.

As it may be seen from table 1, **1a** appears to be more stable than **1b** (molecular energy difference 5.25 kcal/mole in gas phase) and the interactions with the aprotic dipolar solvents suggested further stabilization effects upon **1a.**

Square wave anodic stripping voltammetry experiments were performed in order to explore the electrochemical reactivity of 10*H*-phenothiazine-1-carboxylic acid dissolved in three different solvents and deposited on the surface of a glassy carbon electrode. The voltammograms presented in Figure 2 are showing well defined oxidation peaks corresponding to phenothiazine radical cationic species.

Table 1. Gaussian B3LYP/6-31++G(d,p) computational results for 10*H*-phenothiazine-1-carboxylic acid: optimized geometry, molecular energy (E) and electrostatic charge on heterocyclic nitrogen atom in gas phase and different solvents

Conformer	Environment	E (kcal/mol)	Electrostatic charge on N atom
1b	Vacuum	-692898.748	-0.709
1a	Vacuum	-692904.000	-0.630
	Acetonitrile	-693049.921	0.126
	Chloroform	-693047.637	0.132
	DMSO	-693050.015	0.125

a

b
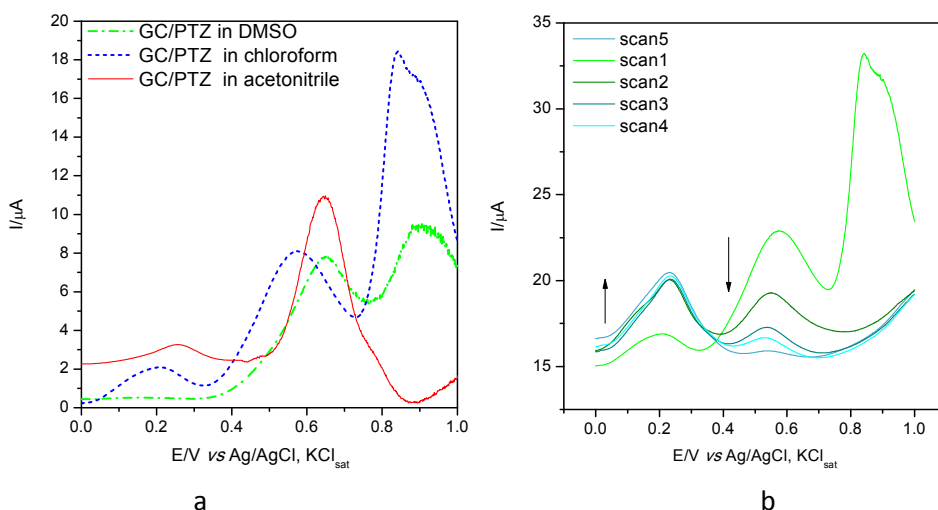
Figure 2. SWASV at glassy carbon (GC) electrodes modified with 10*H*-phenothiazine-1-carboxylic acid (PTZ) a) in different solvents; b) several scans in acetonitrile. Experimental conditions: pH=3, accumulation time 300 s; frequency 25 Hz; potential oxidation processes interval 0-1 V.

In scheme 2 are described the oxidation steps proposed in order to assign the SWASV peaks observed in figure 2. The first monoelectronic oxidation step generates the radical cation **2** and the values of the typical potentials may be correlated to the computational results related to electron density at the heterocyclic nitrogen atom presented in table 1. The lowest oxidation potential (0.25 V) may be assigned to **1a** characterized by higher electron density as compared to **1b,** which in turn may be responsible for the oxidation peak situated at 0.55 V. Further step requires a higher oxidation potential and generates the cation **3** which may end up as a colourless sulfoxide **4**. As it may be seen in figure

2b, after several scans the intensity of the first oxidation peak increases (maybe due to the reversibility of the oxidation processes of **1a**)**,** while the oxidation of **1b** proceeding towards the chemical reaction may explain the consumption of the radical cationic species **2b** and consequently the decrease in intensity of the second oxidation peak.
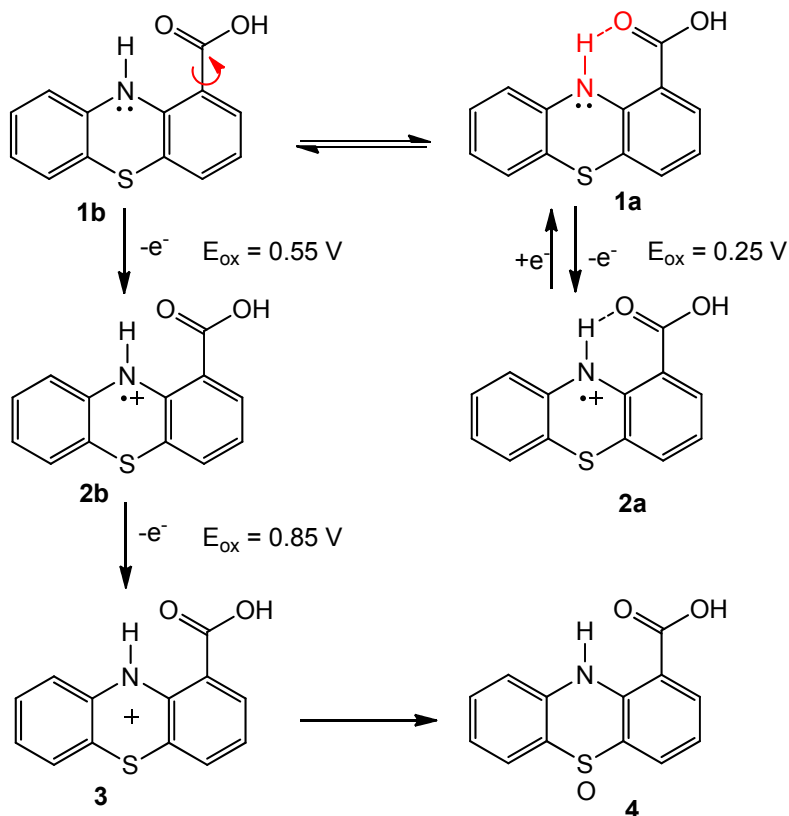
Scheme 2

A characteristic signal of the sulfoxide was recorded by ^{1}H-NMR (in deuterated acetonitrile solution) at chemical shift 11.65 ppm.

The SWASV experiments performed in the presence of MG indicated a decrease in intensity of the first oxidation peak (figure 3a), which may be correlated to steric interactions between **1** and the bulky cationic dye in control for weakening the intramolecular hydrogen bond associations. Calibration curves presented in figure 3b indicate a feeble correlation with the MG concentration and do not sustain the possibility of elaborating an analytical procedure for MG detection.

a   b
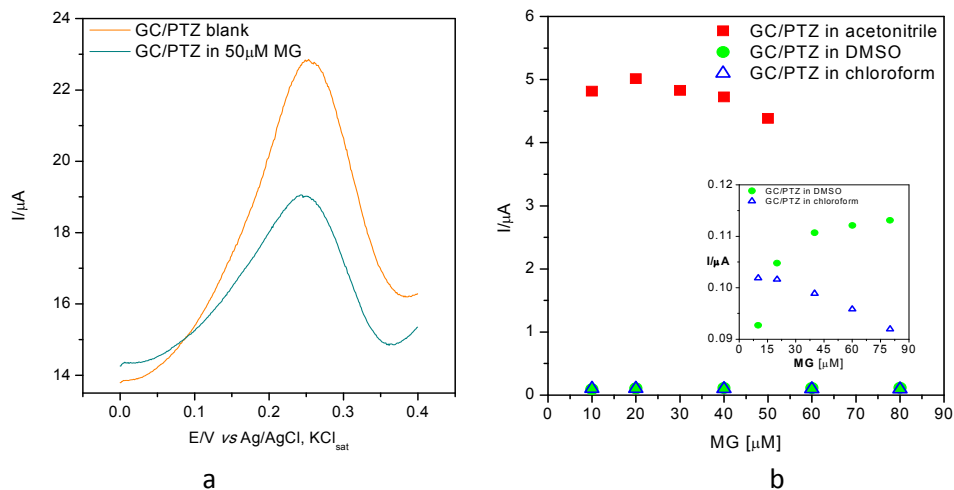
Figure 3. SWASV at GC/10H-phenothiazine-1-carboxylic acid (PTZ) electrodes:
a) in the presence of malachite green (MG). b) Calibration curves obtained for increasing
amounts of MG. Experimental conditions: accumulation time 300 s; frequency 25 Hz;
potential interval 0-0.4 V; electrolyte phosphate buffer (pH 3).

CONCLUSIONS

The oxidation potential of 10*H*-phenothiazine-carboxilic acid appeared to
be lowered by intramolecular hydrogen bond associations. The first monoelectronic
oxidation step generating the radical cation occurred around 0.25 V, this
value being slightly modulated by the nature of the solvent.

No favourable interactions between MG and 10*H*-phenothiazine-carboxilic
acid occurred and, consequently the tested electrochemical system based on
GC/10*H*-phenothiazin-carboxilic acid is not suitable for the detection of MG.

EXPERIMENTAL SECTION

Chemicals

All the chemicals used for the experiments in this study were of analytical
grade quality and were used as received, without further purification or alteration.

Malachite Green oxalate salt was purchased from Penta, Czech Republic
and all solutions were made in pH 3 phosphate buffer (PB). Phosphate buffer
solution was made starting from $NaH_2PO_4 \cdot H_2O$ and Na_2HPO_4 salts and pH
adjusted with *o*-H_3PO_4 acid, all from Merck, Germany.

10H-Phenothiazine-1-carboxylic acid 1 preparation

N-phenylanthranilic acid 6.4 g (0.03 mole), sulfur powder 1.92 g (0.06 mole) and iodine 0.8 g (0.006 mole) were dissolved in 60 ml 1,2-dichlorobenzene. The reaction mixture was heated at 175 °C for 6 h under constant stirring. After cooling at room temperature, 10 ml solution of sodium thiosulphate 40% was added to the reaction mixture. The organic layer was separated and the organic solvent was removed by vacuum distillation. The product was purified by column chromatography on silica gel using eluent toluene to give orange coloured 10*H*-phenothiazine-1-carboxylic acid (1.4 g, yield 19%). M.p. 248 °C (lit. [9])

^{1}H NMR(DMSO-d_6, 400 MHz, ppm): 6,88-7,04 (m, 5H, Ar-H), 7,18 (d, 1H, Ar-H), 7,65 (d, 1H, Ar-H), 9,63(s, 1H, -N-H), 10,15 (s, 1H, -COOH)

Electrode preparation

Before conducting any measurements, the glassy carbon (GC) working electrode was thoroughly cleaned on a piece of felt with γ-alumina slurry until mirror-like shine aspect was obtained. In order to remove any traces of impurities, further cleaning was applied by sonication in acetone and distilled water respectively.

For modifying the electrode, saturated 10*H*-phenothiazine-1-carboxylic acid solutions were prepared, in three different solvents: chloroform, acetonitrile and dimethyl-sulfoxide. Each solution was applied by drop-casting on the electrode's active surface and allowed to dry freely. In the case of DMSO solutions, a warm air current was applied to accelerate the evaporation process. Constant 5μL volumes of solutions were employed for all electrode modification purposes. No other protective coatings were applied on the modified electrode as the evaporated phenothiazine carboxylic acid layer had a good stability during measurements in aqueous solutions.

Electrochemical measurements

All electrochemical experiments were performed on a Metrohm Autolab PGSTAT 302N, electrochemical workstation (Eco Chemie, Netherlands). A three-electrode system composed of a Ag/AgCl, KCl$_{sat}$ reference electrode, a platinum counter-electrode and a bare or modified glassy carbon (GC) working electrode was used. The electrolyte solution contained 0.1 M phosphate buffer adjusted with o-H_3PO_4 at pH 3. All experiments were performed at a room temperature of 25 °C.

REFERENCES

1. K. Madej, P. Koscielniak, *Critical Reviews in Analytical* Chemistry, **2008**, *38* 50.
2. K. Nesměrák V. Červený, J. Hraníček, P. Rychlovský, *Microchemical Journal,* **2013**, *106.* 226.
3. H. Puzanowska-Tarasiewicz, L. Kuzmicka, J. Karpinska, K. Mielech-Lucasiewicz, *Analytical Sciences,* **2005**, *21*, 1149.
4. A.N. Sekretaryova, M.Yu. Vagin, V. Beni, A.P.F. Turner, A.A. Karyakin, *Biosensors and Bioelectronics*, **2014**, *53*, 275;
5. J. Kulysa, T. Buch-Rasmussenb, K. Bechgaard, V. Razumasa, *Journal of Molecular Catalysts,* **1994,** 91, 407.
6. T Hoshino, S. Sekiguchi, H. Muguruma, *Bioelectrochemistry*, **2012**, *84*, 1.
7. B. Brunetti, P. Ugo, L.M. Moretto, C.R. Martin, *Journal of Electroanalytical Chemistry,* **2000**, *491*, 166.
8. H. Dai, H. Xu, X. Wu, Y. Lin, M. Wei, G. Chen, *Talanta, 2010*, *81, 1461.*
9. V.B. Kataria, M.J. Solanki, A.R. Trivedi, V.H. Shah, *Letters in Drug Design & Discovery*, **2013**, *10*(10), 951.
10. A. Sacara, C. Cristea, L.M. Muresan, *Journal of Electroanalytical Chemistry*, **2017**, *792*, 23.
11. J.L. Cook, C.A. Hunter, C.M.R. Low, A. Perez-Velasco, J.G. Vinter. *Angewandte Chemie International Ed.,* **2007**, *46*, 3706.

CHROMATOGRAPHIC ANALYSIS OF SOME ANTIBIOTICS IN WATER AND SEDIMENT SAMPLES COLLECTED FROM THE ROMANIAN TISZA RIVER WATERSHED

VIRGINIA COMAN[a]*, SIMION BELDEAN-GALEA[b], FLORINA COPACIU[a], MIHAELA VLASSA[a], MIUŢA FILIP[a]

ABSTRACT. Antibiotics are natural or semi-synthetic compounds used for many decades in human, veterinary and plant medicine to prevent and/or to treat bacterial infections and also to promote productivity in animal farming. Traces of antibiotics are found in waste, surface and ground waters, the main source of water pollution being considered waste waters from the industrial production, hospitals, livestock farms, households and incompletely metabolized drugs. The uncontrolled input of antibiotics in surface waters can lead to some unexpected health effects and to an increased resistance to these drugs.

The aim of this work consists in the monitoring of six antibiotics (Ampicillin, Amoxicillin, Penicillin G, Ceftazidime, Tetracycline and Doxycycline) in river waters and sediment samples from the Romanian Tisza River Watershed.

Solid-phase extraction (SPE) on Oasis HLB Waters cartridges was used for the isolation of antibiotics from water matrices and ultrasound-assisted extraction (USAE) followed by SPE for the sediment samples. Then, the antibiotics were analysed by high-performance liquid chromatography coupled with diode array detector or mass spectrometer (HPLC-DAD/MS). The developed SPE/USAE-HPLC-DAD/MS procedures were applied to monitor these antibiotics in river waters during thirteen months and to analyse them in some sediment samples. The obtained results showed the presence of Tetracycline, Doxycycline and Ceftazidime in the investigated samples.

Keywords: antibiotics, high-performance liquid chromatography, mass spectrometry, solid-phase extraction, ultrasound-assisted extraction, river waters, sediments

[a] *Babeş-Bolyai University, Raluca Ripan Institute for Research in Chemistry, 30 Fântânele str., Cluj-Napoca, Romania*
[b] *Babeş-Bolyai University, Faculty of Environmental Science and Engineering, 30 Fântânele str., RO-400294, Cluj-Napoca, Romania*
* Corresponding author: virginia.coman@ubbcluj.ro

INTRODUCTION

Antibiotics are natural or semi-synthetic compounds with antibacterial, antifungal or antiparasitical activity [1] used for preventing and treating human and animal diseases, different plant infections and also for advancing growth in livestock farms [2]. The amount of antibiotics released in the European Union environment might be approximately 15,000 tons/year. The main sources of antibiotic pollution come from the industrial production, hospitals, domestic use and their incomplete metabolism [3].

Due to the fact that antibiotics are not completely removed by the sewage treatment plants, they are released into the natural water courses [1] causing potential environmental risks and the extension of antibacterial resistance among the microorganisms [4].

Different studies showed that antibiotics are persistent and pseudo-persistent contaminants [5, 6] causing toxicological impacts on the fauna of natural water bodies [1] including synergistic and antagonistic combination effects [7].

In the aquatic matrices, the concentrations of antibiotics have values of micrograms per liter in hospital effluents and municipal waste waters, nanograms per liter in surface waters, ground water and sea water [8, 9], tens nanograms per grams in estuary and marine sediments [10, 11] and hundreds nanograms per grams in surface water sediments respectively [12, 13]. Consequently, to prevent the risks of environmental exposure, the monitoring of antibiotics that reach the environmental factors is recommended [14, 15].

Taking into consideration the low level of the antibiotic residues in the environmental matrices, the development of sensitive analytical methods for the extraction and the analysis of these compounds represents a major challenge. The most used methods for the extraction of antibiotics from water samples involve solid-phase extraction [6, 8, 9, 12, 13] and miniaturized liquid-phase or solid-phase extraction [16–18] and from sediment samples, ultrasound-assisted extraction [11, 13, 19].

For the analysis of antibiotics, liquid chromatography (LC) techniques coupled with ultraviolet/diode-array (UV/DAD) detector [9, 18], mass spectrometry (MS) detector [9, 20] or tandem MS/MS ones [5, 10–12, 20] were used. Good results have been also obtained by high-performance thin-layer chromatography [6] or capillary electrophoresis [16, 17] techniques.

The aim of this work consists in the monitoring of some classes of antibiotics (penicillins, tetracyclines, cephalosporins) widely used for the human and veterinary treatments in different river water and sediment samples collected from the Romanian Tisza River Watershed using solid-phase extraction (SPE) and ultrasound-assisted extraction (USAE) followed by liquid chromatography coupled with diode-array or mass spectrometry detector.

RESULTS AND DISCUSSION

Two analytical procedures, based on solid-phase extraction followed by high-performance liquid chromatography with diode array detector, respectively mass spectrometer (SPE-HPLC-DAD and SPE-LC-MS), have been developed for the analysis of six antibiotics (Amoxicillin – AMOX, Ceftazidime – CFZ Ampicillin – AMP, Tetracycline – TET, Doxycycline – DOXY and Penicillin G – PEN G) in river water samples collected from the three established monitoring points in the Romanian Tisza River Watershed. For the sediment samples, the ultrasound-assisted extraction was used for the isolation of the target compounds from the matrix followed by the SPE-HPLC-DAD procedure.

The HPLC separation tooks place in less then 12 minutes with very good resolution. For the DAD detection was necessary two wavelengths, 197 nm for penicillins (AMOX, AMP, PEN G) and 272 nm for tetracyclines (TET, DOXY) and ceftazidime (CFZ) (Figure 1).
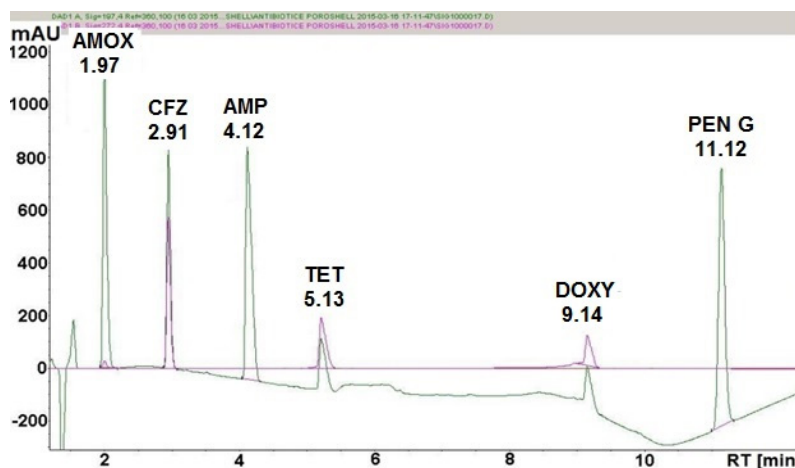
Figure 1. HPLC-DAD chromatogram of studied antibiotics

The developed HPLC-DAD method shows good linearity in the range of 5.21–166.7 µg/mL, correlation coefficients (r) exceeding 0.999 for all selected antibiotics, good repeatability (three replicates) measured for the 0.85 µg/mL concentration, low limit of detection (LOD) and limit of quantification (LOQ) in the range of µg/mL (Table 1). The LOD and LOQ were calculated taking into account the slope of each calibration curve and the corresponding standard deviation.

Table 1. Performances of the developed HPLC-DAD method

Antibiotic	Calibration curve equation	r	LOD [µg/mL]	LOQ [µg/mL]	Repeatability RSD [%]
Amoxicillin	Y = 50.42292X	0.99968	0.61	1.86	5.43
Ceftazidime	Y = 25.64547X	0.99999	0.18	0.57	11.39
Ampicillin	Y = 63.61580X	0.99996	0.25	0.75	9.31
Tetracycline	Y = 15.78180X	0.99970	0.70	2.14	4.55
Doxycycline	Y = 8.71137X	0.99735	0.75	2.29	8.48
Penicillin G	Y = 71.33844X	0.99971	0.25	0.79	9.74

For LC-MS analysis, the selected ion monitoring (SIM) mode was chosen in order to obtain a better sensitivity. In Figure 2, the chromatogram acquired in SIM mode is presented.
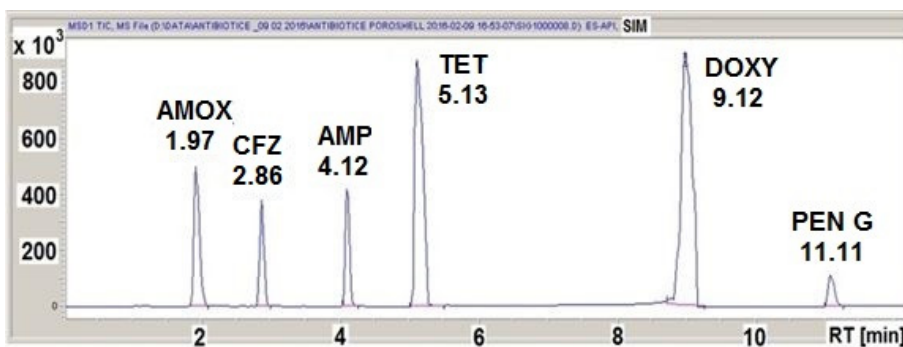
Figure 2. LC-ESI(+)-MS SIM chromatogram of studied antibiotics

The characteristic ion for each studied antibiotic was obtained by electrospray ionisation in positive mode (ESI(+)). In Figure 3 are presented the mass spectra (scan mode ranging from 100 to 1000 uam) and the *m/z* ions for the studied antibiotics.
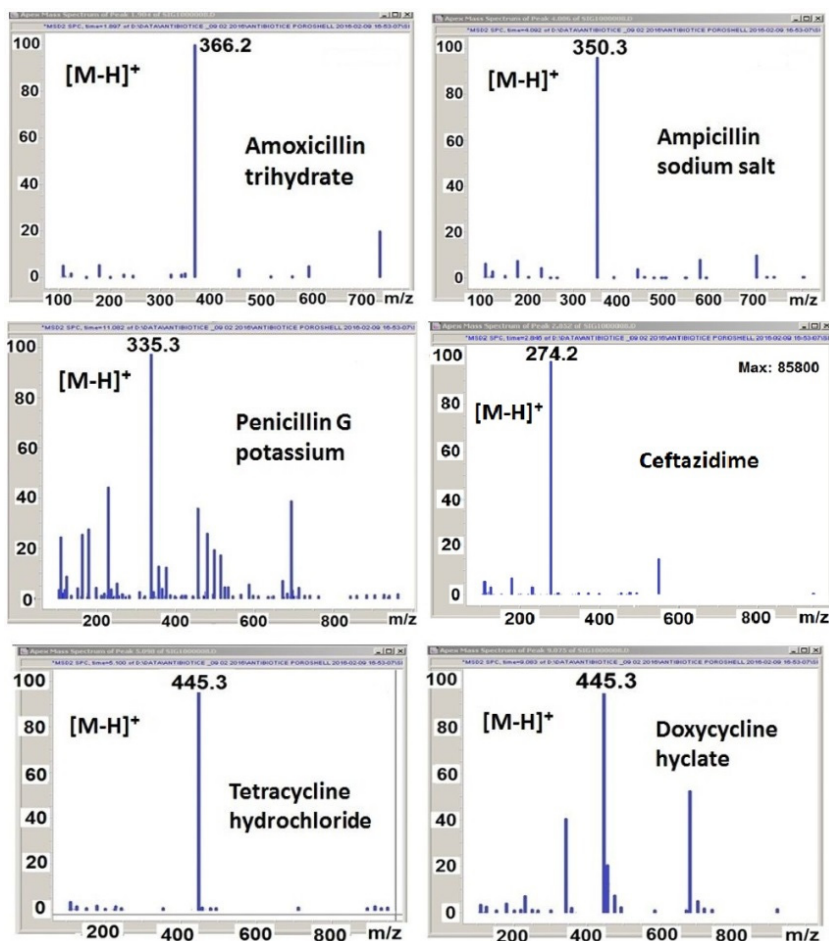
Figure 3. LC-ESI(+)-MS spectra of the studied antibiotics

The developed LC-ESI(+)-MS method shows good linearity in the range of 0.65–166.7 µg/mL, correlation coefficients (r) exceeding 0.99 for all selected antibiotics, good repeatability (three replicates) measured for the 0.85 µg/mL concentration, lower LOD and LOQ in the range of ng/mL (Table 2).

Comparing the two developed LC methods, differing only by detectors, one can observe that these methods have the same linearity (r > 0.99), but the LC-ESI(+)-MS method is ten to hundred times more sensitive than the HPLC-DAD method (Table 3).

Table 2. Performances of the LC-ESI(+)-MS method

Antibiotic	Calibration curve equation	r	LOD [µg/mL]	LOQ [µg/mL]	Repeatability RSD [%]
Amoxicillin	y = 17773.39271x + 115572.17582	0.99383	0.0210	0.0636	4.79
Ceftazidime	y = 11192.38273x + 59245.64014	0.99548	0.0196	0.0595	5.12
Ampicillin	y = 11725.36209x + 39962.45772	0.99654	0.0157	0.0475	3.70
Tetracycline	y = 45458.20719x + 38326.00614	0.99629	0.0178	0.0539	6.74
Doxycycline	y = 67695.85510x – 350854.03308	0.99608	0.0205	0.0622	6.00
Penicillin G	y = 3007.03091x + 36758.78717	0.99084	0.0315	0.0955	3.11

Table 3. Comparison of the performances of the developed methods: HPLC-DAD *versus* LC-ESI(+)-MS

Antibiotic	RT [min]		Correlation coefficient (r)		LOD [µg/mL]		LOQ [µg/mL]	
	DAD	MS	DAD	MS	DAD	MS	DAD	MS
Amoxicillin	1.97	1.97	0.99968	0.99383	0.61	0.021	1.86	0.064
Ceftazidime	2.91	2.86	0.99999	0.99548	0.18	0.019	0.57	0.059
Ampicillin	4.12	4.12	0.99996	0.99654	0.25	0.016	0.75	0.048
Tetracycline	5.13	5.13	0.99970	0.99629	0.70	0.018	2.14	0.054
Doxycycline	9.14	9.12	0.99735	0.99608	0.75	0.021	2.29	0.062
Penicillin G	11.12	11.11	0.99971	0.99084	0.25	0.032	0.79	0.096

However, LC-ESI(+)-MS method can be applied only for the analysis of samples of low complexity (water samples). In the case of complex (sediments) samples, HPLC-DAD method is recommended.

The accuracy has been tested only for Tetracycline and Doxycycline, considering that these antibiotics are the most prevalent in environmental samples. For this purpose, real river water samples were spiked with different amounts of Tetracycline and Doxycycline, and then extracted and analysed by SPE-LC-ESI(+)-MS procedure. The obtained results show good accuracy for both antibiotics, the recovery ranging between 95–100% (Table 4).

Table 4. Accuracy of the SPE-LC-ESI(+)-MS procedure

Antibiotic	Amount [µg/mL]			Recovery [%]	Mean recovery ± SD [%]
	Initial	Added	Found		
Tetracycline	0.58	0.46	1.08	103.84	100.31±3.09
			1.02	98.07	
			1.03	99.04	
	0.58	0.58	1.11	95.68	99.41±3.89
			1.20	103.44	
			1.15	99.13	
	0.58	0.69	1.30	102.36	99.20±4.17
			1.20	94.48	
			1.28	100.78	
Doxycycline	0.98	0.78	1.70	96.66	98.50±2.34
			1.78	101.13	
			1.72	97.72	
	0.98	0.98	1.94	98.98	97.26±1.57
			1.90	96.90	
			1.88	95.91	
	0.98	1.18	2.06	95.37	95.21±2.09
			2.10	97.22	
			2.01	93.05	

The developed SPE-LC-ESI(+)-MS procedure was applied for monitoring of selected antibiotics in the Romanian Tisza River Watershed during 13 months from July 2014 to September 2015, thus covering all four seasons. Our results show the presence of some antibiotics in the river water samples. The most common antibiotics found are in concentrations of µg/L as follows: Tetracycline in the range of 0.10–5.24, Doxycycline in the range of 0.11–2.46 and Ceftazidime in the range of 0.01–4.20 µg/L (Table 5). One can also observe that their concentrations are depending by the time and point of sampling.

Table 5. Antibiotics found in Tisza River Watershed analysed by
SPE-LC-ESI(+)-MS procedure

Sampling date	Sampling point	Antibiotics found and their amounts [μg/L]
July 2014	Vișeu (1)	Doxycycline (0.68), Ceftazidime (2.56)
	Iza (2)	Tetracycline (1.24), Ceftazidime (3.43)
	Tisza (3)	Doxycycline (2.40)
August 2014	Vișeu (1)	Not detected
	Iza (2)	Not detected
	Tisza (3)	Ceftazidime (4.20)
November 2014	Vișeu (1)	Doxycycline (0.11), Tetracycline (0.10)
	Iza (2)	Tetracycline (2.56), Ceftazidime (0.01)
	Tisza (3)	Tetracycline (0.82)
December 2014	Vișeu (1)	Tetracycline (0.11)
	Iza (2)	Tetracycline (0.56)
	Tisza (3)	Tetracycline (0.13)
January 2015	Vișeu (1)	Tetracycline (3.96)
	Iza (2)	Tetracycline (1.24), Doxycycline (0.23)
	Tisza (3)	Tetracycline (2.07)
February 2015	Vișeu (1)	Tetracycline (2.65)
	Iza (2)	Tetracycline (1.42), Doxycycline (0.19)
	Tisza (3)	Tetracycline (2.32)
March 2015	Vișeu (1)	Not detected
	Iza (2)	Not detected
	Tisza (3)	Tetracycline (3.07), Doxycycline (2.16), Ceftazidime (4.15)
April 2015	Vișeu (1)	Ceftazidime (4.19), Penicillin G (3.41)
	Iza (2)	Not detected
	Tisza (3)	Not detected
May 2015	Vișeu (1)	Not detected
	Iza (2)	Tetracycline (5.24)
	Tisza (3)	Penicillin G (4.67)
June 2015	Vișeu (1)	Tetracycline (1.47), Doxycycline (0.78)
	Iza (2)	Tetracycline (3.32), Ceftazidime (0.06)
	Tisza (3)	Tetracycline (1.83), Doxycycline (0.26), Ceftazidime (0.17)
July 2015	Vișeu (1)	Tetracycline (1.01), Doxycycline (0.94)
	Iza (2)	Tetracycline (0.03)
	Tisza (3)	Tetracycline (0.69), Doxycycline (0.19)
August 2015	Vișeu (1)	Tetracycline (0.49)
	Iza (2)	Tetracycline (0.60)
	Tisza (3)	Tetracycline (0.52)
September 2015	Vișeu (1)	Tetracycline (0.78), Doxycycline (0.36)
	Iza (2)	Tetracycline (0.47), Doxycycline (2.46)
	Tisza (3)	Tetracycline (1.88), Doxycycline (0.26), Ceftazidime (0.15)

A SIM chromatogram of an extract of a real river water sample is presented in Figure 4 where one can be observed the presence of Tetracycline and Doxycycline.

Figure 4. SIM chromatogram of a river water extract from
Vișeu River, Sampling point (1), July 2015

Regarding the sediment samples, the results showed the presence of Tetracycline in the range of 143.9 and 248.8 μg/kg and of Doxycycline in the range of 14.6 and 27.9 μg/kg (Table 6). These results are quite logical taking into account that these two antibiotics are the most prevalent in river water samples.

Table 6. Antibiotics found in sediment extracts from Tisza River
Watershed by USAE-SPE-HPLC-DAD procedure

Sampling date	Sampling point	Antibiotics found and their amounts [μg/Kg]
July 2015	Vișeu (1)	Tetracycline (143.9)
	Iza (2)	Tetracycline (156.8), Doxycycline (27.9)
	Tisza (3)	Tetracycline (248.8), Doxycycline (14.6)

CONCLUSIONS

Two analytical procedures, SPE-HPLC-DAD and SPE-LC-ESI(+)-MS, have been developed in order to determine some antibiotics in river water samples collected from the Romanian Tisza River Watershed (Vișeu, Iza and Tisza Rivers).

The developed procedures show good linearity and limits of detection and quantification, being applicable to the analysis of the selected antibiotics in real river water samples. SPE-LC-ESI(+)-MS is more suitable for the analysis of antibiotics in surface waters being more sensitive than HPLC-DAD.

The SPE-LC-ESI(+)-MS procedure has been applied to monitor the target antibiotics in river water samples collected during 13 months. The most found antibiotics were Tetracycline (0.10–5.24 μg/L), Doxycycline (0.11–2.46 μg/L) and Ceftazidime (0.01–4.20 μg/L). Also, Penicillin G was found two times (3.41 and 4.67 μg/L).

For the sediment samples, the USAE-SPE-HPLC-DAD procedure has been developed, based on the previous SPE-HPLC-DAD procedure.

In the analysed sediments, Tetracycline and Doxycycline in concentration of hundred, respectively tens μg/kg were found.

The presence of antibiotics in river waters is a growing environmental problem, therefore the periodical monitoring is recommended.

EXPERIMENTAL SECTION

Chemicals and materials

For the optimization of the extraction protocols and of the qualitative and quantitative analysis, a standard mixture containing the six selected antibiotics (Figure 5) was prepared. The considered antibiotic standards were commercial powders used for oral treatment (Amoxicillin trihydrate 500 mg per capsule with talcum and magnesium stearate as excipients, Tetracycline chlorhydrate 250 mg per capsule with lactose and magnesium stearate as excipients, and Doxycycline 100 mg per capsule as hyclate 119 mg with corn starch, magnesium stearate and talcum as excipients) or for injection (Ampicillin natrium salt 1 g per vial, Penicillin G potassium salt 1.000.000 U.I. per vial, and Ceftazidime 1 g per vial). The antibiotics were purchased from "Antibiotice" Romania (Amoxicillin, Ampicillin, Penicillin G, Tetracycline), "GlaxoSmithKline" Romania (Ceftazidime) and "Sandoz" Romania (Doxycycline).

Standard solutions in the concentration range of 0.65 to 166.7 ng/mL prepared by the dilution of standard mixture in Milli-Q water were used for calibration. Methanol and acetonitrile of HPLC grade purity and formic acid of 99.9% purity were purchased from Merck (Germany). The Milli-Q water was prepared using a Milli-Q Plus water system from Millipore (USA). Before injection, the samples were passed through Teknokroma syringe filters, PTFE 0.45 μm.
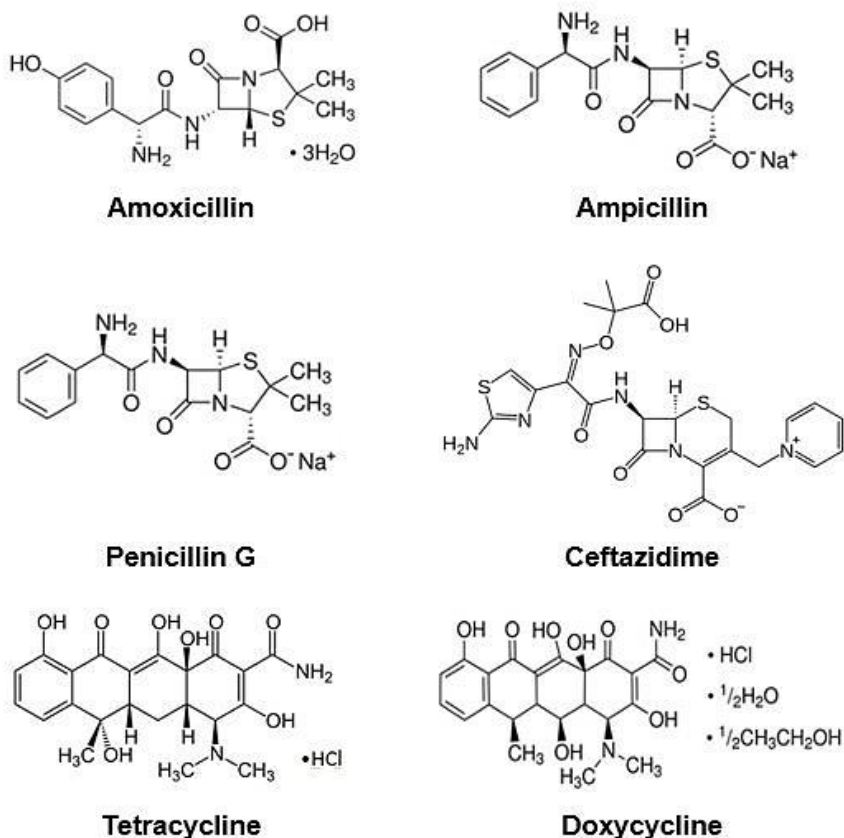
Figure 5. Structure formula of the studied antibiotics

Instrumentation and chromatographic separation

For the chromatographic analyses, an HPLC Agilent 1200 Series system, equipped with G1322A degasser, G1311A quaternary pump, G1329A autosampler, G1315D DAD detector, and G1316B TCC SL column thermostat and a LC-MS system model Agilent 1200 Series coupled with 6110 Quadrupole LC/MS detector with AP-ESI ionization were used. The chromatographic data were collected and processed by means of the ChemStation software.

The separation was carried out on Agilent Poroshell 120 EC-C18 column (4.6 × 150 mm, 2.7 μm) at a flow rate of 1.1 mL/min using a mobile phase consisting in a mixture of (A) acetonitrile and (B) 0.1% formic acid in water (*v/v*) operated under the following gradient (Table 7):

Table 7. Gradient elution used for the separation of target antibiotics

Time [min]	Mobile phase composition [%]	
	A: (Acetonitrile)	B: (0.1% formic acid in water)
0	10	90
3	20	80
6	20	80
8	40	60
10	10	90
13	STOP elution	

The column temperature was fixed at 35ºC. A volume of 20 μL sample was injected for the DAD detection and one of 1.0 μL for the MS detection respectively.

For the DAD detection, two wavelengths were used, one of 197 nm for penicillins and another one of 272 nm for tetracyclines and cephalosporins. MS was operated in SIM mode using positive electrospray ionization (ESI (+)).

Samples collection and extraction conditions

The present study was performed in the Romanian Tisza River Watershed. Two monitoring points were selected on the main tributaries (Vişeu and Iza Rivers) and one on the Tisza River. The first sampling point was located at Vişeu Valley village, near the confluence of Vişeu River with Tisza River, the second one at Sighetu Marmaţiei town where Iza River flows into Tisza River and the third one at Teceu Mic village where Tisza River leaves the Romanian territory (Figure 6).

Monitoring in Tisza River Watershed was conducted over the course of 13 months, from July 2014 to September 2015. During this period, water river samples were collected using a manual water sample device and kept in a brown glass bottle at 5ºC before analyses.

Sediment samples were collected in July 2015 using a stainless steel grab sampler and were kept in glass jars at 5ºC before analysis.

Isolation of the target antibiotics from the water samples was done by solid-phase extraction while from the sediment samples by ultrasound-assisted extraction followed by solid-phase extraction (USAE-SPE).
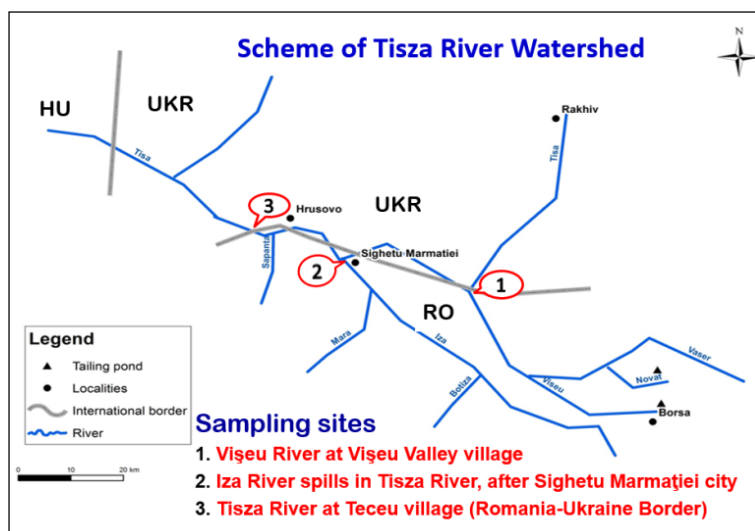
Figure 6. The three monitoring points selected for study

OASIS HLB cartridges (500 mg/6 mL) were used for the extraction of antibiotics from water samples. Before extraction, the cartridges were conditioned by washing with 5 mL methanol and then with 5 mL Milli-Q water. The sorbent was equilibrated by washing with 5 mL solution of 5% methanol in Milli-Q water.

For SPE, a volume of 400 mL river water sample was passed through cartridges at a flow rate of 5 mL/min, subsequent by the elution of retained antibiotics with 5 mL methanol+acetonitrile (1:1, v/v) mixture. After evaporation to dryness under nitrogen, the residue was dissolved in 1 mL acetonitrile and subjected to the HPLC analysis.

For the extraction of antibiotics from sediment samples, 3 g of dried sediment (room temperature) was extracted with 20 mL methanol in an ultrasonic bath for 30 minutes. After centrifugation at 4000 rpm for 15 minutes, the supernatant was collected and evaporated to dryness under nitrogen. The residue was reconstituted in 100 mL distilled water and subjected to the SPE extraction under the procedure used for the river water samples.

ACKNOWLEDGMENTS

REFERENCES

1. K. Kümmerer, *Chemosphere*, **2009**, *75*, 417.
2. J.L. Martinez, *Environmental Pollution*, **2009**, *157*, 2893.
3. S. Manzetti, R. Ghisi, *Marine Pollution Bulletin*, **2014**, *79*, 7.
4. X. Chang, M.T. Meyer, X. Liu, Q. Zhao, H. Chen, J. Chen, Z. Qiu, L. Yang, J. Cao, W. Shu, *Environmental Pollution*, **2010**, *158*, 1444.
5. B. Li, T. Zhang, Z. Xu, H.P. Fang, *Analytica Chimica Acta*, **2009**, *645*, 64.
6. O. Opriș, V. Coman, F. Copaciu, M. Vlassa, *Journal of Planar Chromatography*, **2012**, *25*(6), 516.
7. C. Marx, V. Mühlbauer, P. Krebs, V. Kuehn, *Science of the Total Environment*, **2015**, *524–525*, 269.
8. W.H. Xu, G. Zhang, S.C. Zou, X.D. Li, Y.C. Liu, *Environmental Pollution*, **2007**, *145*, 672.
9. O. Opriş, M.L. Soran, V. Coman, F. Copaciu, D. Ristoiu, *Central European Journal of Chemistry*, **2013**, *11*(8) 1343.
10. X. Liang, B. Chen, X. Nie, Z. Shi, X. Huang, X. Li, *Chemosphere*, **2013**, *92*(11), 1410.
11. H. Shi, Y. Yang, M. Liu, C. Yan, H. Yue, J. Zhou, *Marine Pollution Bulletin*, **2014**, *83*, 317.
12. D. Cheng, X. Liu, L. Wang, W. Gong, G. Liu, W. Fu, M. Cheng, *Science of the Total Environment*, **2014**, *476-477*, 266.
13. J. Xu, Y. Zhang, C. Zhou, C. Guo, D. Wang, P. Du, Y. Luo, J. Wan, W. Meng, *Science of the Total Environment*, **2014**, *497–498*, 267.
14. S. Zhao, X. Liu, D. Cheng, G. Liu, B. Liang, B. Cui, J. Bai, *Science of the Total Environment,* **2016**, *569–570*, 1350.
15. L. Yao, Y. Wang, L. Tong, Y. Deng, Y. Li, Y. Gan, W. Guo, C. Donga, Y. Duana, K. Zhaoa, *Ecotoxicology and Environmental Safety*, **2017**, *135*, 236.
16. B. Suárez, B. Santos, B.M. Simonet, S. Cárdenas, M. Valcárcel, *Journal of Chromatography A*, **2007**, *1175*(1) 127.
17. M.I. Bailón-Pérez, A.M. García-Campaña, C. Cruces-Blanco, M. del Olmo Iruela, *Journal of Chromatography A*, **2008**, 1185(2), 273.
18. A.V. Herrera-Herrera, J. Hernández-Borges, T.M. Borges-Miquel, M.Á. Rodríguez-Delgado, *Journal of Pharmaceutical and Biomedical Analysis*, **2013**, *75*, 130.
19. Y. Li, Q. Li, K. Zhou, X.-L. Sun, L.-R. Zhao, Y.-B. Zhang, *Chemosphere*, **2016**, 147, 25.
20. P. Bottoni, S. Caroli, *Journal of Pharmaceutical and Biomedical Analysis*, **2015**, *106*, 3.

SYNTHESIS AND CHARACTERIZATION OF NOVEL GIOMERS FOR DENTAL APPLICATIONS

**IOANA HODISAN[a,d], CRISTINA PREJMEREAN[b*], IOAN PETEAN[a],
DOINA PRODAN[b], TINCA BURUIANA[c], LOREDANA COLCERIU[d],
LUCIAN BARBU-TUDORAN[e], MARIA TOMOAIA-COTISEL[a,f]**

ABSTRACT. The aim of the present work was to prepare and characterize a series of dental giomers and their corresponding dental adhesive and to evaluate the adhesion of the new materials at the restoration/tooth interface. The experimental giomers were prepared as monopastes by blending the resin matrices, a new pre-reacted glass, a radiopaque glass and fluorhydroxyapatite. The novelty of the work is represented by the using of a polyalkenoic acid based on acrylic acid, itaconic acid and N-acryloyl –L-leucine as the main component of the pre-reacted glass and of the primer in the adhesive system. In addition, the using of an original synthesized urethane tetra-methacrylate Bis-GMA analogue (Bis-GMAexp) as base monomer in the resin represents another element of novelty. The morphology of giomer samples was investigated by scanning electron microscopy. The sealing ability was tested by dye penetration method completed with atomic force microscopy investigation. The microleakage was evaluated using the score method. The results pointed out a remarkable dentin sealing for the new adhesive system and a strong adhesion at Bis-GMAexp-based giomer/ adhesive system/tooth interfaces in substantial agreement with very low value of microleakage.

Keywords: *dental giomers, adhesive system, microleakage, SEM, AFM*

---

[a] [a]*Babeş-Bolyai University, Faculty of Chemistry and Chemical Engineering, 11 Arany J. str., RO-400028, Cluj-Napoca, Romania*
[b] *Babes-Bolyai University, Raluca Ripan Institute of Research in Chemistry, 30 Fantanele str., RO-400294, Cluj-Napoca, Romania*
[c] *Petru Poni Institute of Macromolecular Chemistry, Iasi, Romania*
[d] *Iuliu Haţieganu University of Medicine and Pharmacy, Faculty of Dental Medicine of Cluj-Napoca, 8 Babeş V. str., RO-400012, Cluj-Napoca, Romania*
[e] *National Institute for Research and Development of Isotopic and Molecular Technologies, 65-103 Donath str., RO-400293 Cluj-Napoca, Romania*
[f] *Academy of Romanian Scientists, 54 Splaiul Independentei, 050094 Bucharest, Romania*
 * Corresponding author: cristina.prejmerean@gmail.com

I. HODISAN, C. PREJMEREAN, I. PETEAN, D. PRODAN, T. BURUIANA,
L. COLCERIU, L. BARBU-TUDORAN, M. TOMOAIA-COTISEL

INTRODUCTION

Longevity, fluoride release and fluoride recharge abilities are crucial for the clinical performances of aesthetic dental restorative materials. Considering these requirements, during the last decade, a new class of hybrid materials which combine the chemistry of diacrylic resin composites (DRCs) with the one of the glass ionomer cements (GICs) were introduced on the market by Shofu (Kyoto, Japan). These hybrid materials were named giomers. They present long-term aesthetics and durability (which are characteristics of DRCs) as well as controllable ion release and recharge properties (which represent features of GICs).

Giomers are new restorative materials used in adhesive dentistry based on pre-reacted filler technology, where pre-reacted glass ionomer (PRG) was ground and used as fillers in a polymer matrix. PRG fillers are fabricated by acid–base reactions between fluoride containing glass and poly acrylic acid in the presence of water forming wet siliceous hydrogel.[1] Giomers are fluoride release dental materials [2] having the advantage of inhibiting dental tissues demineralization process [3].This new class of restorative materials combines the bioactivity and biocompatibility of glass ionomer with the physical and optical properties of composites offering the practitioners an excellent alternative for amalgam restoration. The giomers bond chemically to tooth structure by an intermediate adhesive system [4].

Restorative materials used in dentistry should provide a good sealing at the tooth/restorative material interface in order to prevent microleakage and postoperative complication. Adhesive systems used in restorative dentistry provide the sealing between tooth and restorative composites and should create a strong adhesive bond associated with minimal shrinkage of the resin during curing [5].

The adhesive dentistry is known to be confronted with the limitation of the dentin adhesion. That's why it is important to investigate the tooth/ adhesive system/restoration interface for the new materials in order to improve the quality of the sealing of restoration giving the opportunity of obtaining a hermetic restoration without any microleakage [6]. Microleakage was reported as the main reason for replacement of composite resin restoration [7-9]. Microleakage is usually associated with the bacterial penetration through the restoration-tooth interface, causing short-term or/and long-term clinical problems such as postoperative sensitivity, marginal staining, secondary caries, and/or pulpal inflammation and failure of endodontic treatment [10-12]. *In vitro* studies of microleakage are done using methods like: dye penetration method [13], measurement by scanning electron microscope [14], bacterial activity, electrochemical test, fluid filtration [15].

The aim of this work was to prepare and characterize a series of new giomers and their corresponding adhesive system, including the primer and the bonding. The sealing ability was tested by dye penetration method completed with AFM investigation at the interface in order to demonstrate their potential for clinical use.

RESULTS AND DISCUSSION

1. Giomers components

1.1. Resins

The experimental resins were formulated using monomer mixtures of Bis-GMAcom or an original synthesized urethane tetra-methacrylate Bis-GMA analogue (Bis-GMAexp) as base monomer and TEGDMA as diluting monomer.
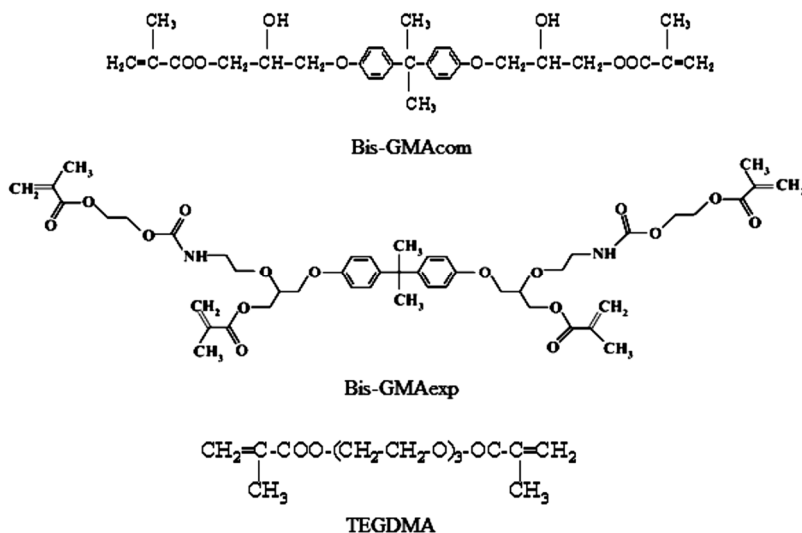
Fig.1. Chemical structures of the monomers used in this study.

The synthesis and characterization of Bis-GMAexp was presented elsewhere [16]. The ratio between the base monomer and diluting monomer was 70/30. In the composition of the resins, besides the methacrylic oligomers and monomers, a photosensitizer, camphorquinone (CQ) in an amount of 0.5% (by weight), and an accelerator N,N-dimethylaminoethyl methacrylate (DMAEMA), in an amount of 1% (by weight), were added.

1.2. Pre-reacted glass ionomer filler

The experimental pre-reacted glass ionomer filler was prepared using the conventionally method employed in the preparation of traditional glass ionomer cements. PRG was prepared by hand-mixing of 50% aqueous solution of PAlk-Leu polyalkenoic acid (ternary copolymer resulted from acrylic acid, itaconic acid and N-acryloyl-L-leucine, average molecular weight 23500) with the superficially active glass powder G having the composition: SiO_2 (49%), Al_2O_3 (22%), CaF_2 (29%), in a weight ratio of 1/2.4. After 24 hours, the PRG was dried in an oven at 95^0C for 24 hours. Finally, it was grounded in a ball mill and sifted to fine powder.

X1000   X30000

2a   2b   2c
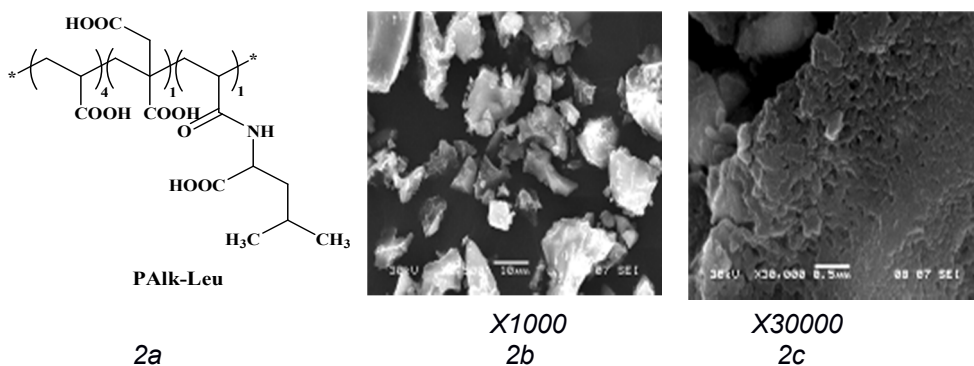
Figure 2. Structure of PAlk-Leu (2a; *structural unit*) and
SEM micrographs of the corresponding PRG (2b, 2c)

SEM images presented in Fig.2 show the morphology of the experimental PRG powder. One can observe the irregular shape of the particles with a sharp particle edges (Fig. 2b).The particle sizes showed an average diameter about 20 μm. The higher magnification details presented in Fig.2c reveal a porous structure of the pre-reacted glass.

2. Giomers

The experimental light-curing giomers were prepared as monopastes by mixing the resin matrices (20%) with the hybrid fillers (80%). For the obtaining of hybrid fillers, the pre-reacted glass ionomer filler (28%) fluorohydroxy-apatite (12%), the silanized radiopaque glass powder (40%) were mixed and then sifted together. Silanation of radiopaque glass was carried out with 3-methacryloyloxypropyl-1-trimethoxy-silane (A-174 silane). The method of obtaining and the characterization of radiopaque glass and FHAP was shown elsewhere [16, 17].

X1500　　　　　　　　　　　　　　　x1500
3a　　　　　　　　　　　　　　　　　3b
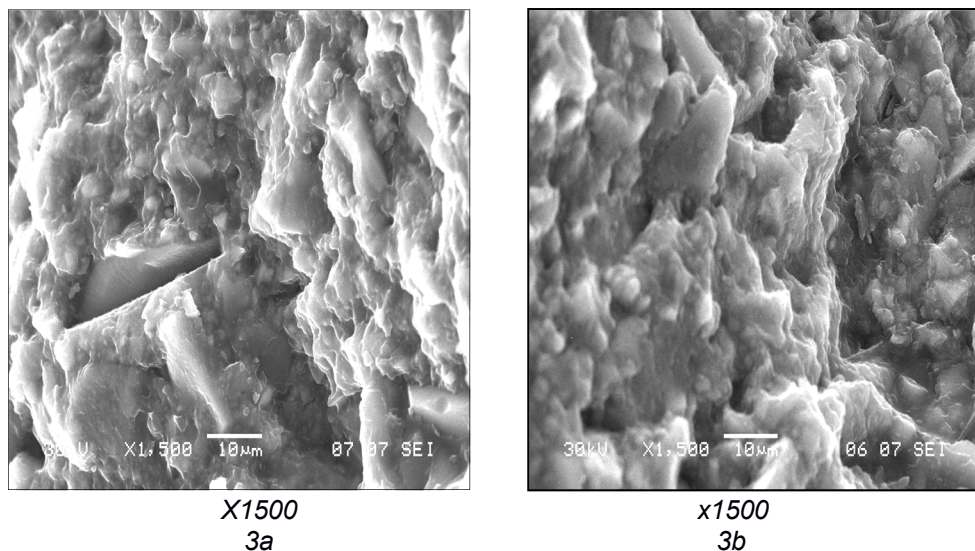
Figure 3. SEM micrographs of the Giomer G1 (3a) and Giomer G2 (3b)

Fig. 3 shows the fracture images of Giomer G1 based on Bis-GMAcom (3a) and Giomer G2 based on Bis-GMAexp (3b). G1 and G2 giomers present a similar surface organization. The morphology of giomer samples is complex consisting of a high amount of fine particles well embedded in a compact polymer matrix structure. A large amount of particles measuring less than 10 microns with sharp or rounded edges (shapes) as well as a few particles having a diameter of about 20 microns can be visualized. Base on the particle size analysis, the first can be attributed to the radiopaque filler particles or small sizes PRG particles and the second ones can be attributed to the large sizes PRG filler particles [16].

3. Obtaining of adhesive system

The adhesive system comprising 3 components: etchant, primer and bonding (known as three-step adhesives systems) were prepared. The primer and bonding were prepared according to the method described elsewhere [26]. The composition of the adhesive system and of the G1 and G2 giomers is shown in Table 1.

Table 1. Composition of adhesive system and of G1 and G2 giomers

Product		Main components	Diluting monomers	Initiating system	Solvents	Filler(s)
Adhesive system	Primer	PAlk-Leu (30%)	HEMA (32%) TEGDMA (10.7%)	CQ (0.18%) CDFI (1.12%)	Water (20%) Acetone (6%)	-
	Bonding	Bis-GMAexp (60%)	HEMA (10%) TEGDMA (28.53%)	CQ (0.49%) DMAEMA (0.98%)	-	-
Giomers	Giomer G1	Bis-GMAcom (14%)	TEGDMA (5.72%)	CQ (0.09%) DMAEMA (0.19%)		SPRG (28%) HAF (12%) Radiopaque glass (40%)
	Giomer G2	Bis-GMAexp (14%)	TEGDMA (5.72%)	CQ (0.09%) DMAEMA (0.19%)		SPRG (28%) HAF (12%) Radiopaque glass (40%)

4. Determination of microleakage

Thirty box-type Class V standardized cavities were prepared on premolar teeth on the facial (the face oriented in the mouth towards the cheek) and oral surfaces (the face oriented towards the tongue) of each tooth. The preparations had one margin in enamel and one margin in dentin. The preparations were divided randomly into two equal groups (n=15) and restored with: group I: giomer G1 and adhesive system; group II: giomer G2 and the same adhesive system. The teeth were thermocycled, then immersed in 2% methyl blue solution for 24 h. The specimens were sectioned longitudinal, buccolingually into slices of 1 mm and the resulted sections were examined for microleakage using a stereomicroscope. The extend of microleakage at the restoration/tooth interface was evaluated assessing scores: 0, 1, 2, 3 for each restoration at the enamel/restoration and dentin /restoration interface.

The microleakage behavior examined using the scoring method is presented in Table 2.

Table 2. Microleakage scores

Groups	Microleakage score in dentin				Microleakage score in enamel			
	0	1	2	3	0	1	2	3
I	3	0	4	8	13	2	0	0
II	5	2	4	4	14	1	0	0

The results, given in table 2, show that almost all the samples presented a minimal microleakage at the enamel margins proving that both groups of giomer restorations were sealed with the experimental adhesive system at this level and the values are comparable with the ones found in the literature for the commercials giomer materials and their adhesive systems [18-20].

The microleakage values in dentin were significantly higher than enamel values. The problem of microleakage has been largely demonstrated mainly below the cement-enamel junction in several studies [21, 22] because the bonding to dentin is far more difficult and less predictable than bonding to enamel. This behavior could be explained by the morphological differences of the tooth structures: dentin and enamel because dentin is less mineralized, about 75% as opposed to enamel which is 98%. Moreover, dentin has a more complex histologic pattern, such as tubular structure and intrinsic wetness [23].

Dentin is more hydrophilic with canalicular structure with 48% vol. Hap, 29% vol. organic materials and 23% vol. water. The dentinal tubules traverse entire dentin, oriented from the dentin-enamel junction towards the pulp. This structure of dentin allows the substance to infiltrate at interface dentin/composite and to travel by water in dentinal fluid along the canalicular system towards the pulp resulting in a higher percentage of dentin microleakage than the enamel.

Between the two groups there were no significant differences concerning the microleakage value. However, it can be noticed that there were only three scores 0 for group I, while there were 5 scores 0 for group II. In addition, there were registered 8 scores 3 for group I, while were obtained only 4 scores 3 for group II.

AFM investigations were made to examine the sealing at the dentin/adhesive system interface, which is a condition for a good restoration. The dentin surface observed by AFM microscopy is presented in Fig. 4. The topographic image, Fig. 4a, reveals the dentin tubule. Peritubular dentin is observed around the tubule in good agreement with literature data [24 – 26].
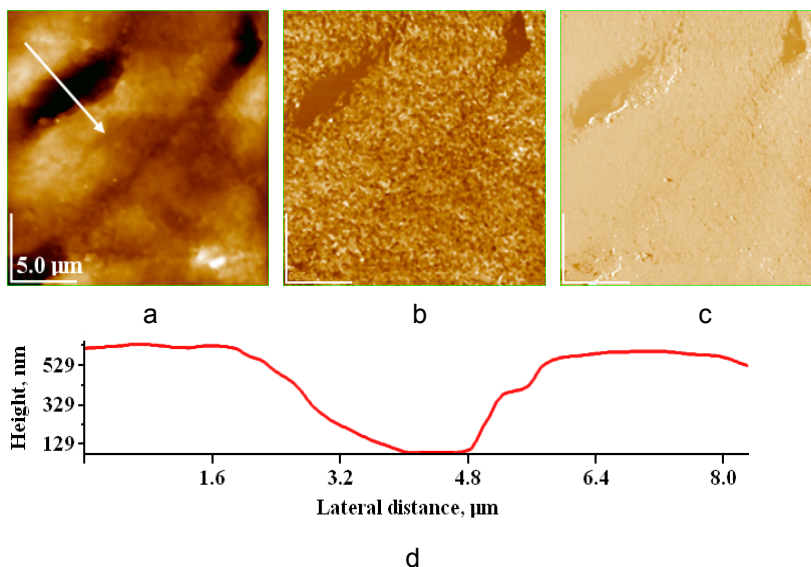
Figure 4. AFM images of dentin at the interface with the G2 giomer restoration:
a) topographic image, b) phase image, c) amplitude image, d) cross section
on white arrow in figure (a). Scanned area 20 μm x 20 μm.

Fig. 4c also reveals the peritubular dentin as a compact matrix having light color and the tubules appear in dark due to their depth. Cross section in Fig. 4d gives the opportunity to measure precisely the size of tubule of about 3 μm [27]. The darker zone in the middle of the scanned area is the adhesive sealing the dentin surface and the tubules and thus, offering a binding with the giomer G2.

CONCLUSIONS

A series of dental giomers (G1 and G2) were prepared by dispersing a novel pre-reacted glass ionomer, a radiopaque glass and fluorhydroxyapatite in the resin matrices. An original synthesized urethane tetra-methacrylate Bis-GMA analogue (Bis-GMAexp) was used as base monomer in giomer G2 while commercial Bis-GMA was contained in G1 giomer. PAlk-Leu (ternary copolymer resulted from acrylic acid, itaconic acid and N-acryloyl-L-leucine) was used as polyalkenoic acid for the obtaining of PRG and as main component of the primer in the adhesive.

The combination of adhesive system and giomer G2 performed better in terms of adhesion to the tooth structures than the same adhesive system in combination with giomer G1.

We can conclude that the giomer G2 containing Bis-GMAexp could be used successfully with the experimental adhesive system based on PAlk-Leu in clinical application.

EXPERIMENTAL SECTION

1. Materials

Reagent grade chemicals of 2,2-bis[4-(2-hydroxy-3-methacryloxy-propoxy)phenyl]propane (Bis-GMA), triethyleneglycol dimethacrylate (TEGDMA), 2-hydroxyethyl methacrylate (HEMA) were purchased from Aldrich Chemical, Milwaukee, WI, USA and used without further purification. Camphorquinone (CQ), N,N-dimethylaminoethyl methacrylate (DMAEMA), diphenyliodonium chloride *(*CDFI) were supplied by Sigma Chemical, St. Louis, MO, USA. PAlk-Leu was synthetized by our group as reported elsewhere [28]. 3-methacryloyloxypropyl-1-trimethoxy-silane (A-174 silane) were purchased from Sigma Aldrich Chemical Co. (Taufkirchen, Germany) and used without additional purification. The oxides and fluorides SiO_2, Al_2O_3, ZnO, CaO, Na_2O, B_2O_3, CaF_2, BaF_2 were purchased from Merk (Darmstadt, Germany).

2. Preparation of the adhesive system

2.1. The experimental primer. In a round-bottomed flask equipped with a stirrer, reflux condenser and a dropping funnel 30g of PAlk-Leu were introduced, and then 32g of HEMA were added. The mixture was stirred at 40°C for 30 min. Then 20g water was dosed from the dropping funnel, and the mixture was stirred further until the complete dissolution. After about 1 h, 10.7g of TEGDMA, in which the components of the initiating system (CQ (0.18g) and CDFI (1.12g)) were previously added, was dosed under continuous stirring for another hour, and finally, 6 g of acetone was added. All operations were done in rooms protected from visible light.

2.2. The experimental bonding. 28.53 g TEGDMA in which the initiator system was dissolved (CQ (0.49g) and DMAEMA (0.98g)) and 10 g HEMA were dosed in the round-bottomed flask in which 60 g bis-GMA had been previously introduced. The mixture was stirred for 2 h at 40°C. All operations were done in rooms protected from visible light.

3. Preparation of the giomers

3.1. The resin. 60g of Bis-GMA type monomer (Bis-GMAcom or Bis-GMAexp) were introduced in a round-bottomed flask equipped with a stirrer, reflux condenser and a dropping funnel. The initiator system, (CQ (0.49g) and respectively DMAEMA (0.98g), was dissolved in 29.47g TEGDMA in another

flask. After complete dissolution, the mixture was dosed under continuous stirring for two hours over the Bis-GMA monomer. All operations were done in rooms protected from visible light.

3.2. The hybrid filler. 35g pre-reacted glass ionomer filler, 15g fluorohydroxy-apatite and 50g silanized radiopaque glass powder were mixed and then sifted together.

3.3.The giomers. The experimental light-curing giomers G1 and G2 were prepared as monopastes by mixing the resin matrices with the hybrid fillers.

4. Sample preparation

Fifteen freshly extracted premolars for orthodontic reason were kept in distilled water at 4°C for 24 hours. Standardized class V cavities measuring 4 mm length 3 mm width and 1.5 mm depth were prepared on facial and oral face of each tooth. The preparation was positioned with the gingival margin in cement (dentin) and the occlusal margin in enamel. The bur used for cavities preparation was a bur no. 4 for a high speed hand piece with water cooling system purchased from Shofu (Kyoto, Japan). The cavities were then divided randomly into 2 groups: group I cavities were restored using adhesive system and giomer G1 and group II was restored with the same adhesive system and giomer G2. The clinical protocol for the restoration included etching the cavities 30 sec with ortophosphoric acid 37% then rinse it off and gently dry the dental tissue. Next step was applying the primer on the dentin area using a microbrush, dry it using the air spray for 3 sec and then applying the bonding on the entire surface of the cavity. Once in place, the bonding was light-cured for 20 sec using light-curing device Spectrum 800 470 nm wavelength (Dentsply Germany). The giomer was placed in the cavity using the incremental oblique layers technique, each layer of maximum 2 mm. The layers were light-cured 20 sec each before applying the next one. Finishing and polishing of the restorations was done using Super Buffs disks from Shofu (Kyoto, Japan). The teeth were thermocycled 500 times in a 5°C-55°C water baths. Each cycle lasted 60 sec. This is an artificial aging method according to the ISO /TS11405:2003 [29]. After that the teeth were bloated dried with paper towels and the roots were sealed with composite resin. The exterior surface of the teeth was isolated using two layers of nail varnish on all their surface except 1 mm around the restoration. All samples were then immersed in 2%methylene blue solution for 24 hours. After rinsing the dye under running water the teeth were dried and embedded in methyl methacrylate and sectioned longitudinally in slices of 1 mm through both restorations using a diamond saw (Isomet 1000, Buehler,USA) under water cooling system [30]. Each slice was examined at optical microscope and scores were assessed for the dye penetration along the restoration /tooth interface according to the ISO standards: 0-no dye penetration; 1-dye penetration till ½ of the wall examined; 2-dye penetration to the full depth of the wall; 3-dye penetration reaches the axial wall.

5. Scanning electron microscopy (SEM). The morphology of the pre-reacted glass particles and of the fracture morphology of giomers was determined by SEM (JEOL, JSM 5510 LV) operated at 30 kV. The samples were prepared by dispersing a thin layer of the glass powders on a carbon tape and coated with 8 nm gold evaporated in an argon atmosphere (Sputter Coater Agar) prior to analysis

6. Atomic force microscopy. The AFM investigation of the surfaces of the tooth slice was done using the scanning probe microscope, AFM, JEOL 4210 equipment operating in the intermittent contact, also known as tapping mode [31-34]. The cantilever used was triangular, with a tip made from silicon nitride (NSC11, Micromasch Co. Estonia). The probe (tip) was on the cantilever, oscillating with a resonant frequency in the range of 260-330 kHz and having a spring constant of 48 N/m. Both a low scanning rate, 1 Hz, and a higher rate, in the range 2-6 Hz, were used, in order to detect possible scanning artifacts or those resulting from the sample preparation. The AFM images consist of multiple scans displaced laterally from each other in Y direction, the resolution being 512 x 512 pixels. An adequate low pass filtering was performed to remove the statistical noise without loss in the structural features of the material. All AFM experiments were carried out under ambient laboratory temperature conditions (about 20^0C). All the images were processed according to standard AFM proceeding.

ACKNOWLEDGEMENTS

REFERENCES

1. M.C. Sunico, K. Shinkai, Y. Katoh, *Operative Dentistry*, **2005**, *30,* 282.
2. T. Itota, T.E. Carrick, M. Yoshiyama, J.F. McCabe, *Dental Materials,* **2004,** *20,* 789.
3. H. Ede Gonzalez, A.U. Yap, S.C. Hsu, *Operative Dentistry*, **2004,** *29,* 578.
4. K. Ikemura, F.R. Tay, T. Endo, D.H. Pashley, *Dental Materials*, **2008**, *27,* 315.
5. J.F. McCabe, A. Walls, "Applied Dental Materials", ninth edition, Blackwell Publishing Ltd., Singapore, **2008**.
6. R.M. Carvalho, J.C. Pereira, M. Yoshiyama, D.H. Pashley, *Operative Dentistry*, **1996,** *21,* 17.
7. I.A. Mjör, *Acta Odontologica Scandinavica*, **1997**, *55*, 58.
8. I.A. Mjör, *Operative Dentistry,* **1985,** *10,* 88.
9. V. Qvist, J. Qvist, I.A. Mjör, *Acta Odontologica Scandinavica*, **1990,** *48,* 305.

10. A.H. Tjan, D.E. Tan*, Quintessence International,* **1991,** *22*, 565.
11. M.J. Taylor, E. Lynch, *Journal of Dentistry,* **1992,** *20,* 3.
12. I. Yavuz, H. Aydin*, Biotechnology and Biotechnological Equipment*, **2005**, *19,* 181.
13. J.B. De Almeida, J.A. Platt, Y. Oshida, B.K. Moore, M.A. Cochran, G.J. Eckert, *Operative Dentistry,* **2003,** *28,* 453.
14. F.M de Goes, M.A. Montes, *Journal of Dentistry,* **2004**, *32,* 391.
15. B. Karagenç, N. Gençoglu, M. Ersoy, G. Cansever, G. Külekçi*, Oral Surgery*, *Oral Medicine*, *Oral Pathology*, *Oral Radiology*, *and Endodontology,* **2006**, *102,* 110.
16. C. Prejmerean, D. Prodan, M. Vlassa, M. Streza, T. Buruiana, L. Colceriu, V. Prejmerean, S. Cuc, M. Moldovan*, Measurement Science and Technology,* **2016**, *27,* 124008.
17. C. Prejmerean, M. Moldovan, C.M. Petrea, D. Prodan, L. Silaghi-Dumitrescu, E. Vasile, G. Furtos, S. Boboia, R. Silaghi-Dumitrescu, *Materiale Plastice,* **2011**, *48,* 279.
18. A. Abo El Naga, *Journal of American Science,* **2012**, *8,* 27.
19. B.M. Owens, W.W. Johnson, E.F. Harris, *Operative Dentistry*, **2006**, *31,* 60.
20. C.E. Dörfer, H.J. Stachle, M.W. Wurst, H. Duschner, T. Pioch, *European Journal of Oral Science*, **2000**, *108,* 346.
21. C. Prati, L. Tao, M. Simpson, D.H. Pashley, *Journal of Dentistry*, **1994**, *22,* 49.
22. K. Derhami, P. Coli, M. Brännström, *Operative Dentistry,* **1995**, *20,* 100.
23. A. Thylstrup, S.A. Leach, V.Quist, "Dentine and Dentine Reactions in the Oral Cavity", Eds., Inform. Print. Ltd., Oxford, **1987**, p. 17.
24. S. Habelitz, M. Balooch, S.J. Marshall, G. Balooch, G.W. Marshall, *Journal of Structural Biology*, **2002,** *138*, 227.
25. L.E. Bertassoni, G.W. Marshall, M.V. Swain, *Micron*, **2012**, *43,* 1364.
26. X. Zheng, H. Pan, Z. Wang, H. Chen, *Journal of Microscopy*, **2011**, *241,* 162.
27. M.B. Lopes, M.A. Sinhoreti, A. Gonini Jr., S. Consani, J.F. McCabe*, Brazilian Dental Journal,* **2009**, *20,* 279.
28. T. Buruiana, M. Nechifor, V. Melinte, V. Podasca, E.C. Buruiana, *Journal of Biomaterials Science Polymer Edition,* **2014**, *25*, 749.
29. International Organization for Standardization (ISO). "Dental materials—testing of adhesion to tooth structure", ISO/TS 11405: **2003** (Edition).
30. S. Deliperi, D.N. Bardwell, C. Wegley, M.D. Congiu, *Operative Dentistry*, **2006**, *31,* 227.
31. C. Prejmerean, M. Tomoaia-Cotisel, E.Vasile, G. Furtos, L. Pop, M. Moldovan, I. Petean, *International Journal of Nano and Biomaterials*, **2011**, *3,* 344.
32. G. Tomoaia, O. Soritau, M. Tomoaia-Cotisel, L.-B. Pop, A. Pop, A. Mocanu, O. Horovitz, L.-D. Bobos, *Powder Technology*, **2013**, *238*, 99.
33. M. Tomoaia-Cotisel**,** A. Tomoaia-Cotisel, T. Yupsanis, G. Tomoaia, I. Balea, A. Mocanu, Cs. Racz, *Revue Roumaine de Chimie,* **2006**, *51,* 1181.
34. O. Horovitz, G. Tomoaia, A. Mocanu, T. Yupsanis, M. Tomoaia-Cotisel, *Gold Bulletin*, **2007**, *40*, 295.

PROVENANCE STUDY ON A SMALL SELECTION OF ROMAN POTSHARDS
(TĂŞNAD-SERE SITE, SATU MARE COUNTY, ROMANIA). 1.

ENIKŐ BITAY[a], BERNADETH KISS-PATAKI[b], GYÖRGY SZAKMÁNY[c], EMIL INDREA[d], IRÉN KACSÓ[d], IOAN BRATU[d], ERZSÉBET VERESS[e]

ABSTRACT. Five representative potshards collected from the Tăşnad-Sere C 52 archaeological site were investigated in order to evaluate the occurring differences of the raw materials used and the technology applied. The structural and compositional differences shown by petrographic analysis (optical microscopy /OM/ and XRD) and FTIR spectroscopy data indicate that according to both the raw materials composition (clay sediments and temper) and the pottery technique the samples studied form two distinct groups**.**

Keywords: ancient ceramics, provenance, optical microscopy, PXRD, FTIR spectroscopy

INTRODUCTION

Correct archaeological conclusions require, besides the typological characterization of the archaeological findings unearthed at a certain site, their complex archaeometric (structural, compositional and technological) characterization. The possible source of the raw materials used and the

[a] *Sapientia Hungarian University of Transylvania, Faculty of Technical and Human Sciences, OP 9 CP 4, RO-540485 Targu-Mures, Romania, ebitay@ms.sapientia.ro*
[b] *Bosch Group in Hungary, Postbox 331, H-1475 Budapest Hungary, bernadethpataki@gmail.com*
[c] *Eötvös Loránd University, Institute of Geography and Earth Sciences, Pázmány Péter allée 1/C, H-1117 Budapest, Hungary*
[d] *National Institute for Research and Developement of Isotopic and Molecular Technologies, Donath Str. 65-103, RO-400293 Cluj, Romania.*
[e] *Transylvanian Museum Society, Napoca Str. 2-4, RO-400750 Cluj, Romania, veresserzsebet@gmail.com*

technical peculiarities together could confirm some of the archaeologist's technology-related suppositions and answer some of the questions related to the dynamics of local or regional trade. [1]

Archaeometric characterization of ceramic vestiges usually is carried out on large sample populations, concluding in the end on the basis of statistical analysis of the experimental data obtained. However, the quantity of the available samples sometimes is strongly limited. This study tries to evaluate the efficiency and reliability of the most frequently applied analytical methods in case of a few-numbered selection of ancient ceramic samples. Five potshard samples collected from the same archaeological site (Tăşnad-Sere, one of the Complex 52 dwellings) were investigated in order to establish their differences by the most traditional mineralogical analyses (polarized optical microscopy (OM), powder X-ray diffraction (PXRD) analysis and Fourier transformed (FTIR) spectroscopy).

ARCHAEOLOGICAL CONTEXT

Tăşnad is located in Satu-Mare County, NW Romania, on one of the main geothermal areas of the country. The settlement and its surroundings are provenly continuously inhabited at least since the Neolithic Age, their Starčevo-Criş and Coţofeni type finds being among the most important ones from the area. The stratigraphy of the location shows generally an approx. 0.30 m thick vegetal soil layer followed in-depth by a 0.30-0.80 m grayish-black culture layer containing an impressive quantity of ceramic remains, mostly Starčevo-Criş IIIB-IVA dated shards [2-5]

The *Tăşnad-Sere* location was necessarily opened to rescue archaeology by reason of the developments effectuated on the neighbouring thermal baths, *Tăşnad-Strand* (Figure 1).
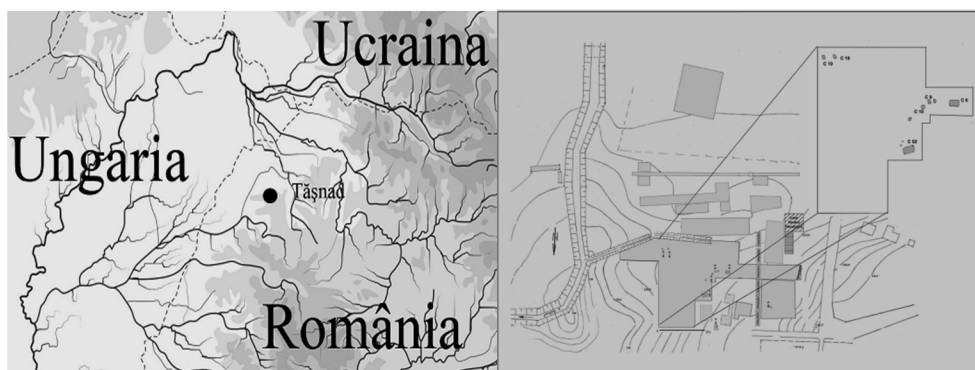
Figure 1. Location of the Tăşnad Sere archaeological site.

On the site excavated during eight salvage campaigns between 1989 and 2006 more than 100 archaeological complexes were discovered: (dwellings, huts, pits, graves, ditches), each holding varied materials (fine pottery, stone pieces, terracotta figurines, animal bones). The complexes unearthed were mostly Neolithic, however, ten Roman sites dating from the 2nd and 3rd centuries AD (three of them without any material remains) were also found. Although the Roman ceramic material is significantly less, they are of great relevancy, being the first such discovery in the area in archaeological context [5-7].

The five Roman-period potshards selected as representative samples for the present study turned up in each others' close vicinity from one dwelling of Complex 52 (*C52*), the richest of the sites, and cover the main Roman-period pottery types found at the site.

RESULTS AND DISCUSSION

Macroscopic and microscopic characterization

The specimens selected for this study are representative pot fragments covering the main pottery types found at the site (Figure 2).

Their first grouping was provided by their **macroscopic features** (Table1): color and homogeneity of the ceramic body, the visible porosity and inclusions (type, shape, dimension, relative distribution, orientation) and the occurrent technological failures or deviations (signs of incomplete firing or over-firing, cracks).

Sample	5-2-1	5-2-2	5-2-3	5-2-4	5-2-5
Outer surface					
Inner surface					
Core					

Figure 2. Macroscopic aspect of the shards selected for characterization.

Sample 5-2-1, a hand-made coarse ceramic tempered with rock fragments and grog (ceramic debris) represents statistically approximately 23 % of the total of findings. It is dark grey, on the outside being covered with a "rusty" crust while on the inner side appears a white, carbonated deposit; most probably both of depositional origin. The homogeneous sample body is moderately porous. Sample 5-2-2 (16 %) is potter's wheel worked from a coarse ceramic paste containing many inclusions of quartzitic sand (naturally tempered?). This shard is sandwich structured with grayish core grading into light reddish-brown zones towards the margins. The wheel-modelled fine ware type sample 5-2-3 (13 %) has homogeneous, uniformly light grey body with approximately plan parallel smooth surfaces.

Shards coded 5-2-4 and 5-2-5 are unique as type. The most porous, slightly cracked, brownish-grey sample 5-2-4 is worked on the potter's wheel from fine ceramic paste and holds a stamped sign on the outside. Sample *5-2-5* is part of a wheel thrown, black painted fine ware with homogeneous grey body; its blackish interior presents stress cracks.

Table 1. Macroscopic features of the samples.

Sample		Macroscopic features		
Code	No.	Color	Paste appearance	Inclusions, pores
5-2-1	49345	dark grey	coarse	moderately porous
5-2-2	49333	sandwich, greyish core, reddish-brown margins	coarse	many inclusions
5-2-3	49301	light grey	fine	-
5-2-4	49275	greyish-brown, stamped	fine	porous
5-2-5	49278	light grey, ornamented	fine	stress cracks inside

Shards coded 5-2-4 and 5-2-5 are unique as type. The most porous, slightly cracked, brownish-grey sample 5-2-4 is worked on the potter's wheel from fine ceramic paste and holds a stamped sign on the outside. Sample 5-2-5 is part of a wheel thrown, black painted fine ware with homogeneous grey body; its blackish interior presents stress cracks.

Microscopic characteristics of the samples are presented by Figure 3 and Table 2.

The 5-2-1 sample has hiatal fabric with anisotropic matrix and many non plastic constituents: mostly monocrystalline quartz associated with some polycrystalline quartz presenting sutured contacts of the individual grains, chert, even a little amount of glass. The argillaceous rock fragments (ARF) in the clayish matrix indicate the use of a clay mixture for the ceramic paste. The sample show limonitic concretions and a grog inclusion with concentric appearance due to the occurred natural transformations and inhomogeneous mixing. This and the anisotropic matrix lead to the conclusion that the possible firing temperature was quite low.

Sample 5-2-2 also has hiatal fabric and presents the same anisotropy characteristics. The identified coarse grain fragments allow a temper grouping. The first group is formed by monocrystalline quartz with strong wavy extinction, moreover strongly oriented quartzite and micaceous quartzite, probably of crystalline metamorphic schist origin. Granitoid fragments and individual K-feldspars are also present. The second group contains vulcanite fragments with plagioclase phenocrysts. Individually broken, zoned plagioclases and weakly altered green amphibole clasts may also originate from the vulcanite. In the vulcanite fragments (and only there) occur a few weakly altered Individual biotite grains; epidote-zoisite grains and rutile are also present as accessories. Fine grained sericite-muscovite minerals are present in the groundmass. Opaque minerals with an isometric appearance (possibly magnetite) occur perhaps as a result of the firing process; isotropic clasts, most probably glass fragments can be observed too. The presence of ARFs with some altered rock fragments and limonitic-hematitic nodules lead to the consideration that the raw material used was a *clay mixture*.

The last three samples are very similar from the point of view of their production technology which employed a higher firing temperature. They are not presenting downright coarse grain sizes except of 5-2-4.

In case of sample 5-2-3 the largest amount of the non plastic inclusions is constituted by monocrystalline quartz with wavy extinction. Polycrystalline quartz grains are also present, suggesting a metamorphic origin. K-feldspars and plagioclases are present only in a few amounts. Occasionally normal extinction monocrystalline quartz of volcanic origin also occurs, as well as a few amounts of parallel oriented sericite-muscovite.

1N   N+   1N   N+
5.2.1 (coarse)   5.2.2 (coarse)

1N   N+   1N   N+
5.2.3 (semifine)   5.2.5 (fine)

1N   N+   1N   N+
5.2.4 (semicoarse)   5.2.4 clear evidence of the melting zone
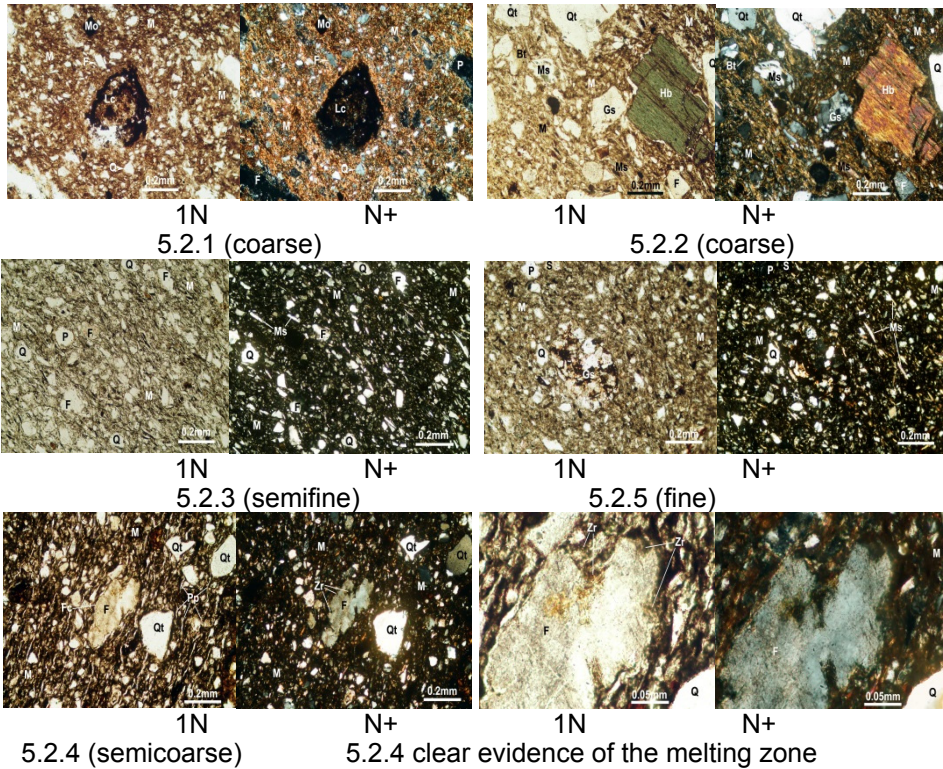
Figure 3. OM petrographic characteristics of the **c**eramic samples.
Microphotos of thin sections with single nicol (1N) and crossed nicols (N+)
M: matrix, Q: quartz, Qt: quartzite, Hb: hornblende, F: feldspar, Ms: muscovite,
Bt: biotite, Gs: gneiss, P: pore, Pp: primary pore, Zr: reaction zone

The large amount of finely grained isometric opaque mineral occurring is probably magnetite formed during firing. The possible raw material in this case too was a *mixture of levigated clays*.

Characterization of sample 5-2-5 roughly follows that of sample 5-2-3, evidencing a series of common features.

Sample 5-2-5, as compared to 5-2-3 is finer and more oriented. It contains a large amount of monocrystalline quartz with both wavy and normal extinction; occasionally K-feldspars occur. The very rare occurrence of zoned plagioclases might indicate a volcanic origin. The sample contains a little more of fine flakes of micas in forms of sericites-muscovites with parallel orientation. Large amount of isometric opaque minerals (magnetite) are also present due to the firing process. The ARFs are dark brown. All these features lead to the consideration that it was made by another clay type or the raw material was better mixed.

Table 2. Mineralogic-petrographic characterization of the ceramics.

Property	Sample				
	5.2.1	5.2.2	5.2.3	5.2.4	5.2.5
Paste	coarse	coarse	semifine	semicoarse	fine
Grain size distrib.*	18% R 36% A 46% L:	24% R 35% A 41% L	8% R 35% A 57% L:	12% R 35% A 53% L:	4% R 36% A 60% L:
Matrix	surface layer: microcryst.-amorphous; core: amorphous-microcryst.	-sandwich structure; -core:black, amorphous; -ext. layers: brownish-red, cryst.; -intermed.: microcryst.-amorphous.	amorphous	amorphous	amorphous
Texture	mostly oriented; homogeneous, elongated primary pores	oriented	oriented; primary and secondary pores	oriented; many elongated pores and contraction cracks	weakly oriented; secondary pores, contraction cracks
Clasts	ceramoclasts, lithoclasts, crystalloclasts	lithoclasts, crystalloclasts			
OM identified main minerals	quartz, quartzite feldspar muscovite biotite hornblende zircon hematite montmorillonite	quartz, quartzite feldspar hornblende muscovite biotite pyroxene titanite gneiss hematite zircon rutile	quartz, quartzite feldspar muscovite biotite hematite zircon rutile	quartz, quartzite feldspar muscovite biotite hornblende rutile staurolite	quartz, quartzite feldspar muscovite biotite gneiss
Grain size distrib.*	18% R 36% A 46% L:	24% R 35% A 41% L	8% R 35% A 57% L:	12% R 35% A 53% L:	4% R 36% A 60% L:
Firing temp.	800-850^{0}C	≈ 850^{0}C	≈ 1000^{0}C	950-100 ^{0}C	>950^{0}C

* R: rudite /pebble/ (mean diameter d_R > 1 mm); A: arenite /sand/ (1 mm > d_A > 0.0625 mm); L: lutite /silt, mud/ (d_L < 0.0625 mm) [8]

The presence of well classified, fine grained non plastic inclusions in samples 5-2-3 and 5-2-5 suggests that in this case the raw material should be naturally tempered and the clay was levigated, whilst in case of samples 5-2-1 and 5-2-2 a deliberate tempered raw material was used, allowing to classify the investigated samples into *two groups*.

The 5-2-4 sample stands for a *transition group* between the two previously mentioned being closer to the second one concerning the production technique, the composition and its hiatal fabrics. The production technique seems to imply a higher firing temperature. The raw material was tempered with coarser grained clasts of vulcanite and crystalline schist origin, similarly to sample 5-2-2, containing, in comparison, a larger amount of polycrystalline quartz and micaceous quartzite and less of vulcanites. Additionally, there are a few plagioclases, K-feldspars, green amphiboles; which one's limonitic concretions and textural features allow the supposition of their clayish origin. Clinozoisite also appears as accessory mineral. The sample contains opaque minerals as 5-2-3 and 5-2-5 (though lesser) supposed to be mostly magnetite resulted from the firing process conducted at higher temperature, or longer time, or both, as indicated by the argillaceous rock fragments (ARF) better fired than those present in samples 5-2-1 and 5-2-2.

PXRD analysis

PXRD analysis was used as complementary petrographic method for OM. [9] Through the OM investigation the phenocrysts present in the ceramic samples could be identified, but the information hided in the groundmass have to be explored by PXRD, with the limitation that PXRD is characterized by a 5% threshold.

The results of the PXRD analysis performed on the ceramic selection investigated are presented on Figure 4 and Tables 3 and 4.

The PXRD patterns of the ceramic samples are in concordance with the optical microscopy data (Table 2).
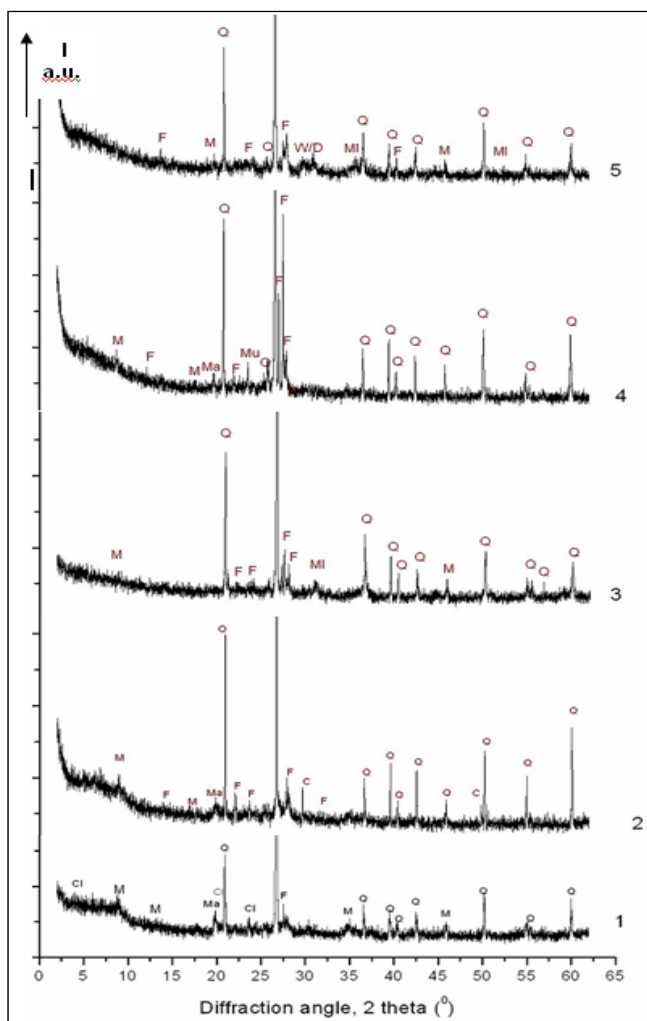
Figure 4. PXRD patterns of the investigated ceramic samples.
Q: quartz, quartzites - SiO_2; M: micas (biotite) - $Mg_{2.001}Al_{1.999}KSi_3O_{12}H_2$;
Mu: muscovites - $Al_{1,94}Si_{3,86}K_{0,86}(O_{12}H_2)$; $Al_{1,96}Si_{3,8}K_{0,94}(O_{12}H_2)$; F: feldspars (mostly
K- feldspars: orthoclase, microcline - $KAlSi_3O_8$, possible some albite - $NaAlSi_3O_8$);
Cl: chlorite - $(Mg,Fe)_3(Si,Al)_4O_{10}(OH)_2 \cdot (Mg,Fe)_3(OH)_6$.

The high and noisy baselines of the diffractograms indicate that the samples contain a large amount of weakly crystallized material, otherwise on the diffractograms appear the same mineral phases over and over again.

Quartzitic minerals (Q) constitute the dominant mineral phase in each case. The rest of the significant diffraction lines correspond to micas, mostly biotite (Bt): $Mg_{2.001}Al_{1.999}KSi_3O_{12}H_2$; K-feldspars (F) like microcline or orthoclase (Orth): $KAlSi_3O_8$, plagioclases like albite: $NaAlSi_3O_8$; muscovites (Mu) of slightly different compositions like Mu2: $Al_{1.94}Si_{3.86}K_{0.86}O_{12}H_2$ and Mu3: $Al_{1.96}Si_{3.8}K_{0.94}O_{12}H_2$; finally, in case of sample 5-2-3 and 5-2-5, an reduced amount of mullite (M): $Al_6Si_2O_{13}$ (Table 4).

Table 3. Relative intensities I_R of the main mineral components

Sample	I_R (%)					
	Bt	Mu2	Mu3	Orth	M	Q
5-2-1	11.2	30.0	-	16.6	-	42.2
5-2-2	9.5	41.8	-	8.9	-	39.8
5-2-3	8.3	25.3	7.7	-	1.3	57.4
5-2-4	2.5	4.0	62.4	-	-	31.1
5-2-5	6.2	36.5	4.8	-	3.8	48.7

The results of the semi-quantitative mineralogical phase analysis permitted by the diffraction data obtained on the five ceramic samples are presented in Table 4.

Table 4. Semiquantitative results of the XRD analysis.

Sample	Mineral*						
	Q	F	Plg	Phy	Ml	Gh	G
5-2-1	xxxx	x	xx	x	x	X	
5-2-2	xxxx	x	xx	x			
5-2-3	xxxx	x	xx			X	x
5-2-4	xxxx	xx	xxx	x	tr		
5-2-5	xxxx	x	xx		x		

Q: quartz; F: K-feldspars; Plg: plagioclases; Phy: "10 Å phases"; Mi: micas;
Gh: gehlenite; G: goethite.
*Number of (x) characterize the mineral phase abundance; tr: only traces.

The relative PXRD peak intensities of the main mineral constituents in case of the different samples (Table 3) as well as the variant heavy mineral contents observed in the OM study indicate that the ceramics investigated, although from the very same archaeological site, are made from raw

materials obtained from at least three different sources. The differences of the firing mineral phases indicate different pottery technologies (different firing conditions) also.

As might be seen above, characteristically all investigated samples presented dominantly high quartz content and contained larger amounts of plagioclases than K-feldspars. Sample 5-2-4 contains some traces of mica, showing comparatively larger K-feldspar and plagioclase content, while both "10 Å phases" and micas are totally absent in case of 5-2-3 ("10 Å phases" are dehydroxylated illite-like phases formed from phyllosilicates which remain in the ceramic material after being fired at relatively low temperatures [10]).

The mineral composition of the supposed raw materials generally corresponds to that of samples 5-2-2, 5-2-3 and 5-2-4, indicating a possible local origin, however, the presence of micas in 5-2-1 and 5-2-5 denote that in these cases the green paste might be prepared using different clay(s).

Due to the very reduced quantity of the 10 Å phases, the ceramics had to be fired above 700-750ºC. In samples 5-2-1 and 5-2-3 even gehlenite ($Ca_2Al[AlSiO_7]$) could be observed, which is peculiar to the fired pots (gehlenite appears at 800°C). [9]

The moderate presence of 10 Å phases in items 5-2-1, 5-2-2 and 5-2-4 could be attributed to their incipient re-hydration during the burial.

PXRD data in conjunction with the optical microscopy data allowed the identification of several thermal processes, mainly affecting the clayish matrix. The most important such processes are sintering (samples 5-2-1 and 5-2-2); formation of isotropic, amorphous and/or glassy areas in the matrix (5-2-3, 5-2-4, 5-2-5); developing of secondary pores and of stress cracks (5-2-3, 5-2-4, 5-2-5); partial decomposition of micas (5-2-3, 5-2-4, 5-2-5); appearance of reaction zones between the quartz clasts and matrix (especially in 5-2-4); melting of quartz rims and formation of a scalloped texture (5-2-4); finally, the almost totally lack of the small 2θ value kaolinite lines in the XRD of all ceramic samples.

On basis of these observations, the firing temperature estimated even in case of samples 5-2-1 and 5-2-2 was at least of 800⁰C, while in case of samples 5-2-3, 5-2-4 and 5-2-5 a firing temperature of approximately 1000⁰C can be assumed.

FTIR spectroscopy

FTIR spectra and the resultant data are presented in the Figure 5 and 6, and respectively in Table 5. Absorption frequencies were assigned considering the available literature data referring to the most common clay mineral components and previous investigations carried on (mainly ancient) ceramic samples [9-19].
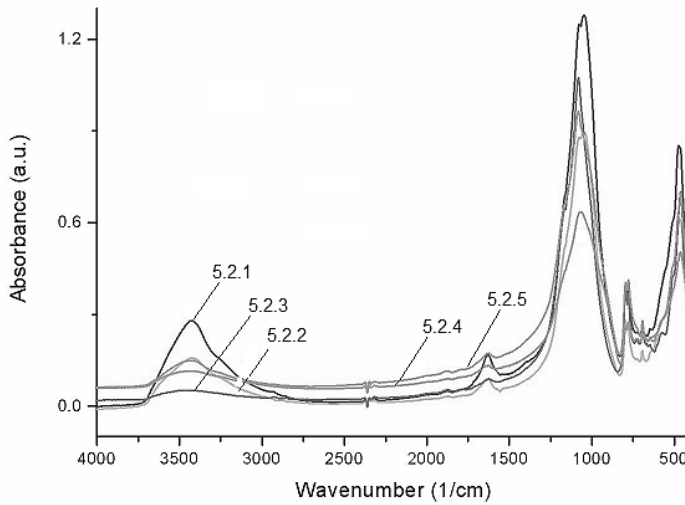
Figure 5. FTIR spectra of the ceramic samples (4000-400 cm^{-1}).

Figure 6 shows in more details the absorption bands of the 1600-400 cm^{-1} spectral domain (the SiO / AlO / MeO region).
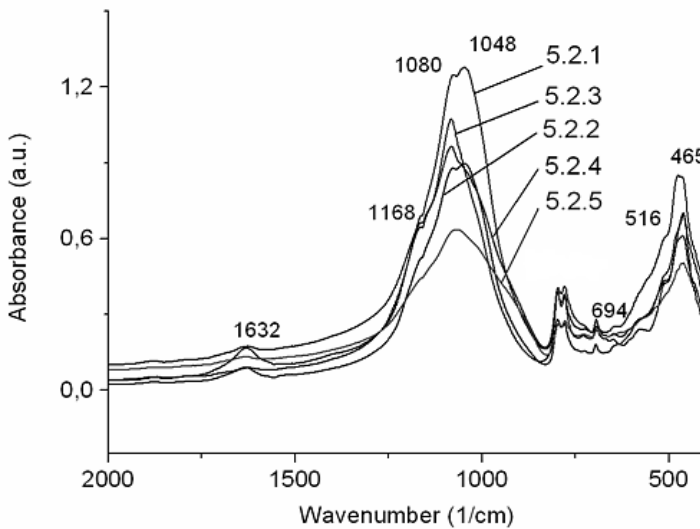

Figure 6. Extended FTIR spectra in the SiO / AlO / MeO domain.

166

Table 5. Experimental absorption frequencies and their assignments. [7-12]

Absorption frequencies (cm^{-1})					Assignment
5-2-1	5-2-2	5-2-3	5-2-4	5-2-5	
3429	3425	3455	3429	3439	Al-O-H (Mo)
			3333 sh		H-O-H, free O-H stretch of ads. water (Mo, Mu)
3285 sh	3285 sh				
2927		2927	2929		
2856		2857			
1631 m	1629 m	1625 v.w	1629 v.w	1631 v.w	H-O-H (Mo)
1162 sh	1162 sh	1164	1166 sh	1164 sh	H-O-H (Mo) Si-O (Mu)
1078	1078	1084	1082	1080	Si-O (Q)
1048	1046		1046 sh	1050	Si-O (Mo) Si-O-Si (Mu)
797	798	797	797	799	Si-O Si-O $\perp$ opt. axis (Q) (Al,Mg)-OH (Mo) Si-O-Al (Mu)
780	778	780	778	780	Si-O$\parallel$opt. axis (Q)
722	725	729	724 sh	723	Si-O-Al (Mu)
693	695	695	693	693	Si-O-Al (Mo, Mu) Si-O (Q)
	572 sh	577	577 sh	575 sh	Al-O-H (Mo)
553 sh					Si-O (Q, Mu)
512 sh	510 sh	512	510 sh	510 sh	Si-O (Q)
476	472 sh		478 sh	474 sh	Si-O(Q, Mo, Mu)
465	461	461	461	463	Si-O (Q, Mu) Si-O-Mg (Mo)
433 sh	431				Si-O (Q, Mo, Mu)

Abbreviations: sh: shoulder, s: sharp, m: medium intensity, w: weak, v, w: very weak; Q: quartz, Mo: montmorillonite, Mu: muscovite.

Infrared spectroscopy is a sensitive monitor of thermal processes (dehydration, dehydroxylation, redox transformations) occurred during the firing of clay minerals. Between 300-500ºC the dehydroxylation of octahedral layers of most clay minerals occur, as reflected by the marked attenuation of the bands due to Al-OH in-plane vibration at 920 cm^{-1} and respectively to translational vibrations involving OH at 522 cm^{-1}. By attaining 600ºC the intensity of hydroxyl bands in the 3700-3200 cm^{-1} region, respectively at 1100 and 920 cm^{-1} strongly decrease or disappear. The silicate structure collapses; a broad, nearly symmetrical band is formed at 1030 cm^{-1}.

Simultaneously, the iron oxides attributed 540 and 580 cm^{-1} bands appear. Between 700-900ºC crystallized hematite is formed, under reducing conditions magnetite also may form. The peak appearing at 572 cm^{-1} is due to Fe-O vibration of iron oxides, but the exact nature of oxide can not be determined from the IR spectrum. Quartz and feldspar are usually present in pottery clays. Bands occurring at 462 and 514 cm^{-1} are assigned to mixed Si-O-Si and O-Si-O bending mode; the band at 470 cm^{-1} is due to Si-O stretching. Sharp bands around 790 along with 695 cm^{-1} in all samples means the presence of quartz (Si-O).

Concerning the discussed samples, the relative weakness or the absence of characteristic OH bands around 3400 cm^{-1} and at 1600 cm^{-1} and the presence of a broad symmetry band centered around 1050 cm^{-1} in all cases means that all items were made of disordered clays and had to be fired above 600ºC. The presence and the intensity of the 3400 cm^{-1} and 1600 cm^{-1} peaks in this case depends on the rehydration processes taking place during the burial, in function of the environmental conditions and the ceramic composition and structure. Consequently, the most porous sample 5-2-1 shows the most intense hydroxyl peaks while they are almost totally missing from the spectrum of the most compact 5-2-3 probe.

Well resolved distinct peaks at 540 and 580 cm^{-1} reveal the presence of iron oxides, confirm that firing temperature was above 600ºC, and indicate that the sample was fired in oxidizing conditions, or at least that air has to be present from the beginning of cooling, which did enable (at least partly) the oxidation of the Fe content to Fe_2O_3 causing the red color of the pottery (air admission during cooling is still a common practice for coloration of the baked clays). The band around 540 cm^{-1} with a weak shoulder at 580 cm^{-1} in the sandwich structured items indicate that the sample is fired under reducing atmosphere, and air (oxygen) is admitted only at lower temperature (sandwich structure: inner black layer with outer red surface – sample 5-2-2).

The FTIR data and their possible interpretation, in concordance with the conclusions resulting from the OM and XRD analysis, confirm the presence of rehydrated amorphous glassy phases and the (re)apparition of $Fe(OH)_2$ and/or $FeO(OH)$. The presence of rehydrated clayish minerals is not excluded either, but their presence is of minimal importance.

CONCLUSIONS

The Tăşnad-Sere Roman potshard selection subjected to investigation is formed by five samples, chosen as the most representative ones regarding the studied archaeological context.

Optical microscopy (OM), PXRD and FTIR spectral analysis are all in agreement when allowing the classification of the samples into two distinct groups and a transitional item.

The first group (samples 5-2-1 and 5-2-2) is formed by deliberate tempered ceramics fired at lower temperatures (850-950ºC). The temper in these cases seems to be partly rock fragments as vulcanites and crystalline rocks (granitoides and crystalline schists). These ceramics could not be used as cooking wares due to their hiatal fabric resulted from the production technology: the thermal dilatation differences appearing in the fine and coarse grain connection zones eventually would cause the break of the ceramic body.

The specimens of the second group (5-2-3 and 5-2-5) were produced from naturally tempered levigated clay paste fired at higher temperatures, resulting suitable cooking wares.

Sample 5-2-4 is transitional between the first and the second group, its mineralogical characteristics approaching it to the first group while technologically (modelling, firing temperature and conditions) matching with the second one.

The concordance of the results obtained by the OM, PXRD and FTIR spectroscopy analysis proves that the pursued archaeometric study is fairly efficient and reliable to categorize and roughly estimate the provenance of the artifacts even in case of a few-numbered selection.

However, for correct conclusions regarding the provenance of the raw materials used it is compulsive the completion of the investigation with element analysis (especially trace element characterization) of the investigated items as well as of the corresponding clayish soils in the neighbourhood of the site (in ancient pottery proximity of the outcrops could assure considerable economic savings). In order to correctly characterize the technical parameters (especially the firing conditions) applied to the production process it is necessary to proceed to supplementary determinations. (like thermoanalytical measurements). [23]

EXPERIMENTAL

In order to estimate the variability of the raw material sources and of the technology used, after a macroscopic characterization, the samples were investigated by petrographic-mineralogic thin layer microscopy (OM), PXRD analysis and FTIR spectroscopy.

Polarized light microscopy was carried out in transmission mode on polished thin sections of d=30 μm, with a Leitz Wetzlar Laborlux 11 Pol microscope provided with Nikon Coolpix 995 camera.

PXRD analysis was performed using a BRUKER D8 Advance diffractometer (working parameters: 45 kV, 45mA, Ni filtered Cu K$_\alpha$ radiation collimated with Soller slits, step-scanning mode with $\Delta 2\theta$ of 0.01° steps, spectral pure Al_2O_3 internal standard). The sample support was uniformly coated with the finely pulverized ceramic sample (agate ball mill, mean particle diameter < 63 μm, PVC-based adhesive). The *crystalline phase composition* was determined using the MATCH! phase identification software and the IUCr/COD/AMCSD reference database [20-22].

FTIR absorption spectra were recorded on KBr-pelletized samples (1 mg finely pulverized sample to 300 mg KBr) in the 4000-400 cm^{-1} region with a JASCO FTIR-6100 spectrometer (1.0 cm^{-1} resolution).

ACKNOWLEDGEMENTS

REFERENCES

1. R. Martineau, A.V. Walter-Simonnet, B. Grobéty, M. Buatier, *Archaeometry,* **2007**, *49*, 23.
2. N. Iercoşan, , *Studii şi Comunicări Satu Mare,* **1994-1995**, *11-12*, 9.
3. C. Astalos, U. Sommer, C. Virag, *Archaeology International*, **2012-2013**, *16*, 47.
4. C. Virag, "Some aspects about the Neolithic settlement from Tasnad (Satu Mare County, Romania)", C. Virag, Ed., Proceedings of the Int. Conf. on Neolithic Cultural Phenomena in the Upper Tisa Basin, Satu Mare 2014, Editura Muzeului Sătmărean, **2015**, 97.
5. *** "Cronica cercetărilor arheologice din România – campania 2004". XXXIX. Sesiune Naţională de Rapoarte Arheologice, Jupiter-Mangalia 2005, M.V. Angelescu, I. Oberlander-Târnoveanu, F. Vasilescu, Eds,: cIMeC – Institutul de Memorie Culturală, Bucuresti, ISBN 973-7930-03-7, **2005**, 375.

6. *** "Cronica cercetărilor arheologice din România – campania 2005", XL. Sesiune Naţională de Rapoarte Arheologice, Constanţa 2006, M.V. Angelescu, F. Vasilescu, Eds:, cIMeC – Institutul de Memorie Culturală, Bucuresti, ISBN 973-7930-07-X, **2006**, 359 and 479.
7. *** "Cronica cercetărilor arheologice din România – campania 2006", XLI. Sesiune Naţională de Rapoarte Arheologice, Tulcea 2006, M.V. Angelescu, F. Vasilescu, Eds:, cIMeC – Institutul de Memorie Culturală, Bucuresti, ISBN 978-973-87004-9-9, **2007**, 365 and 477.
8. R.L. Folk, P.B. Andrews, D.W. Lewis, *New Zealand Journal of Geology and Geophysics*, **1970**, *13*, 937.
9. J. Kiuberis, A. Merkevičius, R. Juškėnas, A. Kareiva, *Materials Science*, **2004**, *10*, 334.
10. G. Cultrone, C. Rodriguez-Navarro, E. Sebastian, O. Cazalla, M.J. de la Torre, *European Journal of Mineralogy,* **2001***, 13*, 621.
11. De Benedetto, G.E., Laviano, R., Sabbatini, L., Zambonin, P.G., *Journal of Cultural Heritage*, **2002**, *3*, 177.
12. S. Shoval, *Optical Materials*, **2003**, *24*, 117.
13. R. Venkatachalapathy, E. Manoharan, S. Dhanapandian, T. Sundareswaran, K. Deenadayalan, "Concepts of Biophysics", Kumar, A., Ed., APH (New Delhi). **2005**, 71.
14. R. Palanivel, G. Velraj, *Indian Journal of Pure and Applied Physics*, **2007**, 45, 501.
15. C. Manoharan, K. Veeramuthu, R. Venkatachalapathy, T. Radhakrishna, R. Ilango, *Lithuanian Journal of Physics and Technical Sciences*, **2008,** *48*, 195.
16. R. Ravisankar, S. Kiruba, P. Eswaran, G. Senthilkumar, A. Chandrasekaran, *E-Journal of Chemistry*, **2010**, *7*, S185.
17. R. Palanivel, U.R. Kumar, *Romanian Journal of Physics*, **2011**, *56*, 195.
18. S. Kramar, J. Lux, *Materials and technology,* **2015**, *49*, 503.
19. S. Kiruba, S. Ganesan, *Spectrochimica Acta Part A: Molecular and Biomolecular Spectroscopy*, **2015**, *145*, 594.
20. *http://www.crystalimpact.com/match/*
21. *http://sdpd.univ-lemans.fr/cod*
22. R.T. Downs, M. Hall-Wallace, *American Mineralogist*, **2003**, *88*, 247.
23. P. Comodi, S. Nazzareni, D. Perugini, M. Bergamini, *Periodico di Mineralogia*, 2006, *75*, 95.

THERMAL ANALYSIS OF PURE AND MULTISUBSTITUTED HYDROXYAPATITE PASTES

EDIT FORIZS[a], FIRUTA GOGA[a], ALEXANDRA AVRAM[a], AURORA MOCANU[a,*], IOAN PETEAN[a], OSSI HOROVITZ[a], MARIA TOMOAIA-COTISEL[a,b]

ABSTRACT. The thermal stability over time of the pure and multisubstituted hydroxyapatite (HAP) pastes, doped with magnesium, silicon, strontium and zinc, synthesized using aqueous precipitation method were investigated by thermal analyses (TG-DTA). Results show high thermal stability of pure and multidoped hydroxyapatite pastes, up to 1000 °C and even after ageing for 1 year, making these pastes promising nano materials for medical applications.

Keywords: hydroxyapatite, doped hydroxyapatites, paste, thermal analysis

INTRODUCTION

The hydroxyapatite, $Ca_{10}(PO_4)_6(OH)_2$ (HAP), composition is similar to bone, has good biocompatibility and bioactivity therefore is increasingly used in medicine, especially in repairing bone defects as bone grafts, coating material for metallic implants, dental implants, and drug delivery systems [1-3]. Nanocrystalline HAP paste is suitable bone substitute in dental and orthopedic surgery for filling bone defects in minimally invasive surgery. HAP pastes have various applications: as tooth pastes for remineralising and repairing of teeth enamel, for the fabrication of 3D printed bioactive ceramic scaffolds [2, 4].

The biological properties of HAP based materials can be improved by the incorporation of divalent essential metal ions. The effect of silicon [5, 6], magnesium [7, 8], strontium [9, 10], manganese [11] and zinc [11-13] as doping elements on characteristics of hydroxyapatite with potential biomedical applications has been studied extensively [1, 2, 11].

---

[a] *Babeş-Bolyai University, Faculty of Chemistry and Chemical Engineering, 11 Arany János str., RO-400028, Cluj-Napoca, Romania*
[b] *Academy of Romanian Scientists, 54 Splaiul Independentei, RO-050094 Bucharest, Romania*
* *Corresponding author amocanu@chem.ubbcluj.ro*

Multidoped hydroxyapatites with improved properties are more suitable for biomedical application, thus many recent studies have focused on simultaneous doping of hydroxyapatite with copper, zinc and carbonate ions [14]; manganese and strontium [15], strontium and copper [16] and magnesium, zinc and silicon [17, 18]. Hydroxyapatite co-doped with strontium and magnesium, strontium and zinc, magnesium and zinc [19] and simultaneously doped with three essential elements Sr, Mg and Mn [20] and Sr, Mg and Zn [21] were also reported.

Continuing our interest in the field of bioactive materials [22-26] we present here some results concerning thermal stability of three HAP pastes simultaneously doped with essential elements magnesium, strontium, silicon and zinc, with previously described compositions [27]. Water content of pastes was determined by thermal analysis. The thermal stability of the pastes was monitored for one year, namely thermal analyses were performed after 4 months and one year from their preparation.

RESULTS AND DISCUSSION

Thermal stability over time, of four hydroxyapatite pastes, with previously reported composition [27] were investigated, namely pure hydroxyapatite (HAP, 1) and doped HAP pastes, containing Mg 1.5 wt%, Zn 0.2 wt% and Si 0.2 wt% (2); Mg 1.5 wt%, Zn 0.2 wt%, Si 0.2 wt% and Sr 5 wt% (3) and Mg 1.5 wt%, Zn 0.2 wt%, Si 0.2 wt% and Sr 10 wt% (4). The pure and doped pastes kept under storage conditions for 4 months, respectively 1 year, at room temperature in well-closed conditions, were heated in air with the rate of 10 °C/min from the room temperature up to 1000 °C. Thermogravimetric data are presented in Table 1 and in Figures 1 and 2.

Table 1. Thermogravimetric data of pure and doped HAP pastes, after 4 months

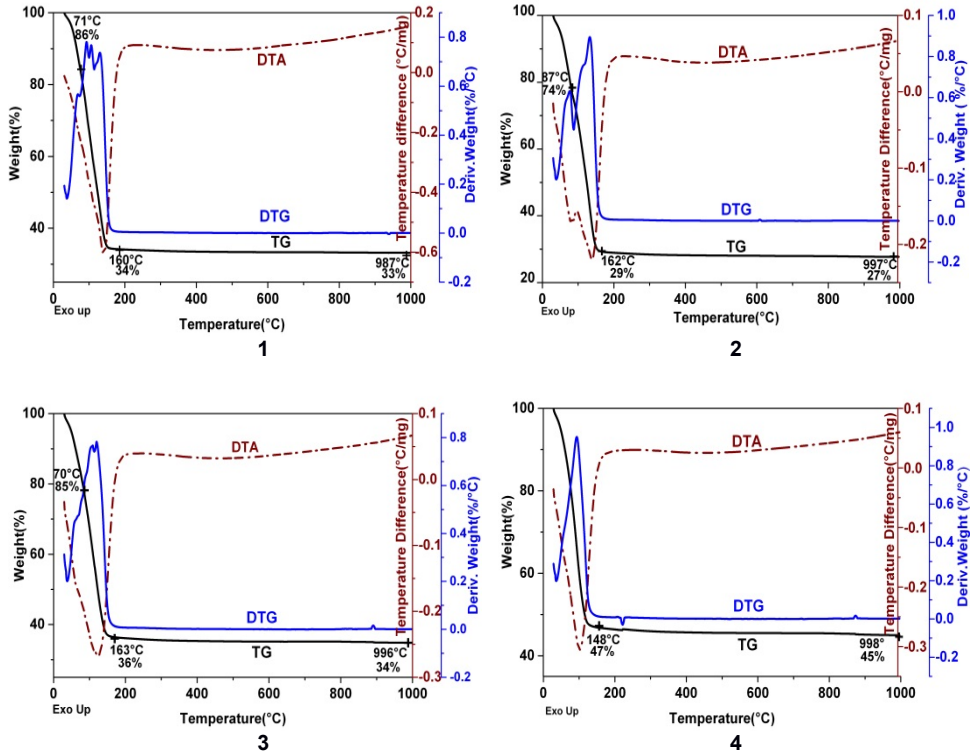| Paste	Temperature (°C)	Weight loss (%)
1. HAP	30-160	65.96
	160-1000	1.19
	30-1000	**67.15**
2. HAP 1.5%Mg, 0.2%Si, 0.2%Zn	30-162	71.08
	162-1000	1.68
	30-1000	**72.76**
3. HAP 1.5%Mg, 0.2%Si, 0.2%Zn, 5%Sr	30-163	64.11
	163-1000	1.67
	30-1000	**65.78**
4. HAP 1.5%Mg, 0.2%Si, 0.2%Zn, 10%Sr	30-150	53.22
	150-1000	1.93
	30-1000	**55.15**

Figure 1. Thermal curves of the four pastes: 1) pure HAP (sample 1); 2) HAP 1.5%Mg, 0.2%Si, 0.2%Zn (sample 2); 3) HAP 1.5%Mg, 0.2%Si, 0.2%Zn, 5%Sr (sample 3); 4) HAP 1.5%Mg, 0.2%Si, 0.2%Zn, 10%Sr (sample 4), after 4 months.

Thermal analysis shows that the thermal curves (TG, DTA) of the pure and the doped HAP pastes have the same shape in the range of 30-1000 °C. After 4 months no significant differences were observed in thermal behavior. The only differences refer to the moisture content of the sample. Thermogravimetric monitoring of weight loss shows that weight of all samples decreases continuously with increasing temperature. The highest weight loss occurs in the range 30-200 °C and can be attributed to very high water content of pastes, since the water molecules surround the hydroxyapatite particles. The corresponding DTA data indicate an endothermic transformation for all samples at around 160 °C (Fig. 1 and 3).
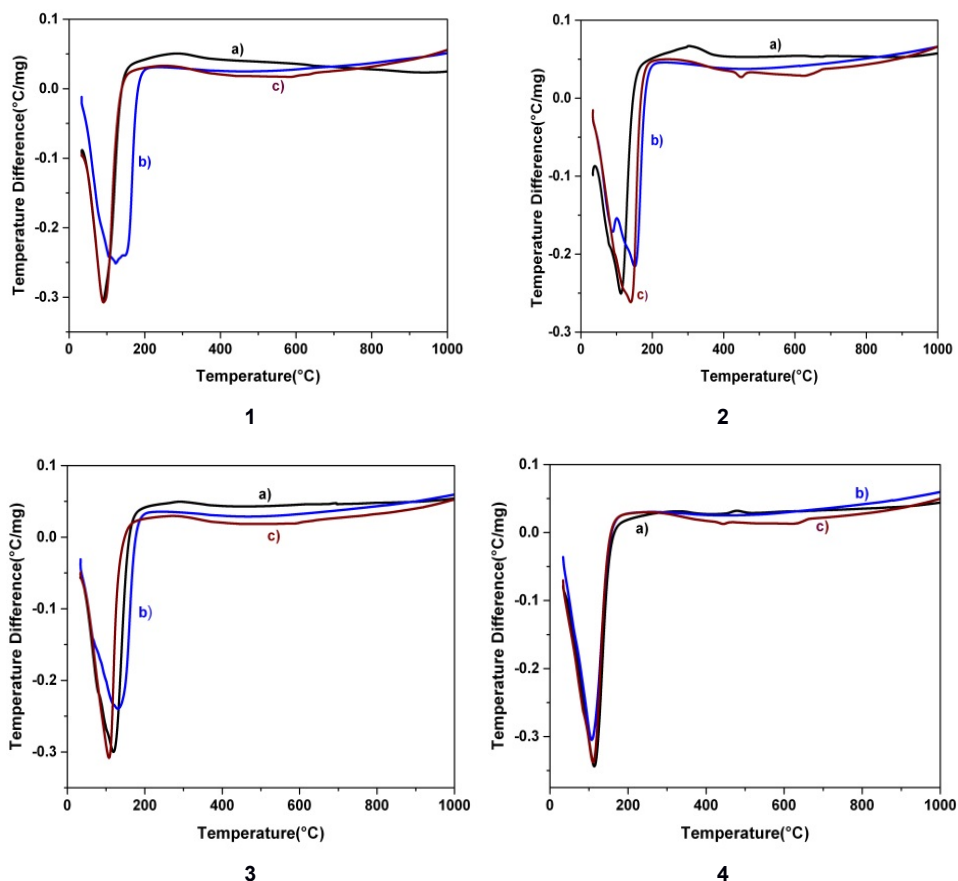
Figure 2. Comparative DTA curves for fresh (a), 4 months (b) and 1 year (c) old samples: 1) pure HAP (sample 1); 2) HAP 1.5%Mg, 0.2%Si, 0.2%Zn (sample 2); 3) HAP 1.5 % Mg, 0.2%Si, 0.2%Zn, 5%Sr (sample 3); 4) HAP 1.5% Mg, 0.2%Si, 0.2%Zn, 10%Sr (sample 4).

The weight loss in the range 30-200 °C was 53.5-71.3%; it indicates the removal of moisture and physically adsorbed water, followed in the temperature range of 200-1000 °C by small gradual weight loss, 1-2%, which can be associated with the removal of chemically adsorbed water on the surface of HAPs particles, in agreement with the literature data [27, 28].

Above 200 °C the thermogravimetric curves became parallel to each other and up to 1000 °C (Figure 1 and 3) with x-axis. Pure and doped HAP pastes are very stable up to 1000 °C, as found for at least one year aged samples.
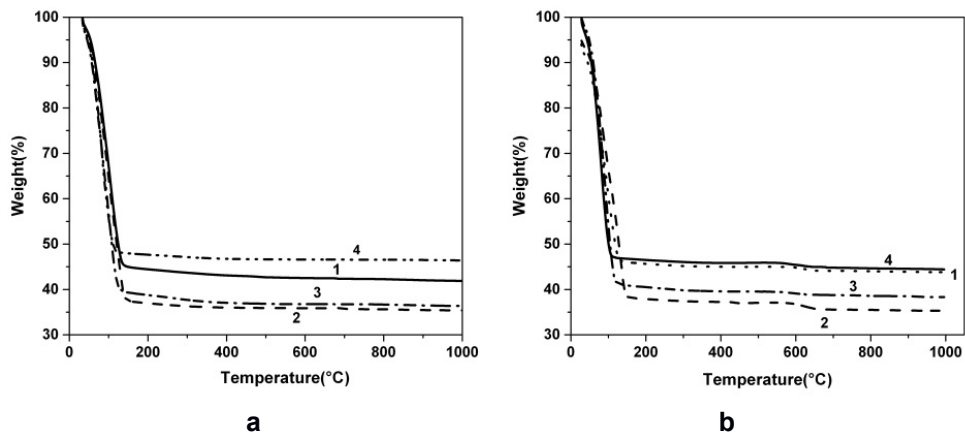
Figure 3. TG curves for fresh pastes (a) and 1 year aged (b) pastes:
1) pure HAP (sample 1); 2) HAP 1.5% Mg, 0.2%Si, 0.2%Zn (sample 2);
3) HAP 1.5%Mg, 0.2%Si, 0.2%Zn, 5%Sr (sample 3); 4) HAP 1.5%Mg,
0.2%Si, 0.2%Zn, 10%Sr (sample 4).

The pure and doped hydroxyapatite pastes may contain small content of carbonate, whose decomposition cause insignificant mass loss. The moisture content of these pastes is high but comparable with those found for commercial available pure HAP paste [27].

CONCLUSIONS

The results of thermal analysis confirm high thermal stability of pure and multidoped hydroxyapatite pastes, up to 1000 °C, even after ageing for 1 year from their preparation. The thermal behavior of pure and doped hydroxyapatite pastes in time shows that this depends mainly on the loss of physically adsorbed and chemically bounded water. The high stability of these ceramic pastes without significant modifications in the structure of pastes makes them appropriately for further use in biomedical applications, as drug delivery systems of antimicrobials and for coating of metallic implants.

EXPERIMENTAL SECTION

Materials and methods

The following compounds were used as starting materials: $Ca(NO_3)_2 \cdot 4H_2O$, $(NH_4)_2HPO_4$, $Mg(NO_3)_2 \cdot 6H_2O$, $Zn(NO_3)_2 \cdot 6H_2O$, $Sr(NO_3)_2$ and tetraethyl orthosilicate $(C_2H_5O)_4Si$, (TEOS). Pure HAP and three doped

hydroxyapatites with the same content of Mg, Zn, Si and different contents in Sr were obtained by a wet precipitation method, previously reported [6, 10, 13, 26]. All chemicals were reagent grade procured from Merck and Sigma-Aldrich, solutions were prepared with double distilled water, deionized in Elgastat purification system.

Synthesis of pure HAP and doped HAP

A pure HAP paste was prepared by wet precipitation method, previously described [6, 10, 13, 26]; using equal volumes of aqueous 0.25 M Ca^{2+} solutions and 0.15 M PO_4^{3-} solutions. The pH of the reaction mixture was fixed at 11.5 using 25% ammonia solution (Ca/P atomic ratio 1.67). The reaction mixture was stirred 24 h at 22 °C, and 24 h at 70 °C. The precipitated solid phase was filtered, washed with distilled water until pH 7. The wet precipitate, considered paste was used as it is.

The doped hydroxyapatites were obtained similarly, with the following modification: the Ca^{2+} containing solution contains also the doping cations (0.25 M in $Ca^{2+}+Mg^{2+}+Zn^{2+}+Sr^{2+}$) in calculated amount for the proposed composition of the doped HAP. The anions containing solution (0.15 M in $PO_4^{3-}+SiO_4^{4-}$) was obtained from $(NH_4)_2HPO_4$, and tetraethyl orthosilicate, TEOS. The pH was fixed at 11.5 by adding a 25% ammonia solution. Equal volumes of the two solutions were mixed at 22 °C keeping the mole ratio (Ca+Mg+Zn+Sr)/(P+Si) at the value of 1.67. The obtained pastes were processed in the same way as the pure HAP.

Characterization methods

Thermal behavior of pure HAP and doped HAP pastes was determined by thermogravimetric analysis (TGA), for the temperature range from 30-1000 °C, using Universal SDTQ600 TA Instruments. Samples were heated in alumina crucibles at a constant heating rate of 10 °C/min, in flowing air, using simultaneous TG/DTG-DTA/DSC techniques.

REFERENCES

1. M. Bayani, S. Torabi, A. Shahnaz, M. Pourali, *Biotechnology & Biotechnological Equipment*, **2017**, *31*(2), 215.
2. N. Eliaz, N. Metoki, *Biomaterials,* **2017**, *10(4)*, 334.
3. V. Hruschka, S. Tangl, Y. Ryabenkova, P. Heimel, D. Barnewitz, G. Möbus, C. Keibl, J. Ferguson, P. Quadros, C. Miller, R. Goodchold, W. Austin, H. Redl, T. Nau, *Scientific Reports*, **2017**, 7:43425.
4. L. Witek, Y. Shi, J. Smay, *Journal of Advanced Ceramics*, **2017**, *6(2)*, 157.
5. Z.-Y. Qiu, I.-S. Noh, S.-M. Zhang, *Frontiers of Materials Science,* **2013**, *7(1)*, 40.
6. Gh. Tomoaia, A. Mocanu, I. Vida-Simiti, N. Jumate, L.-D. Bobos, O. Soritau, M. Tomoaia-Cotisel, *Materials Sciences and Engineering C*, **2014**, *37*, 37.
7. D. Laurencin, N. Almora-Barrios, N.H. de Leeuw, C. Gervais, C. Bonhomme, F. Mauri, W. Chrzanowski, J.C. Knowles, R.J. Newport, A. Wong, Z. Gan, M.E. Smith, *Biomaterials*, **2011**, *32*, 1826.
8. A. Farzadi, F. Bakhshi, M. Solati-Hashjin, M. Asadi-Eydivand, N.A.A. Osman, *Ceramics International*, **2014**, *40*, 6021.
9. C.F. Marques, A. Lemos, S.I. Vieira, O.A.B. da Cruz e Silva, A. Bettencourt, J.M.F. Ferreira, *Ceramics International*, **2016**, *42*, 2706.
10. P.T. Frangopol, A. Mocanu, V. Almasan, C. Garbo, R. Balint, G. Borodi, I. Bratu, O. Horovitz, M. Tomoaia-Cotisel, *Revue Roumaine de Chimie,* **2016**, *61*(4-5), 337.
11. E. Boanini, M. Gazzano, A. Bigi, *Acta Biomaterialia*, **2010**, *6*, 1882.
12. Z.-S. Tao, W.-S. Zhou, X.-W. He, W. Liu, B.-L. Bai, Q. Zhou, Z.-L. Huang, K.-K. Tu, H. Li, T. Sun, Y.-X. Lv, W. Cui, L. Yang, *Materials Science and Engineering C*, **2016**, *62*, 226.
13. C. Garbo, M.Sindilaru, A. Carlea, Gh. Tomoaia, V. Almasan, I. Petean, A. Mocanu, O. Horovitz, M. Tomoaia-Cotisel, *Particulate Science and Technology,* **2017**, *35(1),* 29.
14. O. Livitska, N. Strutynska, I. Zatovsky, I. Nikolenko, N. Slobodyanik, Y. Prylutskyy, M. Epple, O. Prymak, A. Byeda, *Mat.-wiss. u. Werkstofftech*., **2016**, *47(2–3)*, 85.
15. Y. Huang, H. Qiao, X. Nian, X. Zhang, X. Zhang, G. Song, Z. Xu, H. Zhang, S. Han, *Surface and Coating Technology*, **2016**, *291*, 205.
16. Y. Huang, M. Hao, X. Nian, H. Qiao, X. Zhang, X. Zhang, G. Song, J. Guo, X. Pang, H. Zhang, *Ceramics International*, **2016**, *42*, 11876.
17. Gh. Tomoaia, M. Tomoaia-Cotisel, L.-B. Pop, A. Pop, O. Horovitz, A. Mocanu, N. Jumate, L.-D. Bobos, *Revue Roumaine de Chimie,* **2011**, *56 (10-11)*, 1039.
18. Gh. Tomoaia, O. Soritau, M. Tomoaia-Cotisel, L.-B. Pop, A. Pop, A. Mocanu, O. Horovitz, L.-D. Bobos, *Powder Technology,* **2013**, *238*, 99.
19. O. Kaygili, S. Keser, *Materials Letters*, **2015**, *141*, 161.

20. M.P. Moreira, G.D. de Almeida Soares, J. Dentzer, K. Anselme, L.A. de Sena, A. Kuznetsov, E.A. dos Santos, *Materials Science and Engineering* C, **2016**, *61*, 736.
21. D. Gopi, E. Shinyjoy, L. Kavitha, *Ceramics International,* **2015**, *41*, 5454.
22. E. Forizs, A. Debreczeni, A. Patrut, A.-Z. Kun, I.B. Cozar, L. David, I. Silaghi-Dumitrescu, *Revue Roumaine de Chimie,* **2010**, *55(10)*, 697.
23. P. Bombicz, J. Madarasz, E. Forizs, M. Czugler, G. Pokol, S. Gal, A. Kalman, *Zeitschrift fur Kristallographie*, **2000**, *215*, 317.
24. F. Goga, E. Forizs, A. Avram, A. Rotaru, A. Lucian, I. Petean, A. Mocanu, M. Tomoaia-Cotisel, *Revista de Chimie (Bucharest)*, **2017**, *68(6)*, 1193.
25. O. Horovitz, Gh. Tomoaia, A. Mocanu, T. Yupsanis, M. Tomoaia-Cotisel, *Gold Bulletin*, **2007**, *40(4)*, 295.
26. G. Furtos, M. Tomoaia-Cotisel, C. Garbo, M. Senila, N. Jumate, I. Vida-Simiti, C. Prejmerean, *Particulate Science and Technology*, **2013**, *31(4)*, 392.
27. F. Goga, E. Forizs, G. Borodi, Gh. Tomoaia, A. Avram, R. Balint, A. Mocanu, O. Horovitz, M. Tomoaia-Cotisel, *Revista de Chimie (Bucharest)*, **2017**, *68(12)*, in press.
28. Y.Y. Özbek, F.E. Bastan, F. Űstel, *Journal of Thermal Analysis and Calorimetry,* **2016**, *125*, 745.

SYNTHESIS, THERMAL BEHAVIOR AND SPECTROSCOPIC INVESTIGATIONS OF METAL COMPLEXES WITH *N*-MODIFIED GLYCINE AS LIGAND

CARMEN SACALIS[a*], FIRUTA GOGA[a], LEONTIN DAVID[b]

ABSTRACT. The Cu(II), Co(II) and Ni(II) complexes with *N*-modified glycine derived from *p*-nitrophenylserinol were synthesized and characterized by their spectral and thermal properties. The thermal stability of the ligand and synthesized complexes was discussed in the 20-700°C temperature range. The results indicate that the organic compound acts as a bidentate ligand, its coordination involving the carboxylate oxygen and the nitrogen atom belonging to the amino group of the glycine fragment. All complexes correspond to the molar ratio M : L : H$_2$O = 1 : 2 : 2. The shape of the ESR spectra at room temperature and the principal values of the g tensor suggest a pseudotetrahedral local symmetry around the metal ions.

Keywords: glycine, metal complexes, thermal behavior, spectroscopic studies

INTRODUCTION

Amino acids play a crucial role in intra-cellular process of living organism. A lot of biochemical processes involve metal ions. The metal-amino acid interaction can be treated as a model of metal-protein system. The study of model species such as the simple amino acids can assist in the interpretation of more complex system. Complexes of transition metals with amino acids like glycine, very small biomolecules, have received much attention because they proved biological activity such as antibacterial, antimicrobial or antifungal activities [1-4].

[a] *Babeş-Bolyai University, Faculty of Chemistry and Chemical Engineering, 11 Arany Janos str., RO-400028, Cluj-Napoca, Romania*
[b] *Babeş-Bolyai University, Faculty of Physics, 1 Mihail Kogalniceanu str., RO-400084, Cluj-Napoca, Romania*
* *Corresponding author: cbatiu@chem.ubbcluj.ro*

In-vitro studies of coordination complexes of Mn(II), Co(II), Ni(II), Cu(II), Cd(II) with glycine and phenylalanine indicated antimicrobial activity for Gram-positive bacteria such as *Bacillus subtilis* and *Staphylococcus aureus,* and Gram-negative such as *E.coli, Pseudomonas aeruginosa, Proteus vulgaris* and *Candida albicans* [3].

Recently studies of copper (II) complex with glycine report that is a very good antifungal agent for *Phytophthora Capsici*, an important pathogenic species which causes serious disease on plants [5].

Other research indicates that *N*-substituted glycine and their transition metal complexes act as hydrogen buffers in biological reactions [6]. *N*-modified glycines have a lot of applications in biomedicine as analogue of anticonvulsant and antiepileptic agent Milacemide, as *building-units* for *N*-backbone cyclic peptides, even in the detergent industry [7-9].

The ligand **L**=2-[(*1S,2S*)-1,3-dihydroxy-1-(4-nitrophenyl)propan-2-yl-amino]acetic acid (Figure 1), was obtained by a literature procedure by treatment of *p*-nitrophenylserinol with the monochloroacetic acid/Na_2CO_3 system and investigated by spectroscopic methods [10].

Taking into account the important biochemical applications of *N*-modified glycine, we report the synthesis, the spectroscopic and thermogravimetric investigation of the ligand **L** and its transition metal complexes with Cu(II), Co(II) and Ni(II).
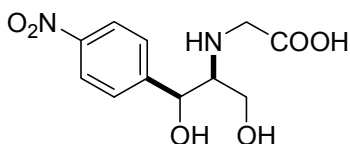
Figure 1. Structure formula of ligand **L** : 2-[(*1S,2S*)-1,3-dihydroxy-1-(4-nitrophenyl)propan-2-yl-amino]acetic acid

RESULTS AND DISCUSSION

The structure of the metal complexes

The complexation reaction of Cu(II), Co(II) and Ni(II) salts with the ligand solution in each case yields a solid product. All complexes are colored, microcrystalline and stable at room temperature. They are also insoluble in water, non-polar organic solvents (diethyl ether, $CHCl_3$, CCl_4, benzene and toluene) but soluble in methanol or DMSO. Higher melting points of these products as well their different colors when compared to that of the ligand **L**, indicate the formation of metal complexes.

The elemental analysis data (Table 1) and thermal analysis data (Table 2) indicate the molar ratio Metal : Ligand : H_2O = 1 : 2 : 2., for each complex.

The UV-VIS spectra in CH_3OH_{abs} for the complexes (**1**-**3**) indicate a slight bathochromic shift by 4-6 nm, but a considerable hyperchromic increase effect of absorbance comparative to the spectrum of the initial ligand (**L**), like the other similar complexes [4, 11, 12]. The shift of $n \rightarrow \pi^*$ characteristic band in the UV spectra attributed to the C=O bond ($26\overline{2}.4$ nm for the ligand; lit. for glycine 270 nm [4]) is due to the involving of the non-bonding electron pairs of the oxygen in the metal-ligand bond formation. The study shows that the absorption spectra of the obtained complexes are determined by the coordinated organic ligand provides from amino acids what is typical for transitional metal complexes [13-15].

Another proof for the complexation process is the HRMS spectrum for the ligand and its metal complexes (Figure 2a-c). The M+1 peak supports the complexation idea with the transition metal ions, for each of them.
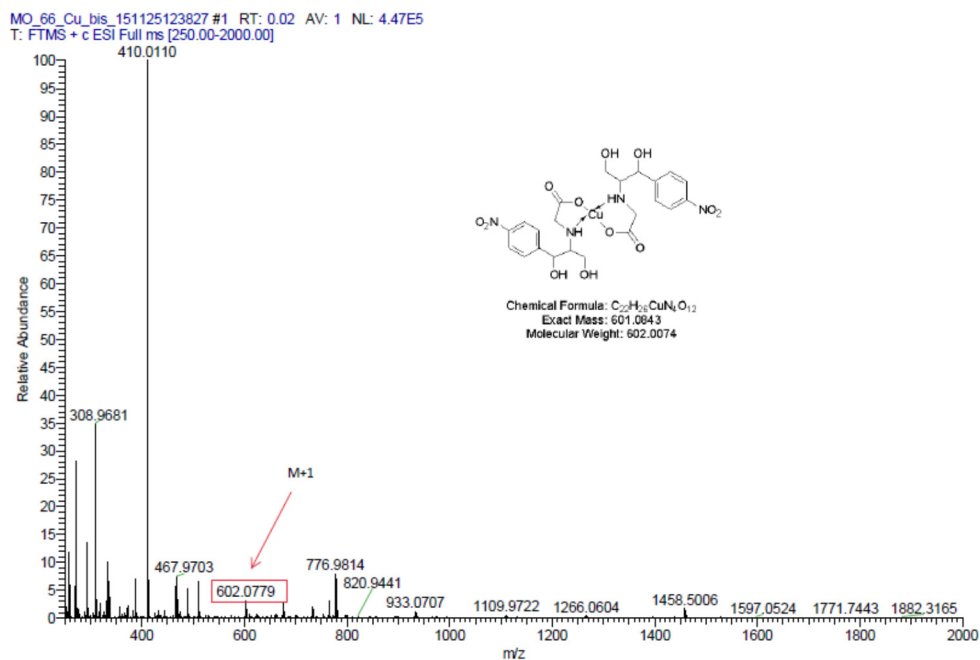

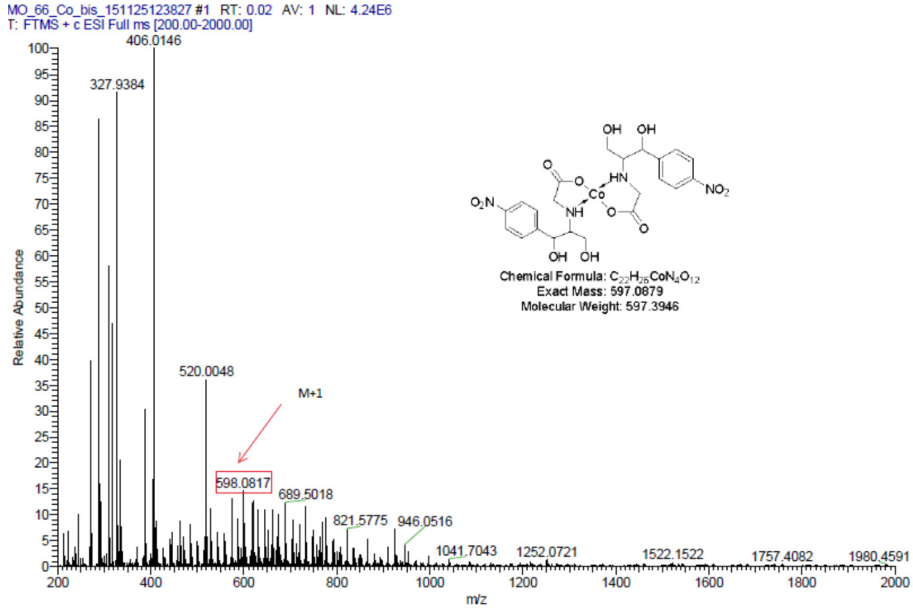**Figure 2a.** HRMS spectrum (ESI) of copper complex

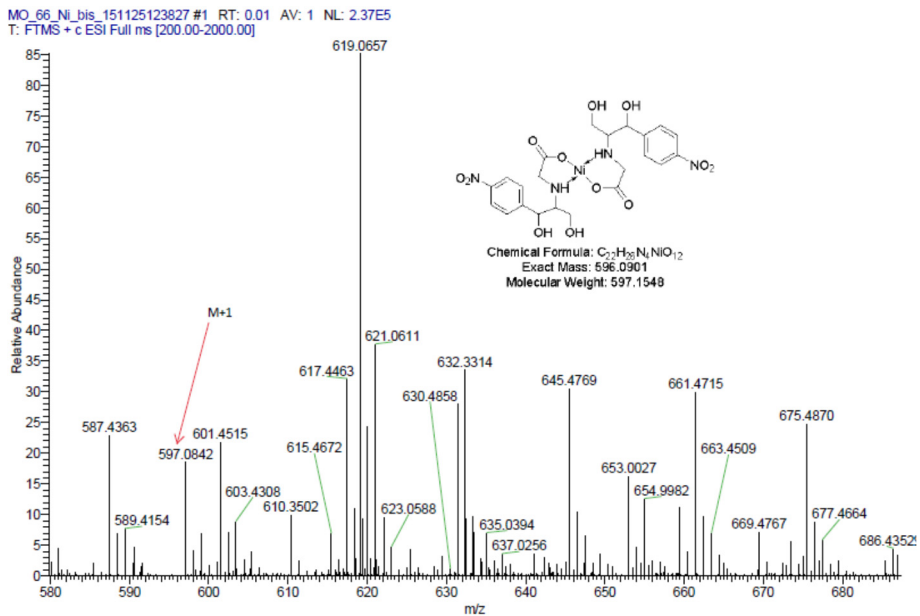**Figure 2b.** HRMS spectrum (ESI) of cobalt complex

Figure 2c. HRMS spectrum (ESI) of nickel complex

Table 1. Physico-chemical and elemental analysis data of the ligand **L** and its metal complexes (**1**-**3**)

Compound		$C_{11}H_{14}N_2O_6$ (**L**)	$C_{22}H_{30}CuN_4O_{14}$ (**1**)	$C_{22}H_{30}CoN_4O_{14}$ (**2**)	$C_{22}H_{30}NiN_4O_{14}$ (**3**)
Molec.Weight		270.2387	638.0380	633.4252	633.1854
Yield [%]		58	94	79	40
Colour		yellow-pale powder	green-turquoise powder	ecru powder	greenish-yellow powder
$[\alpha]_{546}^{25}$ (c=0.5 CH_3OH)		+52.42	-53.13	-92.88	-126.51
Melting point [^0C]		213-4	233-4	285-6	254-5
Visible absorption spectrum data, in CH_3OH_{abs}	Λ_{max} (nm)	262.4	266.9	268.1	267.5
	ε	963	3854	3383	3420
	A	0.499155	1.429968	0.962325	1.088011
Elemental analysis data [%] found. (calcd.)	C	48.57 (48.89)	40.66 (41.41)	40.61 (41.72)	41.67 (41.73)
	H	4.90 (5.22)	4.37 (4.74)	4.32 (4.77)	4.39 (4.78)
	N	10.36 (10.37)	8.77 (8.78)	8.61 (8.85)	8.84 (8.85)

Thermal investigation

The thermal behaviors of the ligand (**L**) and its metal complexes (**1**-**3**) are summarized in Table 2 and Figure 3a-d.

The thermogravimetric analysis indicated that the ligand (**L**) is anhydrous and the decomposition involved three steps. In the temperature range 30-194^{0}C a small endothermic peak at 56^{0}C with a mass loss of 1.12% represented the loss of residual water present in the pores. This phenomenon could be explained by the general synthesis of the ligand from aqueous solution [10].

The first decomposition step occurred in the temperature range 194-240^{0}C and it has been accompanied by an endo peak at 233^{0}C. This process could be assigned to the NO_2 group cleavage from the aromatic ring accompanied by the melting, according to the literature data for other nitro-derivatives analogous [10, 16-18]. In the second stage of decomposition of ligand two exothermic peaks at 248^{0}C, respectively at 347^{0}C, indicated the cleavage of glycine rest accompanied by oxidation processes. The last step occurred in the temperature range 452-700^{0}C and it has been accompanied by two strongly exothermic effects at 580^{0}C and at 616^{0}C which indicated the pyrolysis of organic rest. The theoretic weight loss (50.05%) and the experimental one (49.55%) agree with the loss of remaining organic rest. At 637^{0}C the ligand was completely pyrolized.
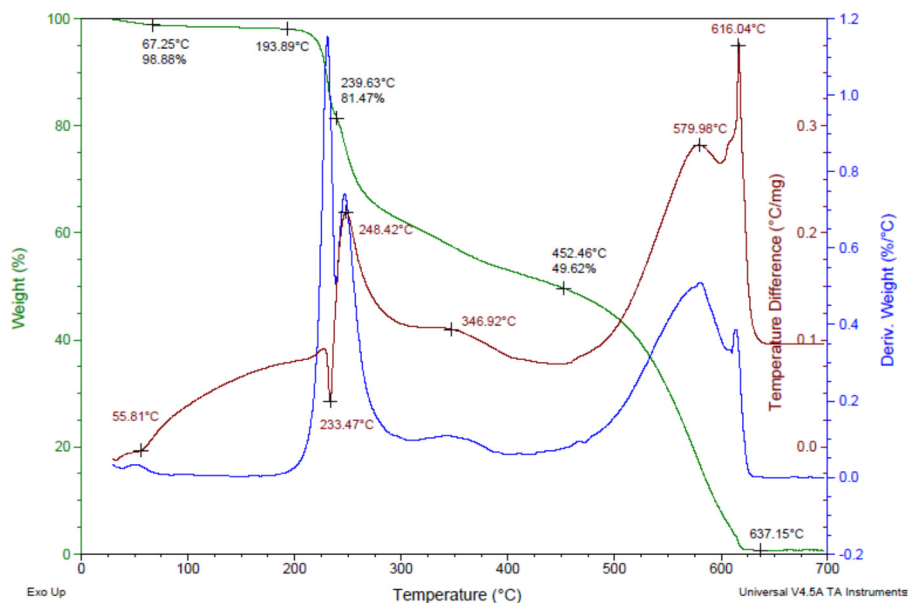
Figure 3a. TG-DTG-DTA diagram for the ligand **L**

The aim of the thermal analysis of the metal complexes is to obtain information concerning their thermal stability of these and to decide whether the water molecules are inside or outside the coordination sphere.

The decomposition of each metal complex occurs in two or three steps. First step corresponds to the loss of water molecules. After that, partial decomposition and then total decomposition of organic ligands takes place. The final products of the pyrolysis are metal oxides.

Thermal decomposition of the copper complex (**1**) was achieved in three stages. These mass losses occur in the temperature range of 30-192^{0}C, 192-250^{0}C and 250-700^{0}C. The first step with an estimated mass loss of 6.40% (calculated 5.64%) could be assigned to loss of 2 moles of hydration water. The second stage of decomposition was observed in the 192-250^{0}C with a mass loss of 40.93% (calculated 38.88%) and corresponds to a glycine rest and nitro-groups loss. The third-stage decomposition takes place at 250-700^{0}C with two exothermic peaks at 325^{0}C, respectively 352^{0}C and corresponds to the pyrolysis of organic rest. The final product is CuO residue.
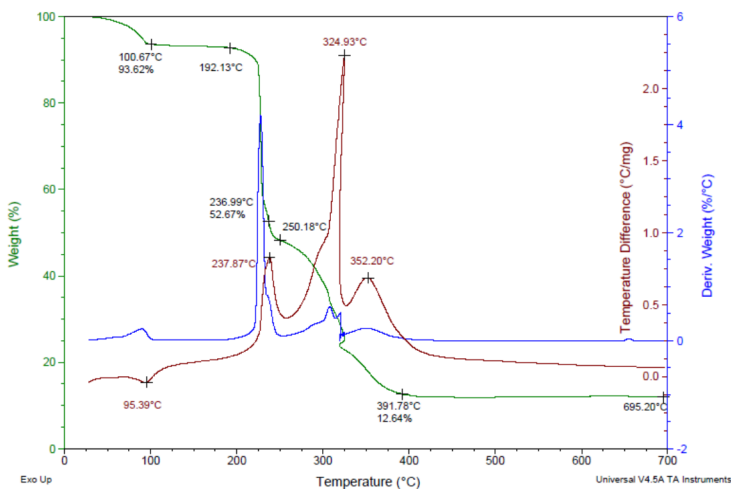
Figure 3b. TG-DTG-DTA diagram for copper complex (**1**)

For the cobalt complex (**2**), the first stage decomposition starts in the range 30-211⁰C, with an endothermic peak at 87⁰C and a mass loss of 6.26% which correspond to the loss of two moles of hydration water (calculated 5.69%). A strong exothermic effect (see Figure 3c), was assigned to the total pyrolysis of metal complex. The recorded mass loss of 81.34% is in good agreement to the calculated data (81.76%). Finally, the metal oxide remains in the crucible.

Figure 3c. TG-DTG-DTA diagram for cobalt complex (**2**)

187

Figure 3d. TG-DTG-DTA diagram for nickel complex (**3**)

Table 2. Thermal analysis data of the ligand **L** and its metal complexes (**1**-**3**)
in air atmosphere (10^0C/min)

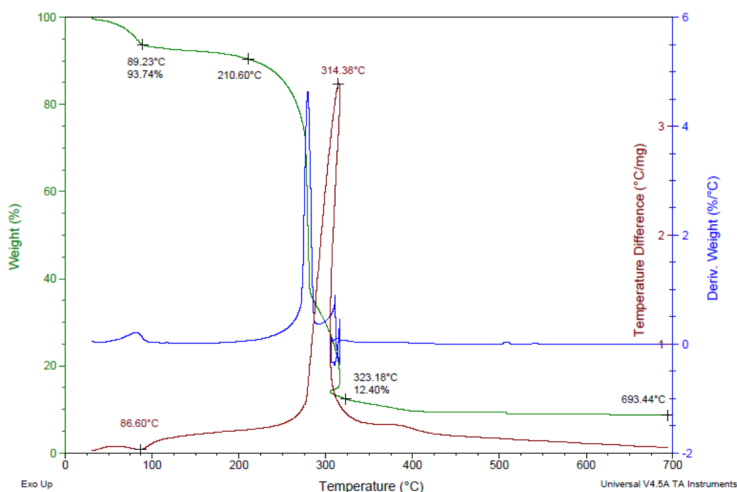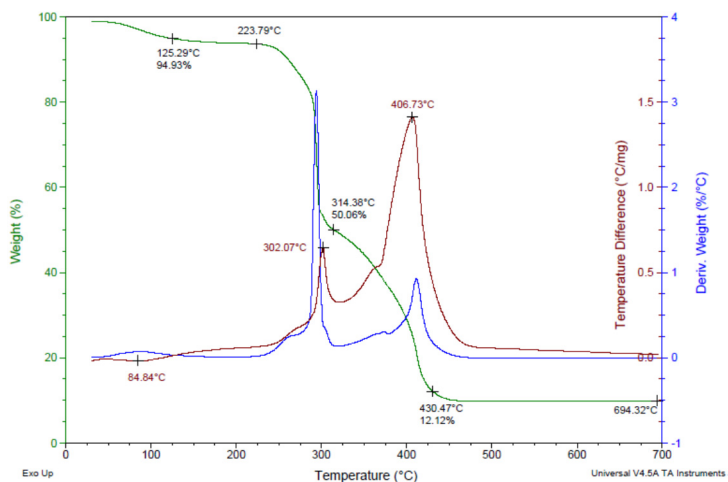| Compound	Heat effect on DTA	Temperature (^{0}C)			Mass loss (%)		Assignment
		T_i	T_{max}	T_f	Calcd.	Exp.	
L	Endo	30	56	194	-	1.12	-residual water present inside pores
	Endo	194	233	240	17.02	17.41	-melting accompanied by NO_2 cleavage group
	Exo	240	248	452	33.03	31.85	-glycine rest ($C_2H_4O_2N$) and
	Exo		347				oxidation process
	Exo	452	580	700	50.05	49.55	-pyrolysis of organic rest
	Exo		616				
Cu(L)•2H$_2$O (**1**)	Endo	30	95	192	5.64	6.40	-2 moles of hydrating water and probably residual water inside pores
	Exo	192	238	250	39.88	40.93	-2 moles of glycine rest and NO_2 groups (2 $C_4H_8O_8N_4$)
	Exo	250	325	700	41.27	40.49	-pyrolysis of organic rest
			352				
					13.21	12.64	CuO residue
Co(L)•2H$_2$O (**2**)	Endo	30	87	211	5.69	6.26	-2 moles of hydrating water
	Exo	211	314	323	81.76	81.34	-quickly cleavage and pyrolysis of organic rest
					12.54	12.40	CoO residue
Ni(L)•2H$_2$O (**3**)	Endo	30	85	224	5.69	5.07	-2 moles of hydrating water
	Exo	234	302	314	41.28	42.76	-2 moles of glycine rest and NO_2 groups (2 $C_4H_8O_8N_4$)
	Exo	314	407	430	40.39	38.89	-pyrolysis of organic rest
					12.54	12.12	NiO residue

T_i=initial temperature, T_{max}=maximum temperature, T_f=final temperature

The TG data showed that the nickel complex starts its decomposition at 85^0C. The first decomposition strep starts with dehydration and corresponds to loss of two moles of water. Organic ligand molecule is stable until 302^0C. The second ant third stages correspond to the organic ligand decomposition. The final product is NiO (12.12% exp., calcd. 12.54%).

ESR spectra

Powder ESR spectra of metallic complexes at room temperature (Figure 4) are typical for pseudotetrahedral monomeric species. The principal values of the g tensor $g_{\parallel}$=2.560 and $g_{\perp}$=2.071 for Cu complex, correspond to a CuN_2O_2 cromophore [19]. Similar value for Co complex ($g_{\parallel}$=2.0719, $g_{\perp}$=2.019) and for Ni complex ($g_{\parallel}$=2.065, $g_{\perp}$=2.071) suggest the same local symmetry around the metal ions.
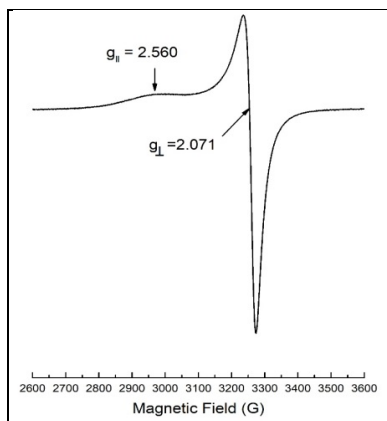
Figure 4. Powder ESR spectrum of copper complex at room temperature

CONCLUSIONS

Three new transition metal complexes (**1**-**3**) of an *N*-modified glycine (**L**) as ligand were synthesized and analyzed by elemental, thermogravimetric analysis and spectral studies. The results are in good agreement with the corresponding formulae: $C_{11}H_{14}N_2O_6$ (**L**), $[Cu(C_{11}H_{13}N_2O_6)_2]\cdot2H_2O$ (**1**), $[Co(C_{11}H_{13}N_2O_6)_2]\cdot2H_2O$ (**2**),respectively $[Ni(C_{11}H_{13}N_2O_6)_2]\cdot2H_2O$ (**3**). The ligand coordinated the metal ions through N and O donor atoms. The ESR spectra at room temperature indicated pseudotetrahedral local symmetry around the metal ions.

During heating in air atmosphere, both the ligand and its metal complexes decompose in multistage. Some stages of pyrolysis are weakly separated one from another. Decomposition of investigated compounds begins with total loss of water, then with gradual destruction of ligand. The final products of pyrolysis are the metal oxides from each of transition metal complexes.

Mass spectra data indicated the M+1 peak corresponding for each of investigated compounds.

EXPERIMENTAL SECTION

Materials and instrumentation

All reagents and chemicals were purchased from commercial sources and used as received. Elemental analyses were determined on Thermo Scientific Flash EA 1112 Elemental Analyzer. Melting points were measured on an ELECTROTHERMAL® instrument and and were not corrected. The electronic absorption spectra were performed on CECIL CE 9500 spectrophotometer. Specific rotations were estimated on a Polamat A Karl Zeis Jena photopolarimeter. GC-MS spectra were recorded on a Gas Chromatograph with Mass Spectrometer Shimadzu® QP 2010 PLUS. Mass spectra were carried out on a LTQ ORBITRAP® XL (Thermo Scientific) instrument which was externally calibrated using the manufacturer's APCI or ESI(+) calibration mix. The samples were introduced into the spectrometer by direct infusion. The EPR measurements were carried out on a Bruker Biospin EMX^{micro} spectrometer operating at X-band (9-10 GHz) with continuous wave at X-band (≈9 GHz). The spectra were recorded at room temperature with a microwave frequency of 9.4353 GHz, microwave power of 2 mW, modulation frequency of 100 kHz, modulation amplitude of 2 G. Thermogravimetry and differential thermal analysis (TG/DTA) curves were recorded with a Thermal Analyzer TA Instruments SDT Q600 V20.9 Build 20 on an interval 30-700^{0}C, at a heating rate of 10^{0}C/min, in alumina crucibles and a dynamic air atmosphere.

General synthesis of the metal complexes

Cu(II), Co(II) and Ni(II) complexes of the ligand L were prepared by following a general method. The metal salt [Cu(NO$_3$)$_2$•3H$_2$O, Co(NO$_3$)$_2$•6H$_2$O or Ni(NO$_3$)$_2$•6H$_2$O] (1.24mmol) was dissolved in 10 mL distilled water. To a solution of ligand (**L**) (2mmol) dissolved in NaOH 1M at pH=12, was added slowly, dropwise, a solution of the metal salt, at room temperature. The mixture was stirred for 2h. By adding a solution of metal ions to a solution of ligand,

immediate color change was observed depending on the metal ion. Also the pH was changed at 5.5-6.00 for the copper complex, 6.50-7.00 for the cobalt complex and 7.00-7.50 for the nickel complex. After standing overnight at room temperature, the resulted precipitates were vacuum filtrated and washed with distilled water and finally dried in air at room temperature.

REFERENCES

1. L. Lomozik, A. Wojciechowska, *Monatshefte für Chemie*, **1985**, *116*, 719.
2. I. Sakiyan, E. Loğoğlu, S. Arslan, N. Sari, N. Sakiyan, *BioMetals*, **2004**, *17(2)*, 115.
3. A. Temitayo, O. Isaac, A. Olugbenga, *International Journal of Chemistry*, **2012**, *4(2)*, 49.
4. A. Marcu, A. Stanila, D. Rusu, M. Rusu, O. Cozar, L. David, *Journal of Optoelectronics and Advanced Materials*, **2007**, *9(3)*, 741.
5. G. Indira Devi, P. Smitha, *International Research Journal of Biological Sciences*, **2013**, *2(6)*, 16.
6. L. Menabue, M. Saladini, *Journal of Crystallographic and Spectroscopic Research*, **1992**, *22(6)*, 713.
7. K. Nishimura, X. Lu, R.B. Silverman, *Journal of Medicinal Chemistry,* **1993**, *36*, 446.
8. G. Byk, C. Gilon, *Journal of Organic Chemistry,* **1992**, *57*, 5687.
9. K. Yahagi, K. Tsujii, H. Hirota, Y. Matsumura*, Eur. Pat. 0248294 A2,* **1987**.
10. M. Darabantu, C. Maiereanu, G. Plé, C. Berghian, E. Condamine, Y. Ramondenc, *Heterocyclic Communications*, **2001**, *7(6)*, 593.
11. L. Zapala, M. Kosińska, E. Woźnicka, L. Byczyński, W. Zapala, *Journal of Thermal Analysis and Calorimetry,* **2016**, *124*, 363.
12. N.S. Al Radadi, S.M.A. Al Ashqar, M. M. Mostafa, *Synthesis and Reactivity in Inorganic, Metal-Organic and NanoMetal Chemistry,* **2011**, *41(2)*, 203.
13. E. Prenesti, S. Berto, P.G. Daniele, *Spectrochimica Acta Part A,* **2003**, *59*, 201.
14. T. Stalin, N. Rajendiram, *Journal of Photochemistry and Photobiology A: Chemistry,* **2006**, *182*, 137.
15. F. Dimiza, S. Fountoulaki, A.N. Papadopoulos, C.A. Kontogiorgis, V. Tangoulis, C.P. Raptopolou, V. Psycharis, A. Terzis, D.P. Kessisoglou, G. Psomas, *Dalton Transactions*, **2011**, *40*, 8555.
16. K. Raha, P.S. Makashir, E.W. Kusian, *Journal of Thermal Analysis and Calorimetry,* **1989**, *35*, 1173.

17. L. Ghizdavu, C. Bălan, L. David, C. Bâtiu, O. Cozar, D. Ristoiu, *Journal of Thermal Analysis and Calorimetry,* **2000**, *62*, 729.
18. L. David, C. Craciun, C. Bălan, O. Cozar, L. Ghizdavu, C. Bâtiu, *Acta Chimica Slovenica,* **2001**, *48*, 407.
19. F. Mabbs, D. Collisson, "Electron Paramagnetic Resonance of *d* Transition Metal Compounds", Elsevier, Amsterdam, **1992**, p.102.

HYPERCOORDINATED ORGANOSELENIUM COMPOUNDS WITH O→Se INTRAMOLECULAR INTERACTIONS

ALEXANDRA POP[a], ROXANA A. POPA[a], CRISTIAN SILVESTRU[a], ANCA SILVESTRU[a]*

ABSTRACT. Single-crystal X-ray diffraction studies revealed a monomeric structure with O→Se intramolecular coordination in compounds $[Me_2C(OH)CH_2][2-(Me_2NCH_2)C_6H_4]Se$ (**1**) and $[2-(O=CH)C_6H_4]Se[S(S)P(OPr^i)_2]$ (**2**). These interactions result in distorted T-shaped coordination geometries around selenium in both compounds and prevent a *C,N*-chelating behavior of the $2-(Me_2NCH_2)C_6H_4$ group in **1** and a bidentate behaviour of the dithiophosphorus ligand in **2**, respectively.

Keywords: *organoselenium compounds; intramolecular coordination; solid state structure; dithiophosphato ligands.*

INTRODUCTION

A continuously increased interest was observed during last years for main group organometallic compounds bearing organic groups with pendant arms capable for intramolecular E→M (E = O, N; M = main group metal or metalloid) interactions, mainly due to the specific properties induced by such an interaction, *e.g.* increased thermal and hydrolytic stability or adjustable conformation rigidity [1,2]. In most cases, the use of functionalized aromatic groups with potential for intramolecular coordination results in chelate species stabilized in a monomeric form. Such compounds proved to be valuable candidates in catalysis, medicine or materials science, as they display

---

[a] *Babeş-Bolyai University, Faculty of Chemistry and Chemical Engineering, Department of Chemistry, Supramolecular Organic and Organometallic Chemistry Centre (SOOMCC), 11 Arany Janos str., RO-400028, Cluj-Napoca, Romania,*
* *Corresponding author: ancas@chem.ubbcluj.ro*

improved catalytic properties, biological activity or thermal behavior than the species without such intramolecular interactions [3,4]. In organoselenium compounds the N→Se intramolecular interaction was observed to reduce the Lewis acidity and to increase the electrophilic reactivity of the chalcogen atom, thus making it more suitable for additional Se→M coordination. In this way, organoselenium compounds bearing organic groups with potential for building hypercoordinated species become useful multidentate ligands using both hard (O, N) and soft (Se) donor atoms [5-10].

During the last years our research interest was focused on organoselenium compounds with organic groups of type $2\text{-}(R_2NCH_2)C_6H_4$ (R = Me, Et, Pr^i) [11-14], $2,6\text{-}(R_2NCH_2)C_6H_3$ [15], $(RN=CH)C_6H_4$ (R = Bn, Mes, Ph) [16] or $2\text{-}(O=CH)C_6H_4$ [17] groups, as well as several metal complexes, either metal organoselenolates [18-20], or compounds bearing the alkoxo functionalized ligands, $[R_2C(OH)CH_2](2\text{-}Me_2NCH_2C_6H_4)Se$ [21]. As a continuation of our studies we discuss here the crystal and molecular structure of two organoselenium(II) compounds with potential for hypercoordination, namely $[Me_2C(OH)CH_2](2\text{-}Me_2NCH_2C_6H_4)Se$ (**1**) and $[2\text{-}(O=CH)C_6H_4)Se[S_2P(OPr^i)_2]$ (**2**), with emphasis on the intramolecular E→Se (E = N, O) possible interactions.

RESULTS AND DISCUSSION

We described previously the synthesis and the solution behavior of compounds $[Me_2C(OH)CH_2](2\text{-}Me_2NCH_2C_6H_4)Se$ (**1**) [21] and $[2\text{-}(O=CH)C_6H_4)Se[S_2P(OPr^i)_2]$ (**2**) [17], but at that time we didn't succeed to obtain single crystals suitable for X-ray diffraction studies.

Single-crystal X-ray diffraction studies

The molecular structures of compounds **1** and **2** were determined by single-crystal X-ray diffraction. The ORTEP-like diagrams with the atom numbering schemes for compounds **1** and **2** are displayed in Figures 1 and 2, respectively, while important interatomic distances and angles are given in Tables 1 and 2, respectively.
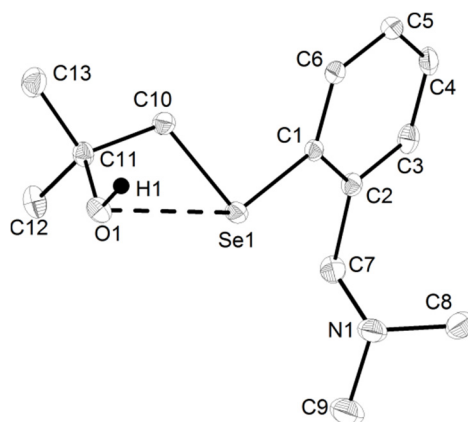
Figure 1. ORTEP-like diagram at 30% probability for compound **1**.
Hydrogen atoms, except H1 were omitted for clarity.

Table 1. Selected interatomic distances [Å] and angles [°] in **1**.

Se1–C1	1.928(4)		C1–Se1–C10	98.20(18)
Se1–C10	1.967(4)		C1–Se1⋯O1	146.48(13)
Se1⋯O1	3.121(3)		C10–Se1⋯O1	50.71(13)

Both compounds have monomeric structures with a distorted T-shaped coordination geometry around selenium (O1⋯Se1−C1 146.48° in **1** and O1⋯Se1−S1 176.10° in **2**) and chelate rings, *i.e.* four-membered SeC_2O in **1** and five-membered SeC_3O in **2**, respectively. In compound **1** the nitrogen-selenium interatomic distance (3.44 Å) is just at the limit of the sum of the van der Waals radii of the two elements [Σr_{vdW} (N,Se) 3.54 Å] [22], while typically such interactions were observed in the range 2.358(2) - 3.135(3) Å in other related species, *i.e.* [2-$(Me_2NCH_2)C_6H_4]_2Se_2$, [2-$(Me_2NCH_2)C_6H_4]_2Se$ [23] or [2,6-$(Me_2NCH_2)C_6H_3]Se^+$ [15]. The OH hydrogen atom is not involved in any intra- or intermolecular interaction. This contrasts with the phenyl substituted analogue [$Ph_2C(OH)CH_2$][2-$(Me_2NCH_2)C_6H_4$]Se, where a strong N⋯H–O interaction of 2.03 Å [Σr_{vdW} (N,H) 2.74 Å] is established [21]. In compound **1** the N1⋯H1 interatomic distance is much greater (6.51 Å) than the sum of the van der Waals radii of these two elements. This behavior can be explained by the constraint determined by the intramolecular O→Se interaction (Se1⋯O1 3.12 Å) [*cf.* Σr_{vdW} (O,Se) 3.40 Å] [22], which prevents any further participation of the OH hydrogen to hydrogen bonding.
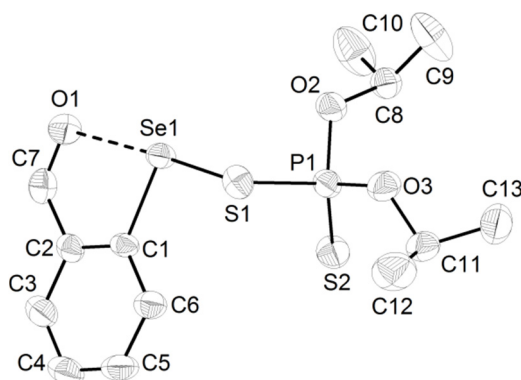
Figure 2. ORTEP-like diagram at 30% probability for compound **2**. Hydrogen atoms were omitted for clarity.

Table 2. Selected interatomic distances [Å] and angles [°] in **2**.

Se1–C1	1.934(4)		C1–Se1–S1	101.41(14)
Se1–S1	2.216(1)		C1–Se1···O1	76.50(15)
Se1···O1	2.575(4)		S1–Se1···O1	176.10(10)
P1–S1	2.0865(16)			
P1–S2	1.9087(19)			

In compound **2** the O→Se intramolecular interaction of 2.575 Å is similar with that one found in [2-(O=CH)C$_6$H$_4$]Se[S(S)PPh$_2$] (2.568 Å) and much stronger than the sum of the van der Waals radii of oxygen and selenium. The dithiophosphorus ligand is coordinated in a monodentate fashion to selenium, with single P−S [P1−S1 2.086(2) Å] and double P=S [P1−S2 1.908(2) Å] bonds [*cf*. P–S 2.077(1) and P=S 1.954(1) Å in Ph$_2$P(S)SH] [24]. These values are similar with those found in the related [2-(O=CH)C$_6$H$_4$]Se[S(S)PPh$_2$] [17] or the compounds of type [2-(^{i}Pr$_2$NCH$_2$)C$_6$H$_4$]Se[S(S)PR'$_2$] (R' = Ph, OPr^i) [13].

CONCLUSIONS

The single-crystal X-ray diffraction studies revealed the presence of O→Se intramolecular interactions in the monomeric species [Me$_2$C(OH)CH$_2$](2-Me$_2$NCH$_2$C$_6$H$_4$)Se (**1**) and [2-(O=CH)C$_6$H$_4$]Se[S(S)P(OPr^i)$_2$] (**2**). In compound **1** the intramolecular O→Se coordination pushed the nitrogen atom in the pendant arm of the 2-(Me$_2$NCH$_2$)C$_6$H$_4$ group away from the coordination sphere of selenium, thus preventing any intramolecular N→Se interaction, while in compound **2** the intramolecular C=O→Se interaction determines a monodentate monoconective behavior of the organophosphorus ligand.

EXPERIMENTAL SECTION

X-ray structure determination

The details of the crystal structure determination and refinement for compounds **1** and **2** are given in Table 3. Data were collected on a Bruker SMART APEX diffractometer by using graphite-monochromated Mo-K_α radiation (λ = 0.71073 Å). The crystals were attached with paraton/N oil on cryoloops. The structures were refined with anisotropic thermal parameters. The hydrogen atoms were refined with a riding model and a mutual isotropic thermal parameter. For structure solving and refinement the software package SHELX-97 was used [25]. The drawings were created with the Diamond program [26].

Table 3. Crystal data and structure refinement for
[Me$_2$C(OH)CH$_2$][2-(Me$_2$NCH$_2$)C$_6$H$_4$]Se (**1**) and [2-(O=CH)C$_6$H$_4$]Se[S(S)P(OPr^i)$_2$] (**2**)

	1	2
Empirical formula	C$_{13}$H$_{21}$NOSe	C$_{13}$H$_{19}$O$_3$PS$_2$Se
Formula weight	286.27	397.33
Temperature (K)	150(2)	293(2)
Wavelength (Å)	0.71073	0.71073
Crystal system	Tetragonal	Monoclinic
Space group	I-4	C2/c
a (Å)	19.9049(12)	28.106(5)
b (Å)	19.9049(12)	8.0787(13)
c (Å)	7.0189(8)	16.977(3)
α (°)	90	90
β (°)	90	114.002(3)
γ (°)	90	90
Volume, (Å^3)	2780.9(5)	3521.5(11)
Z	8	8
Density (calculated) (g/cm^3)	1.367	1.499
Absorption coefficient (mm^{-1})	2.682	2.463
F(000)	1184	1616
Crystal size, mm	0.30 x 0.25 x 0.19	0.20 x 0.22 x 0.38
θ range for data collections, °	1.447 to 24.929	1.60 to 25.00
Reflections collected	13389	16308
Independent reflections	2445 [R$_{int}$ = 0.0484]	3099 [R$_{int}$ = 0.049]
Refinement method	Full-matrix least-squares on F^2	
Data / restraints / parameters	2445 / 0 / 150	3099 / 0 / 185
Goodness-of-fit on F^2	1.037	1.172
Final R indicies [I>2sigma(I)]	R1 = 0.0274	R$_1$ = 0.0536
	wR2 = 0.0588	wR$_2$ = 0.1144
R indicies (all data)	R1 = 0.0288	R$_1$ = 0.0649
	wR2 = 0.0593	wR$_2$ = 0.1192
Largest diff. peak and hole, eÅ^{-3}	0.355 and -0.188	0.751 and -0.261

ACKNOWLEDGMENTS

SUPPLEMENTARY DATA

CCDC 1587750 and 1571839 contain the supplementary crystallographic data for **1** and **2**, respectively. These data can be obtained free of charge *via http://www.ccdc.cam.ac.uk/conts/ retrieving.html*, or from the Cambridge Crystallographic Data Centre, 12 Union Road, Cambridge CB2 1EZ, UK; fax: +44 1223 336 033; or e-mail: deposit@ccdc.cam.ac.uk.

REFERENCES

1. Kin-ya Akiba (Ed), "Chemistry of Hypervalent Compounds", Wiley-VCH, 1999, Weinheim.
2. C.I. Rat, C. Silvestru, H.J. Breunig, *Coordination Chemistry Reviews*, **2013**, *257* 818, and references therein.
3. C. Coza, A. Stegarescu, R. Suteu, A. Silvestru, *Journal of Organometallic Chemistry*, **2015**, *777,* 71.
4. C.A. Caputo, N.D. Jones, *Dalton Trans*actions, **2007**, *41*, 4727.
5. G. Mugesh, H.B. Singh, *Chemical Society Reviews*, **2000**, *29*, 347.
6. T. Wirth (Ed.), "Organoselenium Chemistry: Modern Developments in Organic Synthesis", *Topics in Current Chemistry*, vol. 208, Springer, Berlin, **2000**.
7. G. Mugesh, W.-W. du Mont, H. Sies, *Chemistry Reviews*, **2001**, *101*, 2125 (and references therein).
8. A.J. Mukherjee, S.S. Zade, H.B. Singh, R.B. Sunoj, *Chemistry Reviews,* **2010**, *110*, 4357 (and references therein).
9. K. Kandasamy, H.B. Singh, G. Wolmershauser, *Inorganica Chimica Acta*, 2005, 358, 207.
10. S. Panda, S.S. Zade, H.B. Singh, R.J. Butcher, *European Journal of Inorganic Chemistry*, **2006**, 172.
11. C. Deleanu, J.E. Drake, M.B. Hursthouse, M. Kulcsar, M.E. Leight and A. Silvestru, *Applied Organometallic Chemistry***, 2002**, *16*, 727.
12. M. Kulcsar, A. Silvestru,_C. Silvestru, J.E . Drake, C.L.B. Macdonald, M.B. Hursthouse, M.E. Light, *Journal of Organometallic Chemistry*, **2005**, *690*, 3217.

13. E. Duhamel, A. Pöllnitz, A. Stegarescu, A. Silvestru, *Zeitschrift für Anorganische und Allgemeine Chemie,* **2011**, *637*, 1355.
14. A. Pöllnitz, V. Lippolis, M. Arca, A. Silvestru, *Journal of Organometallic Chemistry*, **2011**, *696,* 2837.
15. A. Pop, A. Silvestru, E.J. Juárez-Pérez, M. Arca, V. Lippolis, C. Silvestru, *Dalton Trans*actions, **2014**, *43*, 2221.
16. A. Pöllnitz, C. Silvestru, J.-F. Carpentier, A. Silvestru, *Dalton Transactions*, **2012**, *41*, 5060.
17. R.A. Popa, A. Pop, C. Silvestru and A. Silvestru, *Revue Roumaine Chimie*, **2016***, 61*, 495.
18. A. Pöllnitz, A. Rotar, A. Silvestru, C. Silvestru, M. Kulcsar, *Journal of Organometallic Chemistry*, **2010**, *695,* 2486.
19. A. Pop, L. Wang, V. Dorcet, T. Roisnel, J.-F. Carpentier, A. Silvestru, Y. Sarazin, *Dalton Transactions*, **2014**, *43*, 16459.
20. A. Pop, C. Bellini, R. Șuteu, V. Dorcet, T. Roisnel, J.-F. Carpentier, A. Silvestru, Y. Sarazin, *Dalton Trans*actions, **2017**, *46*, 3179.
21. A. Pop, R. Mitea, A. Silvestru, *Journal of Organometallic Chemistry*, **2014**, *768,* 121.
22. J. Emsley, "Die Elemente", de Gruyter, Berlin, **1994**.
23. A. Panda, G. Mugesh, H.B. Singh, R.J. Butcher, *Organometallics*, **1999**, *18*, 1986.
24. B. Krebs, G. Henkel, *Zeitschrift für Anorganische und Allgemeine Chemie,* **1981**, *475*, 143.
25. G. M. Sheldrick, *Acta Crystallographica, Section A*, **2008**, *64*, 112.
26. *DIAMOND*, Visual Crystal Structure Information System, Crystal Impact, Postfach 1251, 53002 Bonn, Germany, **2001**.

COMPARATIVE *IN VITRO* STUDY OF
THE DIFFERENT ORTHODONTIC BRACKETS
USING TWO ETCHING TECHNIQUES

**MIHAELA PĂSTRAV[a], ANDREA MARIA CHISNOIU[b],
OVIDIU PĂSTRAV[c*], LAURA SILAGHI DUMITRESCU[d],
CODRUTA SAROSI[d] AND VIORICA TARMURE[a]**

ABSTRACT. Direct bonding of the bracket to the enamel is the elective procedure for the orthodontic treatment. Among various factors influencing the adhesive force at the enamel level, the etching technique seems to be the most important one. The present study aims at evaluating the influence of the storage media and the etching technique used, on the bond strength between different bracket types and dental structures. The results of this study showed that, regardless of the brackets and the immesion solution used, by working with the classic etch and rinse technique the adhesion force is higher than by using a self etching adhesive.

Keywords: SEM, etching technique, in vitro, adhesion

---

[a] *Department of Orthodontics and Orofacial Orthopaedics, Faculty of Dental Medicine, University of Medicine and Pharmacy "Iuliu Hațieganu", 33 Motilor Street, 400001, Cluj-Napoca, Romania*

[b] *Department of Prosthetic Dentistry, Faculty of Dental Medicine, University of Medicine and Pharmacy "Iuliu Hatieganu", 32 Clinicilor Street, 400006, Cluj-Napoca, Romania*

[c] **Department of Odontology and Oral Pathology, Faculty of Dental Medicine, University of Medicine and Pharmacy "Iuliu Hațieganu", 33 Motilor Street, 400001, Cluj-Napoca, Romania*

[d] *"BabesBolyai" University -"RalucaRipan" Chemistry Research Institute, 30 Fântânele Street, 400294,Cluj-Napoca, Romania.*

*Corresponding author: pastravovidiu@yahoo.com

INTRODUCTION

Direct bonding of the bracket to the enamel is the elective procedure for the orthodontic treatment. The processinvolves the enamel, the adhesive and the bracket surface, therefore, the analysis of the twointerfaces: enamel- adhesive and adhesive-bracketis an important subject of research [1]. The different physical and chemical properties of these components could establish the adhesive conditions in orthodontics [2].

There are many factors influencing de adhesive force at the enamel level, such as etching technique, adhesive application, photopolymerisation time, or mechanical properties of resin based materials for bracket bonding [3, 4].

The differences between the bonding forces by using selfetching adhesives or the common etching technique, followed by the use of adhesive, still represents a subject of debate[5, 6].

Schnebel states that the adhesive force of the selfetching systems is not appropriate for bracket bonding and suggests that in order to gain enough bond strength orthodontists should use the classic etching technique [7]. The type of adhesive influences the bond strength, the risc of damaging the enamel and the presence of composite resin on the tooth surface [8].

The bracket type used, as well as the way the orthodontic forces are applied , influence the bond strength and the tensions that appear in the bonding layer and in the enamel [9, 10]. Also, the enviromental factors such as soft drinks accelerate the damage of the enamel surface [11].

At the end of an orthodontic treatment the debondig of the brackets shouldn't influence the enamel surface. Though, during bracket debonding, some undesirable effects can be observed: cracks, scarring scratches, loss of enamel, adhesive scraps on the enamel surface. In addition to bracket debonding, the removal of adhesive residue with a dental bur may also lead to local enamel damage [12].

The purpose of this study was to evaluate the influence of the storage media and the etching technique used on the bond strength between bracket and dental structures.

RESULTS AND DISCUSSIONS

Table 1 shows the average values of the adhesion force for metallic, ceramic and sapphire brackets imersed in Coca Cola, tea and artificial saliva (controls).

Table 1. Mean values of strength bond forces.

Immersion solution	Artificial saliva (control) [MPa]		Coca Cola [MPa]		Tea [MPa]	
Etching technique	Etch and rinse	Self-etch	Etch and rinse	Self-etch	Etch and rinse	Self-etch
Bracket type						
Ceramic	4.1 ± 0.02	4.4 ± 0.12	2.7 ± 0.12	5 ± 0.12	6.9 ± 0.15	6.6 ± 0.07
Metal	20 ± 0.02	11.6 ± 0.15	10.7 ± 0.11	9.1 ± 0.06	29.4 ± 0.02	26.5 ± 0.01
Sapphire	20.3 ± 0.12	10.9 ± 0.11	12.5 ± 0.12	8 ± 0.11	26.2 ± 0.12	15 ± 0.12

The highest strength bond forces were obtained for metallic brackets, using the etch and rinse technique, for the samples immersed in tea solution (29.4 ± 0.02 MPa) - Table 1.

Significant differences were observed between the groups where brackets were bonded using etch and rinse technique compared to those were self-etch technique was used (p< 0,005) - Table 2.

Table 2. Test statistics- Wilcoxon test

	Self-echting technique	Ceramic	Metallic	Saphire
Z	-3,393[b]	-1,726[b]	-2,981[c]	-2,903[c]
Asymp. Sig. (2-tailed)	,001	,084	,003	,004

Based on the negative value ranks we prooved that by using the classic etch and rinse technique the adhesion force is higher than by using a self etching adhesive, regardless of the immesion solution.

SEM evaluation is essential for observing the enamel surface morphology after various bonding and debonding procedures, as well as for subsequently necessity of polishing the tooth surface. The results of our investigation are based on images of the bracket bases (**Figure 1**) and enamel surface after bracket debonding (**Figure 2, 3**). Different aspects of cement debris on the enamel surface, according to the type of etching technique, are visible after debonding for all three bracket types.
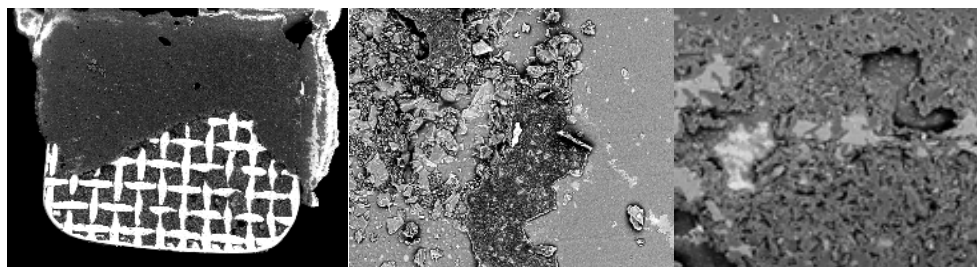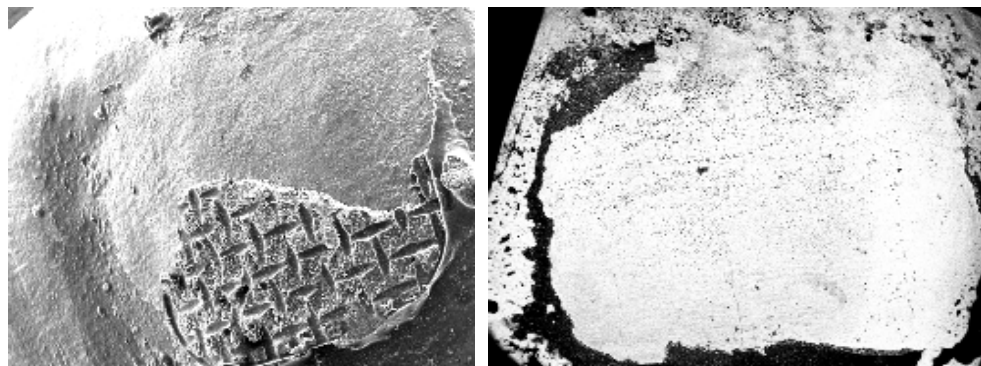
a. Metallic bracket   b. Sapphire bracket   c. Ceramic bracket

Figure 1. SEM images from bracket bases after debonding; 1000 magnification

The use of different materials and etching techniques can determine various degrees of wear that were observed on both the tooth surface and bracket level. The gaps and cracks of different sizes were initiated probably by the shear forces at the bracket-cement interface.

All acid etched enamel surfaces presented a porous, relatively rough aspect on SEM investigation (**Figure 2a, 3a**); in comparison, the self-etched enamel surfaces showed a smooth and almost clean aspect on SEM analysis (**Figure 2b, 3b**). Enamel fractures were frequently observed on tooth surfaces with brackets bonded through etch and rinse technique.

a. Metallic bracket -etch and rinse technique   b. Metallic bracket- self-etch technique

Figure 2. SEM images of the enamel surface after metallic bracket debonding; 5000 magnification
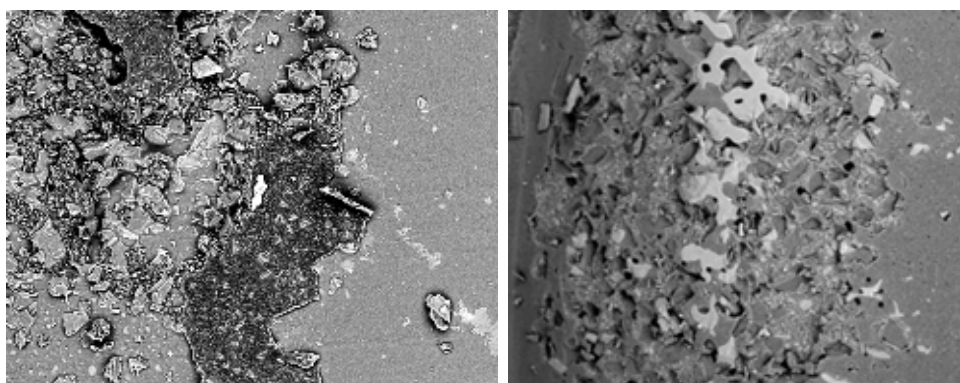
a. ceramic bracket using etch and rinse technique

b. Sapphire bracket using self-etch technique

Figure 3. SEM images of the enamel surface after sapphire bracket debonding; 5000 magnification

Various factors can influence the bonding strength force of the brackets to the enamel such as the type of adhesive, the thickness of the adhesive layer, humidity, geometry of the bracket base,oral habits,etc, but the main one seems to be the etching technique[5-9].

The white spots observed around the brackets are mostly due to bad hygiene or the use of acidic beverages that lower the pH of the oral cavity [13]. Soft drinks consumption can determine erosion of the enamel and corrosion of the materials [14,15]. For this reason we used in our study, the immersion in artificial saliva, but also in Coca Cola and tea.

In our study the highest strenght forces were obtained when using the etch and rinse technique.By enlarging the adhesive surface and creating microretentions at enamel level, adequate conditions were created for adhesive penetration [1,2].

SEM images show us a significantly difference between the debonding appearance of the metallic brackets when comparing to sapphire and ceramic brackets.

In case of etch and rinse technique, after metallic bracket debonding, we can observe a relatively uniform layer of cement, both on the bracket base and on enamel. For the sapphire and ceramic brackets, the largest amount of cement seems to remain on the enamel surface.

In the case of etch and rinse technique, an almost complete distribution of the adhesive layer on the enamel surface after sapphire bracket debonding is observed, when compared to metallic brackets, where the adhesive seems to be distributed on both bracket base and enamel

surface, in varying proportions. When self-etching adhesives are used, most cement layer remains on the enamel surface after debonding sapphire and ceramic brackets.

The concept of an ideal debonding consists of failure at the support/ adhesive interface, and the remained adhesive on the enamel surface to be carefully removed using suitable tools, in order to allow a minimum or no loss of enamel [9, 10]. Cement debris at enamel level can favor plaque adherence, producing demineralized areas and cavities. The residual adhesive may be colored through bacteria action, or due to different alimentary pigments or cosmetics and discolorations can occur, affecting aesthetics [4]. Given the current procedures for debonding and teeth polishing, some layers of enamel could be accidentally removed causing tooth morphology changes and eventual developing of cracks [12]. Literature reports the loss of enamel ranging from 27.5 to 48 μm [12], or 26.1-41.2 μm to 55.6 μm [13], depending on the characteristics of the adhesive system used, the instruments or the final polishing technique. The loss of the enamel is not clinically significant compared to the average thickness of the enamel, which range from 1500 to 2000μm [12]. Finishing is considered an indispensable process to minimize enamel damage during cement removal from enamel after debonding [5, 9,12].

In vitro, orthodontic bonding is carried out in ideal conditions. *In vivo*, the enamel surfaces can easily be contaminated and extra humidity is sometimes unavoidable. It should be noted that, in these cases, the strength of composite resins adhesion, respectively C = C covalent bonds, will decrease. Vallolah et al. [16] reported that the air at the back of the metal bracket mesh net can significantly affect complete polymerization of light-curing composite resin cements, due to the known inhibitor role of oxygen; it can alter the bond strength between metal and composite material support. But this type of failure was found only in the case of light-cured composite resin cements. Careful application of material on the support base and/or using liquid - paste systems, can avoid air entrapment. This type of failure identified at the resin - bracket interface, implies the possibility that after debonding all cement can remain on the enamel surface, which then should be cleaned. The bracket-cement interface carried out in our tests with remaining cement on both the bracket and the enamel, are partially different from the results obtained by Artun and Ozturk [17], Zarrin, Eid and Kehoe [18], which showed a higher amount of residual cement on the brackets after debonding by applying a force on the support base. The differences can be explained by the use of brackets, adhesive cements and techniques in different combinations.

Etching time before bonding is proportional with the quantity of residual adhesive on enamel surfaces [16-18]. Fjeld et al [19] described in their study fewer irreversible changes to the enamel surface after bonding with self-etching adhesives in comparison to conventional etching.

The aspect of enamel after bracket debonding and final polishing, should be comparable to adjacent surfaces. Clinical examination of both dry and wet enamel is important because of the reflection and refraction of light, which can mask some defects on wetted surfaces of enamel [20].

No universally approved protocol has been established for adhesive resin removal after orthodontic bracket debonding, and there is no instrument that can achieve complete composite removal without affecting the enamel surface.

CONCLUSIONS

Regardless of the brackets and the immesion solution used in this study, all results indicate that by using the classic etch and rinse technique the adhesion force is higher than by using a self etching adhesive.

Metallic brackets are preferable to brackets made of monocrystalline alumina in terms of base design for minimum possible superficial destructions of enamel after debonding. Also, for the same reasons, the bonding technique using the total etch and rinse protocol seems to be a more inspired choice than the self-etching adhesives.

Using conservative instruments and techniques becomes very important, due to multiple possibilities for bracket bonding and to surface treatments that may reduce the loss of the superficial layer of enamel.

EXPERIMENTAL SECTION

Three types of brackets (metallic, ceramic and sapphire) were used. All brackets were bonded to enamel using two etching techniques (self-etch and classic) followed by adhesive application.

All samples were altered rapidly by physical and chemical stress, using several immersive solutions at body temperature. The samples from each group (metal, ceramic or sapphire) were randomly distributed in three subgroups immersed and stored for 3 month, in artificial saliva (controls), Coca Cola or tea. The strength bond force on bracket enamel interface was evaluated.

The comparisons within the statistical part were done between the specimens with the same bracket type, immersed in the same solution, ones bonded with the self-etching technique, others using the etch and rinse technique.

By using one single bonding agent, but different etching techniques, the differences area was restricted to the bonding technique.

The bracket bondig procedure was done accordingly to the manufacturers indications and kept in artifical saliva for 24 hours.

The solutions were prepared and used as follows:

1. Black tea (The mélange angles, Breakfast Black tea)-was kept at 37°C for 20 minutes per day, in order to simmulate the necessary time for each person to drink a cup of tea, as well as the temperature.
2. Coca Cola- the probes were immeresed for 20 minutes per day, at 37°C.
3. Control group for this group the probes were immersed in artificial saliva at 37°C, in thermosthatic bath,without any other treatment.

The brackets were debonded three months after the initial moment of the experiment. Strenght bond force was evaluated out using Llyod Universal Testing machine. A sharp blade was used to apply an oclusogingival force at the bracket-adhesive interface, with a speed of 1mm/min.

The values of the strenght bond force were mesured in MPa, using NEXYGEN Plus Materials Testing Software. The statistical analisys was performed using we used the nonparametric two-pired Wilcoxon statistic test, paired type. The specimens were also examined by using scanning electron microscopy (SEM) and energy dispersive X-ray (EDAX) spectrometry.

ACKNOWLEDGEMENT

REFERENCES

1. M. Hashimoto, H. Ohno, E. Yoshida, M. Hori, H. Sano, M. Kaga, H. Oguchi, *European Journal of Oral Science,* **2003**,*111*, 447.
2. C. Raposo, I.L. Santana, *Revista Odontologia Ciencia*,**2012**, *27*,143.
3. B.C. Parrish, T.R. Katona, S.C. Isikbay, K.T. Stewart, K.S. Kula, *Angle Orthodontics*, **2012**, *82*, 131.

4. M. Schroeder, A.C.S. Gama, A.G.V. Moares, L.C. Yamasaki, A.D. Loguercio, J. Bauer, *Dental Materials*, **2011**, *27*, 20.
5. P.S. Fleming, *Evidence Based Dentistry*, **2014**, *15*, 48.
6. A. Elkhadem, N. Orabi, *Evidence Based Dentistry*, **2013**, *14*, 52.
7. A. Schnebel, S. Mateer, A.L. Maganzini, K. Freeman, *Journal of Orthodontics*, **2012**, *39*, 256.
8. T. Lamper, N. Ilie, K. C. Huth, I. Rudzki, A. Wichelhaus, E. Paschos, *Clinical Oral Investigations*, **2014**, *18*, 313.
9. S.E. Elsaka, S. M. Hammad, N. F. Ibrahim, *Progress in Orthodontics,* **2014**, *16*, 33.
10. V. Bolaños-Carmona, B. Zein, M. Menéndez-Núñez, P. Sánchez-Sánchez, L. Ceballos-García, S. González-López, *Dental Materials Journal*, **2015**, *34,* 449.
11. J.A. von Fraunhofer, M. M. Rogers, *General Dentistry*, **2004**, *52*, 308.
12. C. Speera, D. Zimnyb, W. Hopfenmuellerc, E. Holtgrave, *Angle Orthodontist*, **2005,** *75*, 5.
13. J.F. Tahmassebi, M.S.Duggal, G. Malik-Kotru, M.E. Curzon, *Journal of Dentistry,* **2006**, *34*, 2.
14. H.H. Yip, R.W. Wong, U. Hägg, *World Journal of Orthodontics*, **2009**, *10*, 33.
15. J.M. Steffen, *Angle Orthodontist*, **1996**, *66*, 449.
16. A. Valiollah, N. Fatemeh, R. Mehdi, K. Ahmad, Mohammad S. Barati. *Electron physician,* **2017**, *9*, 3584.
17. F. Öztürk, M. Ersöz, S.A. Öztürk, E. Hatunoğlu, S. Malkoç. *European Journal of Orthodontics,* **2016**, *38*, 163.
18. K. Zarrinnia, N.M. Eid, M.J. Kehoe, *American Journal of Orthodontics and Dentofacial Orthopaedics*, **1995**, *108*, 284.
19. M. Fjeld, B. Øgaard, *American Journal of Orthodontics and Dentofacial Orthopaedics,* **2006**, *130*, 575.
20. E. İşman, E.S. Karaarslan, R. Okşayan, A.R. Tunçdemır, S. Üşümez, N. Adanir, M.A. Cebe*, Dental Materials Journal*, **2012**, *31*, 947.

SYNTHESIS, CHARACTERIZATION AND MOLECULAR MODELING OF TRANSITION METAL COMPLEXES WITH THEOPHYLLINE

ATTILA-ZSOLT KUN[a], BETTINA CSURKA[a], FIRUTA GOGA[a], EDIT FORIZS[a,*], ADRIAN PATRUT[a]

ABSTRACT. Mixed-ligand complexes of Cu(II) and Ni(II) with deprotonated theophylline (th) and propane-1,2-diamine (pda) were synthesized and characterized by elemental analysis, IR spectroscopy, and thermal analysis. Calculations and geometry optimization were made applying Mopac 2012 program at the level of semi-empirical method PM6.

Keywords: propane-1,2-diamine, theophylline, mixed-ligand complexes, PM6

INTRODUCTION

Theophylline is a purine alkaloid, with important biological properties. Theophylline (Scheme 1) is used in medicine to treat diseases such as asthma and chronic obstructive pulmonary disease. Transition metal complexes of theophylline may serve as model compounds for studying the interaction between metal ions and the oxopurine bases of nucleic acids. According to the literature, in basic medium the theophyllinato anion coordinates *via* N(7) [1-3] as monodentate ligand. Typically, the neutral theophylline ligand exhibits a similar coordination [4]; however, N(9) coordination was also described [5]. In some cases it acts as bidentate N(7)/O(6) chelating ligand [6,7] or as bridging ligand, involving simultaneously N(7)/O(6) chelation and N(9) coordination [8].

---

[a] *Babeş-Bolyai University, Faculty of Chemistry and Chemical Engineering, 11 Arany János Str., RO-400028, Cluj-Napoca, Romania,*
 * *Corresponding author: eforizs@chem.ubbcluj.ro*
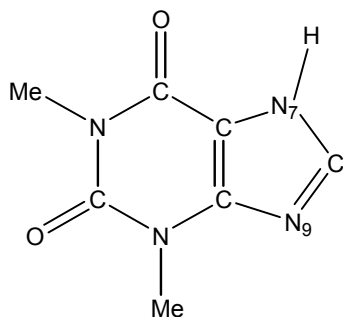
Scheme 1.

Continuing our interest in the field of bioactive materials [9-13] we started a systematic study on the coordination compounds of purine alkaloids. In the last years complexes containing theophylline and various N and N,N-donor ligands were prepared and characterized [14-16]. Here we report the synthesis of two new compounds, with the general formula [M(th)$_2$L], where M: Cu(II) (1), Ni(II) (2) and L: propane-1,2-diamine (pda) is a simple bidentate ligand [17-19]. The complexes were characterized by elemental analyses, FTIR spectroscopy and thermogravimetric analysis. Semiempirical calculations were made on the PM6 level to provide the possible structure of the complexes.

RESULTS AND DISCUSSION

FTIR spectra

The two strong bands in the IR spectrum of theophylline (1714s, 1667s), assigned to the stretching vibration of the carbonyl groups are shifted in the spectra of both complexes toward lower wavenumbers (1700 and 1660 cm^{-1} in **1**, and 1696, 1653 cm^{-1} in **2**) as a consequence of the deprotonation of theophylline at N(7) atom [9,14]. In complexes, the C=N ring vibrations (1566 cm^{-1}) of theophylline are shifted toward lower values, suggesting that the ligand coordinates *via* the imidazole N(7) atom.

There are significant changes in the bands assigned to N–H vibrations, as a consequence of the deprotonation of theophylline at N(7) atom and coordination of the diamine type ligands. The symmetric and antisymmetric stretching vibrations of the coordinated NH$_2$ groups of the diamine can be assigned at 3232 and 3133 cm^{-1} in complex **1**, and 3230 and 3199 cm^{-1} in complex **2**. The v_{CH} vibrations of propane-1,2-diamine are recorded at 2956 – 2878 cm^{-1} for the aliphatic CH$_2$ and CH$_3$ groups.

The FTIR spectra of both complexes, **1** and **2**, suggest that theophylline acts as a monodentate ligand and coordinates the metal ion *via* the N(7) atom. The diamine behaves as a bidentate chelating ligand.

Thermal analysis

The thermogravimetric curve of complex **1** indicates a stepwise decomposition. First 1.69% of adsorbed water was removed. The complex is stable up to 287 °C. In the first well defined endothermic step, the chelating propane-1,2-diamine molecule and a theophylline moieties are eliminated in the temperature range of 287 – 347 °C (experimental weight loss 50,6%, calculated 51%), suggesting that both molecules are strongly bonded (Figure 1).

The next mass loss in the temperature range 380 – 425 °C, corresponds to the release and pyrolysis of second theophyllinato moiety. The last decomposition step is exothermic, showing maxima at 412 °C; the final decomposition product is CuO (exp. solid residue 15 %; calc. 16,04%).
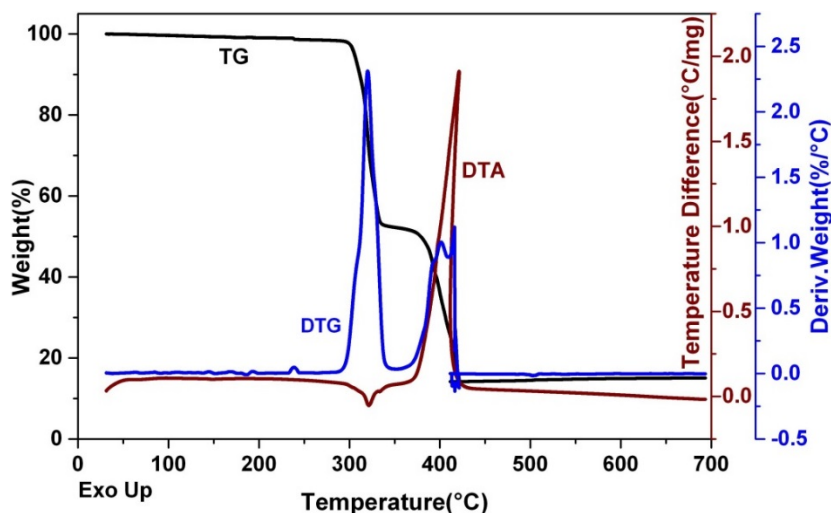

Figure 1. Thermal curves of complex **1**.

The complex **2** undergoes a single step decomposition. First the strongly adsorbed water was eliminated. The complex is stable up to 350 °C; above this value the two theophyllinato moieties and the propane-1,2-diamine molecule are evolved in the same step, in the range 390–440°C (exp. weight

loss 88.5%, calc. 88%). The oxidative decomposition in air is exothermic. The high decomposition temperature is a consequence of the bidentate binding mode of the diamine. The final decomposition product is NiO.
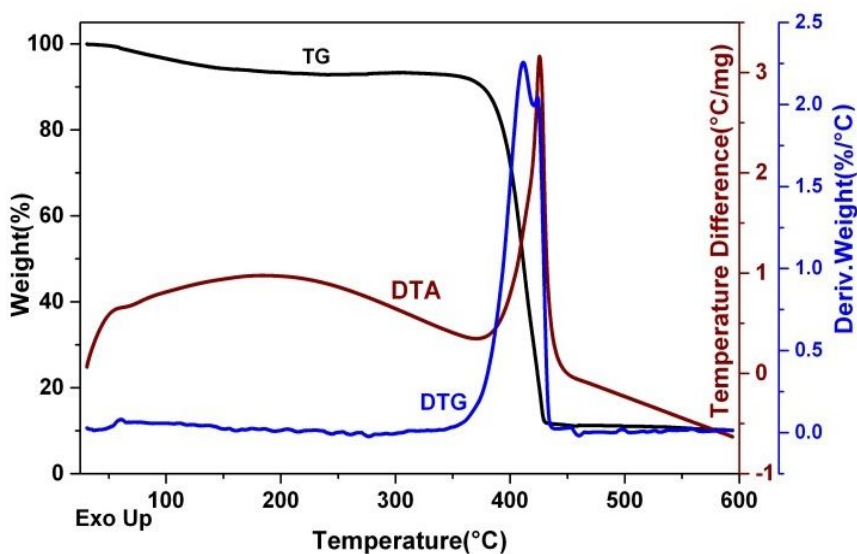

Figure 2. Thermal curves of complex **2**.

Computational details

The assumed starting structures of the complexes were generated by Spartan'06 [20] program. Geometry optimization of the structures was performed using the PM6 [21] semi-empirical method with the Mopac 2012 [22] program. By performing the vibrational analysis of the optimized structures, it was verified that real minimum points were found on the potential energy surface of the molecule. The molecular structure of the complexes **1** and **2** was optimized in the gas phase.

Optimized geometries

The presumed starting structure for complexes containing one propane-1,2-diamine ligand was a distorted tetrahedron. In this case the M(pda) chelate fragment provides only two basic structures assuming an axial or equatorial methyl group. As the two theophyllinate anions can rotate

214

freely around the M-N(7) bonds, a total of 36 rotamers (six-fold rotation around the bonds) were considered. For the Ni(II) complex high-spin (triplet) and low-spin (singlet) states were optimized. Tables 1 to 3 display data of the most stable optimized [M(th)$_2$(pda)] structure types.

Table 1. Data of [Cu(th)$_2$(pda)] complex conformers

Structure	E (kJ/mol)	Cu-N(7), Å	Cu-N(7)', Å	N(7)-Cu-N(7)', °
Cu-ax-1	-346.75	1.910	1.909	95.17
Cu-ax-2	-342.95	1.866	1.866	93.94
Cu-ax-3	-342.05	1.915	1.863	94.20
Cu-eq-1	-355.63	1.907	1.906	94.73
Cu-eq-2	-351.69	1.911	1.862	93.96
Cu-eq-3	-349.92	1.866	1.865	93.95

Table 2. Data of [Ni(th)$_2$(pda)] complex conformers – singlet state

Structure	E (kJ/mol)	Ni-N(7), Å	Ni-N(7)', Å	N(7)-Ni-N(7)', °
Ni-ax-1-s	-609.26	1.880	1.880	92.55
Ni-ax-2-s	-588.07	1.885	1.885	94.22
Ni-eq-1-s	-616.55	1.881	1.881	92.41
Ni-eq-2-s	-597.76	1.884	1.883	94.74

Table 3. Data of [Ni(th)$_2$(pda)] complex conformers – triplet state

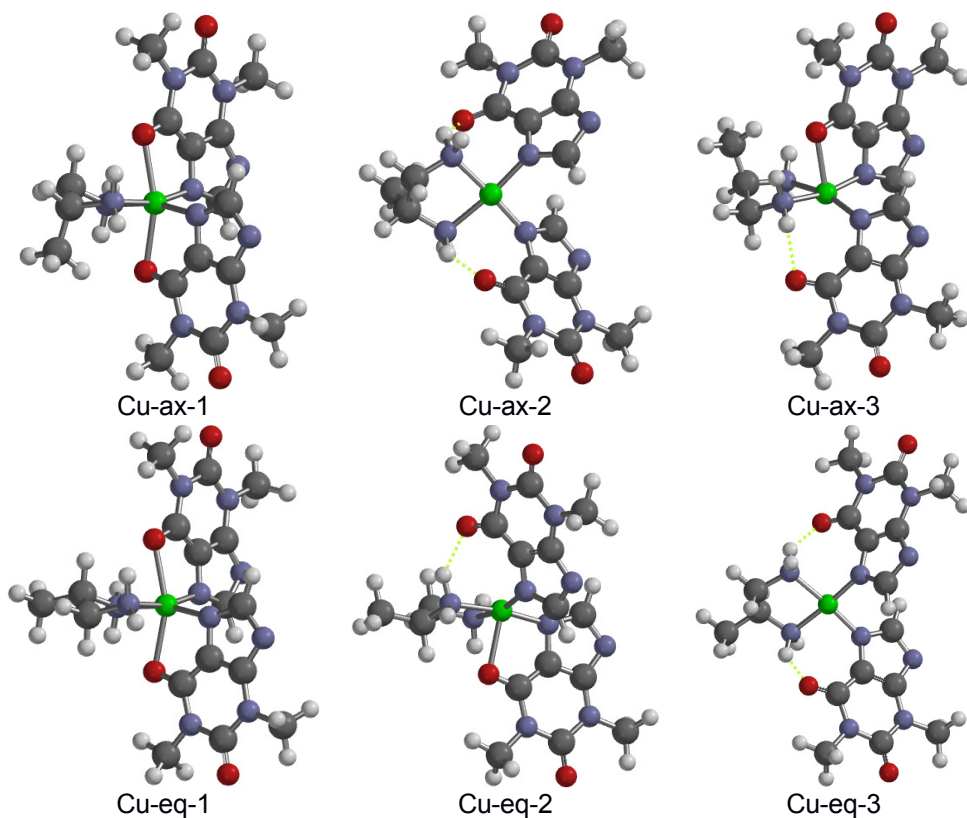| Structure	E (kJ/mol)	Ni-N(7), Å	Ni-N(7)', Å	N(7)-Ni-N(7)', °
Ni-ax-1-t	-530.07	1.928	1.924	148.95
Ni-ax-2-t	-520.29	1.954	1.950	95.70
Ni-eq-1-t	-543.44	1.928	1.926	150.09
Ni-eq-2-t	-540.90	1.951	1.942	96.14

Figure 3. Optimized structures of the complex **1**.

The equatorial orientation of the methyl group on the M(pda) chelate ring is favored energetically by ≈10 kJ/mol, on many occasions the conformation changed from axial to equatorial during the optimization.

Optimization of copper(II) complex rotamers led to 3 different structure types. The most stable structures (Cu-eq-1 and Cu-ax-1) are hexa-coordinated, both theophyllinato anions behaving as N,O chelating ligands, having 2.27 – 2.29 Å Cu-O bond distances and 160 – 165° O-Cu-O bond angles. In the case of Cu-eq-2 and Cu-ax-3, only one theophyllinato anion behaves as a chelating ligand (Cu-O distance 2.1 – 2.3 Å), the second is N(7)-coordinated, and forms an O···H hydrogen bond with the pda ligand. Structures Cu-eq-3 and Cu-ax-2 show a square planar coordination stabilized by two hydrogen bonds. The energy difference between the structure types is low – intermolecular interactions may led to the stabilization of any of them.

Energy results for the optimization of the Ni(II) complex show the stabilization of low-spin (singlet) state by 60-70 kJ/mol.
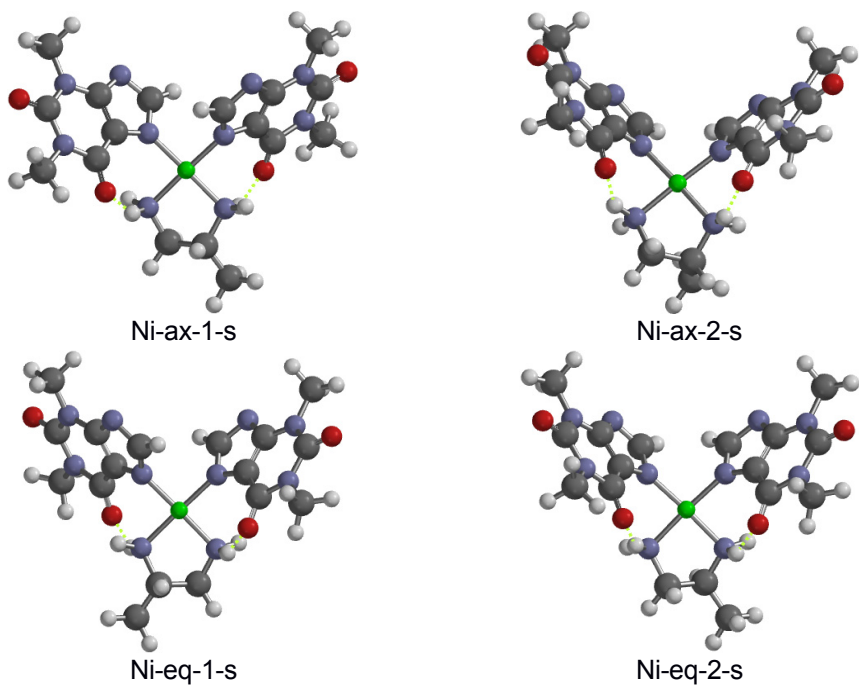
Ni-ax-1-s   Ni-ax-2-s

Ni-eq-1-s   Ni-eq-2-s

Figure 4. Optimized structures of the complex **2** – singlet state.

Ni-ax-1-t   Ni-ax-2-t

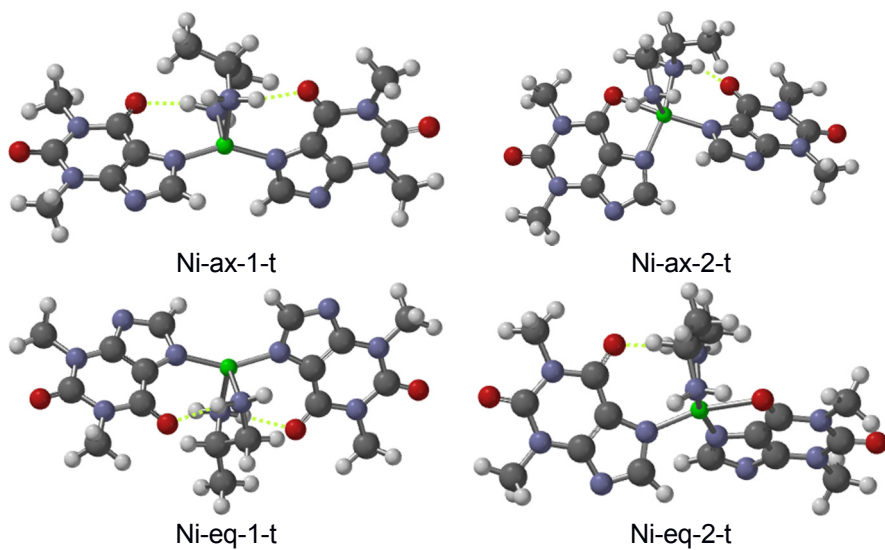Ni-eq-1-t   Ni-eq-2-t

Figure 5. Optimized structures of the complex **2** – triplet state.

The low-spin Ni(II) complex structure shows a square-planar coordination and the stabilization of the complex by hydrogen bonds. The theophyllinato ligands adopt antiparallel orientation (Ni-eq-1-s, Ni-ax-1-s), the parallel orientation (Ni-eq-2-s, Ni-ax-2-s) is higher in energy by ≈ 30 kJ/mol.

CONCLUSIONS

FTIR spectra and thermal data of **2** indicate a tetra-coordinated structure, while a higher coordination of the metal ions with bidentate bonding of diamine and at least of one theophyllinato ligand is suggested for **1**. The theophylline coordinates *via* the N(7) nitrogen or as an N(7)-O(6) bidentate ligand. The obtained theoretical data are compatible with the experimental results.

EXPERIMENTAL SECTION

The complexes were prepared in aqueous solution as previously reported [2, 14]. FTIR spectra were recorded on a Jasco FTIR 600 spectrophotometer in the 4000–400 cm^{-1} range, using KBr pellets. Thermal decomposition was investigated with a Universal V2.3C TA Instruments, at a heating rate of 10°C min^{-1}. The composition of complexes was determined by elemental analysis (C, H, N).

Syntheses of [Cu(th)₂(pda)]·(1). To a suspension of theophylline (0.2 g, 1.1 mmol) in water (10 mL) was added propane-1,2-diamine (0.5 mL). The resulted clear solution was mixed with a second solution of $Cu(CH_3COO)_2 \cdot H_2O$ (0.14 g, 0.7 mmol) in a propane-1,2-diamine–water mixture (1 mL of propane-1,2-diamine in 4 mL of water). The dark violet reaction mixture was stirred for 30 minutes at 40 °C. The resulted violet polycrystalline powder was filtered, washed with ethyl alcohol and dried. Analysis: found (calc. for $CuC_{17}H_{24}N_{10}O_4$ MW 495.74) C 41.08 (41.15), N 28.22 (28.25), H 5.00 (4.88). Yield: 32.7%, M.P.: > 300 °C.

IR (KBr pellet), cm^{-1}: $v(NH_2)$ 3232m, 3133m; $v(CH_2)$ 2953m, 2878m; $v(C=O)$ 1700s, 1660s; $v(C=N)$ 1531s.

[Ni(th)₂(pda)]·(2) was obtained hydrothermally. The theophylline (0.186 g, 1 mmol) was dissolved in 2 mL of distilled water and 0.082 mL of propane-1,2-diamine. Next, 0.117 g (0.5 mmol) of $NiCl_2 \cdot 6H_2O$ aqueous solution (8 mL) was added to this mixture dropwise under stirring. The orange solution was introduced in a 23 mL Teflon-lined stainless steel autoclave and heated at 160°C under

autogenous pressure in an oven for 4 days. The resulting solution was cooled at room temperature at a rate of 5°C/h 5°C h^{1-}. Red crystals were collected, filtered and washed with acetone. Analysis: found (calc. for $NiC_{17}H_{24}N_{10}O_4$ MW 490.89) C 41.28 (41.56), N 28.18 (28.53), H 4.88 (4.93), M.P.: >300 °C.

IR (KBr pellet), cm^{-1}: $v(NH_2)$ 3230m, 3199m; $v(CH_2)$ 2956m, 2879w; $v(C=O)$ 1696vs, 1653vs; $v(C=N)$ 1528m.

Abbreviations: m - medium, s – strong, vs – very strong, w – weak.

REFERENCES

1. T.J. Kistenmacher, D.J. Szalda, L.G. Marzilli, *Inorganic Chemistry*, **1975**, *14*, 1686.
2. W.J. Birdsall, M.S. Zitzman, *Journal of Inorganic & Nuclear Chemistry*, **1979**, *41*, 116.
3. N.S. Begum, H. Manohar, *Polyhedron*, **1994**, *13*, 307.
4. M.B. Cingi, A.M.M. Lanfredi, A. Tiripicchio, M. Tiripicchio-Camellini, *Transition Metal Chemistry*, **1979**, *4*, 221.
5. K. Aoki, H. Yamazaki, *Journal of the Chemical Society - Chemical Communications*, **1980**, 186.
6. D.J. Szalda, T.J. Kistenmacher, L.G. Marzilli, *Journal of the American Chemical Society*, **1976**, *98*, 8371.
7. D. Cozak, A. Mardhy, M.J. Olivier, A.L. Beauchamp, *Inorganic Chemi*stry, **1986**, *25*, 2600.
8. J. Lorberth, W. Massa, M.E. Essawi, L. Labib, *Angewandte Chemie-International Edition in English*, **1988**, *27*, 1160.
9. E. Forizs, L. David, O. Cozar, V. Chis, G. Damian, J. Csibi, *Journal of Molecular Structure*, **1999**, *482*, 143.
10. E. Forizs, L. David, O. Cozar, C. Craciun, M. Venter, M. Kilyen, *Journal of Molecular Structure*, **1997**, *408*, 195.
11. F. Goga, E. Forizs, A. Avram, A. Rotaru, A. Lucian, I. Petean, A. Mocanu, M. Tomoaia-Cotisel, *Revista de Chimie (Bucharest)*, **2017**, *68(6)*, 1193.
12. O. Horovitz, Gh. Tomoaia, A. Mocanu, T. Yupsanis, M. Tomoaia-Cotisel, *Gold Bulletin*, **2007**, *40(4)*, 295.
13. G. Furtos, M. Tomoaia-Cotisel, C. Garbo, M. Senila, N. Jumate, I. Vida-Simiti, C. Prejmerean, *Particulate Science and Technology*, **2013**, *31(4)*, 392.
14. P. Bombicz, J. Madarász, E. Forizs, M. Czugler, G. Pokol, S. Gál, A. Kálmán, *Zeitschrift für Kristallographie*, **2000**, *215*, 317.
15. E. Forizs, A. Debreczeni, A. Patrut, A.-Z. Kun, I.B. Cozar, L. David, I. Silaghi-Dumitrescu, *Revue Roumaine de Chimie*, **2010**, *55(10)*, 697.
16. C. Nagy, C. Somesan, A.-Z. Kun, B. Mihaly, E. Forizs, L. David, *Studia UBB Chemia*, **2011**, *56(3)*, 265.

17. I. Potočňák, M. Vavra, D. Steinborn, C. Wagner, *Acta Crystallographica Section E - Structure Reports Online*, **2008**, *64*, m235.
18. E. Colacio, R. Kivekas, F. Lloret, M. Sunberg, J. Suarez-Varela, M. Bardaji, A. Laguna, *Inorganic Chemistry*, **2002**, *41*, 5141.
19. X. Hu, X. Xu, D. Wang, X. Li, *Acta Crystallographica Section E- Structure Reports Online*, **2008**, *64*, m1636.
20. Spartan'06, Wavefunction, Inc., Irvine, CA **2006**.
21. J.J.P. Stewart, *Journal of Molecular Modeling,* **2007**, *13*, 1173.
22. MOPAC2012, J.J.P. Stewart, Stewart Computational Chemistry, Colorado Springs, CO, USA, HTTP://OpenMOPAC.net (**2012**).